DOCTOR OF PHILOSOPHY

Mineral Dynamics in Sea Ice Brines

Butler, Benjamin

Award date:
2016

Awarding institution:
Bangor University

Mineral Dynamics in Sea Ice Brines

Benjamin Miles Butler

May 2016

A thesis presented for the degree of
Doctor of Philosophy

PRIFYSGOL
BANGOR
UNIVERSITY

School of Ocean Sciences
Bangor University
Wales, United Kingdom

Summary

The sea ice microstructure is permeated by millimetre to micrometre sized inclusions filled with concentrated seawater-derived brine. It is within these brines that the *in-situ* chemical and biological reactions occur. The brines are confined to a temperature-dependent composition, becoming more concentrated and reducing in volume with decreasing temperature. Upon sufficient cooling the coupled effects of lower temperature and higher salinity results in the brine exceeding the solubility of a mineral, which precipitates. Given the complex composition of seawater, there are several minerals that can exceed saturation within the polar temperature spectrum, each with their own dynamics and environmental significance. This thesis investigates mirabilite ($Na_2SO_4 \cdot 10H_2O$), gypsum ($CaSO_4 \cdot 2H_2O$) and hydrohalite ($NaCl \cdot 2H_2O$). The small crystal size (μm), temperature dependence, and solubility of these minerals acts to limit the scope for studying their existence and behaviour in sea ice with field experiments. For these reasons, their dynamics have been investigated in a laboratory setting using synchrotron X-ray powder diffraction experiments, and measurements of mineral solubility in solutions representative of sea ice brines at thermal equilibrium. The experimental observations are supplemented with model predictions, and together are used to provide a comprehensive assessment of the existence, role and effects of mineral precipitation in sea ice. Mirabilite and hydrohalite are found to cause substantial changes to brine composition and the sea ice microstructure, and are observed to interact in accordance with equilibrium crystallisation. The precipitation of mirabilite is also found to have implications for the measurement of sea ice brine salinity. In contrast, the solubility of gypsum displays complex dynamics between 0.2 and -25 °C, and is shown to be highly dependent upon the SO_4^{2-} concentration, resulting in the processes of mirabilite precipitation and dissolution controlling the fate of gypsum in sea ice.

Acknowledgements

My foremost thanks go to my supervisor, Hilary Kennedy, for allowing me the opportunity to study for this PhD and then providing an outstanding level of support along the way. I couldn't have wished for a better supervisor, and I will always be grateful for her generosity.

The time spent working alongside Stathys Papadimitriou in the laboratory has been an absolute pleasure. Being able to bombard Stathys with questions each day accelerated my understanding of marine geochemistry, and helped develop this investigation immeasurably. Equally, I was fortunate enough to work alongside Paul Kennedy prior to his retirement, whose helpfulness and humour never failed to keep me entertained.

Outside of the research group, there are many others that I would like to acknowledge. Firstly Vera Thoss in the School of Chemistry, who has helped me develop as a researcher since my MSc 4 years ago. Collaborating with Vera's research group for aspects of my research was invaluable, and would have been impossible without the additional help of Anna Santoro. The help from Chiu Tang at Diamond Light Source has also been pivotal throughout my studies, and having opportunities to use the world class facilities on Beamline I11 proved a real highlight.

At a personal level, I would like to thank my friends at the School of Ocean Sciences, and elsewhere across North Wales. Together you have made my time in this beautiful part of the world very special. My family and Aisling will no-doubt miss the regular visits to Anglesey and Snowdonia, but not as much as I will.

Lastly I thank my viva committee, Martyn Tranter, David Thomas and David Bowers, for their time and effort. Exchanging ideas with such established cryospheric scientists was a fitting way to finish this process, and I will endeavour to apply their generous advice as I begin a new chapter in my life.

This work was made possible through a NERC Algorithm Studentship, and an additional Student Research Grant from the International Association of Geochemistry. The support from both is gratefully acknowledged.

Thesis overview

Chapter 1 introduces key concepts about sea ice, beginning with its large-scale role as an Earth system before before focussing in upon its microscale properties. In doing so, the current understanding of mineral dynamics within sea ice is reviewed, whilst knowledge gaps are identified, allowing for the aim and objectives of this thesis to be defined.

Chapter 2 details the analytical and modelling methods that encompass the investigations in chapters that follow. This includes details relating to brine and mineral analyses involved in all experimental work, along with a description of the equations that govern models used to describe the growth of first year Arctic sea ice, and mineral–solution equilibria. More study-specific methods are detailed in subsequent chapters.

Chapter 3 is published as a research article in the Journal of Geophysical Research: Oceans (Butler and Kennedy, 2015). This investigation uses synchrotron X-ray powder diffraction to delve into the dynamics of mirabilite, hydrohalite and ice in frozen seawater brines, providing the first X-ray identification for their presence in frozen seawater, and evidence for their interaction with one-another.

Chapter 4 is published as a research article in Geochimica et Cosmochimica Acta (Butler et al., 2016). This investigation defines the solubility of mirabilite in sea ice brines at thermal equilibrium between 0.2 and -20.6 °C, and describes the dynamics of this relatively elusive mineral within context of sea ice by incorporating the measurements into a 1D model for the growth and desalination of first-year Arctic sea ice. Mirabilite is shown to be the first major mineral to precipitate in sea ice, and this chapter provides the foundations upon which the two further experimental chapters are built.

Chapter 5 examines the effect of mirabilite precipitation on the measurement of absolute and practical salinities of sea ice brines, and has been submitted to Marine

Chemistry. The analysis of laboratory measurements, model predictions, and data from the field highlights how mirabilite precipitation in sea ice, and the associated changes in solution composition, are reflected in the different concepts by which salinity can be measured.

Chapter 6 investigates the solubilities of gypsum and hydrohalite down to −25.0 °C. The measurements are used to model the depth profile and temporal evolution of hydrohalite in sea ice over an Arctic winter, and propose the mechanism by which it precipitates so rapidly in sea ice at temperatures below −22.9 °C. The dynamics of gypsum are shown to be complex and highly dependent upon the solubility of mirabilite, which represents the main sulphate sink in sea ice. The gypsum solubility measurements are used to elucidate the potential processes that resulted in its recent identification in sea ice.

Lastly, chapter 7 aims to synthesise the 4 experimental chapters, outlining the general contribution to knowledge, the limitations of this research, and the directions in which future research may wish to venture based on the findings presented herein.

Contents

List of Figures

List of Tables

Chapter 1

Introduction

1.1 The major ions in seawater

Seawater is a complex aqueous solution, within which, every naturally occurring element on Earth has been detected (Millero, 2005). Seawater's composition is dominated by six major ions; Na^+, K^+, Mg^{2+}, Ca^{2+}, Cl^- and SO_4^{2-}; which together account for 99.4 % of the total weight of dissolved salt (Millero et al., 2008). The solution composition found throughout the world ocean today has developed over geological timescales via processes governed by equilibrium reactions (Stumm and Morgan, 1996), and is considered as a steady state system. The steady state properties crucially result in an exceptionally constant composition of seawater's major ions relative to one another (figure 1.1). The constant stoichiometry of seawater's major ions was initially proposed in the 19$^{\text{th}}$ Century (Forchhammer, 1865; Dittmar et al., 1873), and upon oceanographic evidence for the hypothesis, went on to give rise to the concept of salinity, which is a simple measure of the mass of dissolved salt per unit mass of seawater.

Seawater salinity (absolute, S_A) varies from <20 g $kg^{-1}_{solution}$ in hyposaline seas such as the Baltic, to salinities in excess of 40 g $kg^{-1}_{solution}$ in hypersaline water bodies such as the Red Sea (Millero, 2005). The salinity markedly affects the freezing process of seawater. First, the freezing point is lowered by approximately 0.054 °C for every 1 g $kg^{-1}_{solution}$ increase in salinity (Assur, 1960; Vancoppenolle et al., 2007), and for typical oceanic water results in a freezing point of $\sim$−1.8 °C. Second, the extraordinary resistance of ice to incorporating ions into its crystal lattice leads to the rejection of almost all dissolved ions during freezing, which has profound effects on the microstructure of seawater when it freezes (Petrich and Eicken, 2010). These

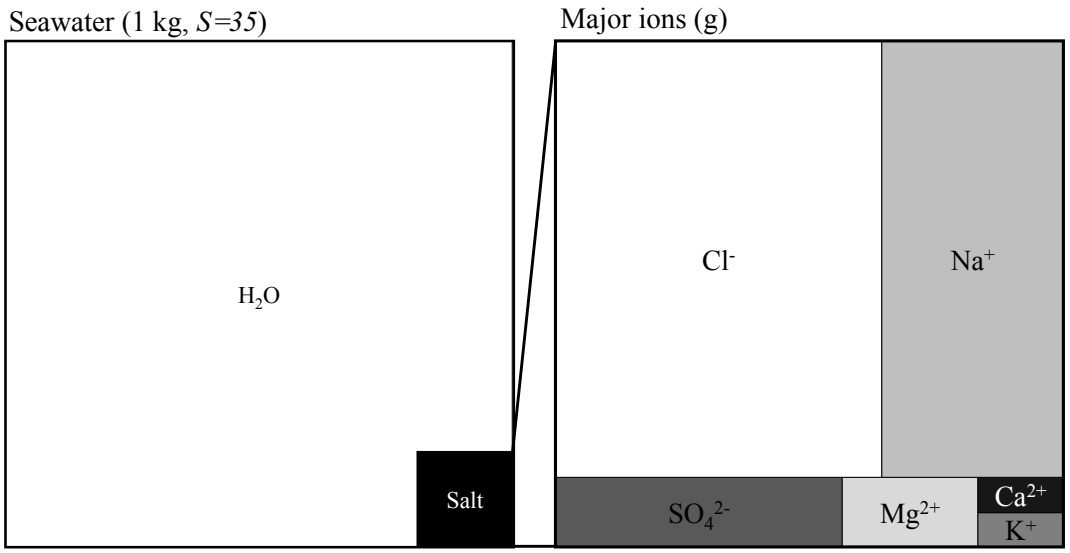

Figure 1.1: Salinity tree map: A representation of the total salt contained in 1 kg seawater (left), and the proportion of the six major ions (g) to one another (right).

two processes combine during the formation of sea ice to create an environment with complex dynamics and global physical and biological importance. To understand the behaviour of salt in frozen seawater on Earth (i.e., sea ice) the role of sea ice as an Earth system will be first be introduced, followed by a description of its growth process and the dynamics of brine inclusions that permeate its microstructure.

1.2 Sea ice

1.2.1 Sea ice as an Earth system

When seawater freezes in high latitude environments on Earth, sea ice forms, which at any one time covers approximately 5 % of the Earth's surface. Arctic and Antarctic sea ice undergo opposing seasonal cycles. The Arctic sea ice maximum is reached between February and March, covering the entire Arctic Ocean, extending from the North Pole to 44 °N with an areal extent of approximately 15.7×10^6 km^2. Between March and September the ice recedes by approximately 11.4×10^6 km^2 to its minimum. Whilst the Arctic sea ice is at its minimum, the sea ice in Antarctica reaches its maximum, covering 18.8×10^6 km^2 between 55 and 75 °S. Antarctic sea ice decreases in coverage by 15.2×10^6 km^2 between September and February (Dieckmann and Hellmer, 2010).

Despite sea ice being a relatively thin ($1 - 2$ m) layer at the interface between the ocean and atmosphere, it plays a crucial role in the regulation of Earth's climate system. Sea ice is highly reflective to incoming solar radiation, therefore having a high albedo, defined as the ratio of incoming to outgoing radiation. The open ocean has an albedo of approximately 0.25, while estimates for the albedo of snow-free first-year sea ice show an approximate doubling of reflected radiation at a thickness of 1 m, with an albedo of 0.47 (Cox and Weeks, 1988). Thick, multi-year ice can have an albedo ranging between 0.60 and 0.85, while the presence of dry snow on top of the ice can increase this to between 0.90 and 0.97 (Grenfell, 1977). Sea ice therefore has a vital role in mediating the surface energy balance in polar regions, and climatic feedback processes associated with its melt will be pivotal in decades to come as polar regions continue to be affected by climate change. (Maykut, 1978).

Moving from the surface to the underside of sea ice brings us to another key feature of this system: its contribution to water mass transformation and water column stability. In the Southern Ocean sea ice contributes to the formation of Antarctic Bottom Water (AABW). The AABW plays a key role in the thermohaline circulation, and is defined as being colder than 0 °C, with salinities typically exceeding 34.6 g $\mathrm{kg}^{-1}_{\mathrm{solution}}$ (Weeks, 2010). This water mass forms along the continental shelf of Antarctica, where the expulsion of cold, saline brines during sea ice formation (see section 2.2) contribute to its low temperature and elevated salinity ($0.05 - 0.15$ g $\mathrm{kg}^{-1}_{\mathrm{solution}}$) (Goosse et al., 1997). Modelling of AABW in the absence of the salt flux from sea ice shows a reduction in AABW formation by more than 40 % (Goosse and Fichefet, 1999). The dense AABW sinks along the Antarctic continental shelf, flowing back towards the equator at a rate of up to 25 Sv (Goosse et al., 1997) as part of the thermohaline circulation.

In the Arctic, sea ice plays a less critical role in the formation of the local deep water mass, North Atlantic Deep Water (NADW). Rather, the formation of NADW is dominated by cooling of warm, saline water transported by the Gulf Stream. The role of sea ice on the water column in the Arctic Ocean is instead dominated by its contribution to the maintenance of the Arctic halocline. The Arctic halocline is characterised by a cool (below -1 °C), less saline (~ 32 g $\mathrm{kg}^{-1}_{\mathrm{solution}}$) layer in the upper $50 - 100$ metres of the water column, overlying warmer, more saline water

(Notz, 2005) (figure 1.2). The halocline inhibits the warmer water interacting with the sea ice and the potential ice loss that could arise in its absence. It is understood that sea ice contributes to the stability of the halocline by an inflow of saline water formed from the sinking of cold, saline brines rejected during sea ice formation. The inflow is carried along the continental shelf that surrounds the Arctic Basin and infiltrates between the colder, fresher, layer above, and NADW below (figure 1.2).

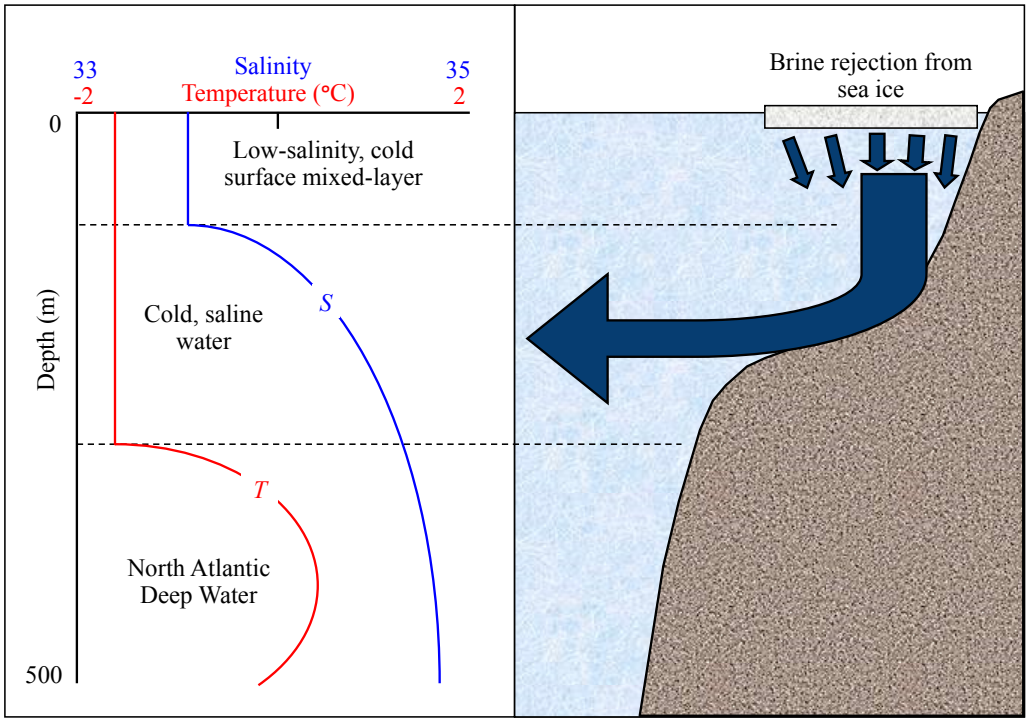

Figure 1.2: Schematic explaining the lateral inflow of cold/saline water, released during sea ice formation, contributing to the maintenance of the Arctic halocline. Figure adapted from Aagaard et al. (1981).

Aside from its physical importance in the Southern and Arctic Oceans, sea ice is one of Earth's major biomes, covering a similar area to that of deserts and tundra (Thomas and Dieckmann, 2002). The hostility of sea ice as a habitat includes extremes in temperatures and salinity, combined with a severely limited availability of space and light. Sea ice is therefore considered a habitat for extremophiles (Thomas and Dieckmann, 2002). The ecology of sea ice is dominated by microalgae, bacteria, viruses, flagellates, fungi and small protozoans (Ewert and Deming, 2013). The organisms reside within the porous microstructure of sea ice (sections 1.2.3 and 1.3), predominantly existing towards the lower parts of the ice where it has greater porosity and, hence, conditions are closer to that of seawater. Krembs et al.

(2000) estimated that $6-41$ % of the interstitial surface area of sea ice may be covered by microorganisms, compared to a range < 1 % for that of soil. The food chain in sea ice is fueled by the availability of nutrients supplied from underlying seawater that infiltrates the ice, and the community plays an important role in the cycling of carbon (Miller et al., 2011) and nitrogen (Rysgaard and Glud, 2004) in polar regions. This biological importance also extends from the ice to the surrounding polar seas, where it has been observed that the abundance of krill in the Southern Ocean is closely linked with the total area of sea ice and the associated availability of microalgae (Loeb et al., 1997).

Given the significance of sea ice as an Earth system, an understanding of its dynamics are essential for an accurate representation of the Earth's polar regions. This becomes especially crucial when accounting for the effects of climate change.

1.2.2 Sea ice in a changing climate

It is expected for polar regions to experience stronger effects of current and impending climate change than other parts of the world for several reasons (Hassol, 2004; Notz, 2005). The first relates to the albedo effect, whereby a greater proportion of incoming solar radiation is absorbed when ice/snow melt uncovers darker land or sea beneath. Secondly, the typically low temperatures in polar regions results in additional absorbed energy contributing to warming, rather than evaporation. Finally, the thinner troposphere in polar regions, compared to temperate and tropical latitudes, requires less energy to facilitate a temperature increase.

Such effects are currently observed most notably in the Arctic. According to the latest IPCC estimates (Vaughan et al., 2013), between 1979 and 2012 the annual coverage of Arctic sea ice decreased by $3.5-4.1$ % per decade, equivalent to a decadal loss of 0.45 to 0.51×10^6 km^2. Furthermore, evidence suggests that for the summer sea ice minimum this decrease is in the range of $9.4 - 13.6$% per decade (0.73 to 1.07×10^6 km^2, figure 1.3). There is evidence to suggest that the rapid summer sea ice retreat is a result of sea surface temperatures that are unprecedented in at least the last $1,450$ years. While Arctic sea ice extent displays clear reductions in recent decades, there is a 'polar paradox' in that the annual mean Antarctic sea ice extent increased at a rate of between 1.2 and 1.8 % per decade between 1979 and

2012. Evidence indicates strong regional differences (Vaughan et al., 2013), and the main exception to the overall increase is the Antarctic Peninsular, which is often cited as the fastest warming region on Earth (Mulvaney et al., 2012). Further more, theories have been proposed to explain the increased coverage of Antarctic sea ice, that include: Enhanced basal melting of Antarctic ice shelves providing a cooler, fresher surface layer underneath the ice that shields it from warmer waters below (Bintanja et al., 2013); and changes in wind-patterns around the Antarctic continent (Holland and Kwok, 2012).

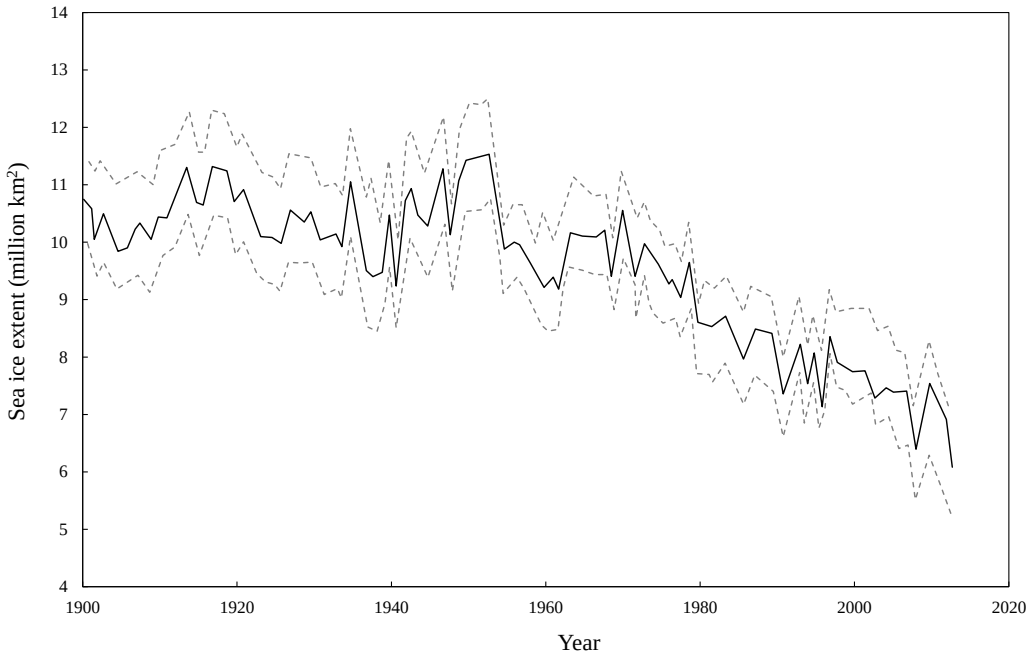

Figure 1.3: The record of Arctic summer sea ice areal extent between 1900 and 2012 (Vaughan et al., 2013). Solid line represents the mean, and dashed lines represent the high and lower estimates.

The physical and biological importance of sea ice, combined with the rapid changes occurring within this system, substantiates the need for a thorough understanding of its dynamics with changing temperature. Hereafter I concentrate upon the *in-situ* processes that occur within the sea ice microstructure, which first requires an understanding of the processes that govern its formation.

1.2.3 Sea ice formation and microstructure

Depending on whether the local atmospheric and oceanic conditions are calm or agitated, the formation of sea ice may occur by two distinct processes. Each process

commences with the crystallisation of millimetre-sized frazil ice crystals once the ocean's temperature drops to below its freezing point (-1.86 °C at $S = 34$). Under calm, non-turbulent conditions, the needle-like frazil crystals accumulate and form a viscous layer at the ocean surface, commonly described as grease ice (Weeks, 2010). The frazil crystals eventually freeze together as the solid fraction of grease ice increases, forming a thin but continuous sheet of young ice, known as nilas (Martin and Kauffman, 1981). When nilas is <5 cm thick it remains transparent to the underlying ocean (dark nilas), but as the ice develops to a thickness of ∼10 cm the nilas takes on a grey-white appearance (light nilas) (Petrich and Eicken, 2010). Once a sheet of nilas is established, the growth process transitions to the thermodynamically driven formation of congelation ice. During an Arctic winter this growth process can result in first-year sea ice reaching a thickness of $1.5 - 2$ m (figure 1.4).

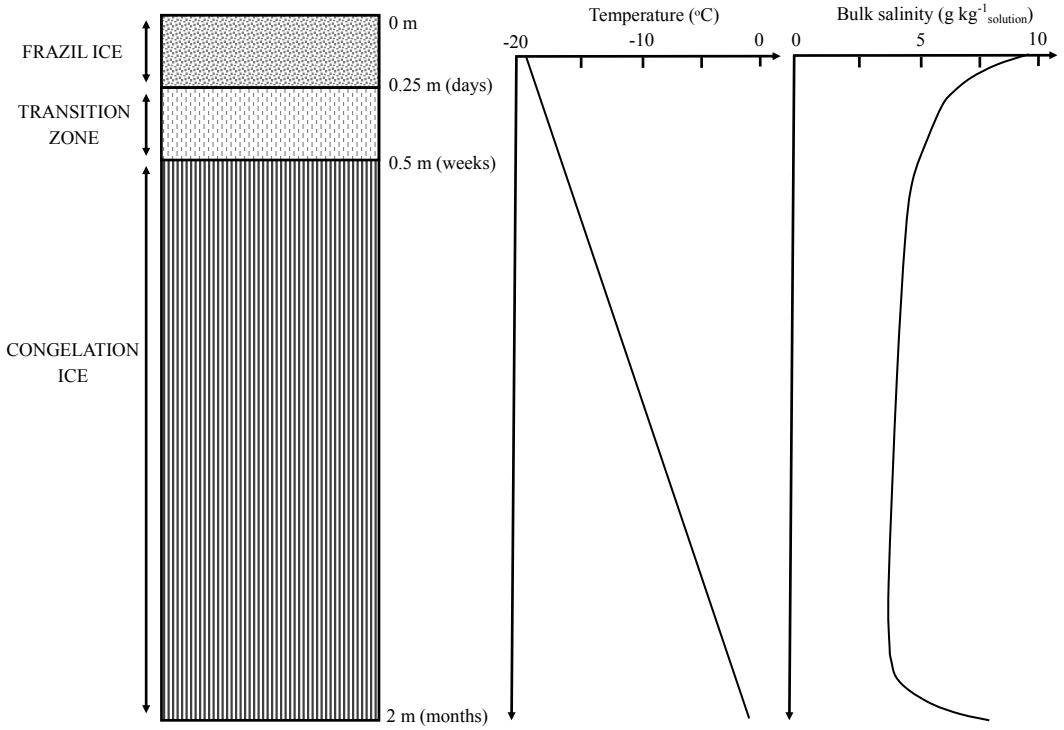

Figure 1.4: Schematic summarising the main ice types formed under calm conditions, and typical temperature and salinity profiles of first-year sea ice. Adapted from Petrich and Eicken (2010).

In contrast, under agitated conditions the associated turbulence prevents frazil ice crystals from developing into nilas. Within a wave field the slushy frazil suspension is

subjected to cyclic compression, during which the crystals eventually freeze together to form flocs with increasing density (Weeks, 2010). These continue to grow in size by accretion from the surrounding frazil ice and solidify through continued freezing between the crystals. Upon frequent collisions with surrounding flocs in a turbulent ocean, the ice develops into flat, round floes known as pancake ice (figure 1.5). Individual pancakes range from decimetres to metres in diameter and commonly exceed 10 cm in thickness (Weeks, 2010). As the pancakes grow and advance upon one-another, they can consolidate into a solid sheet of sea ice. Sheet ice developed in this way is characterised by an uneven surface topography and rough bottom features that reflect the rafting of pancakes prior to consolidation. If pancake ice becomes a consolidated sheet of sea ice, growth may then continue as congelation ice.

Congelation ice growth is a thermodynamically driven process. As long as the temperature at the ice surface remains below the freezing point of seawater, there is an upward heat flux through the ice pack. The flux removes heat energy from the ice-ocean interface, and, providing that it exceeds the heat energy provided to the bottom of the ice by the ocean, results in new ice formation (Notz, 2005). Congelation ice growth therefore occurs downwards, with individual ice crystals growing with a preferred orientation (horizontal c-axis) (Weeks, 2010), resulting in parallel rows of cellular ice projections called dendrites. Concentrated seawater derived brine that is rejected during ice formation accumulates in the channels between dendrites. As the dendrites advance, this brine becomes encapsulated within millimetre to micrometre sized inclusions which act as the site of the *in-situ* chemical and biological reactions within sea ice (Thomas et al., 2010).

The inclusions within congelation ice respond dynamically to temperature, which was comprehensively investigated using microphotography by Light et al. (2003). Inclusions can be classified as either pockets or tubes, whereby pockets display diameters <0.50 mm, while tubes typically have greater vertical than horizontal lengths (figure 1.6). Brine inclusions substantially decrease in size with decreasing temperature in sea ice, while the reverse occurs upon warming, ranging in size from approximately 10 mm near the freezing point of seawater, to 10 μm at ~ -20 °C (Light et al., 2003, 2009). The concentrated brines within the inclusions exhibit ex-

ceptionally high salinities (exceeding 220 g $kg^{-1}_{solution}$), and their dynamics encompass the major geochemical changes in sea ice with changing temperature. Such changes have implications for the physical, chemical and biological properties of sea ice (Assur, 1960; Light et al., 2004, 2009; Butler et al., 2016; Thomas and Dieckmann, 2002). The volume of brine and its composition within sea ice is ultimately controlled by the congelation ice growth process, brine drainage, and local temperature regimes. Therefore these factors must also be introduced.

Figure 1.5: Pancake ice in the Southern Ocean. Photo printed with permission from Erin Dillon (www.erinmdillon.wordpress.com).

1.2.4 Congelation ice growth, temperature regimes and brine drainage

Unlike frazil and pancake ice, the growth of congelation ice can be described thermodynamically by an energy balance between the ice and atmosphere (Maykut, 1978). Furthermore, the entrapment and drainage of brine during congelation ice growth can be described empirically (Cox and Weeks, 1988). Together with climatic information typical of the Arctic Basin, these descriptions can be used to evaluate the

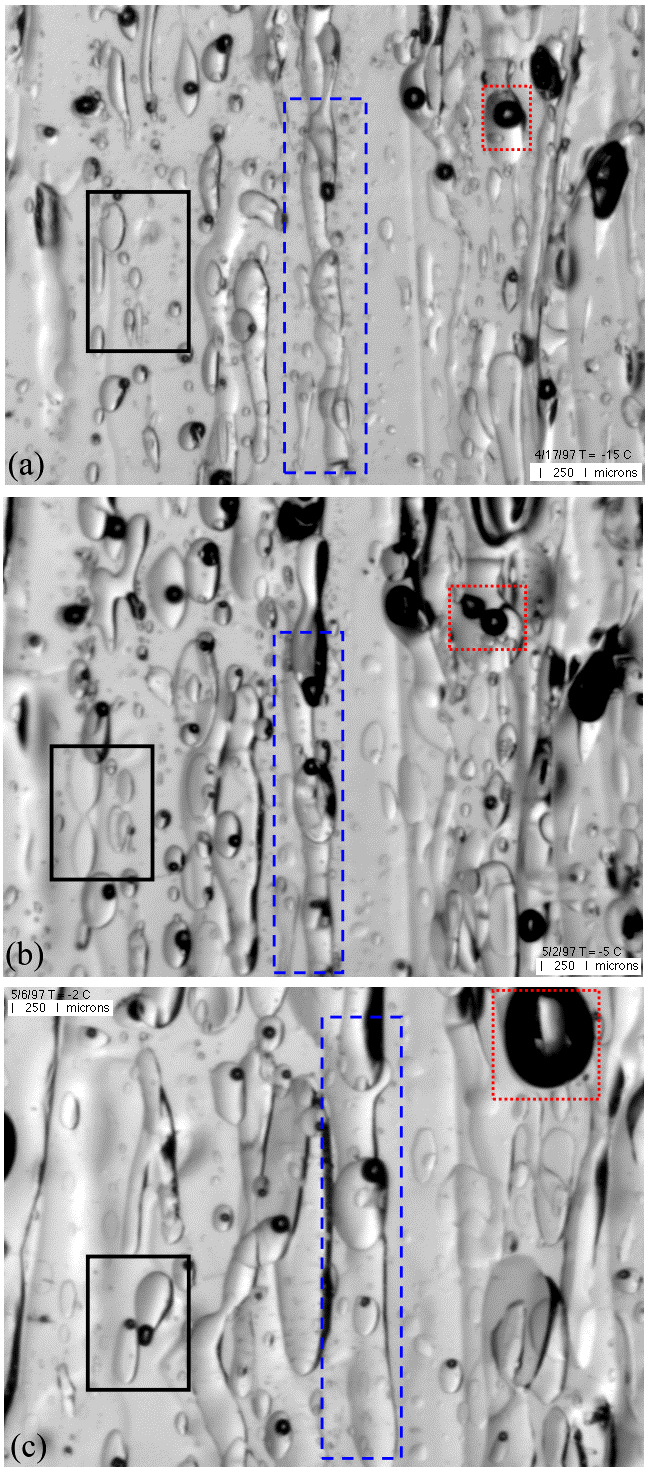

Figure 1.6: Sequence showing changes in the microstructure of first-year congelation ice during warming: (a) −15 °C, (b) −5 °C, and (c) −2 °C. The width of each image is equivalent to 3.5 mm. Black-solid boxes highlight regions of brine pockets, blue-dashed boxes highlight brine tubes, and red-dotted boxes highlight gas bubbles. Printed with permission from the corresponding author of Light et al. (2003).

growth of first-year congelation ice and the evolution of brine content within it.

Maykut (1978) provided an idealised atmospheric temperature regime for the Arctic basin (figure 1.7), which can be combined with similar descriptions of insolation and surface albedo (Maykut, 1978; Cox and Weeks, 1988) to model the growth of snow free, first-year congelation ice using a surface energy balance equation (see section 2.2). Modelling sea ice in this idealised scenario provides information on how first-year sea ice develops over an Arctic winter (figure 1.8). Between October and mid-February, the modelled sea ice thickness increases from 0 to 213 cm, reaching 50 cm within 1 month, 100 cm within 2 months, and 150 cm after ∼3 months. Growth of the ice pack is reflected in the temperature at the ice-atmosphere interface. Prior to the onset of sea ice formation, the surface temperature is −1.8 °C (i.e., the freezing point of seawater), while the air temperature is −15 °C (figure 1.8, middle). Upon freezing, the surface and air temperatures converge rapidly at first because ice replaces seawater as the phase interacting with incoming solar radiation. By mid-February, when the air temperature is −33 °C, the difference between the surface and air temperatures is <1 °C. The temperature profile within the ice column during first-year sea ice growth is understood to be a linear function (Cox and Weeks, 1988; Dugan and Lamoureux, 2011) between the temperature at the ice-atmosphere interface (dependent upon the energy balance) and ice-ocean interface (fixed at the freezing point of the underlying seawater) (figure 1.4). The rate of growth of the ice changes dynamically throughout the winter, initially occurring rapidly, taking 0.1 days to grow by a 0.5 cm depth increment. As the ice pack thickens, this growth rate plateaus, reaching 0.45 days per 0.5 cm of growth by mid-February (figure 1.8, bottom).

In contrast to this idealised scenario, the temperature regime of natural sea ice is governed by local weather patterns and displays substantial variation over hourly timescales. Continuous measurements of the air, ice surface (under 10 cm of snow), and ice column (10 cm below ice surface) temperatures for land-fast sea ice in the coast of Barrow, Alaska (156.5° W, 71.4° N) are displayed in figure 1.7 (Ewert and Deming, 2013). The atmospheric temperature fluctuates by approximately 4.7 °C per day on average, while the ice column temperature is substantially more stable, fluctuating by approximately 0.6 °C per day (figure 1.7). The data also highlight how

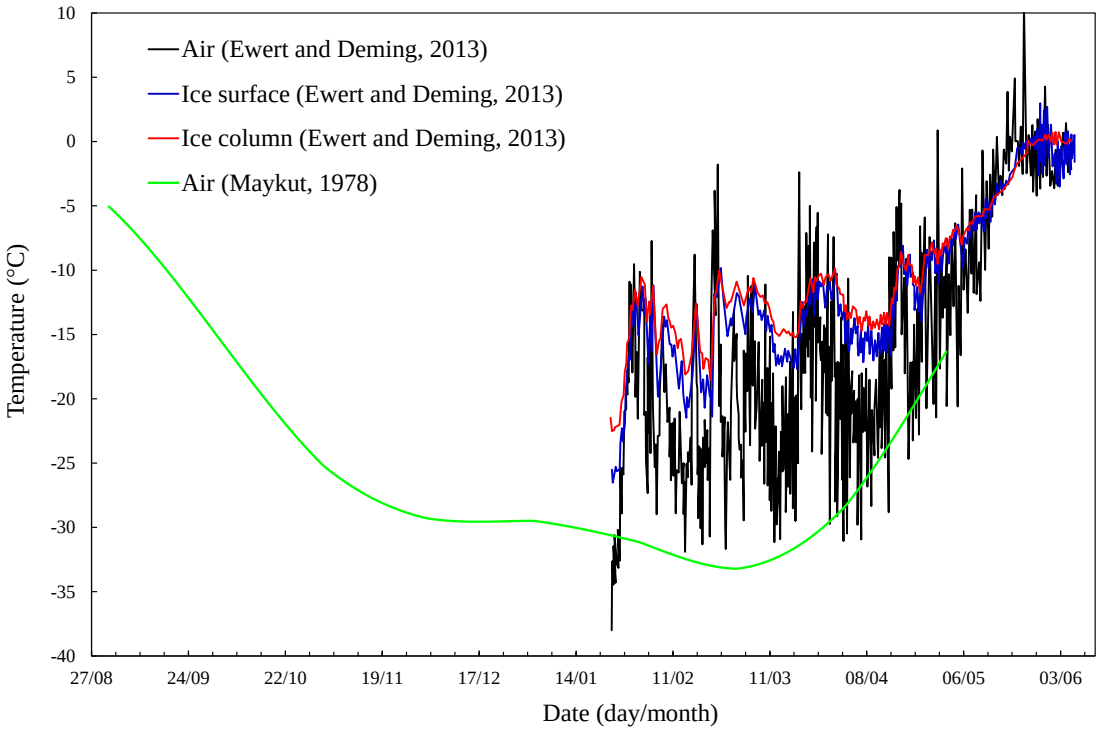

Figure 1.7: Atmospheric temperature for the Arctic basin using the stepwise polynomial function provided by (Maykut, 1978), plotted alongside measured temperature regimes of sea ice at the Mass Balance Observatory Site (Barrow, Alaska, USA) extracted from Ewert and Deming (2013).

the temperature regime experienced within the ice column can be heavily influenced by the insulative properties of snow, which usually covers sea ice (by approximately 30 cm in the Arctic) older than a few days (Sturm and Massom, 2010). The effective thermal conductivity of snow ranges from 0.1 to 0.6 W m^{-1} K^{-1} (Sturm and Massom, 2010), compared to that of sea ice ranging from 2.1 to 2.5 W m^{-1} K^{-1} (Pringle et al., 2007). Snow cover therefore decreases the energy exchange between the atmosphere and sea ice (Sturm and Massom, 2010). For the data displayed in figure 1.7, 10 cm of snow cover present throughout the measurements results in temperatures at the ice surface being on average 5.6 °C warmer than the air temperature, and daily fluctuations reducing to 1.4 °C. Snow cover therefore dampens high frequency temperature variations within the ice pack and aids in maintaining higher temperatures that are more conducive for colonization by microorganisms (Ewert and Deming, 2013). The extent to which snow insulates the ice pack varies with its thickness, grain size and density (Sturm and Massom, 2010), therefore sea ice exposed to identical atmospheric conditions can still vary greatly in the *in-situ*

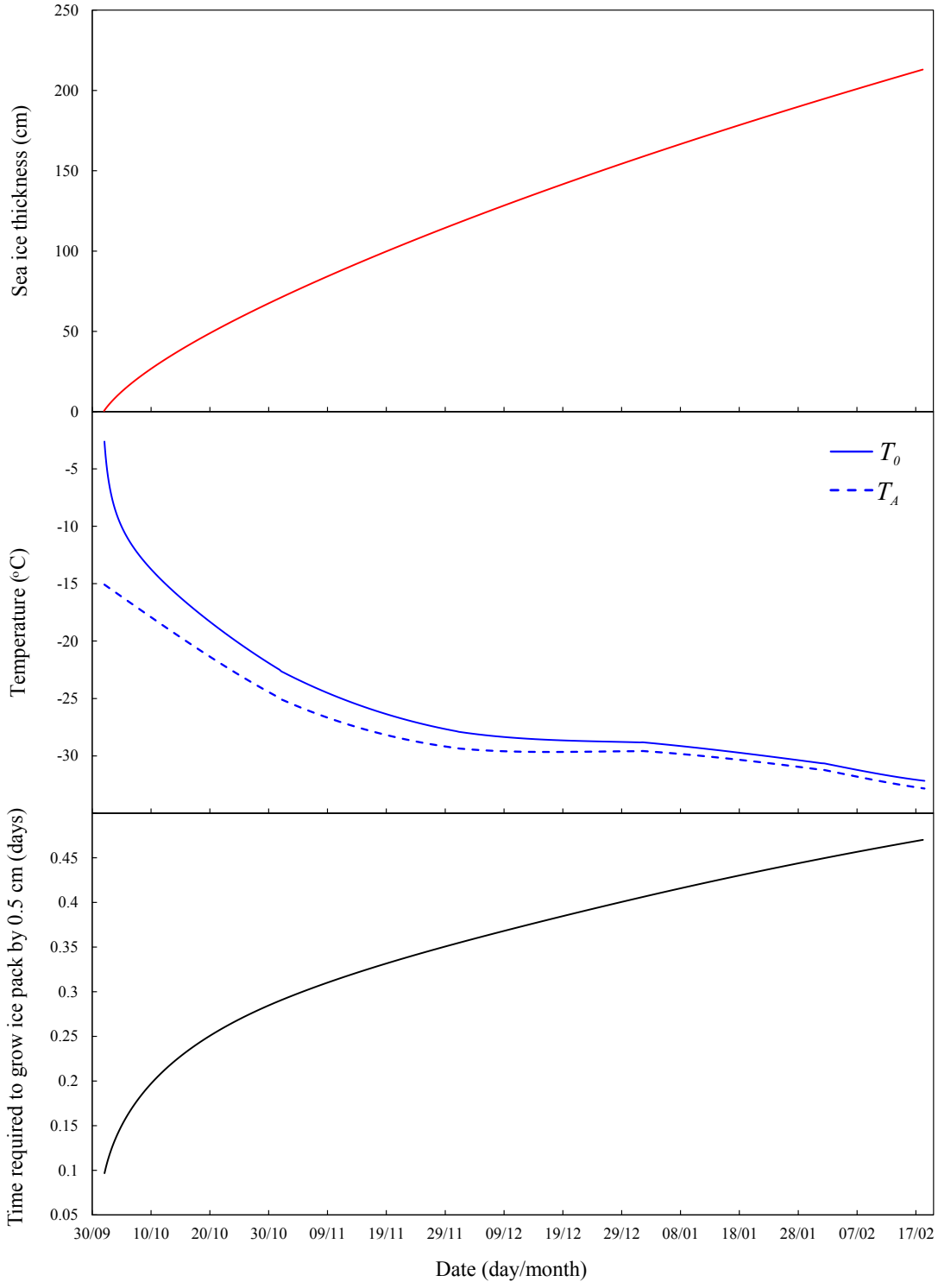

Figure 1.8: Growth of snow-free first-year Arctic sea ice under average climatic conditions of the Arctic Basin using the empirical model described in chapter 2. Growth initiated on the 1st October. Top plot is the ice pack thickness, middle the ambient (T_A) and ice-atmosphere interface (T_0) temperatures, and bottom is the time required for the ice pack to grow by 0.5 cm.

properties of its briny microstructure.

As congelation ice grows, cools, or warms, the porosity of its microstructure responds dynamically. These changes affect the interaction of the interstitial brine with the underlying ocean. If sea ice were to form in a closed system, melting the ice and measuring its salinity (i.e., bulk salinity) would yield the same value as the initial seawater that is froze from. In reality, measurements of the bulk salinity of sea ice typically yield salinities less than 10 g $kg^{-1}_{solution}$ (Eicken, 1992b). This lower salinity arises through desalination processes during sea ice growth.

The desalination of congelation ice during its formation can be described by three mechanisms (defined empirically in section 2.2). First is the initial brine entrapment between dendrites as the ice forms, which is a function of the ice growth rate (Cox and Weeks, 1988). Second is the expulsion of brine from the congelation ice as it cools. This expulsion occurs when pure water freezes within individual brine inclusions. The associated volume expansion of approximately 10 % results in expulsion of brine from the inclusion, and its redistribution within the ice column (Notz and Worster, 2009). The final desalination process is gravity drainage, which occurs within a 'mushy layer' of sea ice close to the ice-ocean interface. This mushy layer describes the permeable properties of a two-phase (solid and liquid), two component (ice and brine) medium, and relates to sea ice with a porosity that exceeds 5 % (Golden et al., 1998; Notz, 2005). The porosity is a function of the bulk salinity and temperature (figure 1.9). As long as sea ice remains permeable, interstitial brine that is denser than the seawater below creates an unstable density profile. This results in gravity drainage as dense brine drains from the ice to be replenished by fresher, less dense seawater (Cox and Weeks, 1988; Notz and Worster, 2009).

The combined effect of desalination processes during first-year sea ice growth results in typical bulk salinities of between 5 and 10 g $kg^{-1}_{solution}$, displaying a 'C' shaped depth distribution (figure 1.4) (Weeks, 2010). The important point here is that, even with desalination, a significant amount of salt remains in sea ice in the form of concentrated brines that are contained within countless brine inclusions. The presence of this brine results in sea ice having very different physical, chemical and biological properties to lake ice (Petrich and Eicken, 2010). This thesis now moves on to explore the major geochemical processes that occur within this brine.

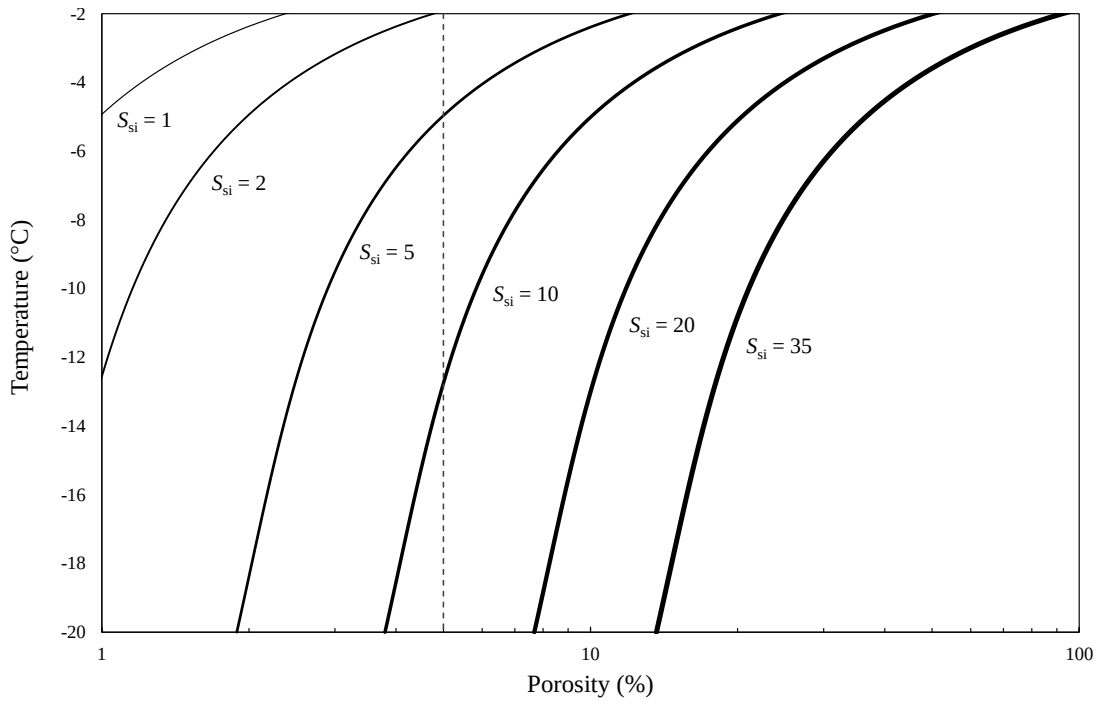

Figure 1.9: The relationship between sea ice porosity and temperature for various bulk sea ice salinities (S_{si}) calculated using the equations of Cox and Weeks (1983). The vertical line at 5 % porosity identifies the point at which sea ice becomes impermeable.

1.3 Mineral dynamics in sea ice brines

As displayed in figure 1.6, brine inclusions that permeate the sea ice microstructure respond dynamically to changing temperature. Crucially, at thermal equilibrium the brine is confined to a temperature-dependent composition, controlled by the dynamics of pure ice and mineral solubility. As sea ice cools, brine volume decreases along with the size of the brine inclusion, whilst the salinity increases, because more pure water is incorporated into the surrounding pure ice matrix to maintain thermal equilibrium (figure 1.10). Due to seawater's relatively complex composition (section 1.1), the combination of changing temperature and solution composition results in supersaturation of the brine with respect to several minerals at various temperatures experienced by sea ice. Therefore, during cooling and warming, the brine undergoes substantial geochemical changes that not only include physical concentration/dilution, but also mineral precipitation/dissolution.

There is a temperature-dependent sequence of minerals that have to precipitate during the freezing of seawater to its eutectic (the temperature at which all salts

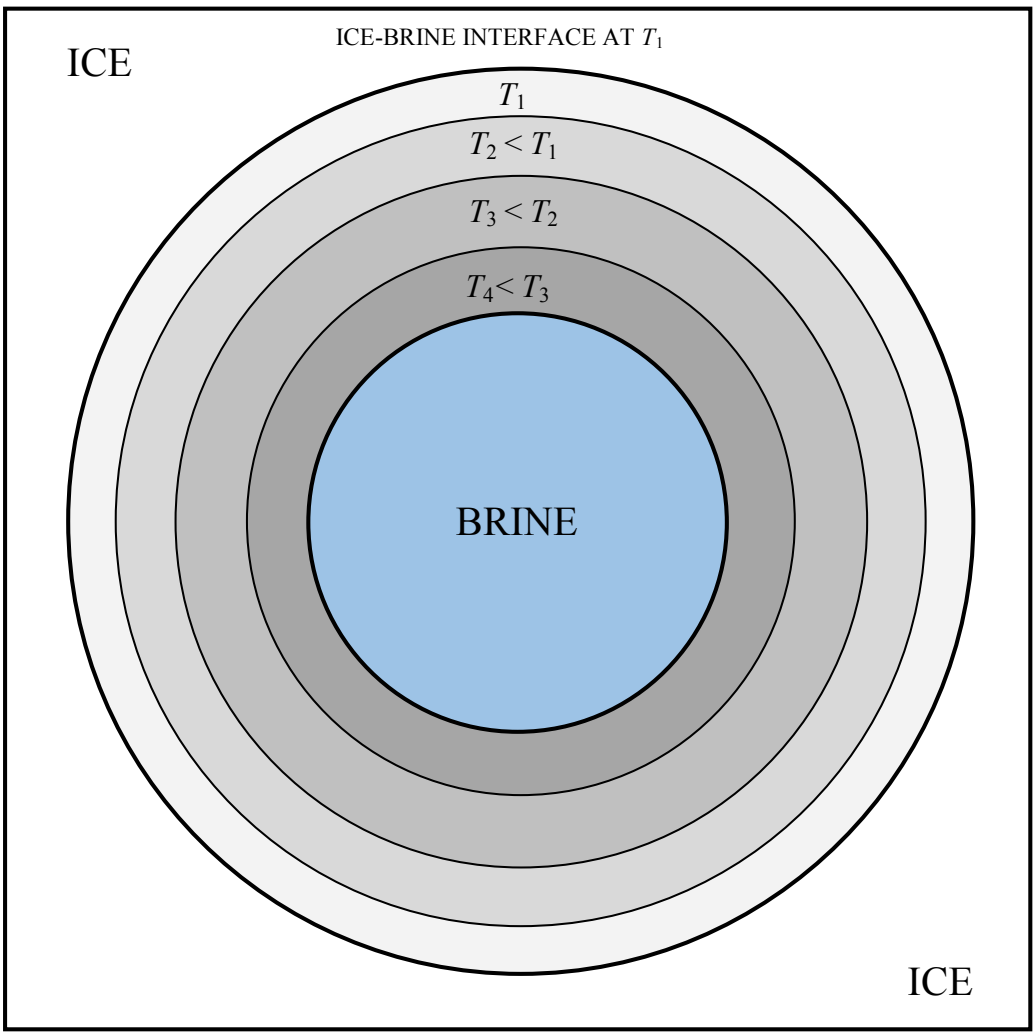

Figure 1.10: Schematic outlining the effect of temperature (T) on the size of individual brine inclusions within sea ice. The inward lines of each circle represents the ice-brine interface at temperature T. Coincident the decreasing brine pocket size is an increase in brine salinity/ionic strength.

have precipitated and all unbound water is frozen). This is ultimately controlled by mineral solubility and the evolving saturation states of the brine as it develops in composition with decreasing temperature (figure 1.11). Investigating the dynamic changes of mineral solubility in sea ice brines as the solution temperature and composition evolves can act to improve the current understanding of sea ice geochemistry.

1.3.1 Mineral solubility

Aqueous solutions in connection with a mineral, such as a mineral within a sea ice brine, can exist in three saturation states; saturated, undersaturated and supersatu-

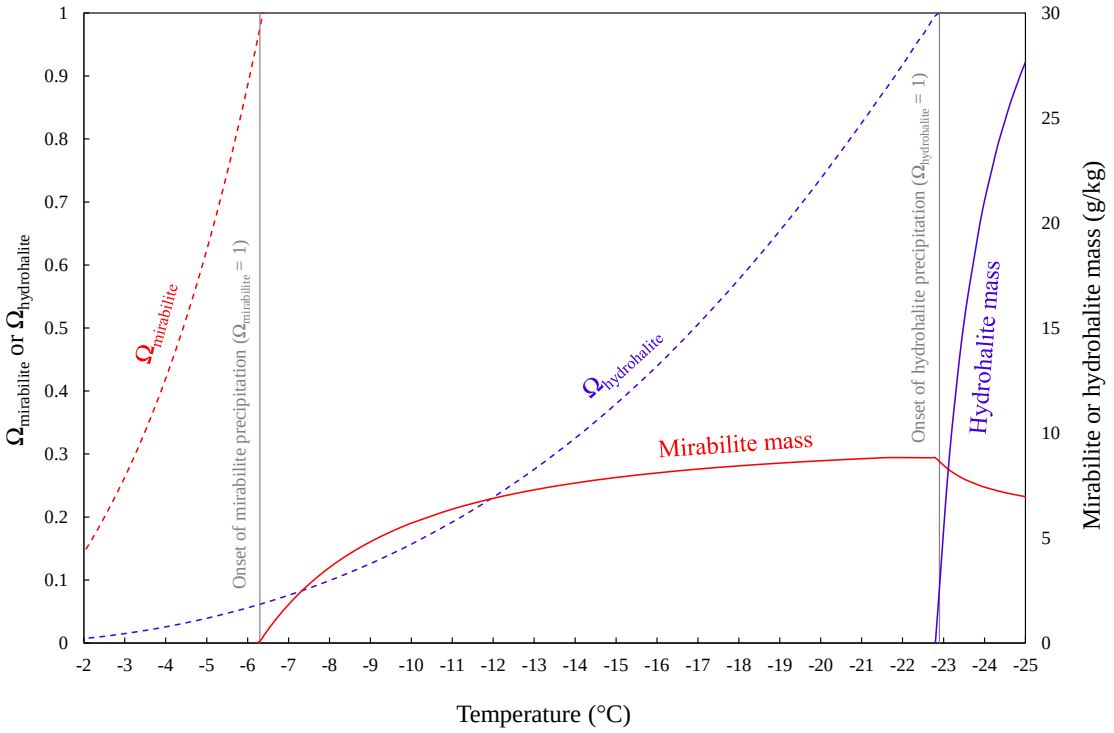

Figure 1.11: An illustration of how the saturation states (Ω, dashed lines) of sea ice brine with respect to mirabilite and hydrohalite evolve at different rates during the freezing of Standard Seawater ($S = 35$) between -2 and -25 °C. When $\Omega < 1$ the brine is undersaturated with respect to the mineral. The point at which $\Omega = 1$ represents the onset of mineral precipitation, beyond which Ω remains at 1 through mineral precipitation (solid lines) unless the conditions result in metastable supersaturation of a mineral, whereby $\Omega > 1$. Data were computed using version 15.1 of the FREZCHEM model.

rated (Koutsoukos et al., 2007). A saturated state occurs when the solution contains the maximum amount of solute that could be dissolved in the defined conditions. In the case of the solubility experiments that comprise a large part of this thesis, the saturation point of the solution is considered to be the point of equilibrium- where the dissolution and precipitation reactions balance. An undersaturated solution exists when less solute is dissolved than at equilibrium under the same conditions. Upon the addition of the undersaturated mineral to an undersaturated solution, it will dissolve. Supersaturated solutions are metastable, and occur when a solution contains more dissolved constituents than is possible for a saturated solution under the same conditions. In this state the salt would be expected to precipitate from the solution if sufficient time is allowed and there are suitable surfaces for crystal nucleation.

Solubility determines the point at which a solution is undersaturated, saturated,

or supersaturated with respect to a mineral. Mineral solubility in an aqueous solution can be strongly altered by temperature and the ionic effects of dissolved electrolytes. Specifically, there are three types of ionic effect that can alter mineral solubilities; these are the common ion effect, the ion association effect and the salt effect. The common ion effect involves the additions of ions that constitute the mineral phase in question being added to the solution. The increase in concentration of this ion is then responsible for a reduction in the solubility of the original mineral phase. For example, adding $NaCl_{(aq)}$ to a solution reduces the solubility of Na_2SO_4 (Wu et al., 2010). Secondly, the ion association effect occurs when ions of opposite charge in a solution are attracted to each other and exist as pairs. The formation of these ion pairs in a solution is understood to augment the solubility of a mineral phase. For example, adding $MgCl_{2(aq)}$ to a solution increases the solubility of $CaSO_4 \cdot 2H_2O$ (Wu et al., 2010). Lastly, strong electrolytes such as KCl can lower the activity coefficients (section 2.1) of ions such as Ca^{2+} and SO_4^{2-}. This lowering of the activity coefficients is caused by the Ca^{2+} and SO_4^{2-} being surrounded by K^+ and Cl^-. This process is known as the salt effect, and results in augmented solubility of a mineral (Wu et al., 2010). The common ion effect and the ion association effects alter a mineral solubility by changing the dissociation equilibrium of the mineral phase. In contrast the salt effect is applied by only changing the activity coefficients of the ions in solution.

Further to the effects of solution composition on solubility, the property also alters upon changing temperature. Most commonly, minerals become more soluble upon increasing temperature (Koutsoukos et al., 2007). For the case of mineral solubility in sea ice brines, the effects of both temperature and the ion effects from changing solution composition contribute to the measured solubility of a mineral. Hence the sequence of minerals to precipitate during freezing seawater to its eutectic is a reflection of the combined forcings. Over the past century, there have been two comprehensive studies aimed at defining this sequence. The two paradigms for seawater freezing derived from these investigations are known as the Gitterman and Ringer-Nelson-Thompson (RNT) Pathways (Gitterman, 1937; Nelson and Thompson, 1954; Marion et al., 1999).

1.3.2 The Gitterman Pathway

The Gitterman (1937) investigation synthetically prepared all experimental solutions. The starting solution represented the composition of seawater with a salinity of 33.33 g $kg^{-1}_{solution}$. This solution was cooled to various temperatures inducing different degrees of freezing and the solution composition analysed for K^+, Ca^{2+}, Mg^{2+}, SO_4^{2-}, Cl^- and CO_3^{2-}. After this initial analysis, new, more concentrated seawater-derived brines were prepared to match the analysed solution compositions, which were then subjected to further cooling. This step by step approach was repeated throughout the temperature range studied, and by-passed the time and labour intensive method of creating sufficient quantities of concentrated brine for freezing experiments. The experiments were allowed to attain equilibrium for up to 1 month. Crucially, precipitated mineral phases were kept in contact with the brine throughout, which proved pivotal in maintaining SO_4^{2-} sources within the system.

The pathway of mineral precipitation predicted from this work (table 1.1) was derived through measured changes in solution composition. Between 0 and −3.5 °C, the results showed compositional changes indicative of ikaite precipitation ($CaCO_3 \cdot 6H_2O$). This was followed by the loss of Na^+ and SO_4^{2-} below −7.3 °C, indicating mirabilite ($Na_2SO_4 \cdot 10H_2O$) precipitation. Gypsum was the third mineral to precipitate, indicated by removal of Ca^{2+} (mirabilite dominated the changes in SO_4^{2-}), which initiated between −12 and −15 °C. At −22.9 °C, rapid changes in Cl^- and intensified ice formation marked the point of hydrohalite ($NaCl \cdot 2H_2O$) precipitation, followed by the precipitation of sylvite (KCl) at −33.0 °C. Finally the precipitation of $MgCl_2 \cdot 12H_2O$ at −36.2 °C coincided with the eutectic temperature along this pathway for seawater freezing, which was derived by identification of temperature plateaus during thermal analysis. It is also described that gypsum precipitation was accelerated below −22.9 °C because the substantial removal of Na^+ from the brine resulted in mirabilite undersaturation and dissolution. The liberated SO_4^{2-} from mirabilite dissolution accelerated gypsum precipitation, measured as a removal of Ca^{2+}.

The Gitterman Pathway, derived from these results, is often referred to as an equilibrium crystallisation process; whereby minerals can interact within the system through changes in solution composition. In contrast, the RNT Pathway is con-

Table 1.1: A comparison of the predicted sequence and temperatures (°C) of mineral precipitation between the freezing point of seawater and its eutectic. Further to the tabulated minerals, ikaite can also precipitate at temperatures ∼−2 °C, however this is understood to be dependent upon brine degassing (Papadimitriou et al., 2013).

Mineral	Gitterman[a]	Ringer-Nelson-Thompson[b]	FREZCHEM[c]
Mirabilite	−7.3	−8.2	−6.3
Gypsum	∼ −12 to −15	N/A	−22.2
Hydrohalite	−22.9	−22.9	−22.9
Sylvite	−33.0	−36.0	−34.0
$MgCl_2 \cdot 12H_2O$	−36.2*	−36.0	−36.2*
Antarcticite	N/A	−53.8*	N/A

[a] Gitterman (1937)
[b] Nelson and Thompson (1954)
[c] Marion et al. (1999); Marion and Kargel (2008)
* Eutectic temperature

sidered representative of a fractional crystallisation process, whereby minerals are removed from the system as they form (Zolotov and Shock, 2001).

1.3.3 The Ringer-Nelson-Thompson Pathway

Though it is known that the investigation by Nelson and Thompson (1954) expanded upon work by Ringer (1906), the latter publication could not be sourced in English and therefore relating information was obtained from later literature.

For the Nelson and Thompson (1954) investigation, surface seawater was collected from 100 miles off the Washington coast (USA) in $20 - 50$ litre glass flasks and filtered. This seawater was subjected to freezing experiments in a freezer capable of maintaining any temperature down to -45 ± 3 °C. Most of the freezing was carried out in a 3 L container with a removable bottom. As the temperature lowered, decreasingly small volumes of brine remained due to large quantities of ice formation. Therefore when the 3 L container did not provide enough brine for analysis or further freezing (< −23 °C), large volumes (100 L) of seawater were subjected to a preliminary concentration by freezing. For samples requiring cooling to between −23 and −26 °C, the seawater was initially frozen to −8 °C. For all samples requiring freezing below −26 °C, the seawater was initially frozen to −17 °C, the brine removed and then subjected to further freezing down to −25 °C and repeated removal of the brine. The −25 °C brine was then frozen to its target temperature in the 3 L

freezing container. Brines were sampled upon reaching thermal equilibrium with the freezer. It is important to note that their protocol for experiments below −23 °C separated brine from the ice and any minerals that had precipitated. All minerals removed from the samples were identified qualitatively by shape and structure on a petrographic microscope. Brines were then analysed for Na^+, K^+, Mg^{2+}, Ca^{2+}, Cl^- and SO_4^{2-}.

The RNT Pathway resulting from the brine and mineral analysis consists five precipitates (table 1.1). Firstly, mirabilite precipitates at −8.2 °C, followed by hydrohalite at −22.9 °C. At −36.0 °C there is the simultaneous precipitation of sylvite and $MgCl_2 \cdot 12H_2O$. At −53.8 °C, the precipitation of antarcticite ($CaCl_2 \cdot 6H_2O$) corresponds with the eutectic temperature of seawater freezing along this pathway.

1.3.4 FREZCHEM model predictions

In addition to the two experimental pathways of seawater freezing, estimations can also be extracted from geochemical models. FREZCHEM (FREeZing CHEMistry) is a thermodynamic model developed for cold aqueous planetary geochemistry (Marion and Kargel, 2008). FREZCHEM can be used to model the scenario of seawater freezing to its eutectic via either fractional or equilibrium crystallisation, though equilibrium crystallisation is considered the most thermodynamically viable route (Marion et al., 1999; Marion and Kargel, 2008). The model estimates mineral equilibria based on computation of ion activities in concentrated aqueous solutions (section 2.1). Here, the FREZCHEM output from freezing seawater to its eutectic via equilibrium crystallisation will be described.

The precipitated mineral sequence predicted by FREZCHEM represents a system that is at thermodynamic equilibrium at all times. Thermodynamic models therefore cannot account for the time required to attain equilibrium. The mineral sequence that FREZCHEM predicts is most similar to that of the Gitterman Pathway because the Gitterman experiments maintained the SO_4^{2-} sources in contact with the solutions and allowed up to 1 month for attainment of equilibrium (Marion and Kargel, 2008). Based on model runs given in Marion et al. (1999) and Marion and Kargel (2008) (table 1.1), FREZCHEM predicts ikaite precipitation at ~ -2 °C

(depending on pCO_2), followed by mirabilite at −6.3 °C. The third mineral to precipitate is gypsum at −22.2 °C. Hydrohalite precipitation initiates at −22.9 °C and accelerates the precipitation of gypsum via the mechanism outlined in section 1.3.2. Sylvite precipitation is initiated at −34.0 °C, followed by $MgCl_2 \cdot 12H_2O$ at −36.2 °C that coincides with the modelled eutectic temperature of seawater.

Out of the minerals in this sequence, mirabilite, gypsum and hydrohalite are the three that this thesis investigates in detail. The weights of these minerals predicted to precipitate from 1 kg of seawater (in absence of brine drainage) by FREZCHEM are displayed in figure 1.12. Mirabilite precipitation approaches concentrations of 8 g kg^{-1} at ∼ −22.8 °C, before its dissolution in the region of hydrohalite precipitation reduces the concentration by ∼2 g kg^{-1}. As mirabilite dissolves, hydrohalite precipitates rapidly, approaching concentrations of 40 g kg^{-1} at −36 °C. The dissolution of mirabilite coincides with accelerated gypsum precipitation, which reaches concentrations of 1.7 g kg^{-1} by −36 °C.

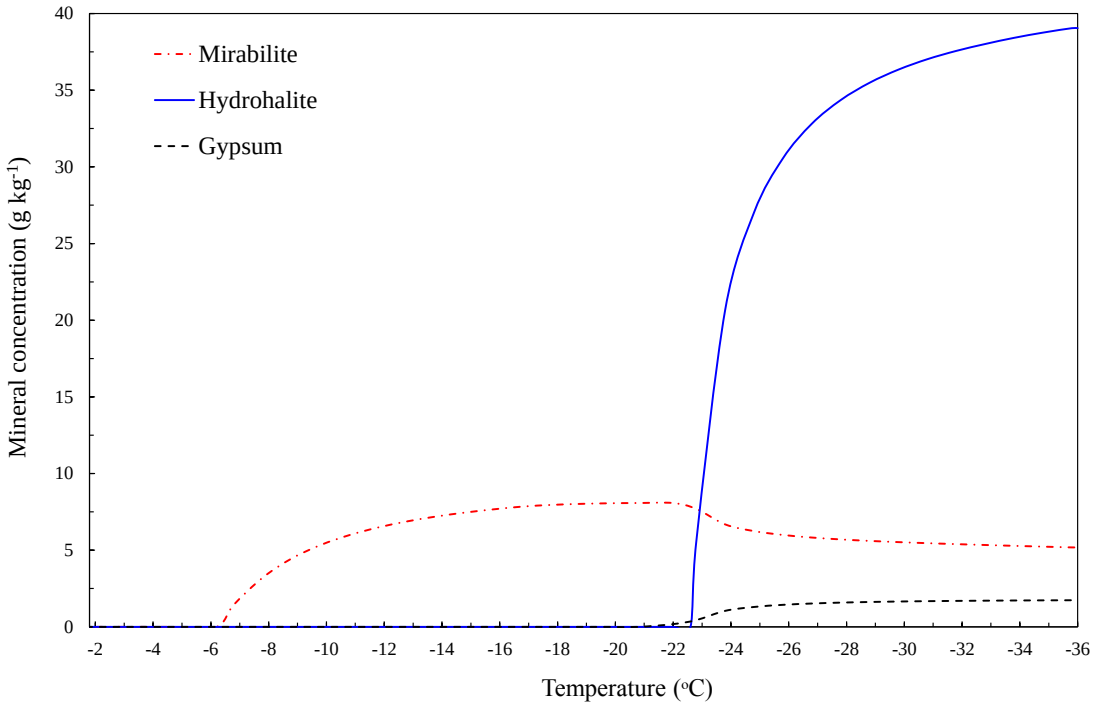

Figure 1.12: The concentration of mirabilite, gypsum and hydrohalite in frozen seawater (salinity= 35 g $kg^{-1}_{solution}$, closed system) between −1.8 and −36.2 °C.

1.4 Sea ice minerals: Current understanding and knowledge gaps

The collective understanding of mineral precipitation in frozen seawater from the Gitterman Pathway, RNT Pathway and FREZCHEM model provides a basis for the dynamics of minerals within the sea ice environment. The site of mineral precipitation in sea ice is within the brine inclusions that permeate its microstructure. The dimensions of the brine inclusions hence constrains that of authigenic minerals that precipitate within them, creating practical constraints for the evaluation of mineral dynamics in sea ice. As a result, there understanding of mineral dynamics in sea ice is limited.

Out of the suite of minerals that may precipitate (table 1.1), only ikaite and gypsum and have been identified in sea ice samples from the field (Dieckmann et al., 2008; Geilfus et al., 2013; Fischer et al., 2013). Ikaite was the first mineral to be identified (Dieckmann et al., 2008), where its extraction from Antarctic sea ice was assisted by the higher temperature for its formation ($\sim$−2 °C) allowing relatively large crystals to precipitate (up to 600 μm) in the porous sea ice matrix. Since its identification in the field, many studies have investigated the dynamics of ikaite, owing to its significance relating to CO_2 exchange between the atmosphere and the surface of polar oceans (Rysgaard et al., 2011, 2012; Geilfus et al., 2012; Papadimitriou et al., 2013, 2014). Recently both ikaite and gypsum were successfully extracted from experimental and natural sea ice in temperatures ranging from −2 to −10 °C. The identification of gypsum is particularly interesting because it is not predicted to precipitate at these temperatures. In contrast to ikaite the dynamics of gypsum are currently unresolved, though it has been proposed as a potential marine deposition in polar seas (Geilfus et al., 2013).

Aside from extraction and identification of minerals from sea ice, there is additional, but limited, evidence of their presence from laboratory observations. Microphotography of sea ice in laboratory experiments qualitatively identified mirabilite and hydrohalite in individual brine inclusions. Mirabilite crystals were observed to sink to the bottom of the brine inclusion, and ranged in size from 1 to 140 μm (Light et al., 2003). At −15 °C mirabilite was present in number densities of $\sim$ 250 crystals per mm^3, occupying 3 % of brine volume (Roedder, 1984; Light et al., 2003). Es-

timates of hydrohalite crystal size by microphotography are between 1 and 1.7 μm in diameter (Light et al., 2003, 2004). In contrast to mirabilite, hydrohalite forms a heterogeneous structure with ice that is distributed throughout the brine inclusions (Maykut and Light, 1995; Light et al., 2003).

There is no evidence for dynamics of the remaining minerals (sylvite, $MgCl_2 \cdot 12H_2O$ and antarcticite) that may precipitate in sea ice. Given the relatively low temperatures required for their formation (table 1.1), their significance in the environment may be limited. However the presence of countless microscopic mirabilite and hydrohalite crystals encapsulated throughout the sea ice matrix results in observable changes to its structural, optical and mechanical properties (Assur, 1960; Maykut and Light, 1995; Light et al., 2004; Carns et al., 2015), whilst affecting the physical and chemical properties of brine inclusions. Of particular climatic interest is the effect of the mineral precipitation on the optical properties of the ice, which becomes more reflective to solar radiation as the proportion of minerals within the medium increases (Maykut and Light, 1995; Light et al., 2004; Carns et al., 2015). Eskimos have long observed that when the ice-surface temperature drops to below -23 °C, travel by sleds becomes more difficult and the ice changes to a bright white colour (Assur, 1960). This observation is coincident with the precipitation of hydrohalite, and its effect on the optical and frictional properties of sea ice. Furthermore, the precipitation of mirabilite and hydrohalite in sea ice results in reductions in brine volume within the microstructure, which ultimately contributes towards sea ice transforming from a substance far weaker than freshwater ice at ~ -2 °C, to being substantially stronger below -23 °C (Assur, 1960). The optical properties fundamentally control the surface albedo of sea ice and therefore contribute to climate forcings in the polar regions, while the physical properties control the strength and movement of sea ice. Furthermore, the geochemical changes resulting from mineral precipitation in sea ice brines results in changes to the conditions inhabited by sympagic biota. For these reasons in particular, thoroughly understanding mineral dynamics within the sea ice system is particularly relevant for providing an accurate representation of this environment.

In account of the current understanding of sea ice minerals, several knowledge gaps have been identified that this thesis aims to investigate. The first aim relates

to the theories of equilibrium and fractional crystallisation for seawater freezing, represented by the Gitterman and RNT Pathways, respectively. There is currently an absence of evidence to show whether the microstructure of frozen seawater facilitates interaction between minerals through changing brine composition. Secondly, the main limitation of the outlined Pathways for seawater freezing, is that there is no consideration of the dynamics of each mineral in undersaturated brines. This limitation combined with the discrepancies between each pathway with respect to the onset of mirabilite and gypsum precipitation (table 1.1), justifies the aim of refining the current understanding of mirabilite, gypsum and hydrohalite dynamics in sea ice. Furthermore, the concentration and depth distribution of these minerals in natural sea ice as it warms and cools have never been estimated, which would aid in determining their role and presence within the environment. Lastly, mineral precipitation in sea ice brines results in non-conservative changes to the standard stoichiometry of seawater (figure 1.1), which may compromise the concepts used to measure salinity. The potential effects of mineral precipitation on accurate measurement of sea ice brine salinity, have never been considered.

In light of these knowledge gaps, this thesis aims to refine the current understanding of mineral dynamics in sea ice. This aim will be achieved through the following objectives:

- Investigate, *in-situ*, whether fractional or equilibrium crystallisation characterises the sequence of mineral precipitation in sea ice
- To define the solubility of mirabilite, gypsum and hydrohalite in sea ice brines at thermal equilibrium from undersaturated and supersaturated conditions
- To use the results from the solubility measurements to express mineral dynamics in sea ice
- To investigate the effect of mineral precipitation on the accurate measurement of sea ice brine salinities

To fulfill the aim and objectives, I use laboratory experiments that include the analysis of frozen seawater-derived brine by synchrotron X-ray powder diffraction, combined with solubility measurements of mirabilite, gypsum and hydrohalite in

solutions representative of sea ice brines at thermal equilibrium. My experiments throughout are supplemented with data from the FREZCHEM model, and a 1D model for the profile properties of sea ice.

Chapter 2

Modelling and Analytical methods

2.1 FREZCHEM modelling

2.1.1 Ion interaction

The FREZCHEM model is designed to compute aqueous electrolyte properties and chemical thermodynamics at sub-zero temperatures. The model accounts for the interaction of ions in concentrated electrolyte solutions using the Pitzer formalism for specific ionic interaction (Pitzer, 1973; Pitzer and Mayorga, 1973), specifically including: long-range electrostatic forces, short-range forces between species, and short-range triple particle interactions (Marion and Kargel, 2008). The effects of these interactions are related to the activity (α) of ions within the solution. Ion activity is a measure of its 'effective', or available, concentration. As ionic interaction in the solution increases, ion activity decreases. Ion activity is related to its molal concentration (m, mol $\mathrm{kg}^{-1}_{\mathrm{H_2O}}$) by an ion activity coefficient (γ), where $\alpha = \gamma\ m$. The ion activity coefficients are used as a measure of how much the presence of dissolved constituent concentrations reduces the ion activity from that in an ideal solution (whereby in an ideal solution ions and atoms do not interact). For an ideal solution of water at infinite dilution $\gamma = 1$, as does the activity of water (a_w). Upon increasing the ionic strength of an electrolyte solution, γ and α decrease, while the a_w also declines based on its relationship to the osmotic coefficient (ϕ):

$$a_w = \exp\left(\frac{-\phi \sum m_i}{55.50844}\right) \tag{2.1}$$

where the constant in the denominator is equal to $1000/MW_{\mathrm{H_2O}}$, with $MW_{\mathrm{H_2O}}$ assigning the molecular mass of water (18.01528). γ and ϕ cannot be measured directly, and instead have to be estimated using the Pitzer formalism within the

FREZCHEM model. In this manner, ϕ and single-ion activity coefficients for cations (γ_M) and anions (γ_X) are calculated by (Marion, 1997; Marion and Farren, 1999):

$$(\phi - 1) = 2/(\sum m_i)\{-A^\phi I^{1.5}/(1 + bI^{0.5}) + \sum\sum m_c m_a (B^\phi_{ca} + ZC_{ca}) + \sum\sum m_c m_{c'} (\Phi^\phi_{cc'} + \sum m_a \Psi_{cc'a}) + \sum\sum m_a m_{a'} (\Phi^\phi_{aa'} + \sum m_c \Psi_{aa'c})\}$$

$$\ln(\gamma_M) = z_M^2 F + \sum m_a (2B_{Ma} + ZC_{Ma}) + \sum m_c (2\Phi_{Mc} + \sum m_a \Psi_{Mca}) + \sum\sum m_a m_{a'} \Psi_{aa'M} + |Z_M| \sum\sum m_c m_a C_{ca}$$

$$\ln(\gamma_X) = z_X^2 F + \sum m_c (2B_{cX} + ZC_{cX}) + \sum m_a (2\Phi_{Xa} + \sum m_c \Psi_{Xac}) + \sum\sum m_c m_{c'} \Psi_{cc'X} + |Z_X| \sum\sum m_c m_a C_{ca}$$

where A^ϕ is the Debye-Huckel constant that depends on temperature; b is a constant ($= 1.2$), B, C, Φ and Ψ are salt interaction coefficients with the superscript ϕ referring to cation-cation or anion anion interactions; z_i is the charge number of the i^{th} ion; m_i is the molality of the i^{th} ion. Subscripts c and a refer to cations and anions while anion-anion or cation-cation interactions are denoted by c' or a'; F is a function of A^ϕ, I, and the salt interaction coefficients from the Pitzer formalism (Plummer et al., 1988; Pitzer, 1991). Lastly, I and Z are defined as:

$$I = 0.5 \sum m_i z_i^2.$$

$$Z = \sum m_i |z_i|$$

with left and right vertical bars denoting a number that is always non-negative.

Using the above equations to derive ϕ, γ_M and γ_X requires estimates of the salt interaction coefficients B, C, Φ and Ψ of the Pitzer formalism, which are defined as a function of temperature by:

$$\mathrm{P}(T)_j = a_{1j} + a_{2j}T + a_{3j}T^2 + a_{4j}T^3 + a_{5j}/T + a_{6j}\ln(T)$$

where j is the j^{th} Pitzer-equation parameter (P). In this form many of the parameters used for the inception of the FREZCHEM model are given in Spencer et al. (1990), while addition and refinement of parameters remains ongoing (Marion et al., 1999; Marion and Kargel, 2008; Marion et al., 2010). From this computation, total ion activities and, hence, mineral solubilities can be obtained.

2.1.2 Mineral solubility with FREZCHEM

Throughout this thesis, mineral solubility is determined, from measurement of brine composition, as the total concentration based stoichiometric solubility product at mineral-solution equilibrium, K^*_{sp}. For a mineral with the formula $\mathrm{M}_x\mathrm{X}_y$, where x and y denote the stoichiometric ratio of cation 'M' and anion 'X', $K^*_{\mathrm{sp},\mathrm{M}_x\mathrm{X}_y} = [\mathrm{M}]^x_{\mathrm{T,eq}}[\mathrm{X}]^y_{\mathrm{T,eq}}$, where the subscript 'T,eq' denotes total ion concentration at equilibrium. The term 'total' ion concentration refers to the combined concentration of paired and unpaired ions, which is an important consideration when dealing with concentrated aqueous solutions (Pytkowicz and Kester, 1969; Pytkowicz and Hawley, 1974; He and Morse, 1993). The Pitzer formalism in the FREZCHEM model explicitly includes the formation of ion pairs when their association constants exceed a critical value (He and Morse, 1993), therefore on occasion these have to be accounted for (see section 4.2.9 for further details).

The FREZCHEM model was used as a tool to derive a modelled K^*_{sp} suitable for direct comparison with the measured K^*_{sp}. FREZCHEM derives the thermodynamic equilibrium solubility product of a mineral, K_{sp}, which is described as a function of temperature at infinite dilution. This is combined with its computation of single ion activity coefficients γ, and the activity of water $\alpha_{\mathrm{H_2O}}$, to calculate the K^*_{sp} which can be directly compared to our measurements. The following rationale, for a hydrated mineral with the composition $\mathrm{M}_x\mathrm{X}_y \cdot z\mathrm{H_2O}$, was applied to gypsum, mirabilite and hydrohalite in this thesis to derive a modelled K^*_{sp}:

$$K_{\mathrm{sp},\mathrm{M}_x\mathrm{X}_y\cdot z\mathrm{H_2O}} = \alpha^x_{\mathrm{M}}\ \alpha^y_{\mathrm{X}}\ \alpha^z_{\mathrm{H_2O}} \tag{2.2}$$

$$= m^x_{\mathrm{M}}\ \gamma^x_{\mathrm{M}}\ m^y_{\mathrm{X}}\ \gamma^y_{\mathrm{X}}\ \alpha^z_{\mathrm{H_2O}} \tag{2.3}$$

$$= K^*_{\mathrm{sp},\mathrm{M}_x\mathrm{X}_y\cdot z\mathrm{H_2O}}\ \gamma^x_{\mathrm{M}}\ \gamma^y_{\mathrm{X}}\ \alpha^z_{\mathrm{H_2O}}. \tag{2.4}$$

When converting from the molal to mol $\mathrm{kg}^{-1}_{\mathrm{solution}}$ concentration units to reflect that measured in my experiments, equation 2.4 was modified with the molal to molar conversion factor θ to be:

$$K_{\mathrm{sp},\mathrm{M}_x\mathrm{X}_y\cdot z\mathrm{H_2O}} = K^*_{\mathrm{sp},\mathrm{M}_x\mathrm{X}_y\cdot z\mathrm{H_2O}}\ \frac{\gamma^x_{\mathrm{M}}\ \gamma^y_{\mathrm{X}}}{\theta^3}\ \alpha^z_{\mathrm{H_2O}}, \tag{2.5}$$

where $\theta = 1 - 0.001S_A/(\mathrm{g\ kg}^{-1}_{\mathrm{solution}})$ (Mucci, 1983; Millero et al., 2008).

2.2 Modelling the temperature-salinity profile of first-year sea ice

The discussion in chapters 4 and 6 incorporates laboratory measurements of mineral solubility into modelled temperature and salinity profiles of snow-free, first-year sea ice. This allowed for an assessment of mineral depth-distribution on a temporal scale.

Growth of snow-free, first-year sea ice was modelled using a surface energy balance equation (Maykut, 1978; Cox and Weeks, 1988) with input variables (as polynomial functions of day number) of temperature, incoming shortwave radiation, incoming longwave radiation, and humidity for the Arctic Basin taken from Maykut (1978). For a given ice thickness, the surface temperature T_0 is the only unknown required to set the energy balance to 0.

$$(1-\alpha)F_r - I_o + F_L - F_E + F_S + F_e + F_c = 0 \tag{2.6}$$

α = surface albedo

F_r = incoming shortwave radiation

I_o = net flux of radiative energy to the ice interior

F_L = incoming longwave radiation

F_E = emitted longwave radiation

F_s = sensible heat flux

F_e = latent heat flux

F_c = conductive heat flux

Equations used to derive the parameters in the energy balance equation were sourced from (Maykut, 1978) and (Cox and Weeks, 1988). T_0 was solved using a solver routine macro in Microsoft Excel to minimise the energy balance by changing T_0. Ice growth was initiated on the 1st October and the model calculated the time taken for the ice pack to grow incrementally in 0.5 cm layers using Stefan's equation (Cox and Weeks, 1988; Leppäranta, 1993), where

$$\Delta t = \frac{\rho L}{\bar{F}_c}\Delta H. \tag{2.7}$$

Δt = time (days) required to grow the ice layer of thickness ΔH (0.5 cm)

ρ = ice layer density (0.93 g cm^{-3})

L = latent heat of freezing (70 cal g^{-1})

$\bar{F}_c$ = average conductive heat flux (W m^{-2})

The time taken to grow each layer automatically adjusted the input values of the surface energy balance needed to solve for T_0 for the next increment of ice growth. This incremental approach resulted in identical depths and T_0 to those given in Cox and Weeks (1988).

The sea ice temperature profiles assumed a linear relationship between T_0 and the bottom of the ice pack (−1.8 °C). The bulk salinity of the ice is governed by the extent of desalination processes. This model assigns the desalination (in absence of flushing from melt ponds at the surface) to three mechanisms: initial salt entrapment, brine expulsion, and gravity drainage (section 1.2.3). The empirical equations used to define each desalination process in the sea ice model were taken from (Cox and Weeks, 1988) to be as follows.

Initial salt entrapment

The initial salinity of the ice S_i is defined as

$$S_i = k_{eff} S_W \tag{2.8}$$

where S_W is the seawater salinity (34 g $kg^{-1}_{\text{solution}}$) while k_{eff} is a coefficient describing the desalination of the ice upon its initial formation, which is dependent on the growth rate. For growth rates (V) greater than 3.6×10^{-5} cm s^{-1}

$$k_{eff} = \frac{0.26}{0.26 + 0.74 \exp(-7243V)} \tag{2.9}$$

and for growth rates lower than 3.6×10^{-5} cm s^{-1}

$$k_{eff} = 0.8925 + 0.0568 \ln V. \tag{2.10}$$

When the growth velocity was below 2.0×10^{-6} cm s^{-1} k_{eff} was assumed to be constant at 0.12.

Brine expulsion

Cox and Weeks (1986) derived the following equation to describe the change in bulk sea ice salinity due to brine expulsion upon cooling from T_1 to T_2:

$$\frac{S_i(T_2)}{S_i(T_1)} = \frac{S_b(T_2)}{S_b(T_1)} \frac{\rho_b(T_2)}{\rho_b(T_1)} \frac{v_b(T_2)}{v_b(T_1)} \tag{2.11}$$

where S_i is bulk ice salinity (g $kg^{-1}_{solution}$), S_b is brine salinity, ρ_b is brine density (g cm^{-3}) and v_b is brine volume (ppt). If the ice is cooled ($T_2 < T_1$), the ratio of the brine volumes at T_2 and T_1 can be expressed as

$$\frac{v_b(T_2)}{v_b(T_1)} = \frac{S_b(T_1)}{S_b(T_2)}^{1/\rho_i} \; e^{c/\rho_i[S_b(T_1)-S_b(T_2)]} \tag{2.12}$$

and equation 2.11 becomes

$$\frac{S_i(T_2)}{S_i(T_1)} = \frac{S_b(T_2)}{S_b(T_1)}^{1-1/\rho_i} \; \frac{\rho_b(T_2)}{\rho_b(T_1)} \; e^{c/\rho_i[S_b(T_1)-S_b(T_2)]} \tag{2.13}$$

where ρ_i is the density of pure ice (0.918 g cm^{-3}) and c is a constant equal to $d\rho_b/dT$ (0.0008 g cm^{-3} °C). Equations for calculating S_b and ρ_b were sourced from (Cox and Weeks, 1986).

Gravity drainage

Gravity drainage was only permitted when the ice brine volume was less than 50 ppt (Golden et al., 1998). At ice brine volumes greater than 50 ppt, the following empirical relationship for brine drainage was used (Cox and Weeks, 1975)

$$\frac{\Delta S_i}{\Delta t} = 1.68 \times 10^{-5} \; \frac{\Delta T}{\Delta z} \; - 3.37 \times 10^{-7} \; v_b \; \frac{\Delta T}{\Delta z} \tag{2.14}$$

where $\Delta S_i/\Delta t$ = the rate of change in salinity due to gravity drainage (g $kg^{-1}_{solution}$ s^{-1}), $\Delta T/\Delta z$ = temperature gradient (°C cm^{-1}) and v_b is the ice brine volume (ppt) of a given layer.

Together, the equations of initial salt entrapment, brine expulsion and gravity drainage computed the salinity profile of snow-free first-year Arctic sea ice. Resulting salinity and temperature profiles were integrated with solubility data to model the mineral distribution in sea ice as the ice pack develops over the Arctic winter (sections 4.4.2 and 6.4.5).

2.3 Experimental Methods

The following methods encompass much of the work carried out for this thesis. Although separate, study-specific, methodologies are given in each chapter that follows, this section provides more detailed information on experimental and analytical protocols.

The bulk of the experimental analysis is comprised of the characterisation of major ions in seawater-derived brines. The experimental accuracy and precision of this analysis was estimated using repeat measurements of local seawater as an internal standard compared to the composition of Standard Seawater (Millero et al., 2008). A summary of the salinity normalised ($S_P = 35$) reproducibility from these measurements compared to Standard Seawater is given in table 2.1.

Table 2.1: The accuracy and precision of brine analyses estimated using repeat measurements of local seawater (normalised to $S_P = 35$) as an internal standard and relating to the composition of Standard Seawater. (Millero et al., 2008)

	Standard Seawater	Measurements $\pm\ \sigma$	$\Delta \pm \sigma$
Ion	mmol $kg^{-1}_{solution}$		%
Na^+	468.97	470.53 ± 7.97 $(n = 29)$	0.33 ± 1.70
K^+	10.21	10.11 ± 0.05 $(n = 9)$	-0.97 ± 0.49
Mg^{2+}	52.82	52.63 ± 0.54 $(n = 82)$	-0.36 ± 1.02
Ca^{2+}	10.28	10.24 ± 0.14 $(n = 82)$	-0.39 ± 1.36
Cl^-	545.87	548.48 ± 6.90 $(n = 38)$	0.48 ± 1.26
SO_4^{2-}	28.24	28.34 ± 0.41 $(n = 35)$	0.35 ± 1.45

2.3.1 Chloride analysis

The Cl^- concentration of brine samples was analysed by a gravimetric Mohr titration with $AgNO_3$. The $AgNO_3$ titrant was prepared as a solution to an approximate concentration of 0.3 mol $kg^{-1}_{solution}$ by dissolving the powdered salt (Sigma) in ultrapure water (MilliQ). The concentration of the titrant was characterised by titrating a range of 6 standards prepared as different weights of recrystallised NaCl (Sigma), and using the Solver routine in Microsoft Excel to minimise the error between titrated and expected Cl^-. Chromate indicator, used to define the titration end-point, was prepared by dissolving 4.2 g of K_2CrO_4 and 0.7 g of $K_2Cr_2O_7$ (Sigma) in approximately 100 g of ultrapure water.

For the titrations, the weight of each sample or standard was measured on a 4 decimal place balance and transferred to a 100 ml glass beaker. The beaker was then filled to ∼75 ml with ultrapure water before addition of 2 ml of chromate indicator. Samples or standards were then titrated gravimetrically with the $AgNO_3$ titrant. The weight of titrant was monitored by using disposable pasteur pipettes (7 ml) to dispense the solution, and weighing their full and empty weights accordingly. The end point of the titration is marked by the development of a permanent orange-red

colour. During the titration, Cl^- was precipitated as insoluble AgCl, and the moles of $AgNO_3$ required to reach the end point was equivalent to the moles of Cl^- within the sample, which was converted to concentration (mol $kg^{-1}_{solution}$) using the original sample weights.

2.3.2 Calcium and magnesium analysis

The concentrations of Ca^{2+} and Mg^{2+} were determined by a potentiometric titration of a measured sample weight using EDTA as the titrant and TRIS-buffered acetylacetone (0.1 M) as the complexing agent. The *p*H of the titration was controlled by the addition of 0.1 M KOH, added until a working *p*H of 8.5 was attained. The concentration of EDTA ($\sim$0.66 M) was calibrated against 6 gravimetrically prepared standard solutions of analytical grade $CaCl_2 \cdot 2H_2O$ and $MgCl_2 \cdot 6H_2O$ (Fisher). Concentrations of the standards ranged from $5 - 43$ mmol $kg^{-1}_{solution}$ for Ca^{2+} and $25 - 208$ mol $kg^{-1}_{solution}$ for Mg^{2+}, with each prepared to resemble the natural ratio of Ca:Mg found in seawater of 1:5. Titrations were conducted on a Metrohm Titrando 808, with automatic two-end point detection, using an ion selective electrode coupled with an Ag/AgCl reference electrode and a combined *p*H glass electrode (all electrodes from Metrohm) for *p*H adjustment. The operational molar Ca^{2+} to acetylacetone ratio was kept at 0.1 for all samples. The concentrations of Ca^{2+} and Mg^{2+} were calculated in Tiamo^{TM} version 2.4 using the embedded concentration of EDTA titrant. These concentrations were converted from mmol L^{-1} to mmol $kg^{-1}_{solution}$ by calculating the solution density using the experimental temperature and sample salinity, based on the equations in Millero and Poisson (1981).

2.3.3 Sodium and potassium analysis

The concentrations of the Na^+ and K^+ were quantified by ion chromatography on a Dionex Ion Exchange Chromatograph ICS 2100 (Thermo Scientific, USA) equipped with a Dionex IonPac CS12A 2×250 mm column (guard column IonPac GC12A). The eluent generator was methanesulfonic acid (20 mM). Samples were passed through the column at 35°C using an isocratic flow of 0.25 ml min^{-1}. Individual standards were prepared for calibration by gravimetric dilution from 1000 ppm certified reference material solutions (Sigma) to a maximum concentration of

250 mg $kg^{-1}_{solution}$. All data was processed by Chromeleon7 software.

2.3.4 Sulphate analysis

Sulphate concentrations were determined via an indirect titration, the method of which was developed from that originally outlined by Howarth (1978), that isolates sulphate by precipitation as barite ($BaSO_4$). To begin the process of extracting the sulphate from the samples, 3 ml of 0.4 M HCl was added to a weighed amount of sample in a 50 ml conical flask. To this was added 4 ml of 0.01 M EDTA, and the mixture heated to 80 °C for 2 minutes on a VWR advanced VMS-C10 hot plate to allow for the chelation of dissolved metals with the EDTA. Once removed from the heat, 10 ml of 0.05 M HCl was added to the hot solutions before being allowed to cool for a further 3 minutes. Once cooled, the addition of 5 ml 10 % $BaCl_2$ (117 g L^{-1} $BaCl_2 \cdot 2H_2O$ (Sigma)) resulted in the precipitation of any SO_4^{2-} as barite, due to this minerals exceptional insolubility. The mixture was left to stand for 20 minutes to allow for the complete precipitation before filtration. Each sample was filtered through a 25 mm diameter, 0.45 μm membrane filter (WHATMAN) using a Millipore vacuum filtration unit. The conical flask was rinsed into the filtration unit 3 times with distilled water. The filter was then flushed with 10 ml of 0.05 M HCl to remove non precipitant ions, followed by a final rinse with 20 ml of distilled water. The filter with the barite precipitate was then transferred back to the original conical flask, and a Metrohm 800 Dosino pump then used to accurately dispense 5 ml of 0.01 M EDTA (average dispensed $\pm\sigma = 4.9702 \pm 0.0035$ g, $n = 10$) into each conical flask, followed by 4 ml of $28 - 30$ % NH_4OH (Sigma) required to drive the pH up for the dissolution of barite. To aid with dissolution, the mixture was heated again to 80 °C for 15 minutes, stirring occasionally. The flask was removed from the heat and allowed to cool to room temperature before 0.5 ml of pH 10 buffer solution (7 g NH_4Cl and 57 ml NH_4OH diluted to 100 ml with distilled water) and 1 drop of indicator solution (0.4 g of eriochrome black T in 30 ml triethanolamine and 10 ml ethanol, Sigma) were added. The excess of EDTA that remained after redissolving the barite precipitate was then titrated with 0.025 M $MgCl_2$ solution until the indicator turned from a deep blue to strong purple in colour. The weight of $MgCl_2$ titrant used was measured to 4 decimal places.

The titration was calibrated using certified 1000 mg L^{-1} SO_4^{2-} solution (Sigma), plotted as a linear function of the weight of titrant against moles of SO_4^{2-}. The standards for calibration we prepared by altering the volume of the certified SO_4^{2-} solution to produce standards containing between 0 and 25 μmoles of SO_4^{2-}. Moles of SO_4^{2-} were converted to concentration (mol $kg^{-1}_{solution}$) using sample weights.

2.3.5 Preparation of synthetic gypsum

Gypsum was prepared using a method based on that described by Wang et al. (2012). 0.5 M solutions of $CaCl_2$ and Na_2SO_4 were prepared by dissolving analytical grade salts (Sigma) in distilled water. The solutions were filtered through 0.2 μm membrane filters (Whatman) to remove solid impurities. To precipitate gypsum, equal volumes of the solutions were mixed at room temperature. The precipitation of gypsum occurred instantaneously, observed as a clouding of the solution with a fine white suspension. The solution was left covered and stirring overnight to allow sufficient time for the reaction to take place. Each batch of gypsum was collected by filtration through a 10 μm plankton net, rinsed with distilled water, and dried by rinsing with cold acetone under vacuum. Dried gypsum was transferred to screw capped bottles and stored at room temperature before use.

2.3.6 Preparation of synthetic mirabilite

The preparation of mirabilite was based upon the method described by Vavouraki and Koutsoukos (2012). 150 g of powdered Na_2SO_4 (Sigma) in 500 ml of distilled water was heated to 40 °C to dissolve the salt. Once dissolved, the solution was cooled to 18 °C. Upon cooling, the solution became strongly supersaturated with respect to mirabilite, and the mineral crystallised within the vessel. Several batches of mirabilite were produced using this method. In some instances the solution required a momentary addition of a thin steel wire to initiate mirabilite crystallisation. Once initiated, the reaction was left overnight before collection by filtration.

Due to mirabilite's susceptibility to decomposition once exposed to the air (Oswald et al., 2008), all glassware for the filtration unit and acetone for rinsing was stored in the freezer at −20 °C for at least 2 hours prior to filtration. Filtration was carried out in several batches to keep exposure to ambient temperatures to a

minimum. Once filtered, the mirabilite was stored in screw capped jars at −20 °C.

2.3.7 Preparation of synthetic hydrohalite

Hydrohalite was prepared based upon the method described by Light et al. (2009). NaCl was added to 1 L of deionised water at room temperature until saturated. The solution was then cooled to −3 °C and left to equilibrate for 48 hrs. During the cooling to −3 °C, halite precipitated due to a reduction in NaCl solubility with decreasing temperature, which was then extracted by filtration through a GF/F filter. The filtered solution was then further cooled to −15 °C and left to equilibrate for a further week whilst hydrohalite crystallised. For filtration, the tendency of hydrohalite to melt incongruently to a saturated solution of halite at temperatures above 0.1 °C (Light et al., 2009) meant that all apparatus had cooled using the same protocol employed for mirabilite. After filtration, hydrohalite was stored in screw capped jars at −20 °C.

2.3.8 Mineral analysis by X-ray diffraction

Much of this work is underpinned by mineralogical analysis of mirabilite, gypsum, hydrohalite and ice by synchrotron X-ray powder diffraction. Detailed accounts of methods used for the mineralogical analysis and interpretation are given in relevant sections, however details of the mineral's crystal structures will be given here. Each mineral has a unique unit cell that repeats throughout its crystal structure. The dimensions and symmetry of the unit cell defines the diffraction pattern of a mineral, and therefore the details of its geometry are essential for qualitative and quantitative crystallographic analysis. Unit cell parameters were sourced from Brand et al. (2009) for mirabilite, Boeyens and Ichharam (2002) for gypsum, Klewe and Pederson (1974) for hydrohalite, and Fortes et al. (2004) for ice. These details are provided in table 2.2, while figure 2.1 displays the parameters of a unit cell. The crystal systems in table 2.2 are classified in terms of geometric symmetries, and within each crystal system there are several classes of space group that define the planes of symmetry within the unit cell. In the monoclinic unit cells of mirabilite, gypsum and hydrohalite, the axis lengths (a, b and c) are independent of one-another, while β is the only angle between the axes (α, β and γ) that is not 90 °. For the hexagonal unit

cell of ice, the length of a is equal to that of b, but independent of c, while all angles between the axes are fixed at 90 °.

Table 2.2: The unit cell parameters of mirabilite (Brand et al., 2009), gypsum (Boeyens and Ichharam, 2002), hydrohalite (Klewe and Pederson, 1974), and ice (Fortes et al., 2004). 1Å $= 10^{-10}$ m.

			a	b	c	β	**Volume**
Mineral	**System**	**Space group**	Å			°	Å^3
Mirabilite	Monoclinic	$P2_1/c$	11.44214	10.34276	12.75486	107.847	1436.794
Gypsum	Monoclinic	$C12/c1$	6.284	15.200	6.523	127.41	494.9
Hydrohalite	Monoclinic	$P2_1/c$	6.3313	10.1178	6.5029	114.407	379.34
Ice	Hexagonal	$P6_3/mmc$	4.49775	4.49775	7.32238	90	128.269

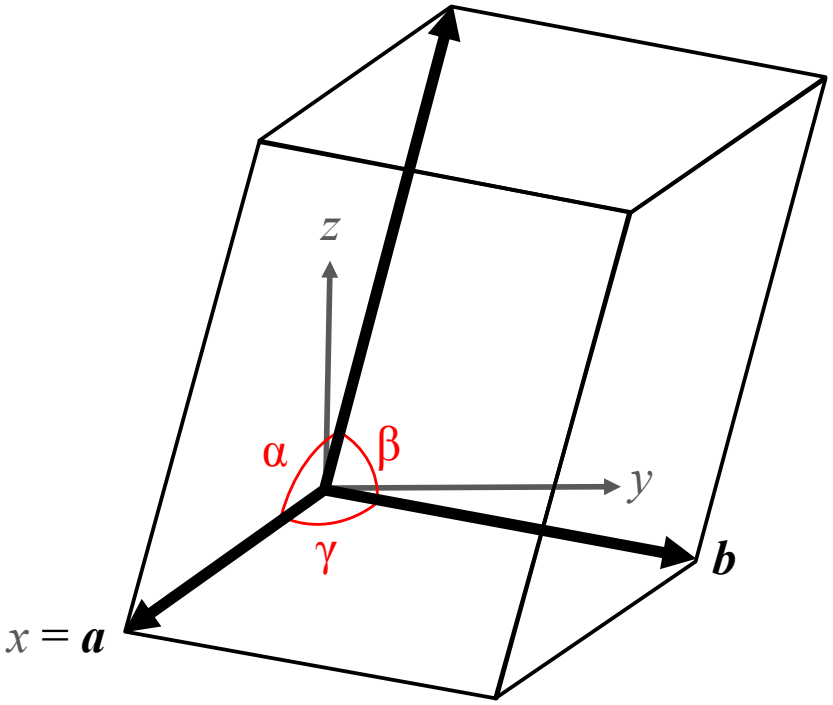

Figure 2.1: The parameters defining the unit cell of a crystal.

2.3.9 Preparation of synthetic seawater brines

While natural seawater brines were prepared for experiments by concentrating local seawater by freezing, the majority of the experiments presented herein used brines that were prepared synthetically to replicate the major composition of Standard Seawater with respect to Na^+, K^+, Mg^{2+}, Ca^{2+}, Cl^- and SO_4^{2-} (table 2.3). The composition of these major ions was replicated, based on the composition of simplified seawater from DOE (1994), by dissolving 5 analytical grade salts in deionised water; NaCl

(Sigma), Na_2SO_4 (Sigma), KCl (Sigma), $MgCl_2 \cdot 6H_2O$ (Fisher) and $CaCl_2 \cdot 2H_2O$ (Fisher). Due to the hygroscropic nature of $MgCl_2 \cdot 6H_2O$ and $CaCl_2 \cdot 2H_2O$, these salts were prepared as solutions prior to use. To prepare $MgCl_2$ and $CaCl_2$ solutions, 1 mole of the powdered salt was weighed out approximately and made up to the mark of a 1 L volumetric flask with deionised water. The resulting solution was then filtered through a 0.2 μm cyclopore track etched membrane filter (Whatman). Once filtered, the solutions were characterised for Ca^{2+} and Mg^{2+} by potentiometric titration (section 2.3.2). The remaining powdered salts (NaCl, Na_2SO_4 and KCl) were each annealed at 250 °C for 3 hours before storage at 50 °C prior to use.

Table 2.3: A comparison of the compositions of Simplified (DOE, 1994) and Standard (Millero et al., 2008) Seawater. The remaining ions in Standard Seawater that are not tabulated include: Sr^{2+}, HCO_3^-, Br^-, CO_3^{2-}, $B(OH)_4^-$, F^-, OH^-, $B(OH)_3$ and CO_2.

	$S_P = 35$	
	Simplified seawater	Standard Seawater
Solute	mol $kg^{-1}_{solution}$	
Na^+	0.46911	0.46897
K^+	0.01021	0.01021
Mg^{2+}	0.05283	0.05281
Ca^{2+}	0.01036	0.01028
Cl^-	0.54922	0.54587
SO_4^{2-}	0.02824	0.02824

The weights of each of the powdered and aqueous salt constituents, and deionised water required to produce a synthetic seawater brine with a desired salinity were calculated using Microsoft Excel. The target solution composition was identical to that of simplified seawater (table 2.3) relative to salinity, though the input values were converted to molality (mol $kg^{-1}_{H_2O}$) for each constituent because this unit is unaffected by changing temperature or pressure (Marion and Kargel, 2008). Upon altering the salinity of the target solution in the Excel spreadsheet, the weight of each corresponding constituent required would increase conservatively. The spreadsheet was set up to adjust for densities and buoyancy factors at room temperature to increase the accuracy of replicating a conservative brine. All solutions were produced gravimetrically using a two decimal place balance (Ohaus), and were made up to total weights exceeding 1 kg to minimise error.

To produce the experimental solutions, a careful sequence of additions was carried

out to prevent the reaction of Na_2SO_4 with $CaCl_2$, which can occur at room temperature in concentrated seawater brines to produce gypsum (Marion et al., 1999). At room temperature, the required deionised water was weighed, followed by the addition of the $MgCl_2$ solution and the NaCl, Na_2SO_4 and KCl powdered salts. The solution was then stirred until all salts had dissolved. The resulting solution was placed in a chiller at 2 °C above its estimated freezing point (Millero and Leung, 1976). Once cooled, the required weight of $CaCl_2$ solution was added to the cooled brine. This method of preparing the synthetic brine bypassed the process of gypsum formation, and produced synthetic seawater brines of conservative composition as identified by full characterisation of the ions in solution (table 4.2).

Chapter 3

An investigation of mineral dynamics in frozen seawater brines by direct measurement with synchrotron X-ray powder diffraction

[Butler, B.M. and Kennedy, H. (2015). An investigation of mineral dynamics in frozen seawater brines by direct measurement with synchrotron X-ray powder diffraction. *Journal of Geophysical Research: Oceans*, 120(8):5686-5697.]

Abstract

Frozen seawater is a composite material with a sponge-like structure. The framework of the structure is comprised of pure ice, and within the pores exists a concentrated seawater brine. When the temperature is reduced, the volume of this residual brine decreases, whilst its salinity increases. As a result of the paired changes to temperature and salinity, the brine eventually becomes supersaturated with respect to a mineral, resulting in the precipitation of microscopic crystals throughout the ice structure. Due to experimental constraints, the current understanding about the formation of these minerals relies on the analysis of the residual brine, rather than the mineral phase. Here, synchrotron X-ray powder diffraction was used to assess the dynamics that occur between ice, brine and mineral phases within frozen seawater brines that were subjected to cooling and warming at sub-zero temperatures. The method was able to detect crystalline phases of ice, mirabilite ($Na_2SO_4 \cdot 10H_2O$) and hydrohalite ($NaCl \cdot 2H_2O$). Results illustrate a highly dynamic geochemical environment where ice-brine-mineral interactions tend towards an equilibrium crystalli-

sation process, which supports the process of seawater freezing that is described by the Gitterman Pathway and FREZCHEM model. This study highlights the power of synchrotron techniques in observing the mineralogical dynamics of inaccessible environmental systems.

3.1 Introduction

When seawater cools to its freezing point, sea ice forms, which consists of pure ice that is punctuated by brine channels and pockets that contain liquid brine and gaseous inclusions (Golden et al., 2007). As the temperature of the seawater derived brine is further decreased below its freezing point, water is again removed as a pure ice phase, the volume of the brine within the inclusions decreases and thus the salinity increases. The coupled changes in solution composition with temperature as seawater is cooled to its eutectic creates a series of supersaturation events within the medium, resulting in the precipitation of a sequence of minerals.

For over a century now, the sequential process by which mineral formation occurs upon seawater freezing has been investigated (Ringer, 1906; Gitterman, 1937; Nelson and Thompson, 1954; Assur, 1960; Marion et al., 1999). The current understanding of mineral dynamics within seawater derived brines is largely based upon analysis of the changes to the major ion composition (Na^+, Cl^-, Mg^{2+}, SO_4^{2-}, Ca^{2+} and K^+) of sub-zero seawater derived brines in a laboratory setting (Ringer, 1906; Gitterman, 1937; Nelson and Thompson, 1954; Assur, 1960). Such studies inferred the identity of the mineral precipitate by quantifying compositional changes to the brine and, where possible, identifying the minerals that formed qualitatively by use of petrographic microscopes. The two main paradigms derived from such experiments that describe the sequence of minerals that precipitate when seawater freezes are known as the Gitterman Pathway, and the Ringer-Nelson-Thompson (RNT) Pathway.

The experiments carried out by Gitterman were designed to retain the minerals in contact with the brine and hence made it possible for subsequent interactions to occur between minerals and solutions as the brine composition continued to change. This pathway was characterised by the sequential onset of precipitation from the developing brine of mirabilite ($Na_2SO_4 \cdot 10H_2O$) at -7.3 °C, gypsum ($CaSO_4 \cdot 2H_2O$) at -15 °C, hydrohalite ($NaCl{\cdot}2H_2O$) at -22.9 °C, sylvite (KCl) at -33 °C, and

finally $MgCl_2 \cdot 12H_2O$ at -36.2°C which is the eutectic temperature for seawater via this mineral sequence. The Gitterman experiments indicated that upon the onset of hydrohalite precipitation, mirabilite would begin to dissolve due to the creation of an undersaturated brine caused by a large reduction in Na^+. The dissolution of mirabilite consequently leads to an increase in SO_4^{2-}, resulting in conditions that enhance the precipitation of gypsum. This pathway results in equilibrium being achieved between all minerals and brine at all stages, and is therefore best likened to an equilibrium crystallisation process whereby previously formed minerals are permitted to interact with the brine.

The studies that derived the RNT Pathway (Ringer, 1906; Nelson and Thompson, 1954) differed from the experimental design of Gitterman, in that at various temperatures studied, minerals were removed from the brine before further cooling, therefore preventing subsequent interaction between minerals and brine. The RNT Pathway follows a different mineral precipitation sequence to the Gitterman Pathway, with mirabilite forming at -8.2 °C, hydrohalite at -22.9 °C, sylvite and $MgCl_2 \cdot 12H_2O$ at -36.0 °C, and a eutectic of -53.8 °C which occurs upon the precipitation of antarcticite ($CaCl_2 \cdot 6H_2O$). The discrepancy of 17.6 °C between the Gitterman and RNT Pathways eutectic temperatures highlights the difference in allowing for mineral interaction within the system. The RNT Pathway best represents a fractional crystallisation process, which involves the removal or isolation of minerals from the system as they form (Sha, 2012).

FREZCHEM is a thermodynamic model that can describe the geochemistry of seawater freezing (Marion et al., 1999; Marion and Kargel, 2008; Marion et al., 2010). Published material by the model's authors on the process of freezing seawater to its eutectic (Marion et al., 1999) uses the process of equilibrium crystallisation and results in a mineral precipitation sequence that best fits the Gitterman Pathway; with the precipitation of ikaite at -2 °C, mirabilite at -6.3 °C, gypsum at -22.2 °C, hydrohalite at -22.9 °C, sylvite at -34 °C and a eutectic that occurs upon the formation of $MgCl_2 \cdot 12H_2O$ at -36.2 °C.

No matter which precipitation pathway seawater undergoes when it freezes, the site of mineral precipitation in sea ice is within the brine inclusions. The dimensions and distribution of brine inclusions within the ice therefore create practical

constraints for the evaluation of mineral dynamics. The brine inclusions within sea ice respond dynamically to changes in temperature, and their size decreases as the temperature is reduced because pure water is removed from the brines by the freezing of ice to the surrounding matrix in order to maintain freezing equilibrium. Therefore minerals that form at higher temperatures, such as ikaite (Papadimitriou et al., 2013), have the opportunity to grow large enough (up to 600 μm) and are stable enough to allow for successful extraction by melting ice in the field (Dieckmann et al., 2008; Geilfus et al., 2013; Fischer et al., 2013). Successful extraction of ikaite and also gypsum from natural and experimental sea ice samples was achieved by Geilfus et al. (2013), who again used careful melting procedures to extract these sparingly soluble minerals. Minerals such as mirabilite and hydrohalite are estimated to be significantly smaller and too soluble to allow extraction by melting ice, and therefore have not been identified from field studies, but rather from laboratory studies. From laboratory experiments mirabilite crystals in sea ice have been estimated to range from 1 to 140 μm in diameter, with number densities of $\sim$270 crystals per mm^3 at -15 °C, resulting in the mineral occupying 3% of brine volume (Roedder, 1984; Light et al., 2003). Estimates of hydrohalite crystal size are between 1 and 1.7 μm in diameter (Light et al., 2003, 2004). Qualitative observations by microphotography indicate that mirabilite crystals occupy only a fraction of the brine volume and tend to sink to the bottom of brine inclusions, whereas hydrohalite forms a heterogeneous structure with ice that is distributed throughout the brine inclusions (Maykut and Light, 1995; Light et al., 2003).

The presence of countless microscopic mineral crystals encapsulated throughout the sea ice matrix results in observable changes to the physical properties of the ice such as its tensile strength (Assur, 1960), and reflectivity (Maykut and Light, 1995; Light et al., 2003, 2009). Of particular climatic interest is the effect of the mineral precipitation on the optical properties of the ice, which becomes more reflective to solar radiation as the proportion of minerals within the medium increases (Maykut and Light, 1995; Light et al., 2004). The optical properties fundamentally control the surface albedo of sea ice and therefore contribute to climate forcings in the polar regions. For these reasons in particular, thoroughly understanding the mineral dynamics within the sea ice system is of particular relevance to our climate and the

models that aim to recreate it accurately.

Given the practical constraints associated with the separation of microscopic, highly soluble minerals from sea ice during melting, coupled with that of using crystallographic techniques in the field, it is not currently feasible to carry out *in-situ* crystallographic studies on sea ice within the natural environment. To obtain a better understanding of mineral precipitation, synchrotron X-ray powder diffraction (SXRPD) was utilised to study the crystallographic formation and dynamics of minerals within seawater derived brines at sub-zero temperatures. The general aim of the study was to examine the potential of the technique to identify and quantify the minerals formed *in-situ* over the temperature range that sea ice experiences during the austral winter. This period is the least studied because field sites are at their most inaccessible, whilst mineral formation is likely to be most active. More particularly, we wished to investigate whether the technique could provide independent evidence of whether or not the changing structure of frozen seawater with decreasing temperature created the conditions that favour equilibrium or fractional crystallisation.

3.2 Methods

3.2.1 Preparation and analysis

Experiments designed to study mineral dynamics during the cooling and warming of sea ice were carried out on Beamline I11 (High resolution powder diffraction) at Diamond Light Source, the UK's national synchrotron facility. The low temperature control capabilities provided by a cryostream on Beamline I11 made it possible to replicate the conditions required for the formation of mineral precipitates in sea ice.

Experiments were carried out on concentrated seawater derived brines in separate cooling and warming experiments. For the cooling experiment the salinity of the brine was $S = 100$ (hereafter termed brine-100), and for the warming experiment the brine salinity was $S = 125$ (hereafter termed brine-125). These brines would be at equilibrium in sea ice at temperatures of -6.0 and -7.7 °C respectively, according to the salinity-temperature ($S_A - t$) relationship of thermally equilibrated sea ice brines, $S_A = 1000(1 - \frac{54.11}{t})^{-1}$ (Assur, 1960), with S_A (in g kg^{-1}) and conductivity based salinity (practical salinity, S) related by $S_A = 1.004715\ S$ (Millero and Huang,

2009). In thermally equilibrated ice-brine systems, t represents the freezing point of brine with a salinity S_A (Assur, 1960). Brine salinities were measured using a portable conductivity meter (WTW Cond 3110) with a WTW Tetracon 325 probe at laboratory temperature (20-26°C). A concentrated seawater derived brine was used in place of seawater in order to help enhance the proportion of mineral salts that could precipitate relative to the dominant mineral phase of ice. It is important to note that using a concentrated seawater brine does not affect the mineral dynamics of the frozen seawater past its freezing point as long as the dissolved constituents of the brine are conservative relative to its salinity and the standard composition of mid oceanic seawater (DOE, 1994; Maykut and Light, 1995). The brines were produced via frigid concentration of filtered seawater from the School of Ocean Sciences, Bangor University. The composition of the brine was confirmed to be conservative with respect to SO_4^{2-}, Na^+ and Ca^{2+}, indicating that the solution had not been affected by the precipitation of any known mineral phase (ikaite, mirabilite, gypsum or hydrohalite) that would be predicted by the Gitterman or RNT Pathways within the temperatures used for freezing.

Calibration of the monochromatic wavelength on Beamline I11 was made using a silicon standard (NIST 640c). For the samples, a 0.5 mm borosilicate capillary was filled with the concentrated seawater derived brine. Data was collected at high resolution (1 mdeg steps) using the Multi-Analysing Crystals detector array on the 2θ circle of the diffractometer. Powder patterns were obtained at a wavelength of 0.826650 $\mathring{A}$ for the cooling experiment, and 0.826404 $\mathring{A}$ for the warming experiment. Temperature was controlled by an Oxford Cryosystems Cryostream Plus with a proven temperature stability greater than 0.1°C and a working range of -193 to 227°C. Due to the small volume of brine inside the capillary, it was found that the sample had to be substantially supercooled before the solution froze.

All diffraction patterns obtained were analysed on TOPAS v5 Academic software using the Fundamental Parameters Analysis method to obtain information on peak positions of each mineral from a Le Bail refinement. Published cell parameters were used as an initial starting point, and were allowed to refine. These values were sourced from Fortes et al. (2004) for ice, Brand et al. (2009) for mirabilite, Klewe and Pederson (1974) for hydrohalite and Boeyens and Ichharam (2002) for

gypsum. Calculated *d*-spacings of the *hkl* reflections from the refinements were used to identify peaks that were specific to each mineral.

Each experiment used only 1 *in-situ* sample that was subjected to changing temperature, therefore the peak intensity obtained from a crystalline phase can be assumed to be proportional to its mass within the sample. For this reason, peak intensity could be used to indicate changes in mineral mass within the sample as a function of temperature (Norrish and Taylor, 1962; Gavish and Friedman, 1973).

Table 3.1: The Miller indices and *d*-spacing ($\mathring{A}$) for the mirabilite, hydrohalite and ice peaks used in the analysis of peak intensity.

Mirabilite		Hydrohalite		Ice	
hkl	*d*-spacing	*hkl*	*d*-spacing	*hkl*	*d*-spacing
0 2 1	4.76568	0 2 1	3.86846	0 1 2	2.67865
1 -3 -1	3.25384	2 -1 -2	2.59857	0 1 3	2.07679
0 2 3	3.19820	1 3 1	2.43683	0 1 5	1.37646

To quantify peak intensity, the three strongest reflections of mirabilite, hydrohalite and ice (the only detectable phases) were chosen for analysis. The Miller indices and *d*-spacings of the chosen peaks of all three phases are displayed in table 3.1. To aid with the calculation of peak intensity, all chosen peaks were fitted to a gaussian distribution using the curve fitting application in Matlab R2014a (Muñoz-Iglesias et al., 2013). Peak intensity is related to its height and area (integrated intensity), both of which can be used individually as indicators of mineral mass within an *in-situ* sample (Norrish and Taylor, 1962; Gavish and Friedman, 1973; Milliman and Bornhold, 1973). Integrated intensity was the preferred method of quantifying the strength of each peak, calculated as the product of peak height (counts) and the full width at half maximum of the peak (2θ) (Norrish and Taylor, 1962), and was thus used for the analysis of all hydrohalite and ice peaks. The strength of the mirabilite reflections, however, was considerably lower than that of hydrohalite and ice, with the three strongest peaks having average heights that were only 4.5 ($n = 30$) and 2.3 ($n = 42$) times greater than the background of the cooling and warming experiments respectively. Due to this relatively low signal, the mirabilite peak areas were found to be affected by background level displacement with changing temperature (figure 3.1). This displacement was found to relate to the amorphous content of the sample. At -36°C when brine-125 would have been close

to its eutectic, the average background level in regions of the identified mirabilite peaks was 129 counts. In comparison, when brine-125 was in purely liquid form, the average background was 213 counts. This increase was sufficient to affect the integrated intensities of mirabilite peaks used in this region and therefore peak height analysis was chosen as the more appropriate method because this parameter is affected by background displacement to a much lesser degree (Gavish and Friedman, 1973). Results from the analysis of combined (sum of the 3 strongest reflections) peak heights (for mirabilite) and combined integrated intensities (for ice and hydrohalite) will be referred to as mass hereafter because it was assumed that relative changes in each of these parameters was representative of an absolute change in the mass of the mineral within each *in-situ* sample.

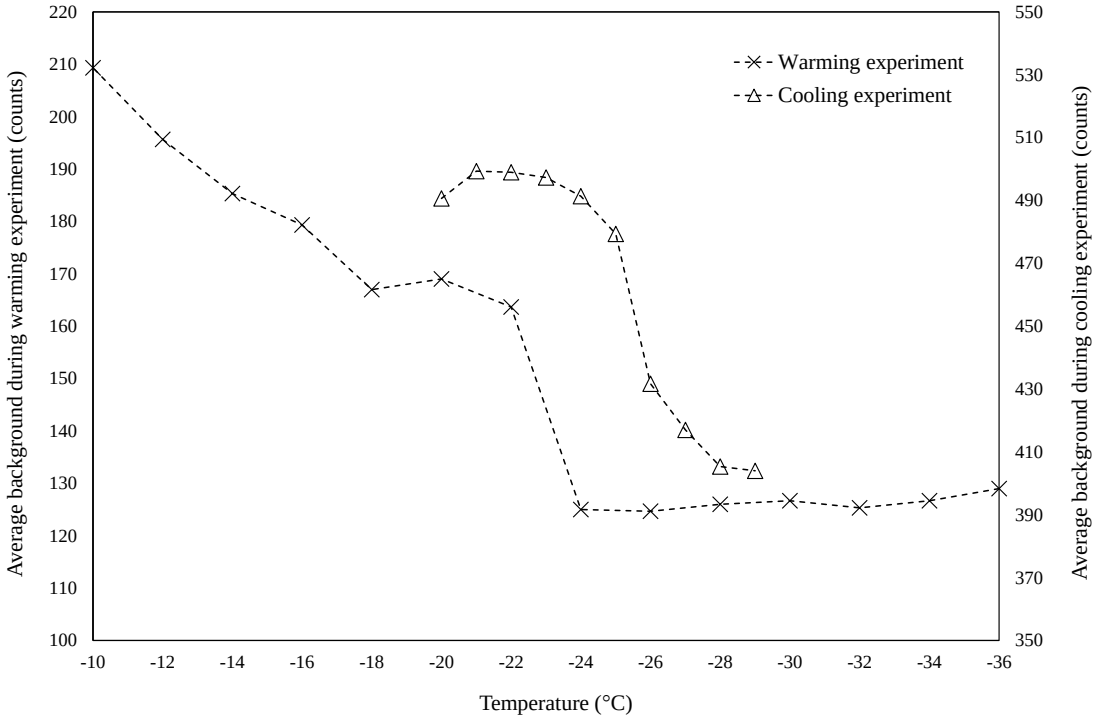

Figure 3.1: The fluctuations in background signal during the cooling and warming experiments, measured as an average taken from each side of the mirabilite peaks that were studied.

3.2.2 Time series

To make an initial assessment of the response of the ice-brine-mineral system to changes in temperature, two time series measurements were taken within which ice, mirabilite and hydrohalite were identified as the only detectable minerals. First,

brine-125 was cooled from ambient to −40 °C and maintained at this temperature, being scanned for 5 minutes at various intervals over a 65 minute period (figure 3.2a). Second, brine-100 was cooled to −40 °C for 1 hour, after which it was warmed to −20 °C for 50 minutes with a 10 minute scan completed at 10, 20 and 50 minutes (figure 3.2b). The temperature changes studied in these initial time series measurements were used to identify a realistic rate of change for subsequent experiments, and were at least an order of magnitude faster than the rate of temperature change used in any subsequent experiments. Although the temperature of the sample was not monitored independently, the small volume of the sample, high thermal conductivity of the capillary and specification of the cryostream would result in a rapid response to any temperature change.

In the first time series experiment, cooling brine-125 to −40 °C led to ice formation within 5 minutes, and hydrohalite within 15 minutes (figure 3.2a). Both approached equilibrium after 25 minutes. The initial precipitation of mirabilite between 15 and 20 minutes was very rapid, followed by a near order of magnitude decrease in its precipitation rate after this time that continued for the remainder of the experiment.

In the second time series experiment when the temperature of brine-100 was increased from −40 °C to −20 °C, all phases responded to the temperature change in the first 10 minutes with hydrohalite completely dissolving, while ice mass decreased and mirabilite mass increased rapidly (figure 3.2b). For the subsequent 40 minutes, ice continued melting while mirabilite continued to precipitate at a much slower rate.

The results of the time series experiments indicated that, with a rapid and large change in temperature, either warming or cooling, equilibrium for ice and hydrohalite was approached within 25 minutes. Mirabilite formation, however, which is reported to have slow kinetics (Weeks, 2010), may not have reached equilibrium. It should be noted that the time series experiments are not representative of the natural rates of temperature change that sea ice may be subjected to, and were rather used to inform the time required in subsequent experiments to ensure that a reasonable approximate for equilibrium conditions was used in subsequent cooling and warming experiments.

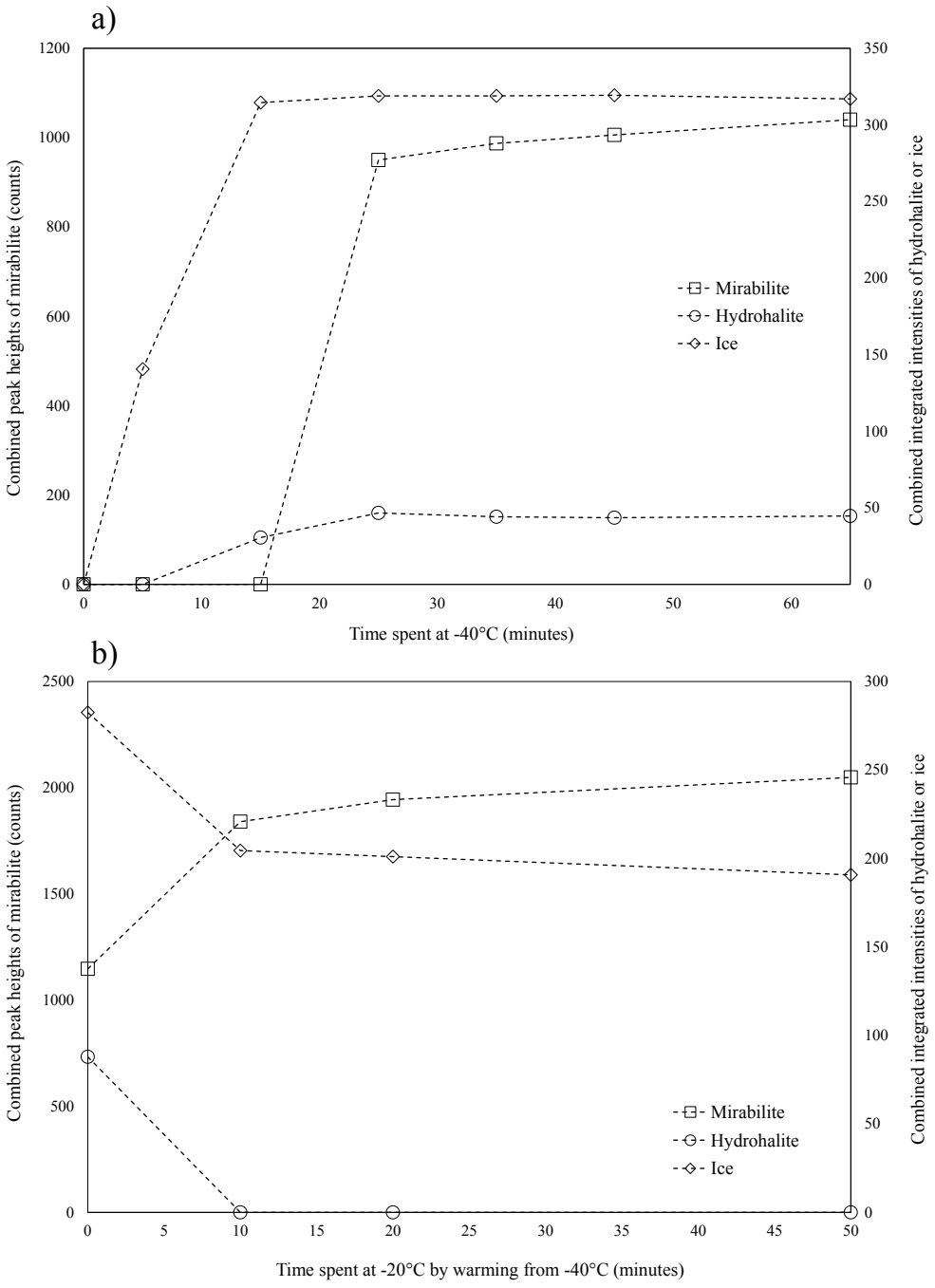

Figure 3.2: **a)** The formation of mirabilite, hydrohalite and ice upon cooling brine-125 from ambient to −40 °C (scan time = 5 minutes). **b** The melting of ice, precipitation of mirabilite and dissolution of hydrohalite upon warming brine-100 from −40 to −20 °C (scan time = 10 minutes).

3.2.3 Cooling and warming experiment protocol

In response to the time series results, the subsequent experiments employed small ($1 - 2$ °C) incremental temperature changes and longer periods at temperature of between 25 minutes and 1 hour that are more representative of diurnal changes that sea ice may experience in the austral winter. First, brine-100 was maintained at -20 °C for 50 minutes before cooling in 1 °C increments from -20 to -29 °C. The cooled sample was maintained at each temperature for 30 minutes before a 30 minute scan. Second, brine-125, that had been cooled and maintained at -36 °C for 45 minutes, was subsequently warmed in 2 °C increments to -10 °C. The warmed sample was maintained at each temperature for 5 minutes before a 20 minute scan. The protocols will be referred to separately as the cooling and warming experiments hereafter.

3.3 Results

In the cooling experiment, the mass of mirabilite increased as brine-100 was cooled from -20 to -24 °C, indicating that the chemically evolving composition of the brine was sustaining its supersaturation with respect to mirabilite (figure 3.3a). As the temperature was lowered beyond -24 °C the mirabilite mass decreased, indicating that the brine became undersaturated with respect to this mineral, resulting in dissolution. The onset of mirabilite dissolution coincided with the first detectable sign of hydrohalite at -25 °C. The mass of hydrohalite then continued to increase rapidly below -25 °C, showing that the brine sustained supersaturation with respect to hydrohalite until the experiment was terminated at -29 °C. Between -24 and -27 °C there was a substantial increase in ice mass (figure 3.3b). The rate of ice formation reduced towards -29 °C when the experiment was terminated. The sharp increase in ice mass between -24 and -27 °C coincided with the precipitation of hydrohalite and dissolution of mirabilite (figure 3.3a). The observed trends in ice formation represent a dynamic balance between the temperature, brine composition and water removal into the hydration waters of mirabilite and hydrohalite.

In the warming experiment, as brine-125 was warmed from -36 to -26 °C the mass of hydrohalite showed a decreasing trend, whilst that of mirabilite increased, indicating that the brine was gradually becoming undersaturated with respect to

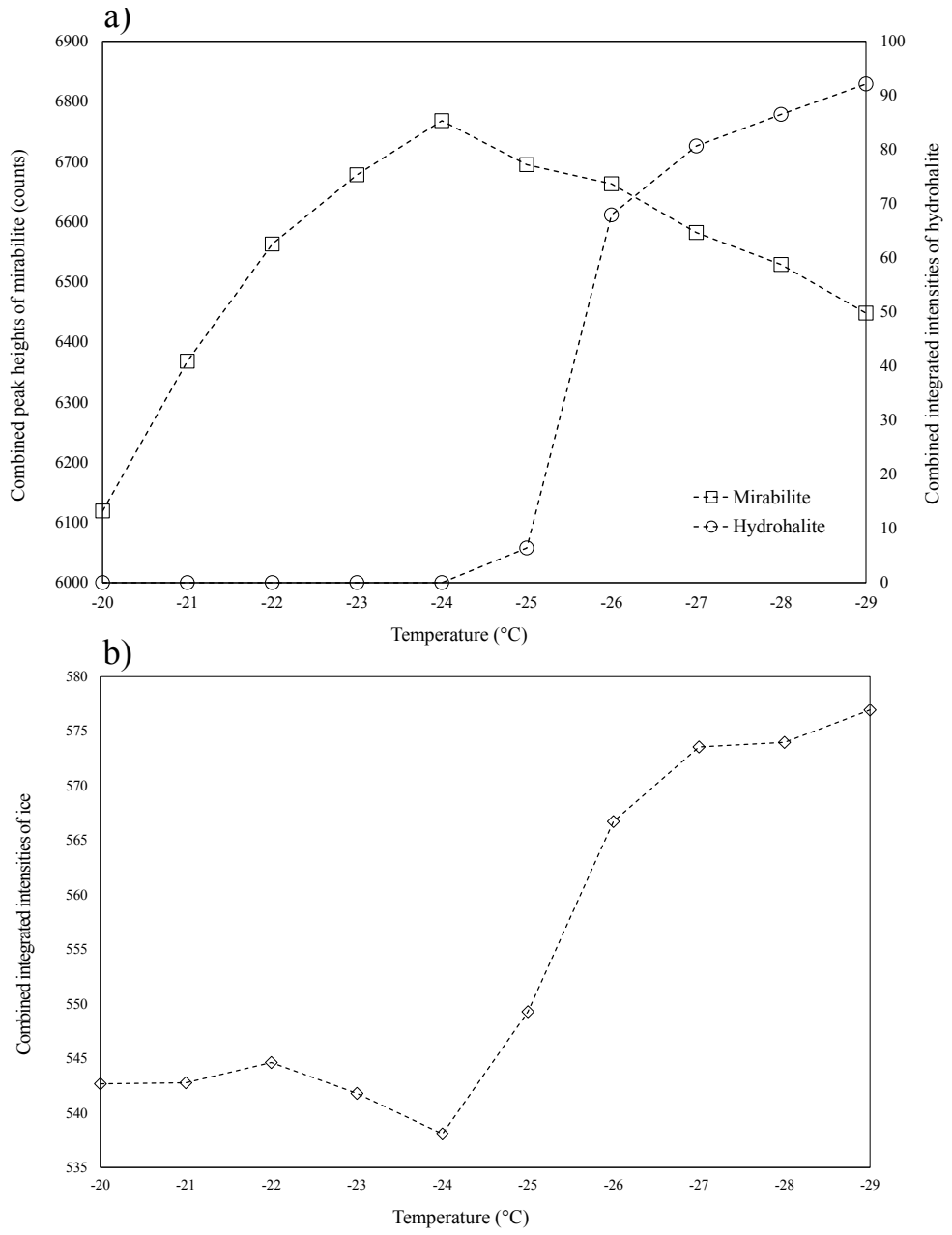

Figure 3.3: Cooling experiment: **a)** The change in combined peak heights of mirabilite and integrated intensities of hydrohalite within brine-125 as it was cooled from −20 to −29 °C. **b)** The change in combined integrated intensities of ice within brine-125 as it was cooled from −20 to −29 °C.

hydrohalite but increasingly supersaturated with respect to mirabilite (figure 3.4a). On further warming above −26 °C the mass of hydrohalite decreased rapidly, resulting in total dissolution by −22 °C. Between −22 and −10 °C, only mirabilite remained, with an increasingly rapid decline in its mass at temperatures warmer than −14 °C. Ice mass upon warming brine-125 from −36 to −10 °C, displayed two nearly linear periods of decrease separated by an accelerated drop in the ice mass which coincided with the temperature for complete dissolution of hydrohalite between −22 and −24 °C (figure 3.4b).

3.4 Discussion

3.4.1 Detected minerals

Taking all experiments into account, temperatures ranged from −10 to −40°C. According to the given pathways for seawater freezing (table 1.1), this temperature range could include the precipitation of ikaite, mirabilite, gypsum, hydrohalite, sylvite and $MgCl_2 \cdot 12H_2O$. In our study; ice, mirabilite and hydrohalite were the only crystalline phases detected.

During the formation of sea ice, the reduction in temperature and increased salinity of the brine results in a raised pCO_2 and reduced pH (Geilfus et al., 2014; Papadimitriou et al., 2014). These conditions, recreated in our experimental runs, would not be expected to precipitate ikaite due its raised solubility (Papadimitriou et al., 2013).

Successful detection of any mineral in our experiments is largely determined by its mass within the sample, which itself is dictated by the initial composition of the seawater/brine, and the number of hydration waters that are incorporated into the mineral. The FREZCHEM model predicts (with ikaite excluded) that the eutectic of seawater will occur at -36.2°C after the precipitation of five minerals in different proportions (figure 3.5). Given that the mass of mirabilite within the samples was approaching the detection limit of the method, indicated by the susceptibility of the signal to background displacement (figure 3.1), it is likely that gypsum and sylvite would have been undetectable due to their relatively low concentrations (3 and 29 times lower than mirabilite, respectively). In contrast, $MgCl_2 \cdot 12H_2O$ is predicted to precipitate in quantities approximately triple that of mirabilite, and therefore

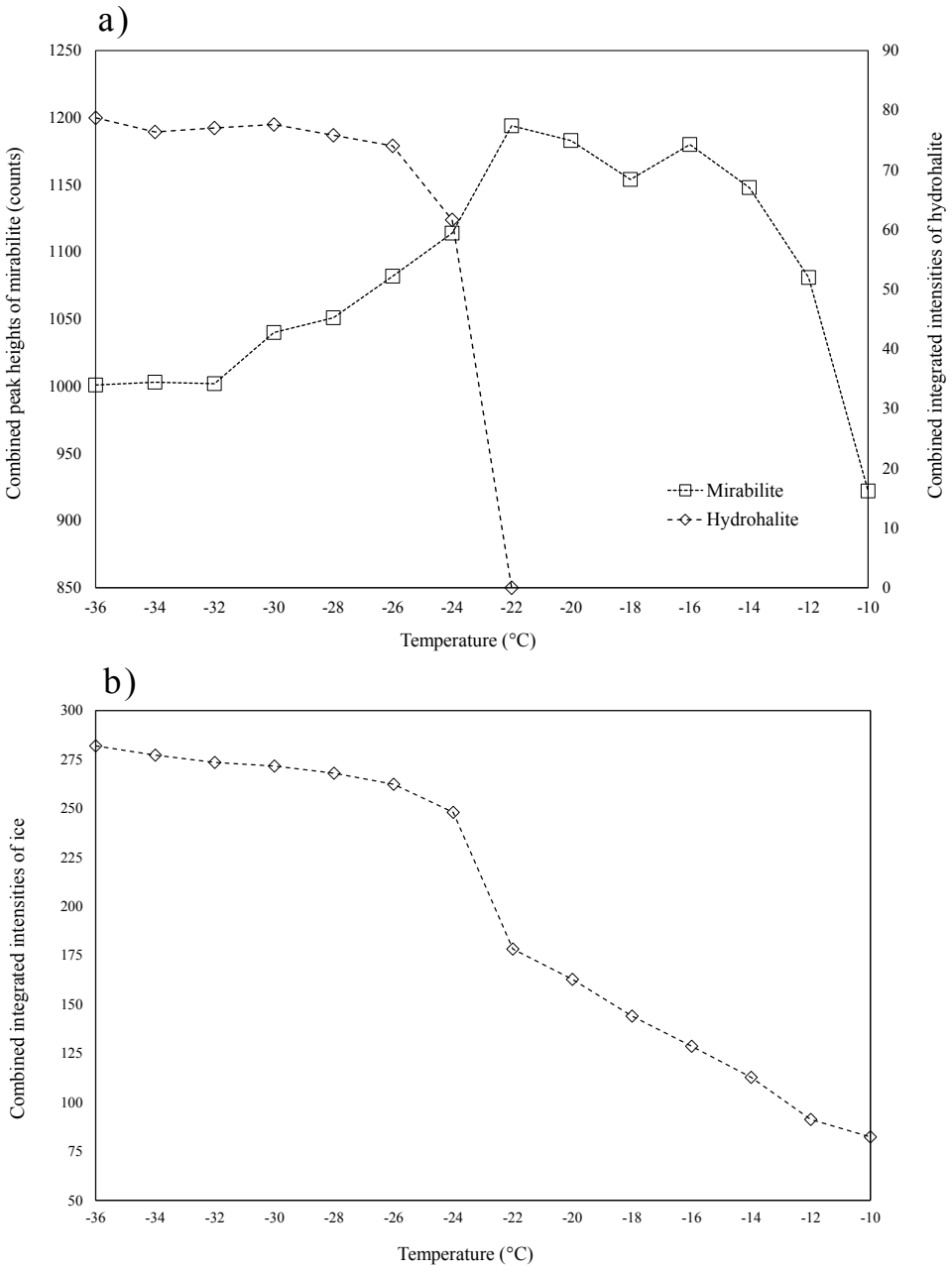

Figure 3.4: Warming experiment: **a)** The change in combined peak height of mirabilite and combined integrated intensity of hydrohalite when brine-125 as was warmed from −36 to −10 °C. **b)** The change in average integrated intensity of ice when brine-125 was warmed from −36 to −10 °C.

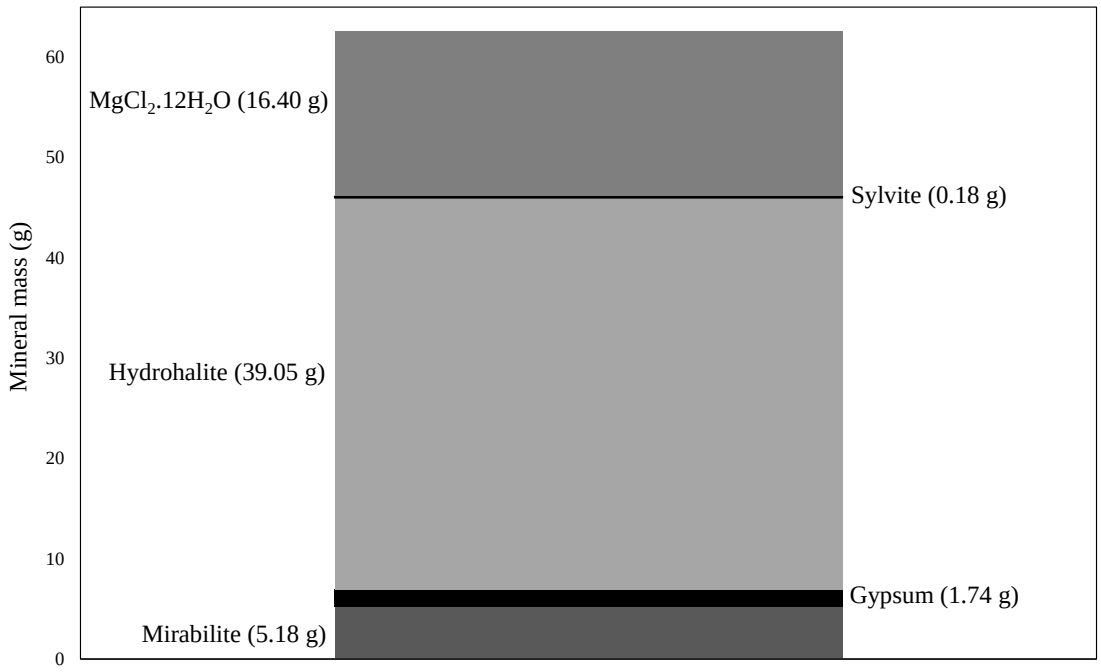

Figure 3.5: FREZCHEM predictions of the precipitated mineral assemblage from freezing seawater ($S = 35$) to its eutectic at -36.2 °C.

should have been detected a temperatures below -36.2 °C. The absence of any peaks that can be attributed to $MgCl_2 \cdot 12H_2O$ throughout our experiments therefore could be accounted for by other factors, such as the possibility of supercooling at the eutectic (Toner et al., 2014), or insufficient equilibration/scan time/replication at temperatures below -36.2 °C (which was only reached during the time series experiment at -40 °C, figure 3.2a). In either case, further experiments specifically designed to assess the mineral dynamics at temperatures approaching and below the eutectic of seawater would be required to define and explain the absence of $MgCl_2 \cdot 12H_2O$.

Despite the absence of several minerals from the cooling and warming experiments, the detected minerals of mirabilite and hydrohalite are likely to be the most abundant minerals in sea ice throughout the temperatures at which it exists in the environment, and are the most influential in controlling the optical properties of sea ice (Light et al., 2004, 2009; Ebert and Curry, 1993). Therefore new evidence detailing their dynamics within the sea ice system is of particular relevance to the polar environments on Earth.

3.4.2 Mirabilite and hydrohalite interaction

This study represents a novel method which utilises *in-situ* SXRPD to unequivocally identify the mirabilite and hydrohalite dynamics within sea ice as the ambient temperature is lowered and raised. The results are the first direct X-ray evidence of mirabilite and hydrohalite presence within frozen seawater brines which can be related to their existence in natural sea ice within the temperature range studied. The technique also provides insights of how the environmental setting within the brine pockets affects mineral dynamics. Whether minerals, once formed, are isolated from the brine preventing any further interaction with the fluid or not has important implications for the proposed pathways by which freezing seawater takes to its eutectic, and prior to this study had never been investigated (Gitterman, 1937; Nelson and Thompson, 1954; Marion et al., 1999).

The cooling experiment showed mirabilite mass increasing between −20 and −24 °C; a result of the coupled effect of decreasing solubility with lower temperature, and the higher Na^+ and SO_4^{2-} concentration as the brine salinity increases (figure 3.3a). Such a trend in mirabilite's solubility with decreasing temperature in sea ice would be expected (Vavouraki and Koutsoukos, 2012; Marion et al., 1999). Instead of a continued increase in mass, mirabilite started to dissolve below −24 °C, coincident with the temperature at which hydrohalite was first detected. Our results are consistent with the changes proposed by Gitterman (1937) and Marion et al. (1999) that the concentrations of Na^+ and SO_4^{2-} in the brine are controlled by mirabilite precipitation until the brine becomes supersaturated with respect to hydrohalite. Either the degree of supersaturation of hydrohalite is higher than that of mirabilite or the kinetics of hydrohalite precipitation is faster, but the result is that the reduction in dissolved Na^+ concentration causes undersaturation of the brine with respect to mirabilite and its dissolution. Mirabilite dissolution will then result in an increase of dissolved SO_4^{2-} in the residual brine.

The warming experiment, which presents data over a wider temperature range, confirms the relative changes in mirabilite and hydrohalite mass (figure 3.4a). As the temperature warmed from −36 °C, the trend seen in the cooling experiment is reversed as hydrohalite dissolves, releasing excess Na^+ into the residual brine and leading to supersaturation and precipitation of mirabilite. At −22°C, the onset of

mirabilite dissolution coincides with the complete dissolution of hydrohalite, driven by the increased solubility of mirabilite at higher temperatures in less saline brines, and the absence of any further hydrohalite dissolution acting as a source of Na^+.

The changes observed *in-situ* during the cooling and warming experiments differ from the results of experiments used to derive the RNT pathway for seawater freezing, which employed a methodology that enforced fractional crystallisation (FC). The changes are however consistent with the concept of equilibrium crystallisation (EC) described by the Gitterman Pathway and FREZCHEM model. FC processes were proposed to be characteristic of samples that are cooled quickly (Zolotov and Shock, 2001), resulting in separation of a mineral from the surrounding matrix (Weeks, 2010). It is therefore surprising to find evidence of EC, within the rapidly cooled samples that were analysed in these experiments. The observation of mineral interaction within our samples implies that mirabilite and hydrohalite were present together in the brine pockets, and that changes in the saturation state of one of the minerals, resulted in a direct and opposite effect on the other.

Despite results supporting the equilibrium crystallisation paradigms described by the Gitterman Pathway and FREZCHEM model with respect to mirabilite and hydrohalite, there is a distinct difference that concerns the precipitation of gypsum. The Gitterman Pathway predicts the onset of gypsum precipitation at -15 °C, while the FREZCHEM model predicts the onset to occur at -22.2 °C before being further fueled by equilibrium reactions between hydrohalite and mirabilite below -22.9 °C. Furthermore, gypsum crystals have recently been detected in laboratory and experimental sea ice (Geilfus et al., 2013). Gypsum was not detected in any sample analysed throughout either the cooling or warming experiment presented here, which as already outlined, may be due to the detection limit of the method. Aside from the limit of detection, there are two further reasons that could help explain the absence of gypsum: 1) gypsum did not precipitate within our samples; 2) the brines were supersaturated with respect to gypsum, but the mineral did not precipitate due to slow kinetics (Weeks, 2010; Reznik et al., 2009).

The solubility of gypsum in the sub-zero seawater derived brines that exist in sea ice has never been determined, and it may therefore be feasible that in the conditions studied, brine-100 and brine-125 never became supersaturated with respect to

gypsum.

The FREZCHEM model and Gitterman Pathway predict gypsum precipitation under the conditions used in this study. The FREZCHEM model is, however, based on equilibrium thermodynamics and therefore does not account for the rate at which chemical reactions occur. Furthermore, the Gitterman pathway is based on experiments that lasted up to 4 weeks, much longer than our study. It is possible that the short time scale employed here did not allow sufficient time for gypsum precipitation. To assess the importance of kinetic control on gypsum precipitation using X-ray crystallography would therefore require a long duration *in-situ* experiment. Furthermore, measuring the solubility of gypsum within sub-zero seawater derived brines would aid in resolving gypsum dynamics in sea ice, and help to explain the source of gypsum crystals that were observed in sea ice by Geilfus et al. (2013).

The final implication of the mineral dynamics observed in our experiments concerns the precipitation/dissolution of hydrohalite, and this mineral's sensitivity to temperature changes. The amount of light scattering that sea ice exhibits has been shown to increase substantially between -24 and -30 °C due to the precipitation of hydrohalite (Light et al., 2004), giving its presence climatic implications for the feedback mechanisms associated with the high albedo of sea ice (Light et al., 2009; Ebert and Curry, 1993). Any change in the temporal or spatial extent of sea ice experiencing low atmospheric temperatures (<-23 °C), or a general warming of minimum winter temperatures may therefore have a significant impact given the sensitivity of hydrohalite solubility between -22 and -25 °C detected in this study. On a more practical level, despite hydrohalite being the most abundant mineral phase in cold sea ice, this sensitivity to temperature and small crystal size (< 1.7 μm (Light et al., 2004)) combine to make it unlikely that hydrohalite crystals could ever be extracted from an environmental sample by melting procedures such as those used by Dieckmann et al. (2008) and Geilfus et al. (2013).

3.4.3 Ice dynamics

The rates of change in ice mass from the cooling and warming experiments (figures 3.3b and 3.4b) provide novel crystallographic data on the way that seawater approaches its eutectic. In both the cooling and warming experiments there was a sharp

increase in ice formation/melt that coincided with the precipitation/dissolution of hydrohalite, indicating that the behaviour of the ice and hydrohalite are interlinked by associated changes in brine composition.

The ice data from the warming experiment displayed less variability than that of the cooling experiment. This difference could reside from the observation of how brines approaching their eutectic can often become supercooled (Toner et al., 2014), but the reverse cannot apply. Although a supercooled brine exists in a thermodynamically unstable state, the phenomenon is observed because crystal nucleation requires the energy intensive process of the formation of an interface between a crystal surface and surrounding solution. This energy is provided by the solution becoming supersaturated (which in the case of freezing seawater would require supercooling) to a point at which the free energy exceeds the energy required for the formation of a stable nucleus upon which the crystal can grow (Toner et al., 2014). If supercooling occurred within our samples, the process could also result in a delayed onset for the precipitation of minerals because there would be no ionic change in solution composition as temperature decreased. Although there is a slight discrepancy between the temperature of precipitation/dissolution for hydrohalite from the cooling and warming experiments (the precipitation of hydrohalite occurred > 1 °C cooler than expected from all known predictions), we are unable to infer as whether the observation is due to supercooling with respect to ice, or supersaturation of the brine with respect to hydrohalite.

The results are the first direct X-ray evidence consistent with a change in rate of ice formation and melt that coincides with the precipitation or dissolution of hydrohalite respectively. The evidence of a hydrohalite-ice interaction within the *in-situ* samples confirms that precipitation or dissolution of hydrohalite affects the freezing point of the brine within the sample, which is governed by its salinity/ionic strength. The ionic constituents of hydrohalite, Na^+ and Cl^-, are the most concentrated solutes within seawater; comprising 86% of the mass of salt in conservative seawater/brine (DOE, 1994). The FREZCHEM model indicates (from a starting salinity, $S = 35$) that 35.2 g hydrohalite/kg frozen seawater is precipitated when the temperature reaches -29°C. The precipitation of hydrohalite removes Na^+ and Cl^- from solution, and at the same time removes pure water to form hydration wa-

ters. The overall effect of hydrohalite precipitation on the brine salinity is therefore a balance between the removal of dissolved constituents and water. Precipitation of 35.2 g of hydrohalite between −23 and −29°C from 1 kg of seawater equates to the removal of 13.4 g H_2O and 21.8 g NaCl, which is equal to a 14.3% reduction in water within the frozen system, and a 71.2% reduction in the salt content by mass. The instantaneous effect of hydrohalite precipitation on the residual brine would therefore be a reduced ionic strength. Simultaneously, this would induce freezing of the brine to concentrate the dissolved constituents to a degree that is sufficient to lower its freezing point and achieve ice-brine equilibrium.

Outputs from the FREZCHEM model (version 15.1 run in equilibrium mode between −10 and −36 °C with a starting composition identical to the standard composition of mid oceanic seawater (DOE, 1994)) showed a similar trend to our observed dynamics of ice (figure 3.6). In comparison, if hydrohalite is disabled from the model, there is no significant change in the rate of ice formation at the point of hydrohalite precipitation. The FREZCHEM model therefore predicts that between −23 and −28 °C, the precipitation of hydrohalite induces the formation of an extra 48.42 g of ice. Other runs of the model that excluded the precipitation of mirabilite, gypsum and sylvite, resulted in no discernable change in the rate of ice formation.

Experimental measurements of ice content during seawater freezing from Assur (1960) and (Richardson, 1976) are also displayed in figure 3.6, and show strong agreement with FREZCHEM. Between −22 and −26 °C the collated data display an average ($\pm 1\sigma$) increase in the rate of ice formation that is 269 ± 55 % greater than the rate between −18 and −22 °C. The trends in ice data are best compared to changes observed in the warming experiment, (plotted on a secondary y-axis, figure 3.6), which displays a rate of change between −22 and −26 °C that is of 246 % larger than that between −18 and −22 °C . The similarity, in both trends and rates, between the data from our experiment and that from traditional studies and model predictions, substantiates the *in-situ* method used here as a reliable and reproducible technique for studying inaccessible geochemical environments at sub-zero temperatures.

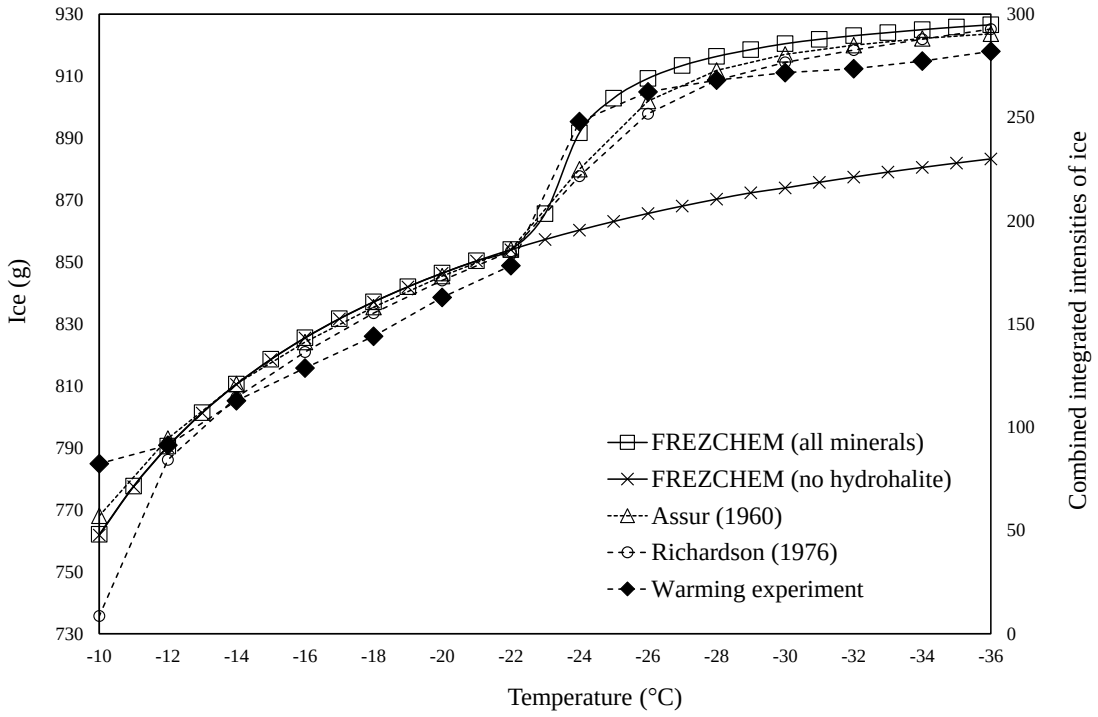

Figure 3.6: The change in ice content upon freezing 1 kg of seawater ($S = 35$) between -10 and -36 °C. The data of water content (g) given by Richardson (1976) were converted to an estimate of ice content by accounting for the published quantities of mineral mass at each temperature. 'FREZCHEM (all minerals)' represents the output obtained when the FREZCHEM model was run with all mineral phases enabled. 'FREZCHEM (no hydrohalite)' represents the output obtained when the FREZCHEM model was run with all minerals other than hydrohalite enabled. Results from the warming experiment are plotted on a secondary y-axis to enable comparison of trends between our observed values and mass measurements.

3.5 Conclusions

Our study provides the first direct X-ray evidence of mirabilite and hydrohalite in frozen seawater brines, the dynamics of which can be extrapolated to highlight the behaviour of these minerals in much of the sea ice on Earth. The results importantly highlight the use of *in-situ* synchrotron techniques for studying the geochemistry of inaccessible environments at low temperatures. Specifically, results from both cooling and warming seawater derived brines at sub-zero temperatures suggest that mineral precipitation occurs via a process that is best described as an equilibrium crystallisation pathway where minerals are allowed to interact. The process is therefore best predicted by the work of Gitterman (1937) and the FREZCHEM model. The 4-way ice-brine-mirabilite-hydrohalite interactions within the frozen

matrix highlighted here make for a highly dynamic geochemical environment that would be impossible to study crystallographically at present without *in-situ* laboratory techniques. Much longer duration experiments, such as those proposed by the new facility at Diamond (Beamline I11 LDE), would allow for a more detailed examination of the seasonal changes in mineral composition within the ice and would be more representative of equilibrium conditions. Further testing at temperatures approaching the eutectic of seawater would aid in elucidating the dynamics of $MgCl_2 \cdot 12H_2O$. The experiment has highlighted the sensitivity of hydrohalite to temperature changes, which is important for the possibility of its physical separation from sea ice in the field, and also with respect to the accelerated rate of ice precipitation and melt associated with its formation and dissolution. Hydrohalite precipitation ultimately acts to drive sea ice towards its eutectic and substantially reduce brine volume within a few degrees of cooling below $\sim -23°C$.

Chapter 4

Mirabilite solubility in equilibrium sea ice brines

[Butler, B.M., Papadimitriou, S., Santoro, A., and Kennedy, H. (2016). Mirabilite solubility in equilibrium sea ice brines. *Geochimica et Cosmochimica Acta*]

Abstract

The sea ice microstructure is permeated by brine channels and pockets that contain concentrated seawater-derived brine. Cooling the sea ice results in further formation of pure ice within these pockets as thermal equilibrium is attained, resulting in a smaller volume of increasingly concentrated residual brine. The coupled changes in temperature and ionic composition result in supersaturation of the brine with respect to mirabilite ($Na_2SO_4 \cdot 10H_2O$) at temperatures below -6.38 °C, which consequently precipitates within the sea ice microstructure. Here, mirabilite solubility in natural and synthetic seawater derived brines, representative of sea ice at thermal equilibrium, has been measured in laboratory experiments between 0.2 and -20.6 °C, and hence we present a detailed examination of mirabilite dynamics within the sea ice system. Below -6.38 °C mirabilite displays particularly large changes in solubility as the temperature decreases, and by -20.6 °C its precipitation results in 12.90 % and 91.97 % reductions in the total dissolved Na^+ and SO_4^{2-} concentrations respectively, compared to that of conservative seawater concentration. Such large non-conservative changes in brine composition could potentially impact upon the measurement of sea ice brine salinity and pH, whilst the altered osmotic conditions create additional challenges for the sympagic organisms that inhabit the sea ice system. At temperatures above -6.38 °C, mirabilite again displays large

changes in solubility that likely aid in impeding its identification in field samples of sea ice. Our solubility measurements display excellent agreement with that of the FREZCHEM model, which was therefore used to supplement our measurements to colder temperatures. Measured and modelled solubility data were incorporated into a 1D model for the growth of first-year Arctic sea ice. Model results ultimately suggest that mirabilite has a near ubiquitous presence in much of the sea ice on Earth, and illustrate the spatial and temporal evolution of mirabilite within sea ice as it grows throughout an Arctic winter, reaching maximum concentrations of 2.3 g kg^{-1}.

4.1 Introduction

Sea ice is a porous medium comprised of a pure ice framework dotted by gas pockets and permeated by channels of concentrated seawater-derived brine (Light et al., 2003; Golden et al., 2007). The lower the temperature of sea ice, the more concentrated the brine becomes as more pure water freezes to maintain thermal equilibrium. Initially the ionic composition of the brine is conservative, but begins to deviate from conservative behaviour upon sufficient reduction in temperature when the brine becomes supersaturated with respect to the hydrated polymorphs of $CaCO_3$, Na_2SO_4, $CaSO_4$ and NaCl (Gitterman, 1937; Nelson and Thompson, 1954; Marion et al., 1999). The precipitation of minerals in this setting is unusual in that, rather than sinking to the ocean floor, they become encapsulated in the pores of the ice (Light et al., 2003) and are therefore retained close to the ice-atmosphere interface. Their presence in the ice affects its structural and optical properties (Assur, 1960; Maykut and Light, 1995; Light et al., 2003, 2009) due to their size distribution and regulatory effect on brine volume. Furthermore, mineral precipitation compromises the concept of practical salinity that is reliant upon constant ionic ratios as in oceanic water, whilst also altering the osmotic conditions of the brine and creating further physiological challenges for sympagic micro-organisms (Thomas and Dieckmann, 2002; Schallenberg et al., 2003).

There is a temperature-dependent sequence of minerals that precipitate in sea ice, with each mineral having a specific temperature for the onset of its precipitation (table 4.1). Several pathways have been proposed as paradigms of this process

(Gitterman, 1937; Nelson and Thompson, 1954; Marion et al., 1999), each with subtle differences in the onset-temperature and composition of the mineral assemblage. This study hereafter will focus on mirabilite ($Na_2SO_4 \cdot 10H_2O$), which is particularly soluble in aqueous solutions above 0 °C (Vavouraki and Koutsoukos, 2012). The decreased temperature and physical concentration of seawater by freezing in sea ice environments creates paired changes to the equilibrium temperature and salinity that can be described empirically (Assur, 1960). Estimates for the onset of mirabilite precipitation during this process range from −6.3 to −8.2 °C (Gitterman, 1937; Nelson and Thompson, 1954; Marion et al., 1999). Average winter temperatures in polar regions are consistently below this range (Eicken, 1992b), therefore mirabilite precipitation would be expected across large areas of sea ice that covers approximately 5 % of the Earth's surface area.

Table 4.1: The minerals predicted to precipitate in frozen seawater, and the temperature (°C) at which their precipitation initiates. Further to the tabulated minerals, ikaite ($CaCO_3 \cdot 6H_2O$) has been shown to precipitate in degassed brines below −2 °C (Papadimitriou et al., 2013).

Mineral	FREZCHEM[a]	Gitterman[b]	Ringer-Nelson-Thompson[c]
Mirabilite	−6.3	−7.3	−8.2
Gypsum	−22.2	∼ −12 to −15	N/A
Hydrohalite	−22.9	−22.9	−22.9
Sylvite	−34.0	−33.0	−36.0
$MgCl_2 \cdot 12H_2O$	−36.2*	−36.2*	−36.0
Antarcticite	N/A	N/A	−53.8*

[a] Marion et al. (1999)
[b] Gitterman (1937)
[c] Nelson and Thompson (1954)
* Eutectic temperature

Mirabilite crystals in sea ice have never been identified in the field, but laboratory studies have hinted at its presence (Gitterman, 1937; Nelson and Thompson, 1954; Light et al., 2003; Butler and Kennedy, 2015). The dimensions and distribution of mirabilite crystals within the ice are constrained by the morphology of the host brine inclusions. Qualitative observation of mirabilite crystals in sea ice by microphotography yielded mirabilite crystals of $1 - 140$ μm in diameter, which at −15 °C were present in densities of ∼270 crystals per mm^3 (Roedder, 1984; Light et al., 2003). Mirabilite is understood to occupy only a fraction of the volume of an individual

brine inclusion (3 % at −15 °C), and has been observed to sink towards the bottom (Light et al., 2003). More recently, the first quantitative identification of mirabilite in frozen seawater-derived brines was confirmed by X-ray diffraction (Butler and Kennedy, 2015). Within the setting of seasonally isolated coastal lake basins in the Canadian Arctic, the winter sea ice cover and associated mirabilite precipitation has resulted in remarkably large and stable accumulations of sedimentary mirabilite (Grasby et al., 2013), highlighting how mirabilite geochemistry in sea ice can affect the surrounding environment.

Despite the likely occurrence of mirabilite with the sea ice system, the dynamics of the mineral in sea ice as a function of temperature have never been accurately investigated. The nature of the sea ice environment creates practical difficulties in assessing mirabilite dynamics, particularly with respect to the size distribution of the brine inclusions and individual mirabilite crystals. However, by idealising the system to an equilibrium environment, it is possible to accurately model the conditions of sea ice brine pockets at equilibrium (with respect to temperature and ionic composition) on a larger, laboratory scale. Using this approach we investigated the solubility of mirabilite between 0.2 and −20.6 °C at 1 atm to elucidate its dynamics in an equilibrium sea ice system with changing temperature. By implementing our solubility measurements, along with FREZCHEM model outputs, into the temperature and salinity profiles described by a 1D model of first-year sea ice, we are able to examine the spatial and temporal distribution of mirabilite in the ice-pack throughout an Arctic winter and hence produce new estimates for its presence within the sea ice system.

4.2 Materials and methods

4.2.1 Preparation of synthetic mirabilite

Mirabilite was prepared using a modification of the method from Vavouraki and Koutsoukos (2012). Anhydrous Na_2SO_4 (150 g, Sigma) was added to deionised water (500 mL) and warmed to 40 °C to dissolve the salt. The temperature was subsequently decreased to 18 °C, which resulted in supersaturation with respect to mirabilite, and precipitation was initiated via the insertion of a thin steel wire into the solution.

Mirabilite dehydrates to thenardite (Na_2SO_4) above 4 °C once exposed to the air (Oswald et al., 2008), therefore all equipment and reagents were stored in the freezer at −20 °C for at least 2 hours prior to extraction of mirabilite by vacuum filtration. Collection of the mineral (through 10 μm mesh) was carried out under gentle vacuum filtration and dried with cold acetone. Once filtered, the mirabilite was stored in screw capped jars at −20 °C.

Synchrotron X-ray powder diffraction

The purity of mirabilite seed, and the recovered seed/precipitate from the incubations was characterised using synchrotron X-ray powder diffraction (XRPD) on Beamline I11 at Diamond Light Source (Harwell Science and Innovation Campus, Oxfordshire, UK). Samples were analysed at −30 °C by use of a cryostream in order to prevent dehydration to thenardite. Patterns were obtained over 20 minute scans using the multi-analysing-crystal detectors. All data were processed on TOPAS v5 software using the Fundamental Parameters Analysis method to obtain information from Le Bail and Rietveld refinements. Published cell parameters were used as an initial starting point for the refinement and were allowed to refine (Brand et al., 2009). Quantitative Rietveld refinements determined that all batches of mirabilite used for the seeding of the incubations were >98.7 % pure, and recovered seed mirabilite had an average purity of 98.3 ± 1.13 %. Deviation from 100 % purity of mirabilite is due to the presence of relatively small amounts of thenardite that likely formed during sample extraction and preparation (Grasby et al., 2013; Vavouraki and Koutsoukos, 2012).

4.2.2 Preparation of seawater brines

Synthetic brines were used throughout the temperature range studied. To confirm the reliability of the mirabilite-brine equilibrium determined in synthetic brines relative to brines derived from natural seawater, we conducted parallel experiments with synthetic and natural brines between 0.2 and −5.0 °C. The initial composition of all brines was conservative with respect to the major ions relative to the Standard Seawater composition from Millero et al. (2008) (table 4.2).

Table 4.2: Salinity normalised ($S_A = 35.165$ g $kg^{-1}_{solution}$) analysis of the total concentration of major ions in natural and synthetic brines demonstrating conservative composition of the initial brines compared to Standard Seawater (Millero et al., 2008), and the accuracy and precision of analyses based on repeat measurements of local seawater.

		Salinity normalised ($S_A = 35.165$ g $kg^{-1}_{solution}$)		
	Standard Seawater	Natural brine ($n = 6$)	Synthetic brine ($n = 17$)	Local seawater
		mmol $kg^{-1}_{solution}$		
Cl^-	545.87	548.42 ± 1.49	548.77 ± 5.98	543.84 ± 1.53 ($n = 10$)
SO_4^{2-}	28.24	28.79 ± 0.50	28.38 ± 0.59	28.14 ± 0.14 ($n = 21$)
Na^+	468.97	472.27 ± 4.40	470.09 ± 9.66	468.51 ± 6.49 ($n = 24$)
Mg^{2+}	52.82	52.26 ± 0.31	52.55 ± 1.10	52.49 ± 0.86 ($n = 70$)
Ca^{2+}	10.28	10.28 ± 0.02	10.36 ± 0.18	10.24 ± 0.27 ($n = 70$)
K^+	10.21	10.24 ± 0.11	10.28 ± 0.10	10.11 ± 0.05 ($n = 9$)

Preparation of natural seawater-derived brines

Seawater, collected from the Menai Strait (53.1806° N, 4.2333° W), was sterilised with UV light and passed through a 0.2 μm filter before being subjected to freezing at −20 °C. Two times per day the ice was sieved from the brine and the brine placed back into the freezer. Although the solutions were cooled to −20 °C, this approach produced a range of solutions of varying salinity, characteristic of sea ice brines down to −5.0 °C (measured practical salinities of up to 86.3). Confirmation that no mineral precipitation (table 4.1) had occurred during brine preparation was obtained through major ion analysis. Thus the natural seawater derived brines displayed conservative concentrations with respect to the 6 major ions in table 4.2. To produce brines of a desired salinity, dilution with MilliQ water was sometimes employed.

Preparation of synthetic seawater brines

The conservative composition of the major ions in seawater was replicated synthetically (table 4.2) by dissolving 5 analytical grade salts (NaCl, Na_2SO_4, KCl (Sigma), and $MgCl_2{\cdot}6H_2O$ and $CaCl_2{\cdot}2H_2O$ (VWR)) in deionised water following the protocol given by Kester et al. (1967).

All brines were produced gravimetrically to total weights exceeding 1 kg to minimise error. A careful sequence of additions was carried out to prevent the reaction of Na_2SO_4 with $CaCl_2$, which can occur at room temperature in concentrated seawater brines to produce gypsum (Marion et al., 1999). At room temperature, the required amount of deionised water was weighed, followed by the addition of the

$MgCl_2$ solution ($\sim$1 mol $kg^{-1}_{solution}$) and the NaCl, Na_2SO_4 and KCl powdered salts. The solution was stirred until all salts dissolved and then placed in a chiller at its estimated freezing point according to the freezing point temperature for seawater given by (Millero and Leung, 1976),

$$T_{fr} = -0.0575S_A + 1.710523 \times 10^{-3}S_A^{1.5} - 2.154996 \times 10^{-4}S_A^2 \qquad (4.1)$$

where T_{fr} is the freezing point (°C) and S_A is the absolute salinity (g $kg^{-1}_{solution}$). After 4 hours, the required weight of $CaCl_2$ solution ($\sim$1 mol $kg^{-1}_{solution}$, kept at 4 °C) was added to the cooled brine and mixed.

4.2.3 Closed bottle incubations

The closed-system incubation technique used here was based on that used to measure the solubility of calcium carbonate polymorphs in seawater (Mucci, 1983) and seawater-derived brines (Papadimitriou et al., 2013). Natural and synthetic brines seeded with synthetic mirabilite were incubated in screw-capped (Teflon-lined) borosilicate ($25 - 500$ mL, DURAN) media bottles at temperatures from 0.2 to -20.6 °C and mirabilite-brine equilibrium was attained from both undersaturation (mirabilite dissolution) and from supersaturation (heterogeneous mirabilite precipitation). All bottles were incubated in triplicate fully submersed in constant temperature circulating chillers and shaken by hand daily to facilitate exposure of the mineral seed to the bulk solution. The incubation temperature was controlled by Grant RC 1400G recirculating baths for temperatures above -5 °C, and Grant TX120/TX150 circulators twinned with Grant R2 refrigeration units for temperatures below -5 °C, with ethylene glycol as the recirculating liquid.

Due to the large temperature range studied, two different approaches were employed for the incubations. First, for experiments between 0.2 and -6.0 °C, conservative seawater brines were incubated at their freezing point according to equation 6.1.

For all incubations below -6.0 °C, use of equation 6.1 overestimates the freezing point by between 0.4 and 2.1 °C (results on this aspect to be presented separately) due to mirabilite precipitation and the associated removal of Na^+, SO_4^{2-} and water of hydration from the brine. Therefore to ensure that the brines were incubated at their freezing points and hence accurately reflected equilibrium sea ice brines, the brines were cooled to at least 2 °C colder than the freezing point predicted

from equation 6.1, resulting in ice formation and mirabilite precipitation. These brines were incubated with both the precipitates of ice and mirabilite retained in the incubation bottle.

4.2.4 Salinity and temperature

The salinity of all brines (before and after incubation) was measured as conductivity-derived practical salinity (S_P) with a portable conductivity meter (WTW Cond 3110) with a WTW Tetracon 325 probe at laboratory temperature (∼20 °C). For salinities exceeding 70, the solutions were diluted gravimetrically with distilled water in order to fit within the dynamic range of the conductivity meter. Chiller temperatures were monitored at 30 minute intervals using data loggers (Tinytag aquatic 2 TG4100), and once per day manually using a type K temperature probe on a CoMARK 9001 thermometer.

4.2.5 Sampling

Samples were taken from the incubated bottles when required and were transferred to 25 mL screw capped polyethylene bottles through disposable syringe filters (25 mm Whatman GD/X with a 0.2 μm pore size). The samples were immediately diluted gravimetrically to a target salinity of ∼35 with deionised water to eliminate the risk of precipitation during refrigerated storage. The major ion composition of the samples was determined within 4 weeks from sampling.

4.2.6 Brine composition analysis

The Ca^{2+} and Mg^{2+} concentrations were determined by a potentiometric titration as described by Papadimitriou et al. (2013). The SO_4^{2-} concentration was determined by precipitation as $BaSO_4$ in EDTA followed by gravimetric titration with $MgCl_2$ (Howarth, 1978). The Cl^- concentration was determined by gravimetric Mohr titration with 0.3 M $AgNO_3$ standardised against recrystallised NaCl. The Na^+ and K^+ concentrations were determined by ion chromatography on a Dionex Ion Exchange Chromatograph ICS 2100. All methods quantified total concentrations, i.e., the combined concentrations of paired and unpaired ions (Pytkowicz and Hawley, 1974; He and Morse, 1993). All reference to measured concentrations hence represents the total ion concentration, symbolised by $[X]_T$, where X = ion. Measurement

reproducibility of all constituents was tested using local seawater (S_A = 33.094 g $kg^{-1}_{solution}$) as an internal standard relative to Standard Seawater (Millero et al., 2008) (table 4.2).

4.2.7 Determination of equilibrium

The solubility of mirabilite is quantified at solid-solution equilibrium. It was necessary to determine the time required for attainment of solid-solution equilibrium at the sub-zero temperatures of this work because reactions can occur at a slower rate than at higher temperatures due to Arrhenius kinetics (Kubicki, 2008). To monitor mirabilite-brine equilibrium as the change in total SO_4^{2-} concentration with time, a separate bottle was incubated at each temperature along with the triplicate bottles used for the solubility determinations. When the change in $[SO_4^{2-}]_T$ determined in brine from the time series bottle was within the analytical error over 1 week, solid-solution equilibrium was considered attained, the incubation was stopped, and the major ion composition of the brine in the triplicate bottles was determined to provide triplicate measurements of mirabilite solubility.

Equilibrium between the mirabilite seed and brine was attained via dissolution at temperatures $\geqslant -6.0$ °C and precipitation at temperatures $\leqslant -6.8$ °C. Between 0.2 and −6.0 °C each experiment equilibrated for an average of 53 days and equilibrium took up to 29 days to be established (figure 4.1, top). Between −6.8 and −20.6 °C the average experiment time was 43 days, and equilibrium was attained at a faster rate of <21 days (figure 4.1, bottom). The results from the time series measurements cannot provide kinetic information because the experimental protocol did not include precisely controlled stirring rates, seed mass or consistent sampling points.

4.2.8 Stoichiometric mirabilite solubility

The solubility of mirabilite was determined as the total concentration-based stoichiometric solubility product at mirabilite-solution equilibrium, $K^*_{sp,mirabilite} = [Na^+]^2_{T,eq}$ $[SO_4^{2-}]_{T,eq}$ (in mol^3 $kg^{-3}_{solution}$), where the subscript 'T,eq' denotes total ion concentration at equilibrium. Use of total ion concentrations was employed because it is most commonly the instantaneous measurable property of natural water composition in geochemical studies. $K^*_{sp,mirabilite}$ was used to determine the saturation

state (Berner, 1980), of the initial solution with respect to mirabilite, defined as $\Omega_{\text{mirabilite}} = \frac{\text{ICP}}{K^*_{\text{sp,mirabilite}}}$, where ICP (ion concentration product) represents the product of the initial $[\text{Na}^+]^2_{\text{T}}$ and $[\text{SO}_4^{2-}]_{\text{T}}$. For all solutions below −6.0 °C the ICP was derived from conservative (unreacted) total ion concentrations estimated as a linear function of the conservative salinity S_A, itself derived from equation 6.1. The solution is undersaturated when $\Omega < 1$ and in a metastable supersaturated state when $\Omega > 1$, with solid-solution equilibrium occurring when $\Omega = 1$.

4.2.9 FREZCHEM modelling

The FREZCHEM code is a thermodynamic model frequently used to investigate geochemical reactions in the cryosphere and is based on the Pitzer formalism of the specific ion interaction model of electrolyte theory for concentrated electrolyte solutions (Marion and Grant, 1994; Marion and Kargel, 2008). Here, it was used as a tool to compare our directly measured $K^*_{\text{sp,mirabilite}}$ with that calculated from its thermodynamic database. To this end, we use the relationship between the total concentration-based stoichiometric solubility product and the thermodynamic solubility product ($K_{\text{sp,mirabilite}}$), i.e., the solubility in the standard state of infinite dilution:

$$K_{\text{sp,mirabilite}} = \alpha^2_{\text{Na}^+}\ \alpha_{\text{SO}_4^{2-}}\ \alpha^{10}_{\text{H}_2\text{O}} \tag{4.2}$$

$$= m^2_{\text{T,Na}^+}\ \gamma^2_{\text{T,Na}^+}\ m_{\text{T,SO}_4^{2-}}\ \gamma_{\text{T,SO}_4^{2-}}\ \alpha^{10}_{\text{H}_2\text{O}} \tag{4.3}$$

$$= K^*_{\text{sp,mirabilite}}\ \frac{\gamma^2_{\text{T,Na}^+}\ \gamma_{\text{T,SO}_4^{2-}}}{\theta^3}\ \alpha^{10}_{\text{H}_2\text{O}} \tag{4.4}$$

where α = ion or water activity, γ_{T} = total ion activity coefficient, m_{T} = total ion molality (mol $\text{kg}^{-1}_{\text{H}_2\text{O}}$) and $\theta = 1 - 0.001 S_A/(\text{g kg}^{-1}_{\text{solution}})$ = unit conversion factor from molality to mol $\text{kg}^{-1}_{\text{solution}}$ using absolute salinity (Mucci, 1983).

In order to compute $K^*_{\text{sp,mirabilite}}$ from equations 4.2 to 4.4, knowledge of $K_{\text{sp,mirabilite}}$, $\gamma_{\text{T,Na}^+}$, $\gamma_{\text{T,SO}_4^{2-}}$ and $\alpha_{\text{H}_2\text{O}}$ is required. Activity coefficients cannot be measured directly, and along with the thermodynamic solubility product of mirabilite and activity of water, were extracted from the FREZCHEM code output of the freezing seawater simulation from 0.2 to −20.6 °C at 1 atm total pressure and (fixed) $p\text{CO}_2$ of 400 μatm. Mirabilite and ice were the only enabled solid phases in the database of the code to simulate the brine-ice-mirabilite equilibrium of our experiments as

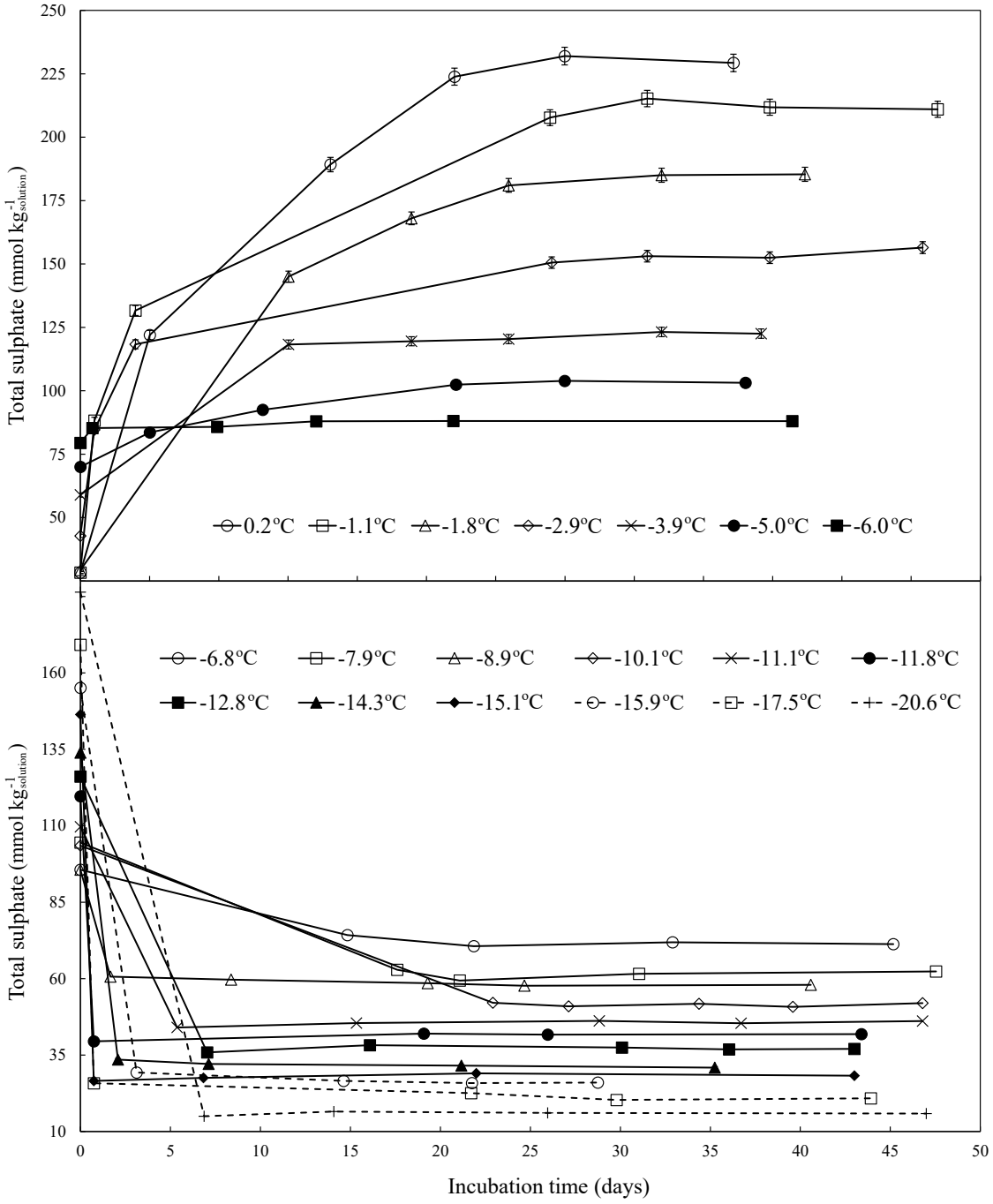

Figure 4.1: The change in $[SO_4^{2-}]_T$ with time during the incubation of equilibrium sea ice brines and mirabilite seed. Top plot displays dissolution experiments (synthetic) between 0.2 and −6.0 °C. Bottom plot displays precipitation experiments between −6.8 and −20.6 °C. Connecting lines are used for illustration only. The final time point represents the solutions used to determine equilibrium concentrations of total Na^+ and SO_4^{2-}. Natural and synthetic brines between 0.2 and −5.0 °C were incubated in tandem and therefore subjected to the same incubation time.

verified by synchrotron XRPD on the extracted mineral seed (section 4.2.1).

When modelling total ion concentrations in complex electrolyte solutions, both paired and unpaired species must be accounted for (Pytkowicz and Kester, 1969; Pytkowicz and Hawley, 1974). Of the two models of electrolyte theory, the specific ion interaction model and the ion association model (Pytkowicz and Kester, 1969), the Pitzer formalism used in the FREZCHEM code is a product of the former (Pitzer, 1973; Pitzer and Mayorga, 1973; Glassley, 2001). The FREZCHEM code computes solution composition and solid-solution equilibria, including the ice-water equilibrium in the freezing mode, by computing single ion activity coefficients based on the parameterisation of all possible ionic interactions as binary and ternary Pitzer coefficients, which are formulated as functions of molality and ionic strength (Marion and Farren, 1999). Thus, single ion activity coefficients in the FREZCHEM output are equivalent to the total ion activity coefficient of the ion association model. The FREZCHEM code does not predict by default chemical speciation in solution as the ion association model does. Occasionally, it requires the explicit addition of ion pairs from the ion association model when their association constants exceed a critical value (He and Morse, 1993). In these instances, the single ion activity coefficient of the FREZCHEM code is that of the unpaired ion, which must be combined with this selective chemical speciation of the ion association model to derive the total ion activity coefficient, borrowing from the ion association model and the equivalence between free (unpaired) and total ion activity,

$$\alpha = \gamma_{\text{free}}\ m_{\text{free}} = \gamma_{\text{T}}\ m_{\text{T}}, \tag{4.5}$$

with α, γ and m as before (Pytkowicz and Kester, 1969).

No ion pairs are included explicitly in the FREZCHEM code for sodium, and so, the FREZCHEM output of our simulated brine composition provides the equivalent of the total molality and total activity coefficient of this ion. Also, no ion pairs are included for SO_4^{2-}, but the code uses the $SO_4^{2-} - HSO_4^-$ equilibrium so both species must be considered. However, the HSO_4^- concentrations predicted by FREZCHEM ranged from 10^{-6} to 10^{-7} mmol $kg_{solution}^{-1}$, which is $6-7$ orders of magnitude lower than the SO_4^{2-} concentrations in this study and their analytical reproducibility (0.59 mmol $kg_{solution}^{-1}$). Thus, neglecting HSO_4^- for the purpose of this study was inconsequential, and so, in our calculations, the unpaired SO_4^{2-} concentration and activity

coefficient in the FREZCHEM output can be considered equivalent to the total values for this ion.

The FREZCHEM code was also run for the scenario of Standard Seawater freezing to −36.2 °C. Here, the FREZCHEM computation employed equilibrium crystallisation similar to that predicted by the Gitterman Pathway (table 4.1), whereby the interaction of mirabilite with hydrohalite through changes in brine composition results in mirabilite dissolution below −22.9 °C (Gitterman, 1937; Marion et al., 1999). This process can result in gypsum precipitation due to the liberation of dissolved SO_4^{2-}(Marion et al., 1999), but such interaction does not occur in the Ringer-Nelson-Thompson Pathway (table 4.1) because their experiments below −23.25 °C used a sequential freezing process that removed mirabilite from the brine prior to the onset of hydrohalite precipitation, hence encouraging fractional crystallisation. Out of the two available paradigms, an equilibrium crystallisation pathway was chosen based on recent observations of mirabilite-hydrohalite interaction in frozen seawater brines by Butler and Kennedy (2015). The weights of mirabilite precipitate estimated by FREZCHEM at 0.1 °C temperature steps were extracted from the code output and incorporated into a 1D model of first-year sea ice to evaluate the spatial and temporal distribution of mirabilite in this complex system.

Validity of our model runs in comparison to published outputs was checked by freezing Standard Seawater ($S_A = 35.165$ g $kg^{-1}_{solution}$, table 4.2) to −10 °C, with all solid phases enabled, yielding $\gamma_{Na^+} = 0.5693$, $\gamma_{SO_4^{2-}} = 0.0272$ and $\alpha_{H_2O} = 0.90761$, which are almost identical to the values given by Marion et al. (2010) of $\gamma_{Na^+} = 0.5698$, $\gamma_{SO_4^{2-}} = 0.0272$ and $\alpha_{H_2O} = 0.90762$.

4.2.10 First-year sea ice modelling

Growth of snow-free, first-year sea ice was modelled using a surface energy balance equation (Maykut, 1978; Cox and Weeks, 1988) with input variables of temperature, short-wave incoming radiation, longwave incoming radiation and humidity for the Arctic Basin taken from Maykut (1978). For a given ice thickness, the surface temperature T_0 is the only unknown required to set the energy balance to 0. T_0 was solved using a solver routine macro in Microsoft Excel to minimise the energy balance by changing T_0. Ice growth was initiated on the 1st October and the model

calculated the time taken for the ice pack to grow incrementally in 0.5 cm layers using Stefan's equation (Cox and Weeks, 1988; Leppäranta, 1993). The temperature profile of the ice was assumed to be linear (Maykut, 1978) between T_0 at the surface and -1.8 °C at the ice-ocean interface. The rejection of brine during ice growth was quantified using the model given in Cox and Weeks (1988) which has been shown to accurately model observed profiles of first year sea ice within environmental variability (Eicken, 1992b) and was recently implemented in a study of hypersaline coastal basins (Dugan and Lamoureux, 2011).

The temperature and salinity data for the ice pack were used to estimate the concentration of mirabilite within the ice after gravity drainage by

$$M_i(T) = M(T)\frac{S_i}{S_{sw}} \tag{4.6}$$

where $M_i(T)$ is the mirabilite concentration (g kg^{-1} sea ice) at temperature T; $M(T)$ is the weight of mirabilite at temperature T that would precipitate from 1 kg of standard seawater (S_A = 35.165 g $kg^{-1}_{solution}$) based on mirabilite solubility measurements and FREZCHEM model output; S_i is the bulk salinity of the ice; and S_{sw} is the absolute salinity of standard seawater, 35.165 g $kg^{-1}_{solution}$.

4.3 Results

The $pK^*_{sp,mirabilite} = -logK^*_{sp,mirabilite}$ from our experiments between 0.2 and -20.6 °C can be separated into two temperature regions (figure 4.2 and table 4.3). The first region occurs between 0.2 and -1.8 °C, within which the changes in mirabilite solubility are purely the result of changing temperature at constant salinity and stoichiometric ion ratios (seawater). The second region of $pK^*_{sp,mirabilite}$ is related to the coupled changes of decreasing temperature and increasing ionic strength in sea ice at brine-ice thermal equilibrium between -1.8 and -20 °C. These relationships were fitted as functions of temperature by non-linear regressions of the form

$$pK^*_{sp,mirabilite}(T) = A + BT + CT^2 + DT^3 + ET^4 \tag{4.7}$$

where T is temperature (Kelvin), and coefficients A to E are given in table 4.4. Between 0.2 and -1.8 °C the $pK^*_{sp,mirabilite}$ increases from 0.80 to 0.96 described by a second order polynomial of temperature (table 4.4, row 1), which represents

Table 4.3: The practical salinity (S_P) of the initial and incubated brines, temperature of incubation, $[Na^+]_T$ and $[SO_4^{2-}]_T$ from each of the bottle incubations at equilibrium, and the resulting measured and modelled $pK^*_{sp,mirabilite}$. D = dissolution, P = precipitation.

Exp. #	Reaction	S_P		T	$[Na^+]_T$	$[SO_4^{2-}]_T$	$pK^*_{sp,mirabilite}$	
		Initial	Final	°C	mmol $kg^{-1}_{solution}$		Observed	FREZCHEM
N-0	D	34.9	47.8±0.1	0.2	836±2	231.53±3.54	0.791±0.007	0.791
S-0	D	35.1	47.8±0.1	0.2	832±0	229.29±3.54	0.800±0.005	0.789
N-1	D	35.1	46.4±0.2	−1.1	799±11	212.86±2.68	0.867±0.005	0.886
S-1	D	35.1	47.0±0.0	−1.1	803±4	210.67±1.11	0.867±0.005	0.883
N-2	D	35.9	46.1±0.1	−1.8	762±4	187.67±4.54	0.962±0.012	0.952
S-2	D	36.2	45.5±0.4	−1.8	760±2	186.41±4.25	0.968±0.008	0.955
N-3	D	53.0	59.3±0.2	−2.9	893±1	154.70±2.53	0.908±0.007	0.905
S-3	D	53.0	59.4±0.1	−2.9	896±1	156.46±1.31	0.901±0.004	0.912
N-4	D	70.0	73.8±0.5	−3.9	1047±19	122.26±2.97	0.873±0.008	0.868
S-4	D	70.2	73.9±0.1	−3.9	1040±6	124.70±0.48	0.870±0.003	0.868
N-5	D	84.8	86.3±0.0	−5.0	1193±5	104.44±2.55	0.828±0.011	0.841
S-5	D	84.8	86.0±0.3	−5.0	1185±1	103.84±1.30	0.837±0.006	0.847
S-6	D	92.9	100.5±0.3	−6.0	1342±2	87.61±0.90	0.802±0.003	0.815
S-7	P	92.9	109.5±0.1	−6.8	1495±7	73.71±0.37	0.783±0.006	0.803
S-8	P	124.0	122.0±0.0	−7.9	1625±4	65.56±0.15	0.762±0.002	0.784
S-9	P	110.8	134.3±0.2	−8.9	1760±11	57.86±0.44	0.747±0.005	0.772
S-10	P	124.0	144.4±0.0	−10.1	1883±5	51.32±0.67	0.740±0.004	0.763
S-11	P	136.1	154.3±0.1	−11.1	1979±6	45.89±0.36	0.745±0.002	0.760
S-12	P	146.8	163.4±0.1	−11.8	2102±7	41.53±0.53	0.737±0.004	0.759
S-13	P	158.0	173.1±0.1	−12.8	2202±7	36.90±0.17	0.747±0.003	0.761
S-14	P	169.1	180.4±0.3	−14.3	2328±12	31.14±0.33	0.773±0.001	0.768
S-15	P	179.5	188.5±0.1	−15.1	2420±9	28.34±0.41	0.780±0.009	0.773
S-16	P	188.0	196.8±0.2	−15.9	2511±5	25.50±0.40	0.794±0.006	0.779
S-18	P	197.6	210.0±0.1	−17.5	2702±4	20.71±0.42	0.821±0.009	0.796
S-21	P	225.9	231.3±0.3	−20.6	2888±9	16.06±0.16	0.873±0.004	0.835

Table 4.4: Coefficients for use with equation 4.7 that describe the change of $pK^*_{\mathrm{sp,mirabilite}}$, $\Omega_{\mathrm{mirabilite}}$, and mirabilite weight (g kg^{-1} of frozen seawater with $S_A = 36.165$) with temperature (K).

	Range		A	B	C	D	E	R^2	σ
	°C	K							
$pK^*_{sp,mirabilite}$	0.2 to −1.8	273.35 to 271.35	3.1937369e3	−2.3362020e1	4.2733631e-2			0.998	0.004
	−1.8 to −20.6	271.35 to 252.55	−1.2139675e3	1.4440716e1	−5.7140676e-2	7.5264329e-5		0.995	0.005
$\Omega_{mirabilite}$	0.2 to −20.6	273.35 to 252.55	3.6734880e4	−4.0275894e2	1.4722142	−1.7941420e-3		1.000	0.073
Mirabilite (g kg^{-1})	−6.4 to −22.9[a]	266.95 to 250.25	−1.6098857 4e6	2.5137484 3e4	−1.4719353 6e2	3.8307825 2e-1	−3.7388253 4e-4	0.998	0.122
	−22.9 to −25.0[b]	250.25 to 248.15	−2.0902432 8e6	2.5237584 6e4	−1.0157407 5e2	1.3627102 4e-1		1.000	0.006
	−25.0 to −36.2[b]	248.15 to 236.95	−1.1913928 5e4	1.4906704 8e2	−6.2162683 9e-1	8.6438906 6e-4		0.999	0.011

[a] Measurements supplemented with FREZCHEM model output
[b] FREZCHEM

a reduction in the solubility of mirabilite with decreasing temperature in seawater. Between −1.8 and −11.8 °C the $pK^*_{\mathrm{sp,mirabilite}}$ decreases from 0.96 to 0.74 before rising to 0.87 at −20.6 °C. This second region between −1.8 and −20.6 °C is described by a third order polynomial of temperature (table 4.4, row 2).

The $pK^*_{\mathrm{sp,mirabilite}}$ between 0.2 and −5.0 °C displays no detectable difference between use of natural or synthetic brines as the experimental medium (figure 4.2). This consistency indicates that mirabilite solubility is unaffected by differences such as pH, carbonate and borate alkalinity, and trace metals within the error of the measurements. For this reason we infer that using synthetic brines for all temperatures below −5 °C was representative of the true mirabilite solubility in naturally derived seawater brines.

The $\Omega_{\mathrm{mirabilite}}$ displays large changes in equilibrium sea ice brines between 0.2 and −20.6 °C (figure 4.3). At 0.2 °C the experimental solution was strongly undersaturated, with $\Omega_{\mathrm{mirabilite}} = 0.04$. By −20.6 °C a conservative seawater brine would be strongly supersaturated, with $\Omega_{\mathrm{mirabilite}} = 18.13$. Between 0.2 and −20.6 °C the change in $\Omega_{\mathrm{mirabilite}}$ in conservative seawater brines is described by a third order polynomial that takes the same form as equation 4.7 (table 4.4, row 3). This relationship was used to estimate the temperature at which $\Omega_{\mathrm{mirabilite}} = 1$, which equates to -6.38 ± 0.07 °C.

4.4 Discussion

4.4.1 Mirabilite solubility

The changes observed in the $pK^*_{\mathrm{sp,mirabilite}}$ (section 4.3) can be better understood by considering the equilibrium concentrations of $[\mathrm{Na}^+]_\mathrm{T}$ and $[\mathrm{SO}_4^{2-}]_\mathrm{T}$ separately (figure 4.4). These ions have different concentrations in standard seawater (table 4.2), with 16.6 times more $[\mathrm{Na}^+]_\mathrm{T}$ than $[\mathrm{SO}_4^{2-}]_\mathrm{T}$, such that the precipitation or dissolution of mirabilite has a greater relative effect on $[\mathrm{SO}_4^{2-}]_\mathrm{T}$ than $[\mathrm{Na}^+]_\mathrm{T}$ in the brine. Between the onset of mirabilite precipitation (−6.38 °C) and −20.6 °C, 91.97 % of $[\mathrm{SO}_4^{2-}]_\mathrm{T}$ is removed from the brine relative to conservative concentration. In comparison, within the same temperature range the removal of Na^+ is 12.90 %. The extent of SO_4^{2-} removal is greater than the increase caused by concentration of the brine as ice forms, therefore a net decrease in $[\mathrm{SO}_4^{2-}]_\mathrm{T}$ with decreasing temperature

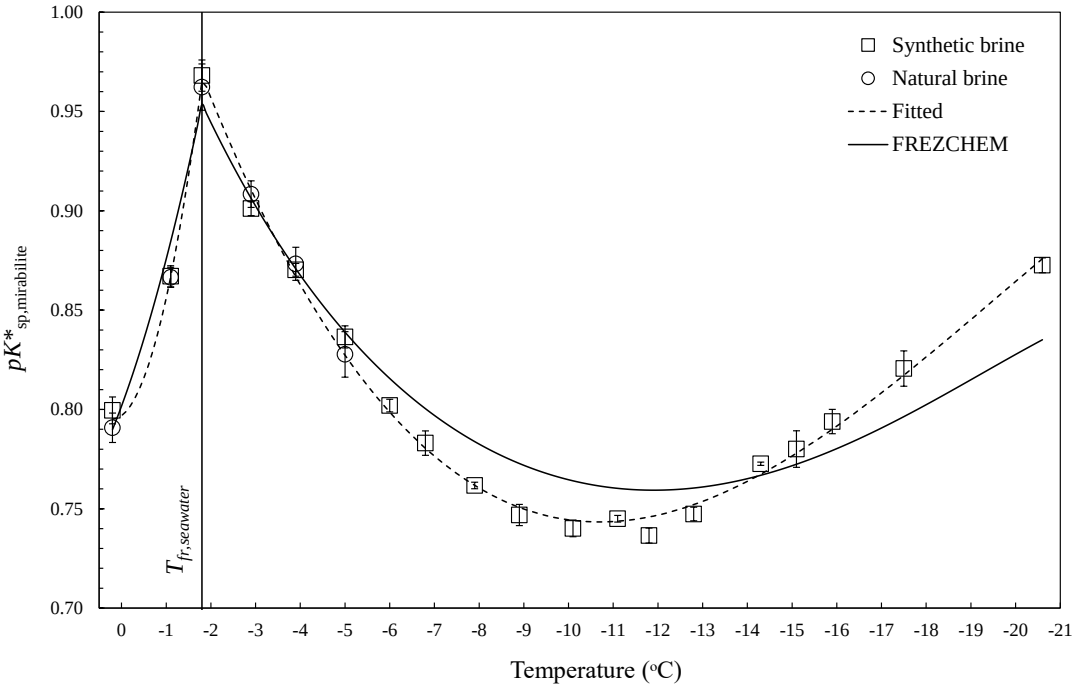

Figure 4.2: Measured $pK^*_{\mathrm{sp,mirabilite}}$ in equilibrium sea ice brines plotted alongside output from the FREZCHEM model. The vertical line at -1.8 °C marks the point of which the solubility product begins to become affected by coupled changes in salinity and temperature as a result of freezing.

is observed whereas $[\mathrm{Na}^+]_\mathrm{T}$ continues to increase, but at a slower rate. Overall, the associated effect on the osmotic conditions in the ice would add to the environmental stress exhibited on microscopic extremophile species that inhabit sea ice, such as viruses, bacteria, microalgae, and protists (Thomas and Dieckmann, 2002; Eicken, 1992a). Furthermore we propose that the particularly large changes in $[\mathrm{SO}_4^{2-}]_\mathrm{T}$ could impact upon the pH of seawater brines measured on the total ($p\mathrm{H}_\mathrm{T}$) and seawater ($p\mathrm{H}_\mathrm{SWS}$) proton scales, where

$$p\mathrm{H}_\mathrm{T} = -\log([\mathrm{H}^+] + [\mathrm{HSO}_4^-]) \tag{4.8}$$

$$p\mathrm{H}_\mathrm{SWS} = -\log([\mathrm{H}^+] + [\mathrm{HSO}_4^-] + [\mathrm{HF}^-]). \tag{4.9}$$

The substantial removal of $[\mathrm{SO}_4^{2-}]_\mathrm{T}$ resulting from mirabilite precipitation could affect the equilibria of the $\mathrm{HSO}_4^- \rightleftharpoons \mathrm{H}^+ + \mathrm{SO}_4^{2-}$ reaction, and therefore have implications for the measurement of pH in such brines. The FREZCHEM model runs of mirabilite precipitation showed a 92.5 % reduction in $[\mathrm{HSO}_4^-]$ between -6.8 and -20.6 °C. In addition to this effect on pH, the non-conservative changes in the ionic

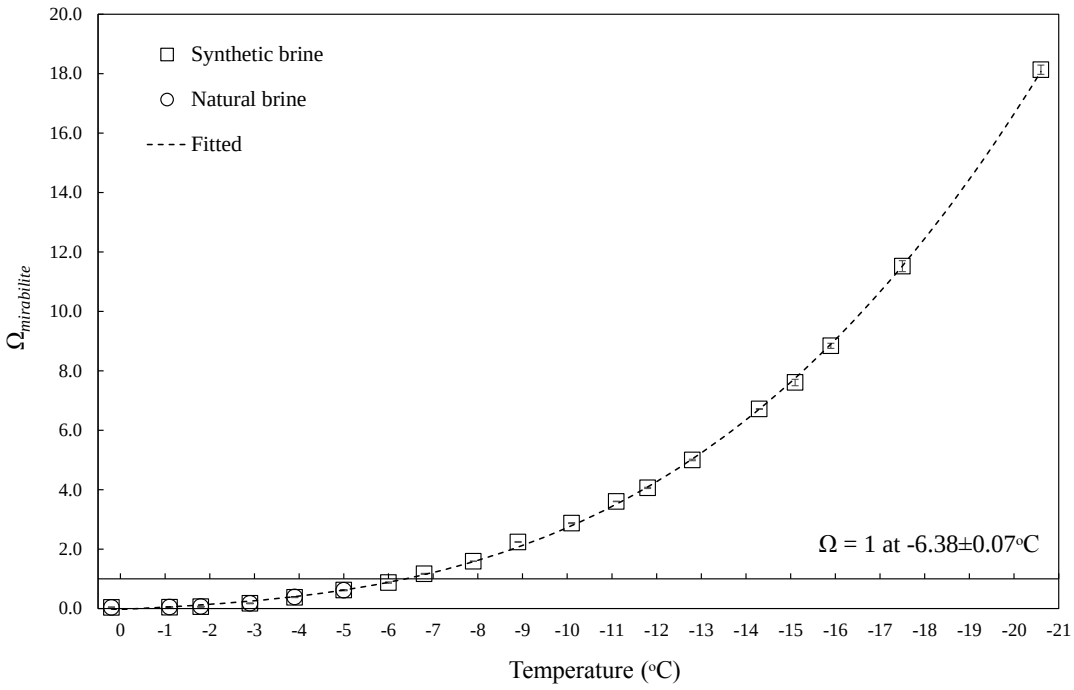

Figure 4.3: $\Omega_{\text{mirabilite}}$ in equilibrium sea ice brines between between 0.2 and -20.6 °C.

composition of the brine due to mirabilite precipitation compromises the concept of practical salinity, which could have consequences for accurate salinity measurement by solution conductivity in polar settings, especially during brine exchange with the surface ocean via convection.

Comparing the observed equilibrium $[Na^+]_T$ and $[SO_4^{2-}]_T$ with the output of the FREZCHEM model runs of our bottle incubations (figure 4.4) yields a very strong correlation throughout the temperature range studied. The average difference between the measured and modelled $[Na^+]_T$ and $[SO_4^{2-}]_T$ is -7.80 ± 23.20 mmol $kg^{-1}_{solution}$ and -1.12 ± 2.15 mmol $kg^{-1}_{solution}$ respectively, close to the experimental uncertainty of 17 mmol $kg^{-1}_{solution}$ for $[Na^+]_T$, and 0.56 mmol $kg^{-1}_{solution}$ for $[SO_4^{2-}]_T$. The agreement between measured and modelled equilibrium concentrations of Na^+ and SO_4^{2-} is consequently reflected in the $pK^*_{sp,mirabilite}$ (figure 4.2). Between 0.2 and -3.9 °C the modelled and measured solubilities show excellent agreement. Between -3.9 and -14.3 °C the model output sits higher than our measurements caused by lower modelled concentrations of $[Na^+]_T$ and $[SO_4^{2-}]_T$ (16 and 1.1 mmol $kg^{-1}_{solution}$ respectively). The reverse occurs between -14.3 and -20.6 °C where the modelled $pK^*_{sp,mirabilite}$ sits below our measurements, and here the difference is dominated

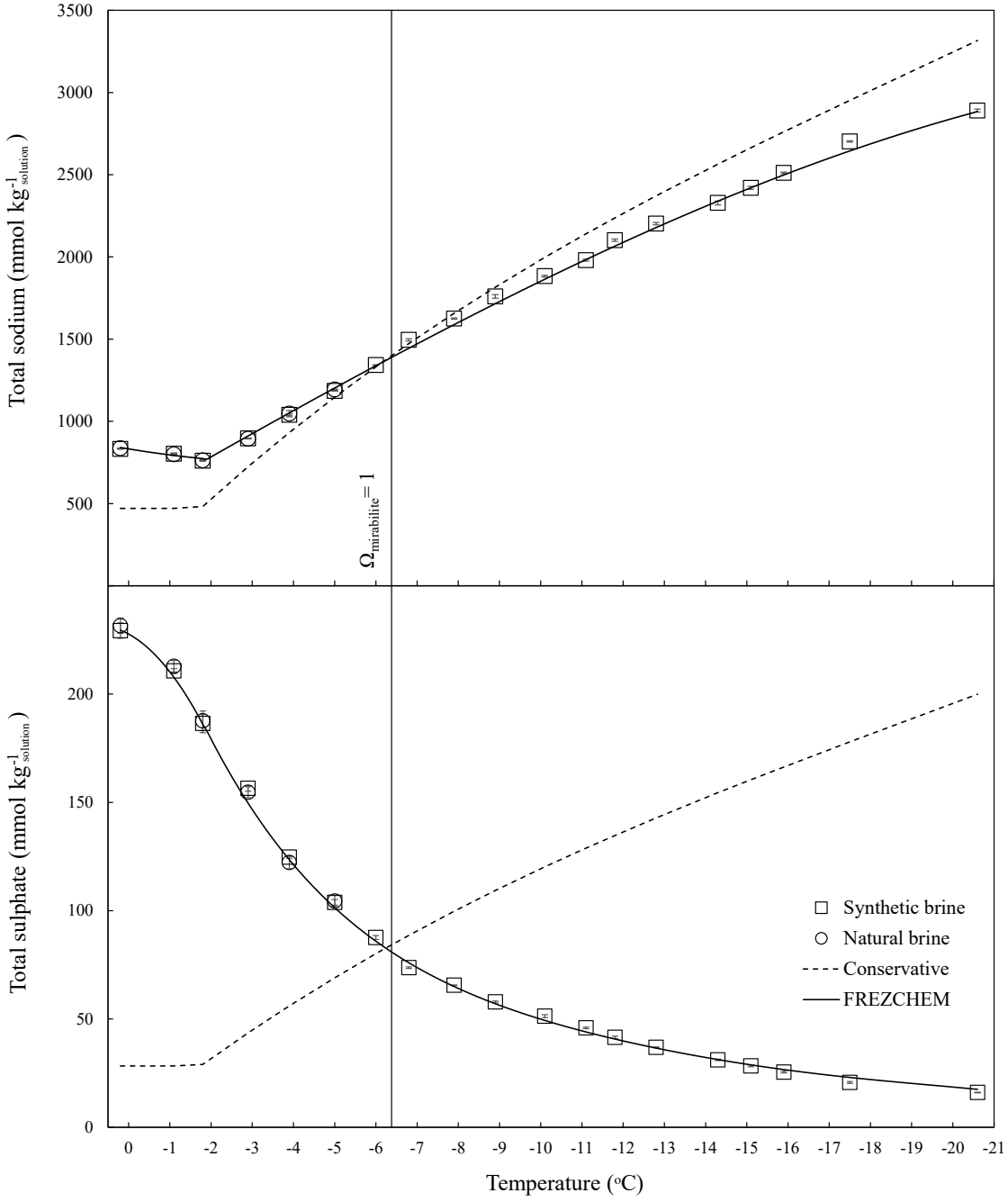

Figure 4.4: The observed equilibrium concentrations of $[Na^+]_T$ (top) and $[SO_4^{2-}]_T$ (bottom) plotted alongside the output of the FREZCHEM model and the composition of conservative seawater relative to the freezing point salinity calculated from equation 6.1.

by FREZCHEM overestimating the $[SO_4^{2-}]_T$ by up to 2.32 mmol $kg^{-1}_{solution}$. The comparable values of modelled and measured $pK^*_{sp,mirabilite}$ (within 0.00 to 0.04 pK unit), coupled with the excellent agreement with respect to the onset of mirabilite precipitation occurring at 6.38 °C (FREZCHEM predicts −6.3 °C (Marion et al., 1999)) indicate that FREZCHEM must adequately compute the total ion activity coefficients, the activity of water, and the thermodynamic solubility product of mirabilite in cold aqueous solutions. Our evidence hence demonstrates that the FREZCHEM model can be a valuable tool in enriching the study of sodium sulphate minerals in inaccessible aqueous environments.

The two pathways for seawater freezing that dominate scientific literature, the Gitterman and Ringer-Nelson-Thompson (RNT) pathways (table 4.1), predict the onset of mirabilite precipitation to occur in frozen seawater at −7.3 and −8.2 °C respectively (Gitterman, 1937; Nelson and Thompson, 1954), considerably different to our measured temperature at which $\Omega_{mirabilite} = 1$. This difference could be accounted for by the length of equilibration time that the Gitterman and RNT studies allowed. Some, but not all, of the Gitterman experiments were equilibrated for up to 4 weeks, whilst Nelson and Thompson (1954) only allowed for the brines to reach thermal equilibrium. Our time series experiments (figure 4.1) highlight the importance of allowing sufficient time for mirabilite to reach equilibrium in sub-zero temperatures. Further, during our experiments it was observed that metastable supersaturated solutions with respect to mirabilite are particularly persistent in the absence of seed. Solutions with $\Omega_{mirabilite}<3$ often required seed crystals to initiate precipitation, while unseeded supersaturated brines at −7 and −8 °C were stable for up to 4 months before seeding. This stability is due to the large unit cell of mirabilite (volume = 1,460 $Å^3$ (Levy and Lisensky, 1978)), which, combined with the effect of activation entropy from the complexity of assembling 40 water molecules in this unit cell means that solutions may need to become heavily supersaturated with respect to mirabilite before precipitation of the mineral occurs homogeneously (Genkinger and Putnis, 2007). Whether the walls of the brine pockets in the sea ice microstructure provide a suitable site for the nucleation of mirabilite at low supersaturations close to −6.38 °C remains to be tested but seems likely given the presence of a surrounding ice matrix, insoluble impurities, and the biogenic exudates

that are understood to facilitate heterogeneous ice nucleation in polar environments (Wilson et al., 2015).

The $\Omega_{\text{mirabilite}}$ in equilibrium sea ice brines can be related to changes within the sea ice system as the temperature increases or decreases. At temperatures higher than −6.38 °C when the brine is undersaturated, mirabilite displays rapid changes in solubility. At −6.0 °C $\Omega_{\text{mirabilite}}$ is near equilibrium at 0.874. By −1.8 °C, the brine is heavily undersaturated, with $\Omega_{\text{mirabilite}} = 0.064$. The current technique for separating sea ice minerals in field samples involves careful melting (Dieckmann et al., 2008; Geilfus et al., 2013), and such large changes in solubility above −6.38 °C would result in dissolution of mirabilite upon increasing temperature, which considering the size of individual crystals being ∼1 to 140 μm in diameter (Roedder, 1984; Light et al., 2003), may occur rapidly. This could explain why mirabilite, although likely present in sea ice below −6.38 °C, has never been observed in the field.

In the supersaturated region investigated here between −6.8 and −20.6 °C, our measurements, supplemented with FREZCHEM model output, were used to estimate the amount of mirabilite that would precipitate in a 1 kg parcel of frozen seawater ($S_A = 35.165$ g $\text{kg}^{-1}_{\text{solution}}$) with varying temperature (figure 4.5). Results were fitted to a stepwise polynomial function of temperature (K) of the same form as equation 4.7, with coefficients given in table 4.4. The mirabilite concentration in the ice increases from 1.62 g kg^{-1} at −6.8 °C to 7.50 g kg^{-1} at −20.6 °C. The increase over this temperature range begins rapidly until ∼−11 °C, before beginning to plateau at colder temperatures as the SO_4^{2-} pool of the brine is gradually depleted. Between −22.9 and −36.2 °C, the dissolution of mirabilite, caused by hydrohalite precipitation (section 4.2.9), reduces mirabilite concentration in the frozen seawater by approximately 2.5 g kg^{-1}. To determine the mirabilite concentration in sea ice while accounting for the drainage of brine during sea ice formation, a model for the temperature and salinity distribution of sea ice was used.

4.4.2 First year sea ice modelling

The coefficients used to describe mirabilite mass in frozen seawater as a function of temperature (table 4.4) have been integrated into a 1D model (via equation 4.6) describing the temperature and salinity profiles (figure 4.6) of first year sea ice in

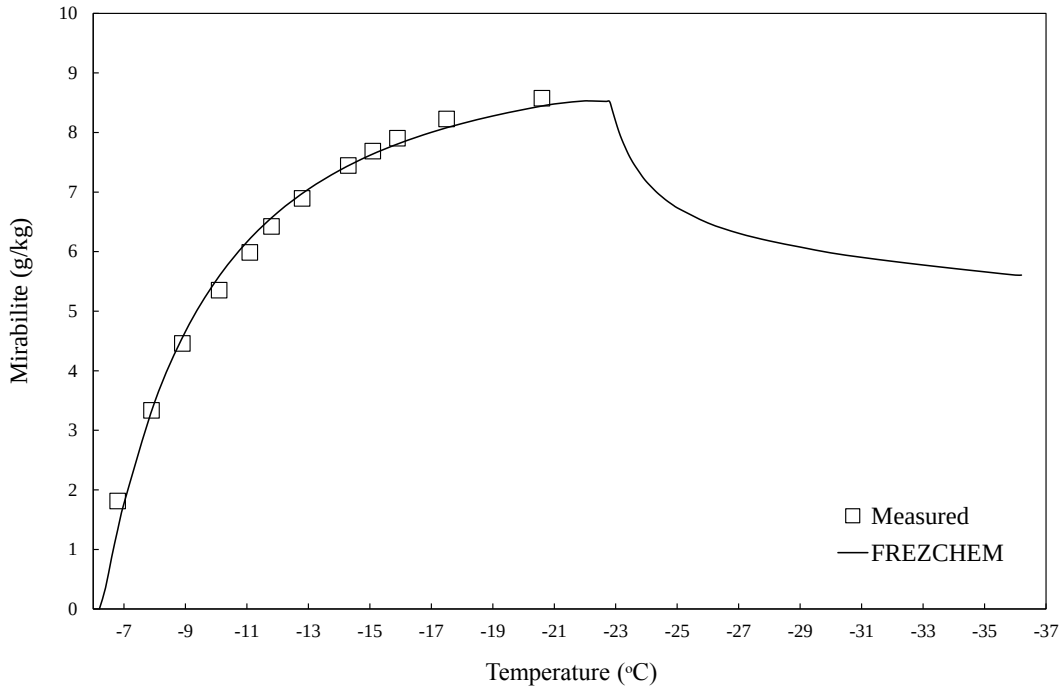

Figure 4.5: The measured and modelled concentration of mirabilite (g kg^{-1}) that precipitates in 1 kg of standard seawater (S_A = 35.165 g $kg^{-1}_{solution}$) frozen between −6.3 and −36.2°C.

the Arctic Basin as it grows over winter months and the distribution of mirabilite within it (figure 4.7).

The model results illustrate the distribution of mirabilite in the ice pack as it develops, and reveal the settings in which the chemical properties of sea ice brines are affected by its precipitation. Mirabilite would have precipitated in the modelled ice pack after 23 hours once a thickness of 5 cm was reached. Initially the mirabilite distribution with depth in the ice displays a near linear decrease with highest concentrations at the surface. As ice thickness increases between 15 and 60 cm, the mirabilite distribution in the upper part of the ice develops towards an 'S' shaped curve, with mirabilite present in the upper three quarters of the ice before the temperature becomes too high to reach mirabilite supersaturation near the ice-ocean interface. After nearly 5 weeks the ice thickness reaches 75 cm, and the temperature in the upper region of the ice falls below the saturation point of hydrohalite (−22.9 °C (Marion et al., 1999)). Precipitation of hydrohalite leads to a large reduction in Na^+ concentration in the brine leading to mirabilite undersaturation and dissolution (Marion et al., 1999; Butler and Kennedy, 2015). The

result of this process is that when the ice temperature drops below −22.9 °C, the distribution of mirabilite develops a reversed 'C' shape towards the surface where mirabilite dissolves and reduces in concentration. After 20 weeks the ice pack is over 2 m thick, and mirabilite is present in the upper 183 cm. Mirabilite concentrations peak in the top 0.5 cm at ∼2.3 g kg^{-1} after 4 weeks when the ice is 60 cm thick, however, the concentration continues to increase with depth over the winter. As a weight percentage of the entire sea ice pack, mirabilite represents $0.05 - 0.10$ %, which equates to average areal mirabilite concentrations of between 69 and $1,571$ g m^{-2} (with varying ice thickness used to calculate ice volume m^{-2}).

Though sea ice is a highly dynamic environment that is difficult to describe empirically, the idealised snow-free, first year sea ice model results presented here highlight the presence of mirabilite throughout the growth of first year sea ice, and also aids in explaining the lack of mirabilite identification in field samples. The maximum modelled mirabilite concentration in bulk sea ice of 2.3 g kg^{-1} (0.23 %) would be below the detection limit for mirabilite crystals by laboratory or synchrotron crystallography. Butler and Kennedy (2015) were able to detect mirabilite in frozen seawater-derived brines by synchrotron X-ray powder diffraction, however the mirabilite concentrations in their samples would have been over 10 times greater (concentrated brines were used with salinities of 100 and 125) than those modelled to exist in bulk sea ice. The near undetectable concentration of mirabilite in bulk sea ice, combined with its small crystal size and rapid change in solubility upon increasing temperature, must contribute to the highly elusive nature of this mineral within the sea ice environment despite the likelihood of its near ubiquitous distribution. Integration of mineral solubility data into thermodynamic (Griewank and Notz, 2013; Turner et al., 2013; Rees Jones and Worster, 2014) or global sea ice models (Gent et al., 2011; Hunke et al., 2015) will help in the determination of the structural and optical properties of the ice, to which the dynamics of mineral precipitates contribute (Assur, 1960; Light et al., 2004), therefore creating a more accurate representation of the energy balance and climate forcings in polar regions.

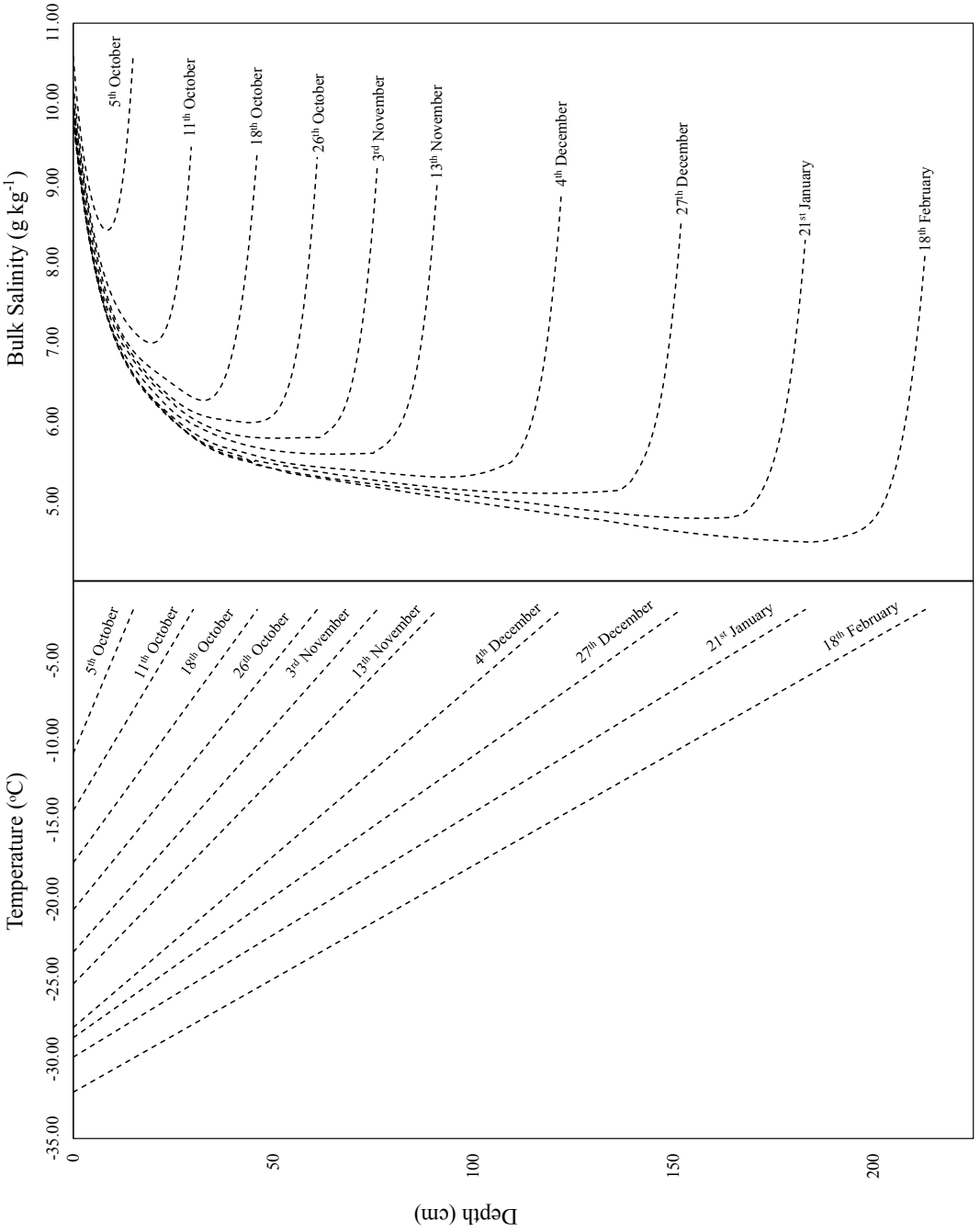

Figure 4.6: Modelled temperature and salinity profiles during the growth of first year sea ice.

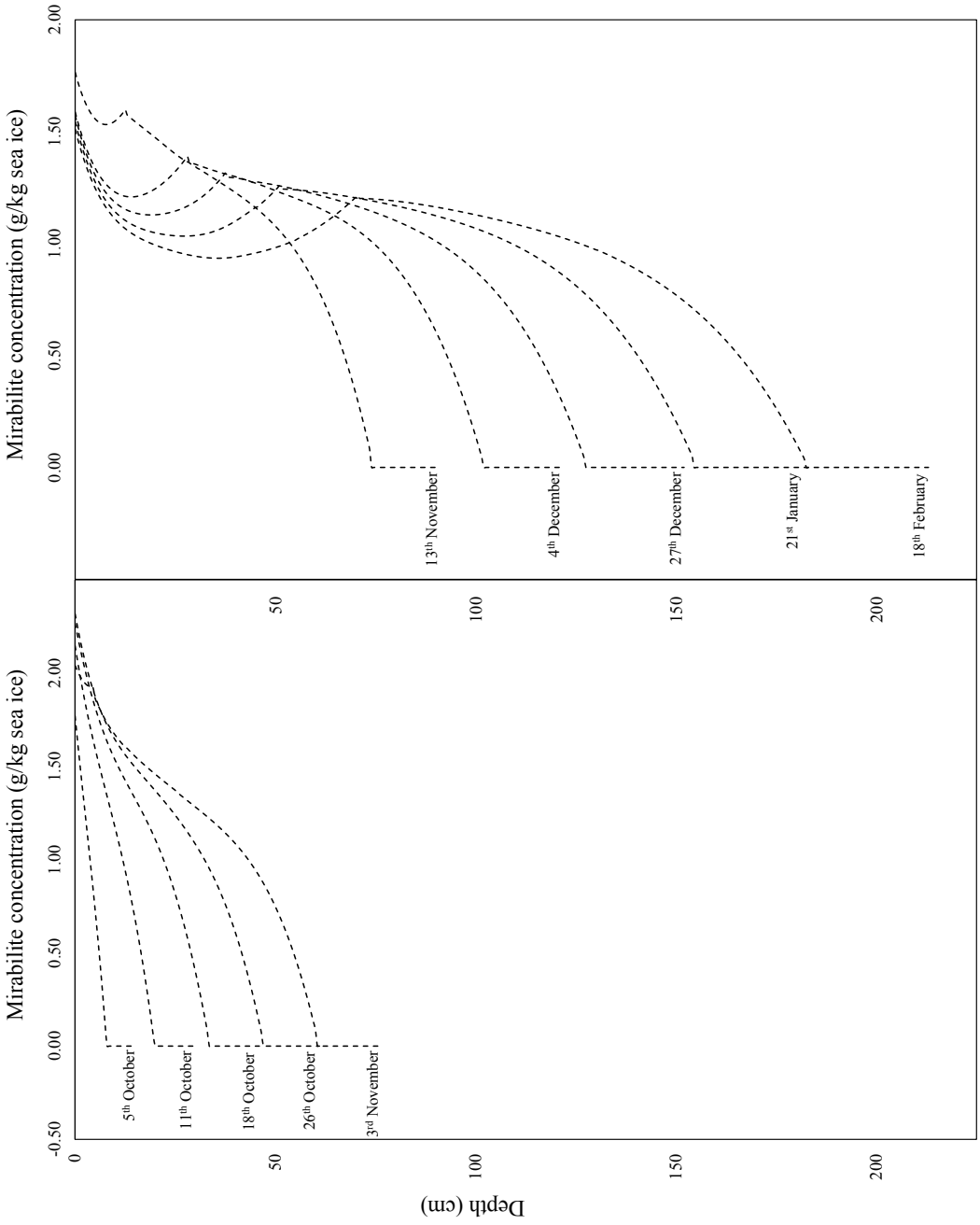

Figure 4.7: Modelled mirabilite distribution in sea ice. Left plot displays profiles for October. Right plot displays profiles between November and February.

4.5 Conclusions

Determination and discussion of mirabilite solubility in equilibrium sea ice brines has revealed the potential role that this mineral has within the sea ice system. Mirabilite solubility displays large changes throughout the polar temperature spectrum from -1.8 to -20.6 °C due to the coupled effects of changing temperature and ionic composition of the brines trapped within the sea ice microstructure. Once mirabilite saturation is attained at -6.38 °C in sea ice, the effect of its precipitation from the brine with further cooling results in a 91.97 % depletion of brine $[SO_4^{2-}]_T$ by -20.6 °C. This $[SO_4^{2-}]_T$ depletion not only has consequences on the *p*H system in sea ice brines, but also when combined with the reduced $[Na^+]_T$, creates implications for the measurement of practical salinity whilst changing the osmotic conditions within the brine compared to that of conservatively concentrated seawater. By supplementing our dataset with model outputs from FREZCHEM and incorporating the results into a 1D empirical sea ice model, the spatial and temporal evolution of mirabilite in snow-free, first year Arctic sea ice has been estimated for the first time. Based on these results, it is shown that mirabilite could precipitate in the ice as soon as 1 day after initiation of congelation ice formation. Mirabilite precipitates in concentrations of up to $\sim$2.3 g kg^{-1} of sea ice in the early stages of sea ice formation, before the ambient temperatures drop below that of hydrohalite precipitation at -22.9 °C, displaying an 'S' shaped depth distribution. At colder environmental conditions later in the winter season, when hydrohalite supersaturation is reached in the coldest upper sea ice layers, mirabilite exhibits a reverse 'C' shaped depth distribution towards the ice surface where mirabilite dissolves by the hydrohalite-driven $[Na^+]$ depletion in the brines in this region. The rapid changes in mirabilite solubility with temperature and its relatively low percent weight in bulk sea ice ($<$0.10 %) are likely reasons for the absence of field evidence for its occurrence. The results ultimately highlight the likelihood that mirabilite is a near ubiquitous mineral in sea ice, while it is demonstrated how solubility data can be incorporated into sea ice models to facilitate a more accurate representation of the polar environment.

Chapter 5

The effect of mirabilite precipitation on the absolute and practical salinities of sea ice brines

Abstract

The sea ice cover of high latitude oceans contains concentrated brines which are the site of *in-situ* chemical and biological reactions. The brines become supersaturated with respect to mirabilite ($Na_2SO_4 \cdot 10H_2O$) below -6.4 °C, and the associated removal of Na^+ and SO_4^{2-} from the brine results in considerable non-conservative changes to its composition. The changes are reflected in the brine salinity, which is a fundamental physico-chemical parameter in the sea ice brine system. Here, measurements of electrical conductivity and brine composition in synthetic sea ice brines between -1.8 and -20.6 °C, obtained during a comprehensive investigation of the brine-mirabilite equilibrium at below-zero temperatures reported elsewhere, are combined with modelled estimates to assess the behaviour of the absolute (S_A) and practical (S_P) salinities of sea ice brines. Results display substantial divergence of S_P from S_A below -6.4 °C, which approaches a 7.2 % difference with decreasing temperature. This is shown to create inaccuracies when S_P is assumed to be equivalent to S_A, firstly by misrepresenting the conditions inhabited by sea ice biota, whilst also creating errors in the calculation of physical sea ice parameters. Our measured and modelled data are used to refine the $S_A - T$ relationship for sea ice brines, implicit of mirabilite precipitation, which is crucial in estimating brine properties in absence of salinity data. Furthermore, because S_P is the parameter measured in field studies, we provide an $S_P - T$ relationship for sea ice brines to

−22.8 °C, which also describes available $S_P - T$ data from sea ice brines in the Southern Ocean, demonstrating the importance of the mirabilite-brine equilibrium in natural sea ice. Finally, we propose a conversion factor for the estimation of S_A from S_P measurement in sea ice brines. This work ultimately highlights careful consideration of salinity concepts when applied to the sea ice system.

5.1 Introduction

The Na−K−Mg−Ca−Cl−SO_4−H_2O system describes 99.4 % of the major dissolved ions in Standard Seawater by weight (Millero et al., 2008), and these ions have long been known to display constant ratios to one another throughout the world ocean (Forchhammer, 1865; Dittmar et al., 1873). This conservative behaviour gave rise to the concept of salinity, which was originally defined as a measure of the mass of dissolved salts per unit mass of seawater and is now termed absolute salinity (S_A) (Lewis, 1980). Accurate and rapid determination of salinity is paramount in the calculation of seawater density (Millero et al., 2008; Pawlowicz, 2015), therefore, since the advent of salinity as a concept, the method of its measurement has evolved to its present form of determination from measurement of electrical conductivity (Fofonoff, 1985; Lewis, 1980). The combined contribution of charged dissolved species to the total electrical conductivity of a solution is a conservative property and its measurement is converted to 'practical' salinity (S_P) by the Practical Salinity Scale (PSS-78). According to the PSS-78 definition (Perkin and Lewis, 1980), the S_P of a solution is derived from the ratio (R_{15}) of the total electrical conductivity of the solution to that of a solution of potassium chloride (KCl) in pure water with a KCl mass fraction of 32.4356 g when both solutions are at 15 °C on the IPTS-68 scale, and zero gauge pressure (Fofonoff, 1985; Lewis, 1980; Millero et al., 2008). Practical salinity is dimensionless, and when $R_{15} = 1$, $S_P = 35$. The reproducibility of conductivity measurements is good enough for deep ocean salinity measurements, which require accuracies within ±0.006 (King et al., 2001), and this is now the dominant method for salinity measurement in both oceanography at sea and in the laboratory. Measurement of S_P also allows for precise calculation of S_A based on the most recent accurate chemical analysis defining $S_A = 35.16504$ g $\mathrm{kg}^{-1}_{\mathrm{solution}}$ in Standard Seawater with $S_P = 35$ (Millero et al., 2008), with $S_A/S_P = 1.004715 \pm 0.0005$ (Jackett

et al., 2006; Pawlowicz, 2012; Millero et al., 2008; Millero and Huang, 2009). This relationship is valid for practical salinities between 2 and 42, which is the working salinity range of the PSS-78 (Lewis, 1980; Pawlowicz, 2012).

The electrical conductivity of a solution is a function of its temperature, the total amount of charged species dissolved in it, and their inter-ionic ratios (Weeks, 2010). Deviations from the constant stoichiometric ratios of Standard Seawater (table 5.1) will occur as a result of any process that leads to non-conservative behaviour of the major ions, with the formation of seawater-derived brines in evaporative or cryospheric environments providing apt examples (McCaffrey et al., 1987; Marion et al., 1999; Grasby et al., 2013; Butler et al., 2016). Amongst the best studied cryospheric environments on Earth is the sea ice cover of high latitude oceans, which extends over approximately 20 million km^2 seasonally (Dieckmann and Hellmer, 2010), covering ∼5 % of the Earths surface. Sea ice undergoes large changes in temperature, chemical composition, and structure throughout its seasonal cycle (Gleitz et al., 1995), which are reflected in the labyrinth of inclusions within the ice that contain rejected liquid brine at local ice-brine (thermal) equilibrium (Weeks and Ackley, 1986; Petrich and Eicken, 2010; Light et al., 2003; Golden et al., 2007). At the low temperature (−1.8 to ∼−35 °C, (Miller et al., 2011)) and hypersaline conditions (up to ∼220 g $kg^{-1}_{solution}$ (Ewert and Deming, 2013)) of sea ice brines, a suite of dissolved salts reach saturation with respect to their, typically hydrated, solid phases, which precipitate. The current understanding of solid-solution equilibria in sea ice states the following sequence of precipitates from sea ice brine as it cools to its eutectic: ikaite ($CaCO_3 \cdot 6H_2O$) at temperatures less than −2 °C (depending on brine pCO_2; (Papadimitriou et al., 2013)), mirabilite ($Na_2SO_4 \cdot 10H_2O$) at −6.4 °C (Butler et al., 2016), hydrohalite ($NaCl \cdot 2H_2O$) at −22.9 °C (Marion et al., 1999; Butler and Kennedy, 2015), sylvite (KCl) at −33 °C, and $MgCl_2 \cdot 12H_2O$ at −36.2 °C (Gitterman, 1937; Nelson and Thompson, 1954). Salt precipitation can result in substantial non-conservative changes in the ionic composition of the brine; recent measurements indicate that mirabilite precipitation results in a reduction of the total concentrations of sodium and sulphate by up to 13 % and 92 %, respectively, by −20.6 °C (Butler et al., 2016). The changes are particularly significant given that these ions contribute approximately 63 % to S_A (table 5.1) and 65 % to

the total electrical conductivity of the solution.

Table 5.1: A comparison of the compositions of Simplified (DOE, 1994) and Standard (Millero et al., 2008) Seawater. The remaining ions in Standard Seawater that are not tabulated include: Sr^{2+}, HCO_3^-, Br^-, CO_3^{2-}, $B(OH)_4^-$, F^-, OH^-, $B(OH)_3$ and CO_2.

	$S_P = 35$	
	Simplified seawater	Standard Seawater
Solute	g kg_{sol}^{-1}	
Na^+	10.7848	10.7815
K^+	0.3992	0.3991
Mg^{2+}	1.2840	1.2837
Ca^{2+}	0.4152	0.4121
Cl^-	19.4715	19.3527
SO_4^{2-}	2.7128	2.7124
H_2O	964.93	964.83
Remaining ions	N/A	0.2285

Salt precipitation in sea ice is confined to the brine inclusions that permeate its structure, ranging in diameter from 10 μm to 10 mm depending on the ice temperature (Light et al., 2003). The physical and chemical properties of the brine define the conditions inhabited by the sympagic (within ice) community, which is comprised of bacteria, microalgae, viruses, fungi, protozoans, and small metazoans (Horner et al., 1992; Thomas and Dieckmann, 2002; Ewert and Deming, 2013). Microscopic biota potentially covers between 6 and 41 % of the brine channel surface area at -2 °C (Krembs et al., 2000), while salt precipitates at colder temperatures may provide additional solid surfaces with which microorganisms can interact (Ewert and Deming, 2013). The salinity of the brine within the inclusions is temperature-dependent (Assur, 1960) and represents one of the major constraints on resident sea ice organisms because it affects the function of proteins and the surrounding osmotic conditions (Ewert and Deming, 2013). Brine salinities in sea ice extend from diluted seawater during ice melt with salinities <30 to salinities exceeding ∼220 during winter months when the ice is at its coldest. For this reason, an accurate representation of brine salinity is required for determining the physico-chemical conditions of the internal sea ice habitat (Thomas et al., 2010; Ewert and Deming, 2013).

Sea ice salinity is most often measured as a bulk property, determined as S_P in melted sea ice samples. Measurements of bulk sea ice S_P are then used to es-

timate the physical parameters of the ice pack, such as brine volume fraction and porosity (Cox and Weeks, 1988; Gleitz et al., 1995; Petrich and Eicken, 2010). In such instances, the salinity of the internal brines can be estimated as S_A from the ice temperature via available liquidus equations (Assur, 1960; Cox and Weeks, 1986; Notz and Worster, 2009), assuming local ice-brine equilibrium, i.e., $T_{\rm ice} = T_{fr}$, where T_{fr} = the freezing point of internal sea ice brine. These equations describe ice, water and salt mass balance as a function of temperature and are based on dissolved salt analysis provided in the seminal work on seawater freezing by Nelson and Thompson (1954). The accuracy of the original measurements, with respect to mirabilite precipitation in particular, has recently been evaluated from a comprehensive assessment of mirabilite solubility in equilibrium sea ice brines (Butler et al., 2016). Discrepancies include indications for mirabilite-brine disequilibrium in the freezing experiments of Nelson and Thompson, and a warmer onset temperature of mirabilite precipitation (-6.4 °C) than previously thought (-8.2 °C). These discrepancies will be reflected in the liquidus ($S_A - T_{fr}$) equations for the ice-brine equilibrium (Assur, 1960; Cox and Weeks, 1986; Notz and Worster, 2009). In light of these recent developments, there is scope for refinement of the $S_A - T_{fr}$ relationship. In addition, while the liquidus equation in sea ice yields the S_A of the internal brines from ice temperature measurements, S_P is the property that is directly measured in sea ice brines as afforded by the available oceanographic instruments and protocols. Such brine samples are typically obtained by centrifugation or by drilling bore holes through the surface to varying depth in the ice (sackhole brines), and represent conditions that extend well into the temperature-salinity region of salt precipitation (Krembs et al., 2000; Papadimitriou et al., 2004; Munro et al., 2010; Norman et al., 2011; Garrison et al., 2003). Universally in sea ice research, the difference between brine S_A (from the liquidus equation) and S_P (as typically measured directly) is assumed to be insignificant or is ignored (Munro et al., 2010; Garrison et al., 2003; Norman et al., 2011). Therefore, there is also a pressing need for rigorous evaluation of the relevance of S_P measurements and of the S_A and S_P relationship in non-conservative sea ice brines.

Here, we examine the effect of salt precipitation on the practical and absolute salinities of synthetic sea ice brines at thermal equilibrium between -1.8 to -20.6 °C

using laboratory measurements of S_A and S_P during an extensive investigation of the mirabilite-brine equilibrium at below-zero temperatures reported in Butler et al. (2016). In addition, we use the FREZCHEM thermodynamic code and equations for the electrical conductivity of individual ions (McCleskey et al., 2012) to model S_A and S_P in our experimental conditions. The FREZCHEM code has been developed for the study of cold aqueous geochemistry (Marion and Kargel, 2008) and has been used in the investigation of physical-chemical processes in sea ice (Marion et al., 1999; Grasby et al., 2013; Geilfus et al., 2013; Papadimitriou et al., 2013), and is particularly accurate in computing ice-brine-mirabilite equilibria in sea ice brines (Butler et al., 2016). Lastly, measured and modelled data are compared to $S_P - T$ data of natural sea ice brines from the Southern Ocean (Gleitz et al., 1995; Norman et al., 2011). Together, the data are used to assess and refine the existing $S_A - T$ relationship compared to several empirical liquidus equations currently in use; to define a novel $S_P - T$ relationship for sea ice brines implicit of mirabilite precipitation; and to develop a conversion factor that can account for the changing S_A to S_P ratio in sea ice brines affected by mirabilite precipitation.

5.2 Methods

5.2.1 Closed bottle incubations

A detailed account of the experimental protocol carried out for this investigation is provided in Butler et al. (2016). Synthetic brines were prepared with the method of Kester et al. (1967) according to the composition of simplified seawater (DOE, 1994) with respect to NaCl, KCl, $MgCl_2$, $CaCl_2$, and Na_2SO_4 (table 5.1). Synthetic brines were used in order to simplify the protocol for the determination of S_A, requiring the measurement of 6 ions per sample compared to the 14 per sample that would be required for natural solutions (table 5.1). The brines were incubated in screw-capped (Teflon-lined) borosilicate media bottles at 2 °C below their estimated freezing point according to the salinity/freezing-point relationship for seawater in Millero and Leung (1976). The experimental temperatures ranged from −1.8 to −20.6 °C, when the only known salt to precipitate from the solution is mirabilite at temperatures $\leqslant -6.4$ °C (Butler et al., 2016).

5.2.2 Measurement of absolute and practical salinities

The absolute salinity (S_A^{meas}) of the experimental solutions was obtained by mass balance from measurement of the total ion concentrations in solution (Na^+, K^+, Mg^{2+}, Ca^{2+}, Cl^-, and SO_4^{2-}). The Na^+ and K^+ concentrations were determined by ion chromatography on a Dionex Ion Exchange Chromatograph ICS 2100. The Mg^{2+} and Ca^{2+} concentrations were determined by potentiometric titration as described by Papadimitriou et al. (2013). The Cl^- concentration was determined by gravimetric Mohr titration with 0.3 M $AgNO_3$ standardized against NaCl purified by recrystallization. The SO_4^{2-} concentration was determined by precipitation as $BaSO_4$ in EDTA followed by gravimetric titration with $MgCl_2$ (Howarth, 1978). Repeat measurements of local seawater were used as an internal standard relative to the composition of Standard Seawater (Millero et al., 2008). This comparison provided an estimate of accuracy of the measurements, which was 0.33 % for Na^+, -0.97 % for K^+, -0.36 % for Mg^{2+}, -0.39 % for Ca^{2+}, 0.48 % for Cl^-, and 0.35 % for SO_4^{2-}. Molar concentrations (mol kg_{sol}^{-1}) were converted to mass concentrations (g kg_{sol}^{-1}) using the atomic masses provided by the International Union of Pure and Applied Chemistry (IUPAC). The S_A^{meas} (g kg_{sol}^{-1}) was then calculated as follows:

$$S_A = \sum_{i=1}^{n} c_i MW_i \tag{5.1}$$

where the i^{th} of n constituents has a concentration of c_i (mol kg_{sol}^{-1}) and molecular mass MW_i (g mol^{-1}) (Pawlowicz, 2012). The combined analytical and experimental errors yield an estimated accuracy of 0.22 ± 1.38 % for S_A^{meas}.

At present, there is no standard way of measuring practical salinities outside of the range specified in PSS-78, and in high salinity media, such as sea ice brines, samples are analysed by warming to laboratory temperature followed by gravimetric dilution with pure water to values within the measurable range of PSS-78 (Pawlowicz, 2012; Norman et al., 2011; Gleitz et al., 1995; Papadimitriou et al., 2007). Here, practical salinity was measured (S_P^{meas}) using a portable conductivity meter (WTW Cond 3110) with a WTW Tetracon 325 probe at laboratory temperature ($20-26$ °C) following gravimetric dilution with distilled water to a target S_P of 35. The electrical conductivity (k) and, hence, the values of S_P^{meas} given by this instrument are automatically corrected to 25 °C (k_{25}). The conductivity meter was calibrated in the

$k_{25} = 10-95$ mS kg cm^{-1} mol^{-1} conductivity range, covering an S_P range of $10-70$, against a Guildline AUTOSAL oceanographic salinometer (instrument accuracy in $S_P = \pm 0.002$). For the calibration we used local seawater ($S_P = 33 - 34$) and a range of diluted (with ultrapure MilliQ water) and concentrated (by freezing, Butler et al. (2016)) solutions prepared from it. The S_P measured by this instrument can be described as a second order polynomial function of k_{25} ($R^2 = 1.000$, $n = 336$), where

$$S_P = -0.039056 + 0.572499k_{25} + 0.001589k_{25}^2 \tag{5.2}$$

with an estimated standard error of ± 0.14. Lastly, the S_P measured by the conductivity meter was multiplied by the dilution factor to obtain S_P^{meas}.

5.2.3 Prediction of absolute salinity with FREZCHEM

Using the chemical composition of our synthetic brines and enabling only the formation of ice and mirabilite in its solid phase database, the thermodynamic code FREZCHEM (Marion and Kargel, 2008; Marion et al., 2010) was used to model the absolute salinity (S_A^{mod}) of equilibrium sea ice brines. The code was run in 0.1 °C steps between -1.8 and -22.8 °C, and ion concentrations from the output were retrieved at each temperature step. The temperature minimum of the model run is beyond that covered by the laboratory experiments (-20.6 °C) and covers the full temperature range in which mirabilite is the major salt precipitate affecting brine composition in sea ice (Marion et al., 1999; Butler and Kennedy, 2015). In order to calculate S_A^{mod} using equation 5.1, the molal (mol kg$^{-1}_{\text{H}_2\text{O}}$) concentrations of the code output were converted to mol kg$^{-1}_{\text{sol}}$ by

$$\text{mol kg}^{-1}_{\text{sol}} = m \left(\frac{1000}{1000 + \sum_i m_i MW_i} \right), \tag{5.3}$$

where m_i and MW_i are the molality and molecular mass (g mol^{-1}) of the i^{th} ion in solution, respectively (Marion and Kargel, 2008).

5.2.4 Modelling practical salinity with ionic molal conductivities

Because our S_P^{meas} is based on the total electrical conductivity measured in the synthetic brines as k_{25}, the same property was modelled (S_P^{mod}) using equations from

McCleskey et al. (2012). The S_P^{mod} was calculated for the same chemical composition as the brines from the FREZCHEM modelling, whilst ensuring that the conductivity calculations were carried out within their specified ionic range (McCleskey et al., 2012). The chemical composition of the brines extracted from the FREZCHEM model were normalised to an ionic strength of 0.72 mol $\mathrm{kg}_{\mathrm{H_2O}}^{-1}$ by the required dilution factor using a solver routine in Microsoft Excel. This dilution step was employed in order to replicate our experimental procedures. The electrical conductivity of each ion i in the solution at 25 °C was calculated by

$$k_{25,i} = \lambda_i m_i \tag{5.4}$$

where λ_i is the ionic molal conductivity and m_i is the ion molality. The λ_i is calculated as a function of ionic strength (I, molal) and temperature T (°C) by

$$\lambda_i = \lambda^\circ(T) - \frac{A(T)I^{0.5}}{1 + BI^{0.5}} \tag{5.5}$$

where B is an empirical constant, while λ° and A are functions of temperature described by the equations given in table 5.2. The ionic strength was calculated using

$$I = 0.5 \sum m_i z_i^2 \tag{5.6}$$

where z_i is the charge of the i^{th} ion.

The ionic molal conductivities of each ion calculated from equations 5.4 to 5.6 were summed to give the total electrical conductivity of the solution at 25 °C (k_{25}). Solution conductivities (mS kg cm^{-1} mol^{-1}) were then converted to S_P according to equation 5.2, and were multiplied by the dilution factor to attain the undiluted S_P^{mod} of the brine.

Table 5.2: Equations and constants from McCleskey et al. (2012) used for calculating λ°, A and B for use in equation 5.5, where T is temperature (°C).

Ion	λ°	A	B
Na^+	$0.003763T^2 + 0.877T + 26.23$	$0.00027T^2 + 1.1410T + 32.07$	1.7
K^+	$0.003046T^2 + 1.261T + 40.70$	$0.00535T^2 + 0.9316T + 22.59$	1.5
Mg^{2+}	$0.010680T^2 + 1.695T + 57.16$	$0.02453T^2 + 1.9150T + 80.50$	2.1
Ca^{2+}	$0.009645T^2 + 1.984T + 62.28$	$0.03174T^2 + 2.3340T + 132.3$	2.8
Cl^-	$0.003817T^2 + 1.337T + 40.99$	$0.00613T^2 + 0.9469T + 22.01$	1.5
SO_4^{2-}	$0.010370T^2 + 2.838T + 82.37$	$0.03324T^2 + 5.8890T + 193.5$	2.6

5.2.5 Comparison with natural sea ice brine salinities

Our measured and modelled practical and absolute salinities were compared to available sea ice brine salinity data from Gleitz et al. (1995) and Norman et al. (2011). The two studies contain measurements of S_P for sea ice brines that were extracted through drainage into sack-holes. The field dataset spans a brine temperature range from -1.3 to -12.4 °C, with S_P ranging from 29 to 179. All samples were taken from the seasonal ice zone of the Southern Ocean between 1991 and 2007.

5.3 Results

Both S_A^{meas} and S_P^{meas} increase at nearly identical rates down to -6.4 °C as increasing quantities of pure water are removed as ice to maintain thermal equilibrium (figure 5.1). In these experimental brines with a conservative composition, $S_A^{\text{meas}}/S_P^{\text{meas}} = 0.9995 \pm 0.0035$, which is 0.52 % lower than the value of 1.004715 ± 0.0005 in Standard Seawater (Millero et al., 2008; Jackett et al., 2006). This difference is not significant ($p > 0.05$ as tested with a two-tailed t-test with unequal variance), and we attribute it to the use of simplified synthetic seawater composed of 6 major ions (table 5.1). Below -6.4 °C, S_P^{meas} increases at a greater rate than S_A^{meas}, coincident with the redistribution of ions consequent of mirabilite precipitation. By -20.6 °C, S_P^{meas} is 5.7 % higher than S_A^{meas}, which results in $S_A^{\text{meas}}/S_P^{\text{meas}}$ reducing from 0.9995 to 0.9458.

Measured and modelled data displayed good agreement (figure 5.1). The average difference between S_A^{mod} and S_A^{meas} was 0.89 ± 1.30 %, while that between S_P^{mod} and S_P^{meas} was -0.62 ± 1.36 %, resulting in $S_A^{\text{mod}}/S_P^{\text{mod}}$ being consistently lower than that derived from our measurements by 0.014 ± 0.003. Modelled brines at temperatures above -6.4 °C display an $S_A^{\text{mod}}/S_P^{\text{mod}} = 0.9868$, which reduces to 0.9327 at -22.8 °C when S_P^{mod} is 7.4 % higher than S_A^{mod}.

Whilst the S_P^{mod} has inherent inaccuracies (McCleskey et al., 2012), agreement (within 1 %) with the measurements allows its use as a means to assess the changes in the relative contribution of each major ion to the total electrical conductivity of the brines and, hence, S_P. A likewise evaluation can be done with respect to S_A using S_A^{mod} (table 5.3). The decrease in $S_A^{\text{mod}}/S_P^{\text{mod}}$ at temperatures below -6.4 °C (figure 5.1) is due to compositional changes in the brine relating to the removal of

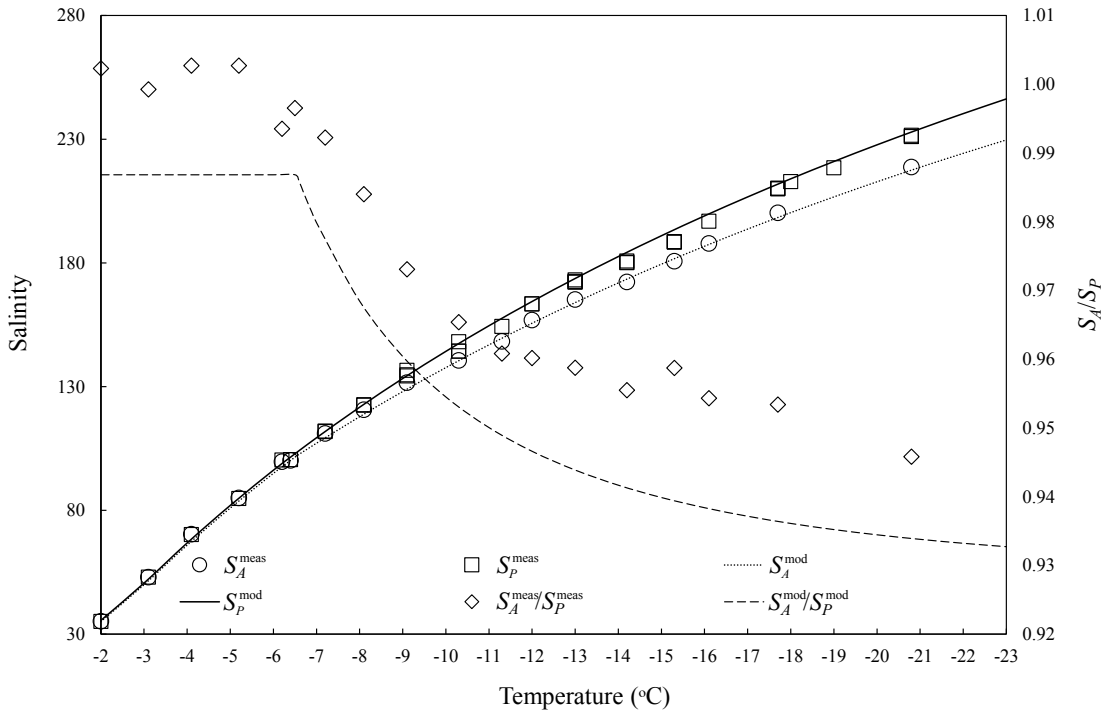

Figure 5.1: Measured and modelled S_A and S_P of equilibrium sea ice brines between -1.8 and -22.8 °C, and the associated S_A/S_P.

Na^+ and SO_4^{2-} from solution to mirabilite, as well as water in the mirabilite hydration water molecules. The largest decrease in solution conductivity and, hence, S_P^{mod}, is due to SO_4^{2-} removal from solution to mirabilite, while the contribution of Na^+ removal is much smaller because of its 16.6 times larger background concentration (Millero et al., 2008). As a result, the contribution of the remaining ions to the electrical conductivity and S_P^{mod} increases accordingly. For all ions other than Na^+, the change in percent contribution to S_A^{mod} is greater than that to S_P^{mod}, but it is the overall redistribution of the ion contributions that affects the $S_A^{\mathrm{mod}}/S_P^{\mathrm{mod}}$ relationship observed (figure 5.1). The overall effect of the redistribution of ions (table 5.3) on S_A^{mod} and S_P^{mod} was hence tested according to their modelled outputs at a normalised ionic strength of 0.72 mol $\mathrm{kg}_{\mathrm{H_2O}}^{-1}$ (figure 5.2). The trends at normalised ionic strength indicate that changes induced by mirabilite precipitation between -6.4 and -22.8 °C display a lesser overall effect on S_A^{mod} than S_P^{mod}, both increasing in salinity by 0.3 and 2.3, respectively.

Table 5.3: The % contributions of the 6 constituent ions to S_A^{mod} and S_P^{mod} from conservative simplified seawater (DOE, 1994), to a sea ice brine at ice-brine-mirabilite equilibrium at −22.8 °C at 2 °C resolution.

T	$\%S_A^{\mathrm{mod}}$						$\%S_P^{\mathrm{mod}}$					
°C	Na^+	K^+	Mg^{2+}	Ca^{2+}	Cl^-	SO_4^{2-}	Na^+	K^+	Mg^{2+}	Ca^{2+}	Cl^-	SO_4^{2-}
Conserv.	30.754	1.138	3.662	1.184	55.525	7.737	26.435	1.091	6.317	1.291	61.394	3.472
−6.8	30.731	1.155	3.715	1.202	56.340	6.857	26.254	1.100	6.371	1.302	61.914	3.058
−8.8	30.663	1.203	3.869	1.252	58.673	4.341	25.746	1.126	6.520	1.333	63.372	1.903
−10.8	30.625	1.229	3.953	1.279	59.947	2.967	25.476	1.140	6.600	1.349	64.146	1.289
−12.8	30.603	1.245	4.004	1.295	60.719	2.134	25.315	1.148	6.648	1.359	64.609	0.922
−14.8	30.588	1.255	4.037	1.306	61.223	1.591	25.210	1.153	6.679	1.365	64.908	0.684
−16.8	30.578	1.262	4.060	1.313	61.569	1.218	25.139	1.157	6.699	1.369	65.112	0.523
−18.8	30.571	1.267	4.076	1.319	61.816	0.951	25.089	1.160	6.714	1.372	65.271	0.408
−20.8	30.565	1.271	4.083	1.322	61.998	0.755	25.052	1.162	6.725	1.375	65.364	0.323
−22.8	30.562	1.274	4.097	1.325	62.134	0.607	25.024	1.163	6.734	1.376	65.443	0.260

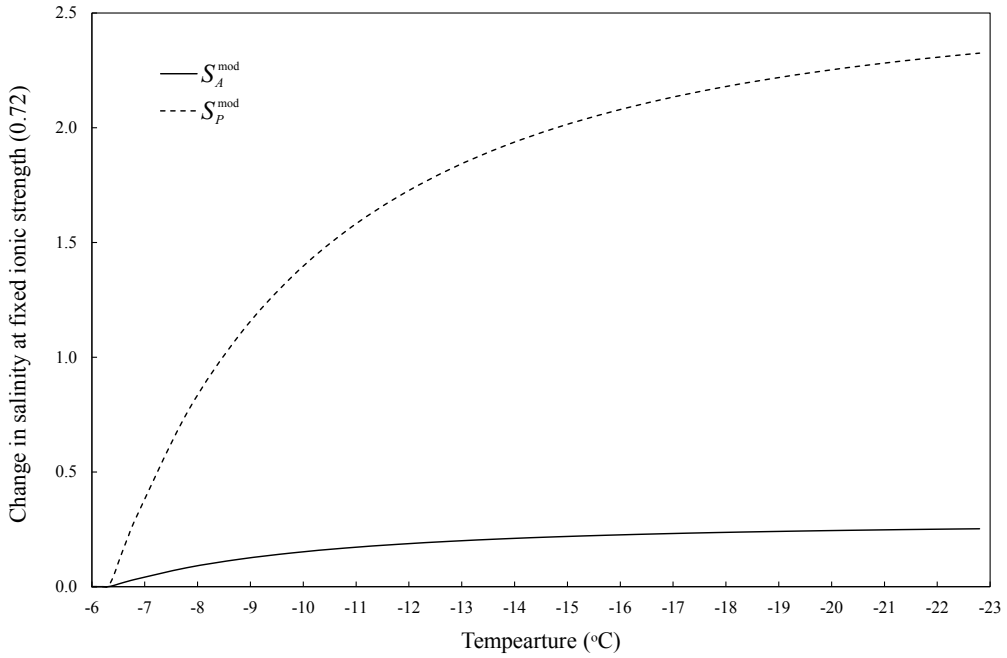

Figure 5.2: The change in S_A^{mod} and S_P^{mod} as a function of temperature, when the ionic strength of the brines are normalised by dilution to 0.72 mol $\mathrm{kg}^{-1}_{\mathrm{H_2O}}$.

5.4 Discussion

5.4.1 The absolute salinity–temperature relationship in sea ice brines

Phase equations of sea ice, including the $S_A - T_{fr}$ relationship of sea ice brines at thermal equilibrium, are a common tool for estimating brine salinities when only temperature or bulk data is available (Cox and Weeks, 1986, 1988; Garrison et al., 2003; Ewert and Deming, 2013; Collins et al., 2008). For this reason, accurate and up to date equations are a prerequisite for estimating the brine salinity reliably, and hence defining one of the key environmental constraints imposed upon sympagic biota.

The most comprehensive assessment to date of the $S_A - T_{fr}$ relationship of sea ice brines at thermal equilibrium is that of Assur (1960), who used major ion measurements (Na^+, K^+, Mg^{2+}, Ca^{2+}, Cl^- and SO_4^{2-}) in frozen seawater from Nelson and Thompson (1954), to deduce empirical equations from salt, water and ice mass balance. Assur (1960) used two discrete functions to describe the $S_A - T_{fr}$ relationship of sea ice brine, which converged at -8 °C, the temperature at which mirabilite

precipitation was understood to initiate (Nelson and Thompson, 1954). Since 1960, Cox and Weeks (1986) and Notz and Worster (2009) have simplified the two original functions by fitting the same data to single polynomials for use in sea ice models (figure 5.3, top).

Although our values of S_A^{mod} are derived from synthetic seawater with a simplified ionic composition (table 5.1), the ions included in the composition account for 99.4 % of the total S_A of Standard Seawater (Millero et al., 2008), and the 0.6 % difference is within the estimated error of S_A^{meas}. This reflects the accuracy of FREZCHEM in describing Na^+ and SO_4^{2-} in sea ice brines as outlined in Butler et al. (2016). For these reasons, we use S_A^{mod} between −1.8 and −22.8 °C to refine the $S_A - T_{fr}$ relationship of sea ice brines, implicit of the most recent understanding of mirabilite precipitation (Marion et al., 1999; Butler et al., 2016), to be:

$$S_A(T_{fr}) = 2.2330 - 19.3188T_{fr} - 0.6574T_{fr}^2 - 0.0110T_{fr}^3 \tag{5.7}$$

$$T_{fr}(S_A) = -0.174808 - 0.044057S_A - 1.08933 \times 10^{-4}S_A^2 - 5.54349 \times 10^{-7}S_A^3, \tag{5.8}$$

where T_{fr} is the brine freezing point (°C) and S_A is in g kg_{sol}^{-1}. Regressions used to derive equations 5.7 and 5.8 (and equations throughout) were computed using the Data Analysis Toolpak in Microsoft Excel ($S_A(T_{fr})$: $R^2 = 1.000$, $\sigma = 0.807$, $p < 0.001$; $T_{fr}(S_A)$: $R^2 = 1.000$, $\sigma = 0.044$, $p < 0.001$). We propose these equations for sea ice brines between −1.8 and −22.8 °C at brine-ice and brine-ice-mirabilite equilibrium. At −22.9 °C and below, hydrohalite precipitation results in further changes in brine composition and ionic ratios, and, therefore, an investigation of brine S_A and S_P below this temperature would require additional consideration of hydrohalite dynamics (Marion et al., 1999; Light et al., 2009; Butler and Kennedy, 2015).

Our refined $S_A - T_{fr}$ relationship generally corresponds well with the equations of Assur (1960), Cox and Weeks (1986), and Notz and Worster (2009) (figure 5.3, top). Major differences are seen firstly around the temperature at which mirabilite begins to precipitate in sea ice, which recent investigation determined to occur at −6.4 °C (Butler et al., 2016) rather than the previously thought temperature of −8.2 °C (Nelson and Thompson, 1954; Assur, 1960), and secondly at temperatures below −17 °C. Compared to our refined $S_A - T_{fr}$ relationship of sea ice brines

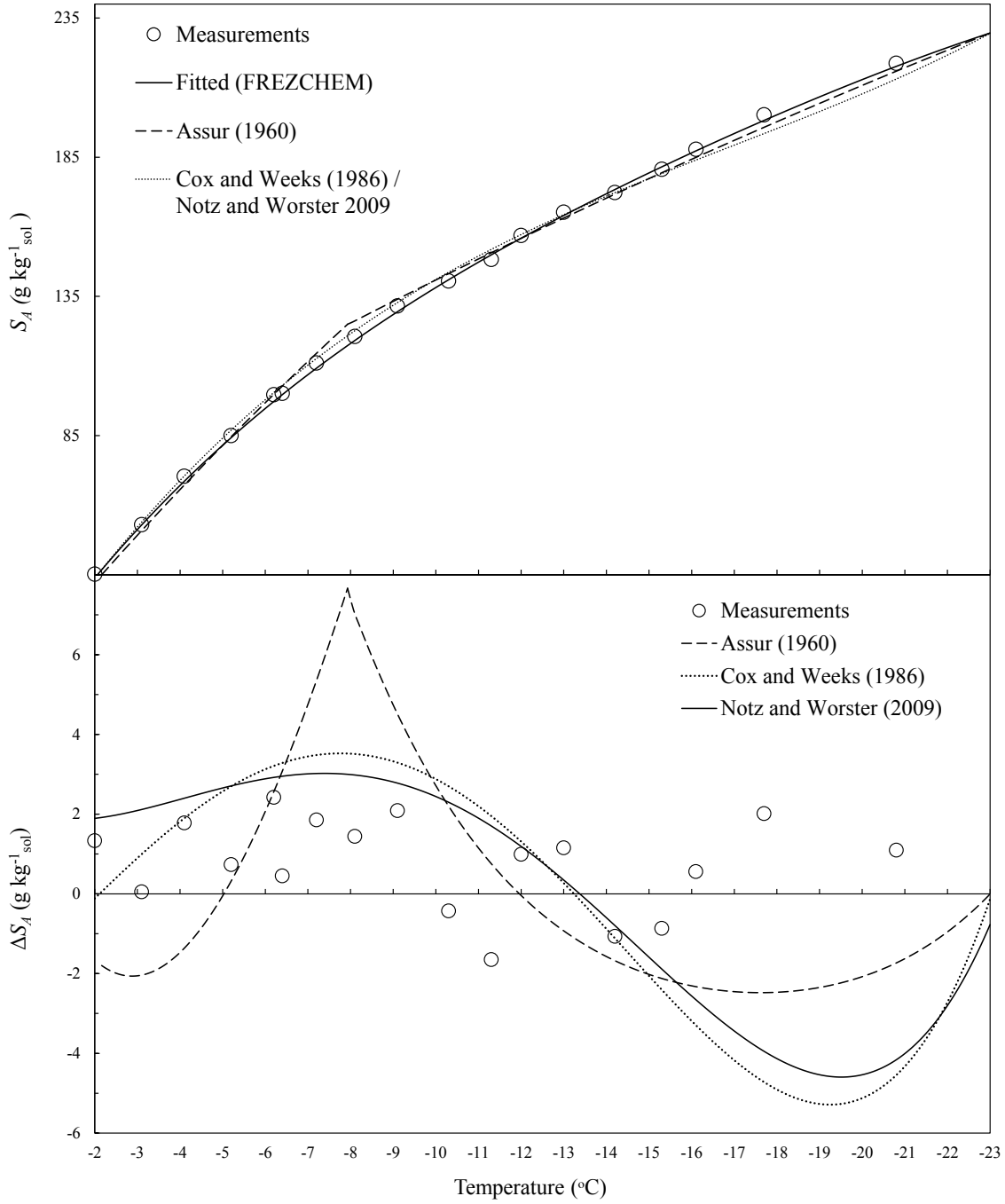

Figure 5.3: Top: A comparison of the refined $S_A - T_{fr}$ relationship (equation 7) with that of Assur (1960), Cox and Weeks (1986), and Notz and Worster (2009). Bottom: The ΔS_A of our measurements and other $S_A - T_{fr}$ equations, when compared to our refined $S_A - T_{fr}$ relationship of equation 5.7.

(equation 5.7), the previous equations over-estimate S_A by the greatest extent at -8 °C ($3.1 - 7.7$ g kg$^{-1}_{\text{sol}}$) and underestimate it by $2.5 - 5.3$ g kg$^{-1}_{\text{sol}}$ below -17 °C (figure 5.3, bottom). The average error (ΔS_A) of our S_A^{meas} relative to equation 5.7 is 1.38 g kg$^{-1}_{\text{sol}}$, compared to ΔS_A of 3.10, 3.14 and 2.83 g kg$^{1}_{\text{sol}}$ relative to the equations

of Assur (1960), Cox and Weeks (1986), and Notz and Worster (2009), respectively. This analysis therefore indicates that incorporating up-to-date information about mirabilite dynamics (Butler et al., 2016) into the $S_A - T_{fr}$ relationship of equilibrium sea ice brines results in a more accurate description of brine salinities. The reduction in error compared to previous liquidus equations can be attributed to experimental and analytical limitations in the original investigation of Nelson and Thompson (1954), mainly relating to insufficient mirabilite equilibration in their experiments (Butler et al., 2016).

5.4.2 The practical salinity−temperature relationship in sea ice brines

Practical salinity is the property measured in sea ice field studies and it is almost exclusively assumed that $S_P = S_A$ (Gleitz et al., 1995; Krembs et al., 2000; Papadimitriou et al., 2004; Munro et al., 2010; Norman et al., 2011). This assumption is reasonable for brines that retain the ionic stoichiometry of Standard Seawater (table 5.1). However, it is now evident that the S_A/S_P of standard seawater is compromised in sea ice brines below −6.4 °C due to mirabilite precipitation. Our measured and modelled results indicate that S_P increases at a greater rate than S_A between −6.4 and −22.8 °C, approaching differences of > 7 % as the temperature decreases (figures 5.1 and 5.2). This deviation substantiates the need for careful consideration of the S_A/S_P relationship in research involving sea ice brines with salinity measured on the practical scale as per typical field sampling protocols.

Existing state equations are related to S_A rather than S_P (section 5.4.1), which is not representative of the method by which sea ice brine salinity is measured in the field. Therefore, similarly to the $S_A - T_{fr}$ relationship for sea ice brines, an $S_P - T_{fr}$ relationship, implicit of mirabilite precipitation, can also be derived from this investigation. Owing to the accuracy of S_P^{mod} compared to our measurements (section 5.3), we fitted the modelled results between −1.8 and −22.8 °C first to an equation that yields S_P as a function of ice temperature T (°C) at ice-brine equilibrium:

$$S_P(T) = 2.6105 - 18.8791T_{fr} - 0.5193T_{fr}^2 - 0.0070T_{fr}^3, \tag{5.9}$$

with $R^2 = 1.000$, $\sigma = 0.295$ and $p < 0.001$. Secondly, we derive an equation

describing the brine freezing point (T_{fr}) as a function of S_P, where

$$T_{fr}(S_P) = 0.3145 - 0.0605S_P + 3.1575 \times 10^{-5}S_P^2 - 6.7696 \times 10^{-7}S_P^3, \qquad (5.10)$$

with $R^2 = 1.000$, $\sigma = 0.016$ and $p < 0.001$. Equation 5.10 can be used to accurately calculate the brine freezing point when only S_P data is available, which is typically the case for sea ice brines in field studies.

The $S_P - T_{fr}$ (equation 5.9) and $S_A - T_{fr}$ relationships (equation 5.7) are compared to available sea ice brine $S_P - T_{fr}$ data from the field (section 5.2.5) in figure 5.4. Between -2 and -6 °C, the field data follow our $S_P - T_{fr}$ and $S_A - T_{fr}$ relationships as would be expected while conservative physical concentration of seawater ions during freezing keeps the S_A/S_P relationship constant and close to that in Standard Seawater. Below -7 °C the field brine S_P continues to increase at a greater rate than our $S_A - T_{fr}$ relationship, consistent with the divergence of S_P and S_A as a result of mirabilite-brine equilibrium, and is more accordant with our $S_P - T_{fr}$ relationship that is implicit of mirabilite precipitation.

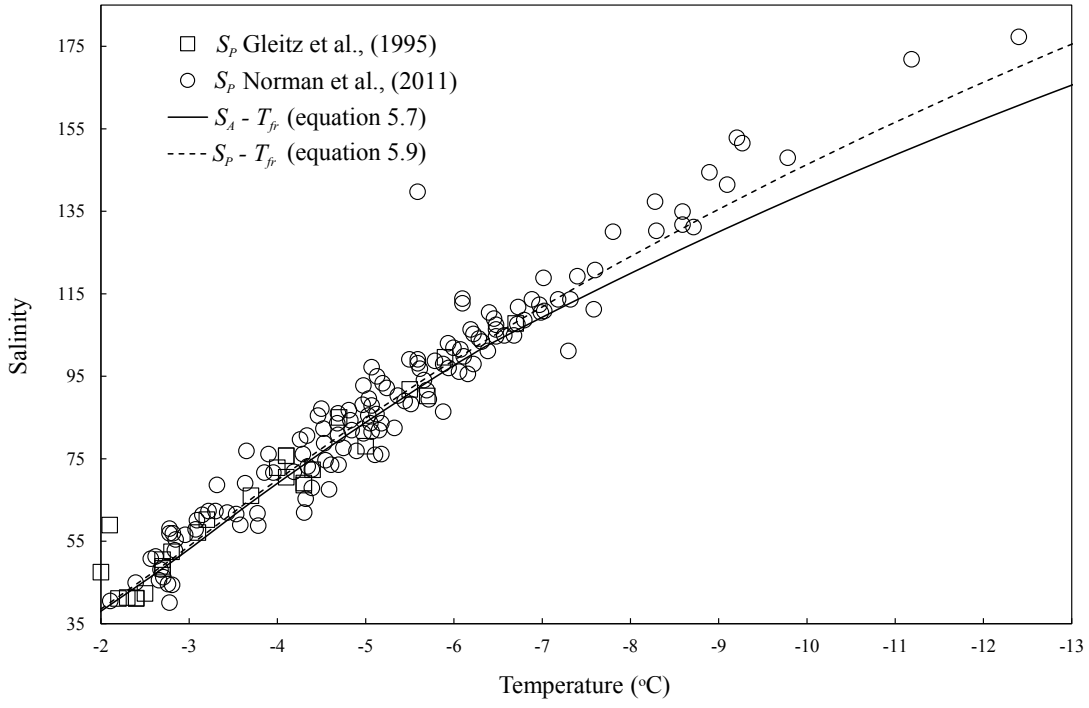

Figure 5.4: The S_P of natural sea ice brines, taken from Gleitz et al. (1995) and Norman et al (2011), compared to our $S_A - T_{fr}$ (equation 5.7) and $S_P - T_{fr}$ (equation 5.9) relationships.

Norman et al. (2011) discuss that their measurements (figure 5.4), spanning from -1.3 to -12.4 °C ($n = 184$), evidently fit the empirical equation given in Assur (1960),

$$S_A = 1000 \left(1 - \frac{54.11}{T}\right)^{-1}, \tag{5.11}$$

which, as explicitly stated by Assur (1960), is only valid for use in sea ice brines down to -8 °C, prior to the onset of mirabilite precipitation. It would therefore not be expected for the field sea ice brine data to follow equation 5.11, unless the brine remained strongly supersaturated with respect to mirabilite, which is seemingly unlikely given its rapid change in solubility between -6 and -12 °C (Butler et al., 2016). Our data analysis instead indicates that the S_P measured in field sea ice brines obeys a similar $S_P - T_{fr}$ relationship to that of equation 5.9 due to mirabilite precipitation and its consequent effect on brine composition. Whilst there are no measurements of S_A in natural sea ice brines that can be sourced for a direct comparison with the S_P measurements from the literature, all available data suggests that the universal assumption of an $S_A - S_P$ equivalence in sea ice brines is inaccurate in the region of mirabilite precipitation ($\leqslant -6.4$ °C).

The effect of using the easily measurable S_P instead of S_A for the calculation of brine density, brine volume, brine freezing point, and the conversion factor (θ) between mol $\mathrm{kg}^{-1}_{\mathrm{H_2O}}$ and mol $\mathrm{kg}^{-1}_{\mathrm{sol}}$ at -22.8 °C were evaluated here (table 5.4). All the differences (Δ) stem from the divergence of S_P from S_A displayed in figures 5.1 and 5.2, which deviate by 7.4 % at -22.8 °C. In relation to the sea ice properties, use of S_P results in a 13.26 kg m^{-3} overestimation of the brine density and an underestimation of brine volume fraction (v_b/v) by 0.0027 (7.8 %). These differences, combined with a 3.15 °C underestimation of brine T_{fr} upon use of S_P highlight how any calculation of sea ice properties requires careful consideration of salinity, while the equivalence of S_A and S_P cannot be relied upon when dealing with non-conservative sea ice brines. Lastly, the use of S_P in calculation of θ, the concentration conversion factor, results in a 2.15 % underestimation of concentrations. Such differences could easily result in considerable inaccuracies when converting concentration units for use in thermodynamic models, such as FREZCHEM, or in models of ionic molal conductivities (McCleskey et al., 2012).

Table 5.4: The effect of using S_P rather than S_A (g kg_{sol}^{-1}) measurement upon the calculation of key physical sea ice parameters at −22.8 °C, with an idealised bulk sea ice S_A of 10 g kg_{sol}^{-1}.

	Brine Salinity	ρ_b [a]	$\frac{v_b}{v}$ [b]	T_{fr} [c]	θ [d]
		kg m^{-3}		°C	
S_A	229.71	1183.77	0.0314	−22.76	0.7703
S_P	246.28	1197.02	0.0341	−25.91	0.7537
$\Delta(S_A - S_P)$	−16.57	−13.26	0.0027	3.15	0.0166
$\Delta S_A(\%)$	−7.21	−1.12	7.7900	−13.84	2.1511

[a] $\rho_b = 1000(1 + 0.0008S_A)$ (Cox and Weeks, 1986)
[b] $\frac{v_b}{v} = \frac{\rho_{si} S_{si}}{\rho_b S_A}$ (Cox and Weeks, 1983) where ρ_{si} is sea ice density (fixed at 0.926 g cm^{-3}) and S_{si} is the bulk sea ice salinity.
[c] Equation 5.7
[d] $\theta = 1 - 0.001S_A$ (Mucci, 1983)

5.4.3 Estimating absolute salinity from practical salinity

To facilitate a more accurate description of in-situ sea ice properties, we formulated a conversion factor (Φ), which may be used to estimate S_A from measurement of S_P in natural sea ice brines (S_P^{nat}) within the range of mirabilite precipitation. We assume that $S_A = S_P$ prior to mirabilite precipitation ($T > -6.4$ °C). For temperatures below −6.4 °C (brine $S_P > 103$), we derive Φ using the S_P^{nat} from Gleitz et al. (1995) and Norman et al. (2011) combined with S_A calculated from equation 5.7 and the ice temperature reported in the field studies, implicitly assuming ice-brine equilibrium. We hence defined Φ as:

$$\Phi = \frac{S_A}{S_P^{\text{nat}}}, \tag{5.12}$$

which was fitted to a linear regression as a function of S_P^{nat} ($R^2 = 0.64$, $\sigma = 0.02$ and $n = 38$):

$$\Phi(S_P^{\text{nat}}) = 1.1411 - 1.6674 \times 10^{-3} S_P^{\text{nat}}. \tag{5.13}$$

By calculating Φ from equation 5.13, the S_P^{nat} of sea ice brines may then be converted to an estimate of absolute salinity, S_A^{conv}, by

$$S_A^{\text{conv}} = S_P^{\text{nat}} \Phi. \tag{5.14}$$

Figure 5.5 displays how Φ can effectively account for the effects of mirabilite precipitation on the salinity of sea ice brines, providing an estimate of S_A, whilst still

exploiting the practical advantages of S_P measurement in the field. Equation 5.13 can be used to derive Φ for values of S_P^{nat} ranging from 103 to 177. Use of Φ within this range reduced the average error of available data, relative to S_A (equation 5.7), from 6.81 ± 5.36 %, to -0.23 ± 3.22 %. Further measurements of S_P and S_A in natural sea ice brines could act to refine a more accurate and precise description of this parameter throughout the entire temperature range in which sea ice brines are affected by mirabilite precipitation.

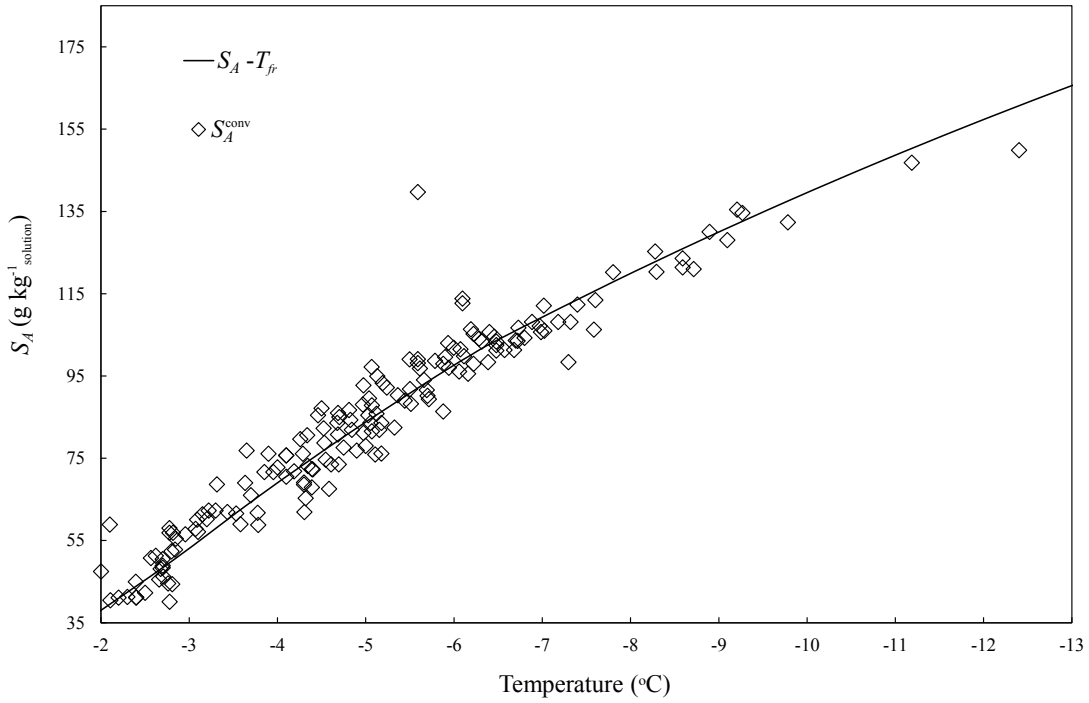

Figure 5.5: The S_A of natural sea ice brines versus brine temperature. The S_A was computed from S_P measurements in field samples of sackhole brines using equations 5.13 and 5.14. The field $S_P - T_{fr}$ data were taken from Gleitz et al. (1995) and Norman et al. (2011). The solid line represents the refined $S_A - T_{fr}$ equation of this study (equation 5.7).

5.5 Conclusions

Measurements and modelling of the ionic composition and electrical conductivity of synthetic sea ice brines between -1.8 and -22.8 °C has revealed how mirabilite precipitation below -6.4 °C affects the S_A and S_P of the brine to a measurable, and different, extent for each parameter. We have first refined the $S_A - T_{fr}$ relationship for sea ice brines to account for the new and comprehensive information about

mirabilite precipitation in sea ice brines. Our analysis has shown that, between −6.4 and −22.8 °C, the S_P increases at a greater rate than S_A due to the redistribution of individual ion contributions to the total electrical conductivity of the solution and the total concentration of dissolved salts. As a result, it is highlighted that the widespread assumption of S_A and S_P equivalence in sea ice brines incurs and propagates errors in the calculation of key physical parameters of the sea ice system, whilst misrepresenting the conditions inhabited by sympagic organisms. Existing data of field sea ice brine S_P from the Southern Ocean is in agreement with our modelled and measured data from synthetic seawater brines. We therefore propose that the observed $S_P - T_{fr}$ relationship in natural sea ice brines is a reflection of mirabilite precipitation in the field temperature region where this reaction is expected to occur ($T \leqslant -6.4$ °C). Given the ease with which electrical conductivity can be measured for S_P in both field and laboratory investigations of the sea ice system, compared to the measurement of S_A, its functionality as a field measurable parameter is still unrivalled at present. We have therefore formulated a conversion factor for estimation of S_A from measurement of S_P in sea ice brines affected by mirabilite precipitation. Similar work in the coldest temperature region of sea ice, between −23 °C and the eutectic, where other minerals are understood to precipitate and interact, could aid in maintaining S_P as an accurate measurement of salinity in such hypersaline and non-conservative conditions.

Chapter 6

Gypsum and hydrohalite dynamics in equilibrium sea ice brines

Abstract

Sea ice is permeated with millimetre to micrometre sized brine inclusions that contain concentrated seawater-derived brine. The composition of the brine is determined by the local temperature within the ice. Reducing the temperature results in further formation of pure ice within the inclusions as thermal equilibrium is attained, resulting in a smaller volume of increasingly concentrated residual brine. The coupled changes in temperature and ionic composition results in supersaturation of the brine with respect to a suite of minerals, each with its own distinctive dynamics, which consequently precipitate within sea ice at various temperatures. Two of these minerals, gypsum ($CaSO_4 \cdot 2H_2O$) and hydrohalite ($NaCl \cdot 2H_2O$), display highly different dynamics within sea ice brines, which are ultimately controlled by each minerals solubility. To examine the existence and role of gypsum and hydrohalite in sea ice, their solubilities have been measured in solutions representative of sea ice brines at thermal equilibrium. Gypsum is found to display complex behaviour between 0.2 and -25.0 °C, and its precipitation is shown to be highly dependent on the solubilities of mirabilite and hydrohalite. Measurement of hydrohalite solubility between -14.3 and -25.0 °C shows that its dynamics change distinctly between undersaturated and supersaturated conditions, with the onset of its precipitation occurring at -22.9 °C. The solubility measurements are related to the dynamics of gypsum and hydrohalite in the sea ice system, providing detailed information about their behaviour which cannot be investigated in the field at present. The hydrohalite data is incorporated into a 1D model for the growth of first year sea ice, and

is found to precipitate once the incoming shortwave radiation to the region drops to 0 W m^{-2}, reaching concentrations within the ice pack of 10 g kg^{-1}. The complex dynamics of gypsum are found to be unsuitable for this kind of idealisation. Results ultimately highlight that hydrohalite precipitates rapidly in sea ice due to the formation of a eutectic aggregate, which may affect the structural properties of the ice. Gypsum precipitation in sea ice is feasible in conditions of metastable mirabilite supersaturation, and at temperatures below −22.9 °C, but it is proposed that these dynamics may be dependent on the sea ice microstructure and the availability of suitable mineral nucleation sites.

6.1 Introduction

When sea ice forms in high latitude environments, the exceptional resistance of ice to incorporating dissolved ions into its crystal lattice results in rejection of salts and the formation of a concentrated seawater-derived brine (Petrich and Eicken, 2010). The brine becomes trapped within inclusions of the sea ice microstructure as it forms, which range in size from approximately 10 mm to 10 μm (Light et al., 2003). The lower the temperature, the more concentrated the brine becomes, whilst brine volume and the inclusion diameter decrease. At thermal equilibrium the brines are confined to a temperature-dependent chemical composition that is governed by mineral solubility and the dynamics of pure ice.

The Na−K−Mg−Ca−SO_4−Cl−H_2O system describes 99.4 % of the total dissolved ions in Standard Seawater by weight (Millero et al., 2008), hence when sea ice cools, these major ions dominate the geochemical changes. The combined effect of decreasing temperature and physical concentration of the sea ice brine as it cools, creates supersaturated solutions with respect to a suite of minerals. Each mineral in the series has a distinct solubility, and they therefore become supersaturated at different temperatures between the onset of freezing and its eutectic (the temperature at which all salts have precipitated and all unbound water is frozen) (Gitterman, 1937; Nelson and Thompson, 1954; Marion et al., 1999). Upon supersaturation the minerals precipitate authigenically within the brine inclusions of the sea ice microstructure (Dieckmann et al., 2008; Light et al., 2003; Geilfus et al., 2013) and so become part of the heterogeneous sea ice matrix; contributing to its optical, me-

chanical, thermal and structural properties (Assur, 1960; Light et al., 2004; Carns et al., 2015), whilst also representing the major *in-situ* geochemical changes.

The suite of minerals that can precipitate within sea ice as it cools are predominantly hydrated phases, and can include: ikaite ($CaCO_3 \cdot 6H_2O$), mirabilite ($Na_2SO_4 \cdot 10H_2O$), hydrohalite ($NaCl \cdot 2H_2O$), gypsum ($CaSO_4 \cdot 2H_2O$), sylvite (KCl), $MgCl_2 \cdot 12H_2O$ and antarcticite ($CaCl_2 \cdot 6H_2O$). Ikaite can precipitate below -2 °C if primary productivity within the ice decreases the brine pCO_2 sufficiently (Papadimitriou et al., 2013), and has been identified in natural and experimental sea ice (Dieckmann et al., 2008; Geilfus et al., 2013). Mirabilite becomes supersaturated in sea ice brines at -6.4 °C, becoming the main sink of SO_4^{2-} upon further cooling (Butler et al., 2016; Marion et al., 1999). Mirabilites solubility in sea ice brines above -6.4 °C has hindered its identification in sea ice samples from the field, but it has been identified in laboratory experiments by microphotography (Light et al., 2003) and synchrotron X-ray powder diffraction (Butler and Kennedy, 2015). Hydrohalite is the most abundant mineral that can precipitate in sea ice due to the dominance of Na^+ and Cl^- in the composition of seawater (Light et al., 2009; Millero et al., 2008), and is understood to precipitate below -22.9 °C (Gitterman, 1937; Nelson and Thompson, 1954; Marion et al., 1999; Butler and Kennedy, 2015). The presence of hydrohalite in sea ice has never been recorded in the field, but has been identified in laboratory experiments (Butler et al., 2016). Gypsum has recently been identified in experimental and natural sea ice (Geilfus et al., 2013), but its dynamics are poorly understood and are believed to be highly dependent upon the solubility of mirabilite and the brine SO_4^{2-} pool (Gitterman, 1937; Marion et al., 1999). Consequentially there is conflicting evidence regarding the precipitation of gypsum in sea ice (Gitterman, 1937; Nelson and Thompson, 1954; Marion et al., 1999; Geilfus et al., 2013). Little is known about the precipitation of the remaining minerals: sylvite, $MgCl_2 \cdot 12H_2O$ and antarcticite. Sylvite is understood to precipitate below -34 °C, while $MgCl_2 \cdot 12H_2O$ precipitation at -36.2 °C is often cited as coinciding with the eutectic temperature of seawater when Ca^{2+} has been removed as gypsum (Gitterman, 1937; Marion et al., 1999). In the case that gypsum precipitation is inhibited or hindered via chemical or structural constraints within the sea ice microstructure, the eutectic temperature instead coincides with the precipitation of

antarcticite at −53.8 °C (Nelson and Thompson, 1954).

This investigation focuses upon the dynamics of gypsum and hydrohalite. Gypsum has been predicted to precipitate in sea ice for near 8 decades (Gitterman, 1937), however the identification of gypsum crystals in experimental and natural sea ice has only recently been achieved (Geilfus et al., 2013). It has been proposed as a potential marine deposition in polar seas (Geilfus et al., 2013), and the eutectic of seawater occurs at a temperature 17.6 °C warmer when gypsum precipitates (Marion et al., 1999). Originally, experiments carried out by Gitterman (1937) identified that gypsum precipitated at temperatures below approximately −15 °C. More recently, Marion et al. (1999) applied model predictions (FREZCHEM) with experimental analysis of frozen seawater brines seeded with gypsum at −15, −20 and −26 °C. From this work it was proposed that gypsum becomes supersaturated at −22.2 °C before its precipitation is accelerated below −22.9 °C. The accelerated precipitation of gypsum in this case is dependent upon mineral interaction within the system, where it is proposed that removal of Na^+ from the brine through hydrohalite precipitation results in undersaturation with respect to mirabilite, which liberates SO_4^{2-} as it dissolves. The liberated SO_4^{2-} increases the degree of supersaturation with respect to gypsum, which hence precipitates at an increased rate (Gitterman, 1937; Marion et al., 1999).

Gypsum precipitation was not observed in the seminal work on seawater freezing by Nelson and Thompson (1954) because minerals were removed from the brine as they formed, during a sequential freezing process. Similar experiments on synthetic seawater brines by Gitterman (1937) maintained mineral precipitates in contact with the brine throughout, and the conserved SO_4^{2-} source facilitated gypsum precipitation. The different approaches taken by (Gitterman, 1937) and Nelson and Thompson (1954) are considered to be representative of equilibrium and fractional crystallisation pathways, respectively (Marion et al., 1999; Marion and Kargel, 2008; Butler and Kennedy, 2015). In an experimental approach representative of equilibrium crystallisation, the dissolution and precipitation of mirabilite consequent of hydrohalite precipitation and dissolution, respectively, was observed during cooling and warming of frozen seawater brines, but gypsum was not identified (Butler and Kennedy, 2015). In contrast, the recent identification of gypsum in experimental

and natural sea ice at temperatures between −2 and −10 °C (Geilfus et al., 2013), contributes to a complex description of gypsum dynamics in this system.

All modelled (Marion et al., 1999) and measured (Gitterman, 1937; Nelson and Thompson, 1954) data predict that hydrohalite precipitates in sea ice below −22.9 °C. From the onset, its precipitation is rapid, and by −30 °C, 87 % of NaCl has been removed from the brine (Richardson, 1976). In frozen seawater from a starting salinity of 35 g kg_{sol}^{-1} (in absence of brine drainage), hydrohalite concentrations can approach 4 wt % by −40 °C (Richardson, 1976; Light et al., 2003). Precipitation of hydrohalite has been shown to be closely associated with accelerated ice formation, which substantially reduces the volume of brine remaining in the ice (Richardson, 1976; Butler and Kennedy, 2015). Its presence is understood to distinctly affect the structural-optical properties of sea ice (Light et al., 2004; Carns et al., 2015) and therefore affect climate forcings in polar regions. Furthermore, Eskimos have long observed that when the ice-surface temperature drops to below −23 °C, travel by sleds becomes more difficult and the ice changes to a bright white colour (Assur, 1960). This observation is coincident with the precipitation of hydrohalite, and its effect on the optical, mechanical and frictional properties of sea ice. Despite these observations, its presence has only ever been identified in laboratory experiments on frozen seawater brines (Butler and Kennedy, 2015) and sea ice (Light et al., 2003).

To develop a greater understanding of gypsum and hydrohalite dynamics in sea ice as a function of temperature, we have measured their solubility in sea ice brines at thermal equilibrium. The investigation expands upon recent work defining mirabilite solubility in similar conditions (Butler et al., 2016). The solubility of both gypsum and hydrohalite were measured to a minimum temperature of −25.0 °C. Equilibrium was attained from both undersaturation and supersaturation of the brine with respect to each mineral. Because of the high solubility of hydrohalite, the maximum temperature for its measurement was −14.3 °C. Gypsum, with its potential for a much more dynamic behaviour in sea ice brines (Gitterman, 1937; Marion et al., 1999; Geilfus et al., 2013), was studied between 0.2 and −25.0 °C, and experiments were designed to take into consideration the behaviour of mirabilite and hydrohalite.

Given the dominance of hydrohalite as a mineral precipitate in sea ice, its solubility data has been incorporated into a 1D model for snow-free first-year sea ice,

allowing for evaluation of its depth distribution and temporal dynamics as the ice pack grows. The complex dynamics of gypsum, however, are shown to be unsuitable for this idealisation.

6.2 Methods

6.2.1 Mineral preparation

Gypsum, hydrohalite and mirabilite were prepared based on the methods described in Wang et al. (2012), Light et al. (2009), and Butler et al. (2016), respectively. Care was taken when extracting hydrohalite and mirabilite via vacuum filtration to prevent dehydration to their anhydrous phases (Vavouraki and Koutsoukos, 2012; Light et al., 2009). Gypsum was stored in screw capped bottles at room temperature, whilst hydrohalite and mirabilite were stored at −20 °C.

6.2.2 Preparation of seawater-derived brines

Synthetic brines were used throughout the temperature range in which gypsum and hydrohalite solubilities were studied. Given the dominance of Na^+ and Cl^- in the composition of seawater and their tendency to remain as free ions in solution (Millero et al., 2008; Marion and Kargel, 2008), the use of synthetic seawater-derived brines compared to brines derived from natural seawater, was anticipated to have little effect on hydrohalite solubility (Gitterman, 1937; Nelson and Thompson, 1954). For this reason only synthetic brines were used for hydrohalite experiments. To confirm the reliability of the gypsum-brine equilibrium determined in synthetic brines down to −25 °C, we conducted parallel experiments with natural brines between 0.2 and −5.0 °C. Synthetic (NaCl, Na_2SO_4, $CaCl_2$, $MgCl_2$ and KCl) and natural seawater-derived brines were prepared so that they replicated the conservative composition of Seawater (section 2.3) prior to cooling and seeding, confirmed by full characterisation of the major ions (Butler et al., 2016).

6.2.3 Synchrotron X-ray powder diffraction

The purity of mineral seeds used to study dissolution and precipitation reactions was characterised using synchrotron X-ray powder diffraction on Beamline I11 at Diamond Light Source (Harwell Science and Innovation Campus, Oxfordshire, UK).

Mineral samples were analysed at −30 °C by use of a cryostream in order to prevent dehydration to anhydrous phases. All data were processed on TOPAS v5 software using the Fundamental Parameters Analysis method to obtain information from Le Bail and Rietveld refinements. Published cell parameters for hydrohalite (Klewe and Pederson, 1974), gypsum (Boeyens and Ichharam, 2002) and mirabilite (Brand et al., 2009) were used as an initial starting point for the refinements and were allowed to refine. Quantitative Rietveld refinements determined that all batches of gypsum displayed 100 % purity, while mirabilite (Butler et al., 2016) and hydrohalite displayed evidence of ∼1 % impurities of their anhydrous phases as a result of mineral dehydration during sample preparation and analysis (Grasby et al., 2013; Vavouraki and Koutsoukos, 2012).

6.2.4 Closed bottle incubations

Mineral solubility was determined using a closed-system incubation technique based on that used to measure mineral solubility in seawater and seawater-derived brines (Mucci, 1983; Papadimitriou et al., 2013; Butler et al., 2016). Solutions of increasing salinity with decreasing temperature, representative of sea ice brines at thermal equilibrium, were seeded with hydrohalite or gypsum and incubated in screw-capped (Teflon-lined) borosilicate (25 − 500 mL, DURAN) media bottles, and mineral-brine equilibrium was attained from both undersaturation (mineral dissolution) and supersaturation (heterogeneous mineral precipitation). All bottles were incubated in triplicate fully submersed in constant temperature circulating chillers and shaken by hand daily to facilitate exposure of the mineral seed to the bulk solution. Incubation temperatures were controlled by Grant RC 1400G re-circulating baths when above −5 °C, and Grant TX120/TX150 circulators twinned with Grant R2 refrigeration units when below −5 °C, with ethylene glycol as the recirculating liquid.

Due to the large temperature range studied, three different approaches were employed for the incubations. Between 0.2 and −6.0 °C sea ice brines are understood to behave conservatively (with respect to Na^+, K^+, Mg^{2+}, Ca^{2+}, Cl^- and SO_4^{2-}) during freezing (Butler et al., 2016), that is, while the brines become more concentrated the ionic ratios remain the same. Seawater brines with absolute salinities of $35 - 100$ g kg_{sol}^{-1} were made up, then cooled and incubated at their freezing point

according to the following equation from Millero and Leung (1976),

$$T_{fr} = -0.0575 S_A + 1.710523 \times 10^{-3} S_A^{1.5} - 2.154996 \times 10^{-4} S_A^2 \qquad (6.1)$$

where T_{fr} is the freezing point (°C) and S_A is the absolute salinity (g kg_{sol}^{-1}) before seeding.

A second protocol was required for experiments undertaken between −6.8 and −22.2 °C because the conservative seawater brines, when cooled, precipitated mirabilite (Butler et al., 2016). As the same process is understood to occur in the natural environment, it was necessary to allow the brine to attain equilibrium with ice and mirabilite before it was used in subsequent experiments for gypsum and hydrohalite solubility. Conservative seawater brines were made up (Butler et al., 2016), cooled to at least 2 °C colder than their freezing point predicted from equation 6.1 and incubated. Once brine-ice-mirabilite equilibrium had been attained, the solutions were extracted through syringe filters (0.2 μm, WHATMAN) and the filtrate transferred to triplicate bottles (25 ml) before subsequent seeding with gypsum or hydrohalite.

At the coldest experimental temperatures (−23.7 and −25.0 °C) a third protocol was necessary to account for the precipitation of hydrohalite and the associated reduction in brine volume. Conservative seawater brines were made up (Butler et al., 2016) to a salinity of ∼225 g kg_{sol}^{-1} in 500 ml bottles and subsequently cooled to −20 °C before allowing mirabilite to precipitate and reach brine-mirabilite equilibrium. With no further manipulation of the brines they were cooled to either −23.7 or −25.0 °C, resulting in ice and hydrohalite precipitation (without hydrohalite seed). After 1 month at the target temperature, brines from these bottles were filtered (0.2 μm, WHATMAN) and transferred to triplicate bottles (25 ml) before seeding with gypsum or hydrohalite. The reason for seeding with hydrohalite in the 25 ml bottles, despite prior attainment of brine-hydrohalite equilibrium, was because the temperature in these smaller bottles displayed less spatial variation when sampling than the original 500 ml bottles. This allowed for a more accurate determination of equilibrium temperature, and, hence, hydrohalite solubility.

6.2.5 Gypsum solubility experimental protocol

The solubility of gypsum was measured between 0.2 and −25.0 °C using all three closed bottle incubation protocols outlined above. Natural and synthetic brines were

incubated in tandem between 0.2 and −5.0 °C, while only synthetic brines were used for the remainder of the experiments.

Additional bottle incubations were also undertaken using the second protocol to examine the potential of gypsum precipitation in solutions supersaturated with respect to mirabilite. Although mirabilite reaches supersaturation in sea ice brines at −6.38 °C, it has been observed that metastable supersaturated solutions with respect to mirabilite are particularly persistent in absence of mineral seed at supersaturations experienced in sea ice between −7 and −8 °C (Butler et al., 2016). To this end, metastable solutions supersaturated with respect to mirabilite, were maintained at −7.1 °C ($S_A = 112.2$ g kg_{sol}^{-1}, $\Omega_{mirabilite} = 1.252$) and −8.2 °C ($S_A = 123.1$ g kg_{sol}^{-1}, $\Omega_{mirabilite} = 1.717$), and seeded with gypsum.

Further bottle incubations were also carried out using the third protocol at −23.7 and −25.0 °C. Here, gypsum dynamics were measured in brines that had attained equilibrium via ice, mirabilite and hydrohalite precipitation (Gitterman, 1937; Nelson and Thompson, 1954; Marion et al., 1999; Light et al., 2009; Butler and Kennedy, 2015). These experiments were designed to test the extent to which mirabilite dissolution, consequent of hydrohalite precipitation during equilibrium crystallisation (section 6.1), fuels gypsum precipitation (Marion et al., 1999). To facilitate this, the brines at −23.7 and −25.0 °C were separated into two incubation conditions, whereby both were incubated with gypsum seed, one of which had the additional presence of excess mirabilite seed. The additional presence of mirabilite was designed to provide a SO_4^{2-} source to the brine, which would affect the solubility of gypsum.

By considering gypsum solubility in solutions characterised by mirabilite precipitation, supersaturation and dissolution; gypsum solubility was measured from both dissolution and heterogeneous precipitation reactions. Gypsum solubility was quantified by measurement of total ion concentrations of calcium and sulphate.

6.2.6 Hydrohalite solubility experimental protocol

The solubility of hydrohalite was measured in synthetic seawater-derived brines between −14.3 and −25.0 °C using the second and third closed bottle incubation techniques. Between −14.3 and −22.0 °C the brines attained equilibrium via hy-

drohalite dissolution. In the experiments at −23.7 °C and −25.0 °C, equilibrium was attained via hydrohalite precipitation that did not require the addition of hydrohalite seed. Hydrohalite solubility was quantified by measurement of total ion concentrations of sodium and chloride.

6.2.7 Sampling

Samples were taken from the incubated bottles when required and were transferred to 25 mL screw capped polyethylene bottles through disposable syringe filters (25 mm Whatman GD/X with a 0.2 μm pore size). The samples were immediately diluted gravimetrically to a target salinity of ∼35 with deionised water to eliminate the risk of precipitation during refrigerated storage. The major ion composition of the samples was determined within 4 weeks from sampling. Chiller temperatures were monitored at 30 minute intervals using data loggers (Tinytag aquatic 2 TG4100), and once per day manually using a type K temperature probe on a CoMARK 9001 thermometer.

6.2.8 Brine analysis

The Na^+ and K^+ concentrations were determined by ion chromatography on a Dionex Ion Exchange Chromatograph ICS 2100. The Mg^{2+} and Ca^{2+} concentrations were determined by potentiometric titration as described by Papadimitriou et al. (2013). The Cl^- concentration was determined by gravimetric Mohr titration with 0.3 M $AgNO_3$ standardised against NaCl purified by recrystallisation. The SO_4^{2-} concentration was determined by precipitation as $BaSO_4$ in EDTA followed by gravimetric titration with $MgCl_2$ (Howarth, 1978). All methods quantified total concentrations, i.e., the combined concentrations of paired and unpaired ions (Pytkowicz and Hawley, 1974; He and Morse, 1993). All reference to measured concentrations hence represents the total ion concentration, symbolised by $[X]_T$, where X = ion. Repeat measurements of local seawater were used as an internal standard relative to the composition of Standard Seawater (Millero et al., 2008). This comparison provided an estimate of accuracy of the measurements, which was 0.10 % for $[Na^+]_T$, 0.97 % for $[K^+]_T$, 0.62 % for $[Mg^{2+}]_T$, 0.39 % for $[Ca^{2+}]_T$, 0.37 % for $[Cl]_T$, and 0.35 % for $[SO_4^2]_T$.

6.2.9 Determination of brine-mineral equilibrium

The solubility of a mineral in a solution is quantified at solid-solution equilibrium. Tandem experiments were therefore used to determine the point at which the gypsum and hydrohalite seeds had attained equilibrium with the brine. Mineral-brine equilibrium was monitored at each temperature by measurement of the change in $[Ca^{2+}]_T$ (for gypsum solubilities) and $[Cl^-]_T$ (for hydrohalite solubilities) with time, by use of a separate bottle incubation subjected to identical protocols described in section 6.2.4, sampled at various time intervals after seeding. When the change in $[Ca^{2+}]_T$ or $[Cl^-]_T$ determined in samples from the time series bottle was within the analytical error over 1 week, we assigned this to indicate attainment of equilibrium. The time series measurements were not intended as an assessment of dissolution/precipitation kinetics and therefore did not include precisely controlled stirring rate or consistent sampling points. The average time that the experiments were therefore given to attain gypsum or hydrohalite equilibrium, was 65 and 28 days, respectively.

6.2.10 The stoichiometric solubility product of gypsum and hydrohalite

The solubility of minerals in sea ice brines is a function of temperature and solution composition (Papadimitriou et al., 2013; Butler et al., 2016), and here is defined as the stoichiometric solubility product, K^*_{sp}. The $K^*_{sp,gypsum} = [Ca^{2+}]_T[SO^{2-}_4]_T$, while the $K^*_{sp,hydrohalite} = [Na^+]_T[Cl^-]_T$, both with units of mol^2 kg$^{-2}_{solution}$. The K^*_{sp} was used to determine the saturation state, Ω (Berner, 1980), of a conservative seawater brine with respect to gypsum or hydrohalite, defined as $\Omega = \frac{ICP}{K^*_{sp}}$, where ICP (ion concentration product) represents the product of the initial $[Ca^{2+}]_T$ and $[SO^{2-}_4]_T$ for gypsum, or $[Na^+]_T$ and $[Cl^-]_T$ for hydrohalite. The solution is undersaturated when $\Omega < 1$, and in a metastable supersaturated state when $\Omega > 1$. The point and conditions at which $\Omega = 1$ relates to the brine and mineral being at equilibrium, and can be used to determine the temperature at which a mineral begins to precipitate in sea ice (Papadimitriou et al., 2013; Butler et al., 2016).

The K^*_{sp} of a mineral is hereafter reported as the negative logarithm, pK^*_{sp}. Further, equations fitted to solubility data as functions of temperature are most com-

monly given in terms of absolute temperature (K). We hence fitted our measurements to non-linear regressions as functions of temperature using the Data Analysis Toolpak in Microsoft Excel, to the form

$$pK^*_{\mathrm{sp}}(T) \text{ or } \Omega(T) = A + BT + CT^2 + DT^3 \tag{6.2}$$

where T is temperature (K), and coefficients A to D are given in table 6.1.

6.2.11 FREZCHEM and first year sea ice modelling

The FREZCHEM code is a thermodynamic model frequently used to investigate geochemical reactions in the cryosphere and is based on the Pitzer formalism of ionic interactions in concentrated electrolyte solutions (Marion and Grant, 1994; Marion and Farren, 1999; Butler et al., 2016). Here, it was used as a tool to compare our directly measured $K^*_{\mathrm{sp,gypsum}}$ and $K^*_{\mathrm{sp,hydrohalite}}$ with that calculated from its thermodynamic database. Model runs replicated the temperature and solution compositions studied in this investigation. The protocol employed to run the FREZCHEM model (version 15.1) and extract gypsum and hydrohalite solubilities was based on that used for ikaite (Papadimitriou et al., 2013) and mirabilite (Butler et al., 2016) solubilities, and accounted for the $SO_4^{2-} - HSO_4^-$ equilibria and the $CaCO_3^0$ ion pair (natural brine only) to derive total ion activities (section 4.2.9). Molal (mol $kg^{-1}_{H_2O}$) concentrations extracted from the model were converted to mol kg^{-1}_{sol} by,

$$\text{mol kg}^{-1}_{\mathrm{sol}} = m \left(\frac{1000}{1000 + \sum_i m_i MW_i} \right), \tag{6.3}$$

where m_i and MW_i are the molality and molecular mass (g mol^{-1}) of the i^{th} ion in solution, respectively (Marion and Kargel, 2008).

Version 15.1 of FREZCHEM model used in this investigation is one of the newest available updates. For this reason, the output for gypsum differs slightly from that described for seawater freezing from older versions (Marion et al., 1999; Marion and Kargel, 2008). Our model runs first predict a 'window' of gypsum precipitation between −6.4 and −9.3 °C, similar to that described in Geilfus et al. (2013). Upon cooling below −9.3 °C FREZCHEM then predicts a region of gypsum undersaturation, before precipitation initiates again below −17.3 °C. Within these described

regions, the weight of gypsum that precipitates (< 0.2 g kg_{sol}^{-1}) is an order of magnitude lower than those predicted to occur upon a hydrohalite-mirabilite-gypsum interaction below -22.9 °C (Marion and Kargel, 2008).

The FREZCHEM code was also run for the scenario of Standard Seawater freezing to -36 °C. Here, the FREZCHEM computation employed equilibrium crystallisation similar to that predicted by the Gitterman Pathway, whereby the interaction of mirabilite with hydrohalite through changes in brine composition results in mirabilite dissolution below -22.9 °C (Gitterman, 1937; Marion et al., 1999). An equilibrium crystallisation pathway was chosen based on recent observations of mirabilite-hydrohalite interaction in frozen seawater brines by Butler and Kennedy (2015). The weights of hydrohalite precipitate estimated by FREZCHEM at 0.1 °C temperature steps were extracted from this output and incorporated into a 1D model of first-year sea ice, as described in Butler et al. (2016) for the case of mirabilite precipitation. The model calculated the depth and salinity profiles of the ice pack, which were used to estimate the concentration of hydrohalite within the ice after desalination processes by

$$H_i(T) = H(T)\frac{S_i}{S_{sw}} \tag{6.4}$$

where $H_i(T)$ is the hydrohalite concentration (g kg^{-1} sea ice) at temperature T; $H(T)$ is the weight of hydrohalite at temperature T that would precipitate from 1 kg of Standard Seawater ($S_A = 35.165$ g kg_{sol}^{-1}) based the FREZCHEM model output; S_i is the bulk salinity of the ice; and S_{sw} is the absolute salinity of standard seawater, 35.165 g kg_{sol}^{-1}.

The complex dynamics of gypsum are shown to be unsuitable for this idealisation, however the incorporation of hydrohalite solubility data into the sea ice model allowed for evaluation its temporal depth distribution as the modelled ice pack grew throughout an Arctic Winter.

6.3 Results

6.3.1 Gypsum solubility between 0.2 and −22.2 °C

The $pK^*_{sp,gypsum}$ between 0.2 and -5.0 °C displays no detectable difference between use of natural or synthetic brines as the experimental medium (figure 6.1). This consistency indicates that gypsum solubility, as with mirabilite solubility (Butler

Table 6.1: Coefficients for use with equation 6.2 that describe the change in solubility product pK^*_{sp} and saturation state Ω of gypsum and hydrohalite with temperature (K).

	Range		A	B	C	D	R^2	σ
	°C	K						
$pK^*_{sp,gypsum}$	0.2 to −1.8	273.35 to 271.35	7.8871287e2	−5.7598725	1.0554382e-2		0.868	0.005
	−1.8 to −5.0	271.35 to 268.15	2.1151892e3	−1.5748129e1	2.9348641e-2		0.999	0.005
	−5.0 to −22.2[a]	268.15 to 250.95	−1.8167179e3	2.1378285e1	−8.3629854e-2	1.0892019e-4	0.993	0.008
Ω_{gypsum}	0.2 to −1.8	273.35 to 271.35	9.4425558e2	−6.9204629	1.2682971e-2		0.949	0.003
	−1.8 to −6.8	271.35 to 266.35	−1.4732875e5	1.6448060e3	−6.1202247	7.5900980e-3	0.999	0.010
	−6.8 to −22.2[a]	266.35 to 250.95	3.3343577e3	−3.8584742e1	1.4835926e-1	−1.9001908e-4	0.990	0.010
$pK^*_{sp,hydrohalite}$	−14 to −22.8	259.15 to 250.35	1.2839471	−9.4961523e-3			1.000	0.000
	−22.8 to −26.0	250.35 to 247.15	−1.2285077e2	1.0287111	−2.1664221e-3		1.000	0.001
$\Omega_{hydrohalite}$	−14 to −22.8	259.15 to 250.35	7.8679083e1	−5.50716264e-1	9.6040378e-4		1.000	0.000
	−22.8 to −26.0	250.35 to 247.15	2.0188738e3	−1.4909085e1	2.7357085e-2		1.000	0.001
Hydrohalite (g kg^{-1})	−22.9 to −25.0	250.25 to 248.15	281.8533065e5	−3.4052324e5	1.3713739e3	−1.8409842	1.000	0.189
	−25.0 to −36.0	248.15 to 237.15	1.7928766e5	−2.2241856e3	9.3475908	−1.2993734e-2	0.998	0.122

[a] Extrapolated to −22.8 °C in figures 6.1 and 6.2

et al., 2016), is unaffected by differences such as pH, carbonate and borate alkalinity, and trace metals within the error of the measurements. For this reason we infer that using synthetic brines for all temperatures below −5 °C was representative of the gypsum solubility in naturally derived seawater brines.

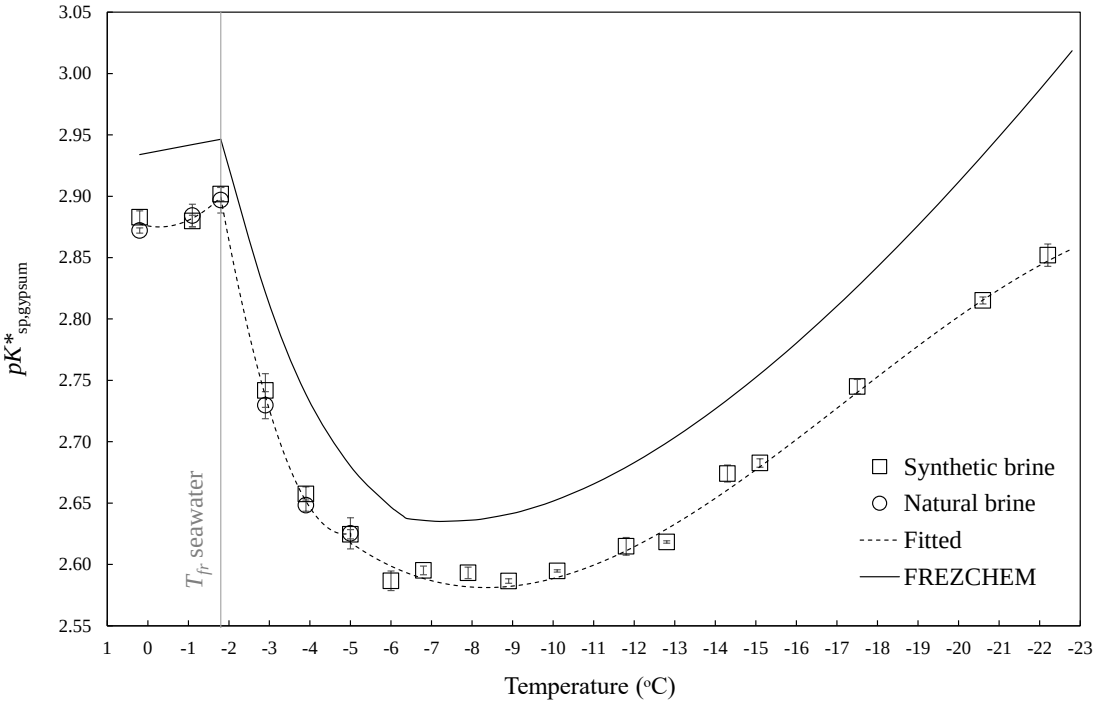

Figure 6.1: Measured $pK^*_{\mathrm{sp,gypsum}}$ in equilibrium sea ice brines plotted alongside output from the FREZCHEM model. The vertical line at −1.8 °C marks the point of which the solubility product begins to become affected by coupled changes in salinity and temperature as a result of freezing.

The changes in $pK^*_{\mathrm{sp,gypsum}}$ between 0.2 and −1.8 °C occur over a region of changing temperature at constant salinity. Here, the $pK^*_{\mathrm{sp,gypsum}}$ increases from 2.878 to 2.900, which represents a slight reduction in gypsum solubility as the temperature is lowered (figure 6.1 and table 6.2). Between −1.8 and −6.0 °C, $pK^*_{\mathrm{sp,gypsum}}$ decreases from 2.900 to 2.587 while temperature decreases but brines undergo conservative concentration to maintain brine-ice thermal equilibrium. Between −6.0 and −22.2 °C, $pK^*_{\mathrm{sp,gypsum}}$ increases from 2.587 to 2.852 under the influence of decreasing temperature, increasing ionic strength, and removal of SO_4^{2-} due to mirabilite precipitation at ice-brine-mirabilite equilibrium (Butler et al., 2016).

The $pK^*_{\mathrm{sp,gypsum}}$ was fitted to 3 stepwise polynomial functions of temperature (K) between 0.2 and −22.2 °C (table 6.1, rows 1 to 3). The $pK^*_{\mathrm{sp,gypsum}} - T$ equation,

fitted to our measurements between −5.0 and −22.2 °C was extrapolated down to −22.8 °C so that it extends to the point at which hydrohalite precipitation initiates.

Ω_{gypsum} displays quite complex changes in equilibrium sea ice brines between 0.2 and −22.2 °C (figure 6.2 and table 6.2). At 0.2 °C the seawater had an undersaturation of $\Omega_{\text{gypsum}} = 0.219$, increasing only slightly to 0.246 at −1.8 °C. This change is described by a second order polynomial function of temperature (table 6.1, row 4). As the solution cools further below −1.8 °C (the freezing point of seawater), the Ω_{gypsum} increases sharply towards saturation as the brine becomes conservatively concentrated, reaching 0.979 at −6.8 °C. This increase is described by a third order polynomial function of temperature (table 6.1 1, row 5). Between −6.8 and −22.2 °C the Ω_{gypsum} becomes increasingly undersaturated whilst mirabilite precipitates, decreasing to 0.767. Here, the change is described by a third order polynomial function of temperature (table 6.1, row 6). As with the $pK^*_{\text{sp,gypsum}}$, we extrapolate this fitted equation between −6.8 and −22.2 °C, down to −22.8 °C.

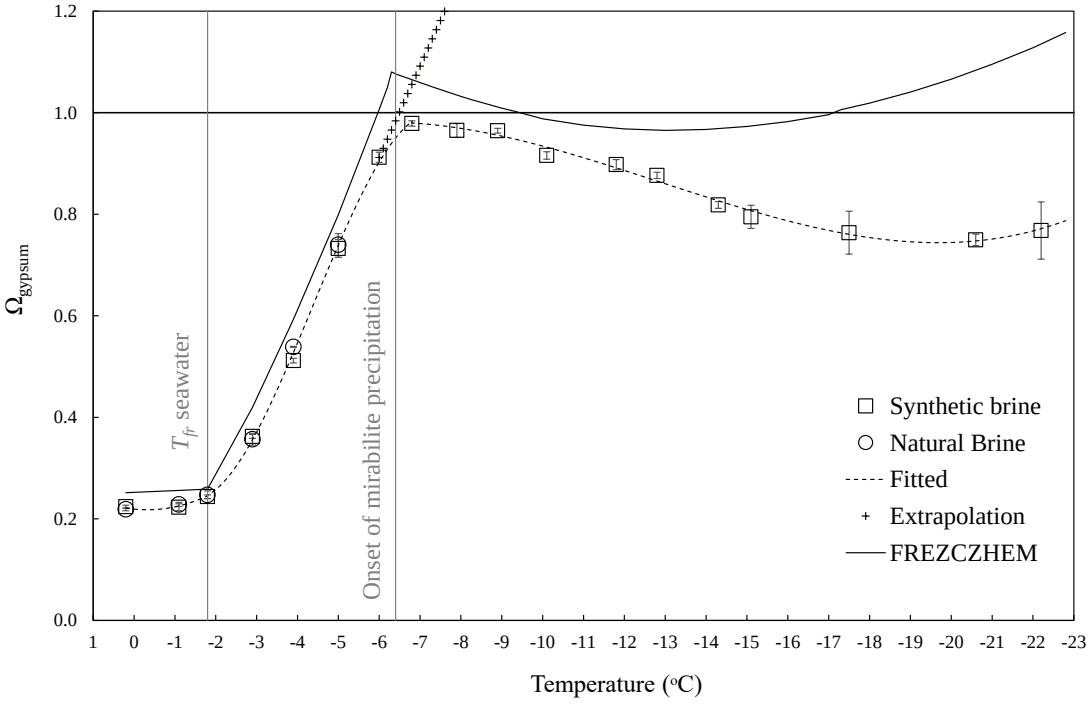

Figure 6.2: The measured Ω_{gypsum} in equilibrium sea ice brines plotted alongside the output from the FREZCHEM model. The vertical line at −1.8 °C marks the point of which the saturation state begins to become affected by coupled changes in salinity and temperature as a result of freezing, while that at −6.4 °C marks the onset of mirabilite precipitation.

Table 6.2: The absolute salinity (S_A) of incubated brines prior to seeding with gypsum, incubation temperature at point of sampling, $[Ca^{2+}]_T$ and $[SO_4^{2-}]_T$ at equilibrium, and the resulting measured and modelled $pK^*_{sp,gypsum}$ and Ω_{gypsum}. The S_A measured between 0.2 and −6.0 °C are of conservative brines, while those at −6.8 °C and below were measured at brine-ice-mirabilite equilibrium.

Exp. #	S_A	T	$[Ca]^{2+}]_T$	$[SO_4^{2-}]_T$	$pK^*_{sp,gypsum}$		Ω_{gypsum}	
	g kg^{-1}_{sol}	°C	mol kg^{-1}_{sol}		Observed	FREZCHEM	Observed	FREZCHEM
NG-0	35.1	0.2	27.80±0.17	48.29±0.06	2.872±0.002	2.933	0.219±0.003	0.252
SG-0	35.3	0.2	27.79±0.21	47.13±0.73	2.883±0.005		0.224±0.007	
NG-1	35.3	−1.1	28.11±0.37	46.43±0.37	2.884±0.009	2.942	0.228±0.004	0.256
SG-1	35.3	−1.1	28.44±0.19	46.38±0.19	2.880±0.005		0.223±0.007	
NG-2	35.2	−1.8	28.22±0.10	44.94±0.95	2.897±0.011	2.946	0.247±0.008	0.259
SG-2	35.2	−1.8	28.09±0.15	44.64±0.33	2.902±0.005		0.244±0.004	
NG-3	53.2	−2.9	31.72±0.52	58.73±0.52	2.730±0.011	2.822	0.357±0.012	0.420
SG-3	53.0	−2.9	31.01±0.42	58.46±1.25	2.742±0.014		0.362±0.004	
NG-4	70.3	−3.9	32.60±0.13	68.94±1.05	2.648±0.005	2.739	0.539±0.001	0.593
SG-4	70.4	−3.9	32.10±0.28	68.56±0.37	2.658±0.006		0.512±0.005	
NG-5	85.2	−5.0	30.87±0.21	76.78±1.74	2.625±0.013	2.680	0.740±0.022	0.799
SG-5	85.0	−5.0	30.22±0.09	78.54±0.48	2.625±0.004		0.733±0.018	
SG-6	99.7	−6.0	31.79±0.10	81.47±1.26	2.587±0.008	2.647	0.912±0.010	1.006
SG-7	111.1	−6.8	34.58±0.23	73.46±0.40	2.595±0.004	2.636	0.979±0.005	1.065
SG-8	120.6	−7.9	38.92±0.50	65.56±0.28	2.593±0.005	2.636	0.965±0.005	1.035
SG-9	131.6	−8.9	42.10±0.17	61.55±0.49	2.587±0.002	2.641	0.964±0.005	1.011
SG-10	140.6	−10.1	46.09±0.09	55.16±0.07	2.595±0.001	2.653	0.916±0.007	0.986
SG-12	156.9	−11.8	53.00±0.25	45.81±0.57	2.615±0.007	2.679	0.898±0.010	0.969
SG-13	165.2	−12.8	61.62±0.30	39.08±0.17	2.618±0.001	2.699	0.876±0.006	0.965
SG-14	173.8	−14.3	65.34±0.70	32.42±0.45	2.674±0.007	2.734	0.818±0.007	0.968
SG-15	180.7	−15.1	69.11±0.33	30.05±0.38	2.683±0.003	2.755	0.795±0.023	0.973
SG-18	200.2	−17.5	76.10±0.65	23.65±0.35	2.745±0.006	2.826	0.764±0.042	1.008
SG-21	218.7	−20.6	88.52±0.98	17.29±0.15	2.815±0.003	2.934	0.750±0.011	1.083
SG-22	225.3	−22.2	92.28±0.39	15.24±0.38	2.852±0.009	2.995	0.767±0.056	1.135

6.3.2 Gypsum dynamics in metastable mirabilite supersaturation

In the experiments carried out under metastable conditions of mirabilite supersaturation, the brines had $\Omega_{\text{mirabilite}}$ values of 1.252 and 1.717 at −7.1 and −8.2 °C, respectively, prior to seeding. Mirabilite would almost certainly not precipitate in these conditions homogeneously (Butler et al., 2016). Seeding these brines with gypsum resulted in gypsum precipitation in place of mirabilite precipitation. At −7.1 and −8.2 °C, 3.7 ± 0.14 mmol $\text{kg}_{\text{sol}}^{-1}$ and 7.54 ± 0.47 mmol $\text{kg}_{\text{sol}}^{-1}$ of gypsum precipitated, respectively. These changes are equivalent to $\Omega_{\text{gypsum}} = 1.171$ at −7.1 °C and $\Omega_{\text{gypsum}} = 1.358$ at −8.2 °C.

Subsequent seeding of these solutions with synthetic mirabilite resulted in heterogeneous mirabilite precipitation. The associated removal of SO_4^{2-} created undersaturated solutions with respect to gypsum, which dissolved. The brines then went on to attain equilibrium with the same $[Ca^{2+}]_T$ and $[SO_4^{2-}]_T$ observed in figure 6.1 and table 6.2.

6.3.3 Hydrohalite-mirabilite-gypsum interaction

At −23.7 and −25.0 °C, brines prevented from interacting with mirabilite were found to be slightly supersaturated with respect to gypsum, by approximately 7.6 and 9.0 mmol $\text{kg}_{\text{sol}}^{-1}$, respectively (equating to Ω_{gypsum} of 1.070 at −23.7 °C and 1.083 at −25.0 °C). When identical brines were seeded with synthetic mirabilite subsequent to hydrohalite precipitation, its dissolution (as observed in Marion et al. (1999) and Butler and Kennedy (2015)) and the consequent availability of SO_4^{2-}, facilitated enhanced gypsum precipitation. At −23.7 and −25.0 °C the mirabilite dissolution resulted in gypsum precipitation by 24.09 mmol $\text{kg}_{\text{sol}}^{-1}$ ($\Omega_{\text{gypsum}} = 1.266$) and 80.44 mmol $\text{kg}_{\text{sol}}^{-1}$ ($\Omega_{\text{gypsum}} = 2.264$), respectively. These results are not included in figures 6.1 or 6.2 because the processes measured are proposed to be highly dependent upon the microstructure of the brine inclusions, and required extensive experimental manipulation and time in order to facilitate mineral dissolution and precipitation. These aspects will be considered in the discussion that follows.

6.3.4 Hydrohalite solubility

The $pK^*_{\mathrm{sp,hydrohalite}}$ from the experiments between −14.3 and −25.0 °C displays excellent agreement with that of the FREZCHEM model (figure 6.3 and table 6.3). We therefore combined our results with the FREZCHEM model output when deriving coefficients for use with equation 6.2 because our experimental error was greater than the difference between measured and modelled solubility. Between −14 and −22.8 °C, $pK^*_{\mathrm{sp,hydrohalite}}$ increases from −1.178 to −1.092, representing a decrease in hydrohalite solubility with decreasing temperature as the ionic strength of the initial brine develops at ice-brine-mirabilite equilibrium. Here, the $pK^*_{\mathrm{sp,hydrohalite}}$ is described by a linear regression as a function of temperature (table 6.1, row 7). At temperatures ⩽−22.9 °C, hydrohalite precipitation results in a rapid increase to the $pK^*_{\mathrm{sp,hydrohalite}}$, which reaches −0.980 at −25.0 °C. This increases is described by a second order polynomial function of temperature (table 6.1, row 8).

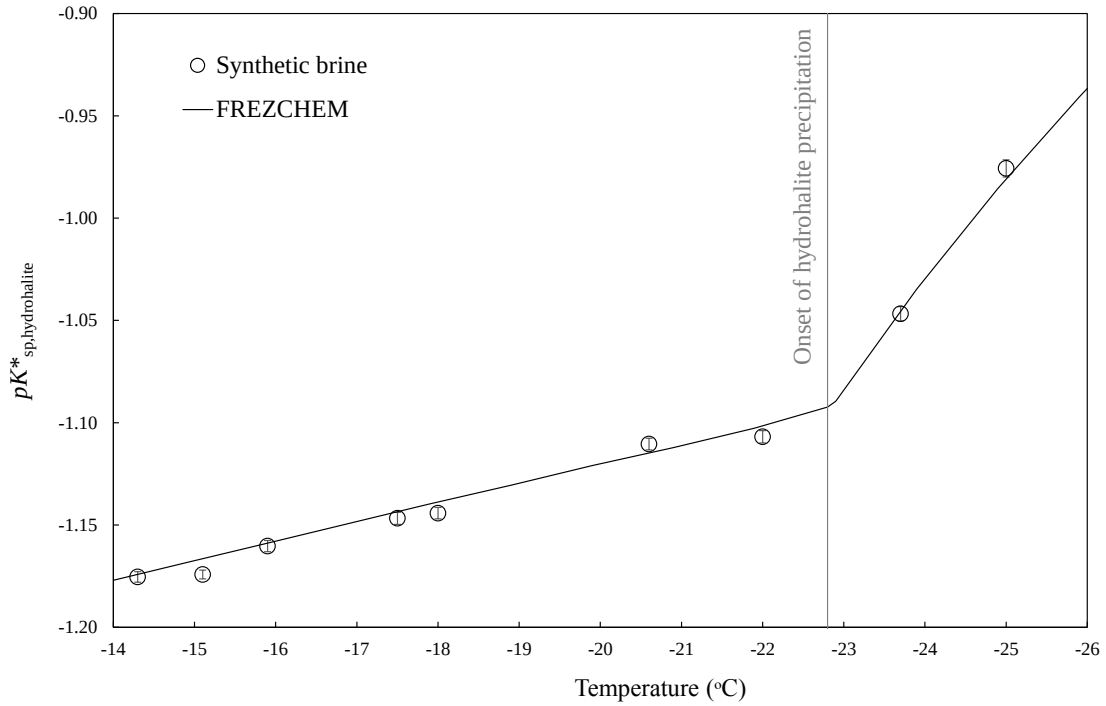

Figure 6.3: Measured $pK^*_{\mathrm{sp,hydrohalite}}$ in equilibrium sea ice brines plotted alongside output from the FREZCHEM model. The vertical line at −22.9 °C marks the point of which the solubility product begins to become affected by the precipitation of hydrohalite.

$\Omega_{\mathrm{hydrohalite}}$ displays very similar trends to the $pK^*_{\mathrm{sp,hydrohalite}}$ (figure 6.4 and table 6.3), increasing from 0.455 at −14 °C to 0.999 at −22.8 °C. Here, the relationship

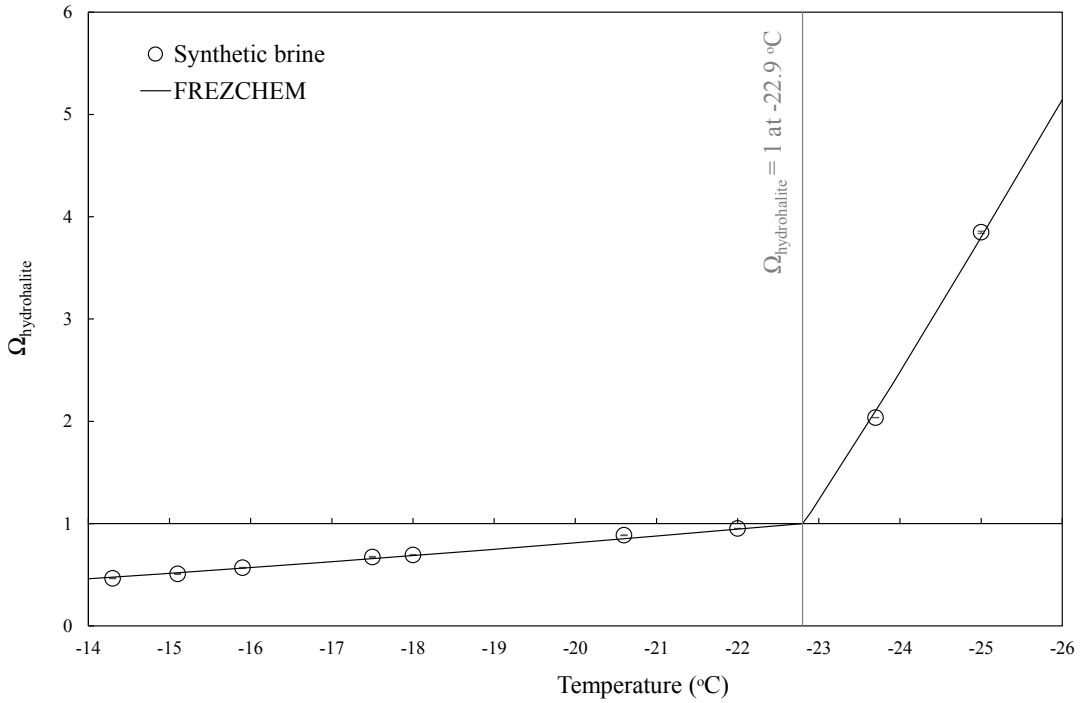

Figure 6.4: Measured $\Omega_{\text{hydrohalite}}$ in equilibrium sea ice brines plotted alongside output from the FREZCHEM model. The vertical line at -22.9 °C marks the point of which the saturation state begins to become affected by precipitation of hydrohalite.

is described by a second order polynomial function of temperature (table 6.1, row 9). At -22.9 °C and below, the $\Omega_{\text{hydrohalite}}$ was estimated for a conservative brine by calculating the conservative concentrations of Na^+ and Cl^- when restored to their seawater stoichiometry (Millero et al., 2008) using the measured and modelled $[Mg^{2+}]_T$. This method increased the $[Na^+]_T$ and $[Cl^-]_T$ until the Na:Mg and Cl:Mg molar ratios were restored to 8.8791 and 10.3351 respectively (based on the composition of Standard Seawater in table 5.1). The estimations of $\Omega_{\text{hydrohalite}}$ in this supersaturated region show that it increases rapidly upon initiation of hydrohalite precipitation, reaching 5.008 at -26 °C. This rapid increase can be described by a second order polynomial function of temperature (table 6.1, row 10).

6.4 Discussion

6.4.1 Gypsum solubility between 0.2 and -22.2 °C

The gypsum solubility measurements (figures 6.1 and 6.2) are implicit of mirabilite precipitation at all temperature $\leqslant -6.4$ °C because it is the first mineral to precip-

Table 6.3: The absolute salinity (S_A) of incubated brines prior to seeding with hydrohalite (see footnote for exceptions), incubation temperature at point of sampling, $[Na^+]_T$ and $[Cl^-]_T$ from each of the bottle incubations at equilibrium, and the resulting measured and modelled $pK^*_{sp,hydrohalite}$ and $\Omega_{hydrohalite}$. D = dissolution, P = precipitation.

Exp. #	Reaction	S_A	T	$[Na^+]_T$	$[Cl^-]_T$	$pK^*_{sp,hydrohalite}$		$\Omega_{hydrohalite}$	
		g kg^{-1}_{sol}	°C	mmol kg^{-1}_{sol}		Observed	FREZCHEM	Observed	FREZCHEM
H-14	D	173.8[a]	−14.3	3596±26	4164±5	−1.175±0.003	−1.174	0.465±0.003	0.476
H-15	D	180.7[a]	−15.1	3591±18	4159±8	−1.174±0.002	−1.166	0.508±0.001	0.520
H-16	D	187.8[a]	−15.9	3503±20	4130±3	−1.160±0.003	−1.159	0.568±0.004	0.564
H-17	D	200.2[a]	−17.5	3403±33	4120±12	−1.147±0.003	−1.144	0.672±0.006	0.657
H-18	D	201.3[a]	−18.0	3398±35	4102±11	−1.144±0.004	−1.139	0.693±0.004	0.687
H-21	D	218.7[a]	−20.6	3181±28	4053±4	−1.110±0.002	−1.114	0.886±0.003	0.852
H-22	D	225.9[a]	−22.0	3173±40	4031±7	−1.107±0.003	−1.102	0.953±0.001	0.945
H-24	P	225.3[b]	−23.7	2720±36	4094±8	−1.047±0.004	−1.047	2.037±0.001	2.105
H-25	P	225.3[b]	−25.0	2274±22	4158±18	−0.976±0.005	−0.983	3.848±0.011	3.794

[a] S_A measured at brine-ice-mirabilite equilibrium

[b] These brines were further cooled to the given temperature, which initiated ice and hydrohalite precipitation.

itate from the Na−K−Mg−Ca−Cl−SO_4−H_2O system (Butler et al., 2016). The implicit effects of mirabilite precipitation can be isolated from the dynamics of gypsum by interpreting the $[Ca^{2+}]_T$ and $[SO_4^{2-}]_T$ separately (figure 6.5). Below −6.4 °C, the removal of SO_4^{2-} during mirabilite precipitation exceeds the rate at which it becomes concentrated during freezing of the brine, causing the $[SO_4^{2-}]_T$ to reduce substantially (figure 6.5, bottom). Contrastingly, the changes in $[Ca^{2+}]_T$ (figure 6.5, top) can be attributed to the dynamics of gypsum. The measurements of $[Ca^{2+}]_T$ at brine-gypsum equilibrium exceed that of conservatively concentrated seawater, replicating our observation that gypsum dissolved in all of these experiments. The measurement of gypsum dissolution is reflected in Ω_{gypsum} (figure 6.2), which remains undersaturated (< 1) between 0.2 and −22.2 °C.

In terms of solubility ($pK^*_{sp,gypsum}$, figure 6.1), gypsum only displays slight changes between 0.2 and −1.8 °C. Upon cooling in these constant salinity conditions, gypsum solubility increases by 0.78 ± 0.49 mmol kg_{sol}^{-1}. The magnitude of this change contrasts greatly to that displayed by mirabilite under identical conditions, which decreases in solubility by 43.37 ± 5.39 mmol kg_{sol}^{-1} (Butler et al., 2016). Upon further decrease in temperature between −1.8 and −6.0 °C, when the solution becomes conservatively concentrated, gypsum displays an increase in solubility, evidenced by negative changes in $pK^*_{sp,gypsum}$ (figure 6.1). This increased gypsum solubility upon increasing salinity (Shaffer, 1967) is in accord with ion association effects in an increasingly concentrated solution (Koutsoukos et al., 2007). Despite the increasing solubility of gypsum between −1.8 and −6.0 °C, the coinciding physical concentration of the solution results in the Ω_{gypsum} increasing from 0.246 to 0.912, i.e., less gypsum has to dissolve to attain equilibrium. In contrast, under identical conditions, $\Omega_{mirabilite}$ has been observed to increase at a faster rate between −1.8 and −6.0 °C, from 0.065 to 0.875 (Butler et al., 2016). The Ω_{gypsum} measured in our experiments reaches a maximum of 0.98 at −6.8 °C, notably not exceeding saturation. Below −6.8 °C mirabilite precipitation dominates due to a continually rapid reduction in its solubility (section 4.4.1), and the consequent removal of SO_4^{2-} from the brine (92 % of SO_4^{2-} is removed from the mirabilite at −20.6 °C (Butler et al., 2016)) thwarts the chances of Ω_{gypsum} exceeding 1.

Below −6.8 °C the $[Ca^{2+}]_T$ shows a growing deviation from that of conservative

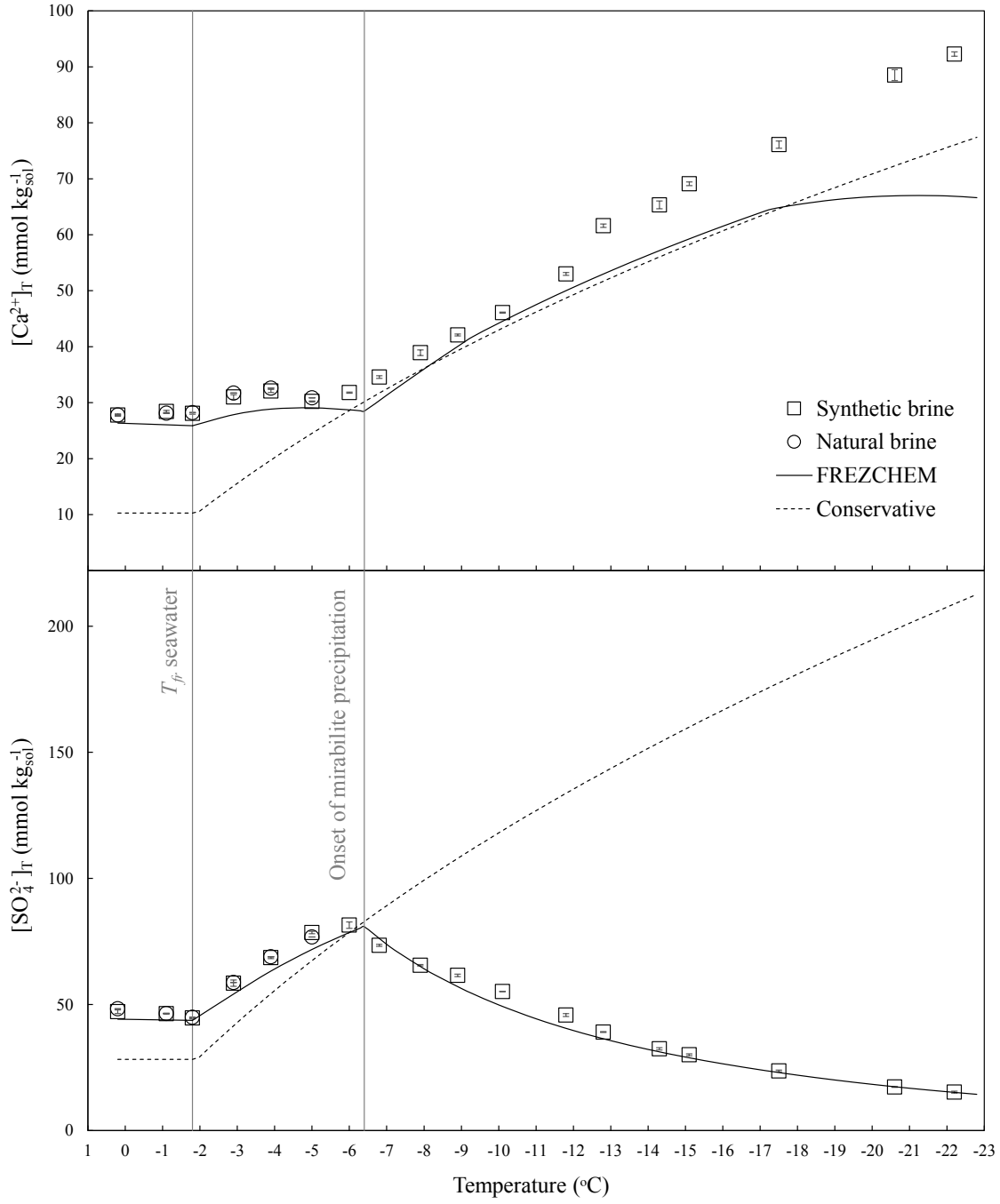

Figure 6.5: $[Ca^{2+}]_T$ and $[SO_4^{2-}]_T$ in equilibrium sea ice brines between 0.2 and -22.8 °C. The vertical line at -1.8 °C marks the point of which the solubility product begins to become affected by coupled changes in salinity and temperature as a result of freezing, while that at -6.4 °C marks the onset of mirabilite precipitation. The dashed line represents the estimated concentration based on a conservatively concentrated solution in absence of gypsum dissolution or precipitation

concentration (figure 6.5, top) and the FREZCHEM model prediction, demonstrating the measurement of elevating levels of gypsum dissolution within these brines upon decreasing temperature. Interestingly, the observed deviation between the measured and modelled $[Ca^{2+}]_T$ is not mirrored in the $[SO_4^{2-}]_T$ (figure 6.5, bottom). We propose this discrepancy to be a result of mirabilite scavenging any SO_4^{2-} that is liberated during gypsum dissolution. This mechanism is supported by the observation that, in our experiments below −6.8 °C, when $[Ca^{2+}]_T$ increased after seeding the brines with gypsum, the $[SO_4^{2-}]_T$ displayed negligible variation. Furthermore, transparent prismatic crystals were consistently observed in the mineral seed extracted from the bulk solution upon termination of the experiments. These crystals displayed transformation to a white powder upon warming to room temperature, concomitant with regular observations of mirabilite dehydration to thenardite (Grasby et al., 2013; Vavouraki and Koutsoukos, 2012). Furthermore, precipitation of mirabilite in the experimental solutions would not be expected without an additional SO_4^{2-} source given the care taken in assuring that mirabilite-brine equilibrium had been attained prior to seeding with gypsum (Butler et al., 2016). The combined changes in $[Ca^{2+}]_T$ and $[SO_4^{2-}]_T$ as gypsum dissolved, results in Ω_{gypsum} decreasing by 0.21 between −6.8 and −22.8 °C. This trend suggests that a substantial shift in solution composition would have to arise in order for gypsum to suddenly reach saturation at colder temperatures.

A direct comparison of the measured gypsum solubility with that predicted by the FREZCHEM model (figure 6.1), shows how the FREZCHEM computation mirrors, but sits consistently overestimates (0.069 ± 0.024), the $pK^*_{sp,gypsum}$. The higher $pK^*_{sp,gypsum}$ predicted by FREZCHEM represents a lower modelled solubility than the measurements. The differences between measured and modelled $pK^*_{sp,gypsum}$ can be assigned to the deviations in $[Ca^{2+}]_T$ and $[SO_4^{2-}]_T$ between the two datasets (figure 6.5). Between 0.2 and −10.1 °C the difference is assigned to FREZCHEM underestimating the $[Ca^{2+}]_T$ and $[SO_4^{2-}]_T$ by 2.03 ± 0.98 and 3.14 ± 3.05 mmol kg_{sol}^{-1}, respectively. Between −10.1 and −22.2 °C FREZCHEM's underestimation of $[SO_4^{2-}]_T$ reduces from a 5.82 to 0.15 mmol kg_{sol}^{-1}, likely due to the models accurate representation of mirabilite dynamics (Butler et al., 2016). Conversely, while the FREZCHEM model predicts $[SO_4^{2-}]_T$ increasingly accurately, its underestimation of

$[Ca^{2+}]_T$ increases from 1.54 to 25.33 mmol kg_{sol}^{-1} within the same temperature range. The underestimation of gypsum solubility by FREZCHEM is also exhibited in the Ω_{gypsum} (figure 6.2), where the model predictions sit consistently above that of our measurements. Between 0.2 and −22.2 °C our measurements indicate that gypsum would not exceed saturation in sea ice brines, however the FREZCHEM model shows two regions of gypsum supersaturation: first between −6.4 and −9.3 °C, and secondly $\leqslant$−17.3 °C (figure 6.2).

Compared to its accurate computation of mirabilite (Butler et al., 2016) and hydrohalite (figures 6.3 and 6.4) dynamics in sea ice brines, FREZCHEM's accuracy with respect to gypsum solubility is inadequate for a completely accurate description of its solubility in sea ice brines, particularly between −10 and −22.8 °C. In order for the FREZCHEM model to calculate gypsum solubility (accounting for the formation of ion pairs), it has to compute ion activity coefficients ($\gamma_{Ca^{2+}}$, $\gamma_{SO_4^{2-}}$, $\gamma_{CaCO_3^0}$ and $\gamma_{HSO_4^-}$), the activity of water (a_w) and the thermodynamic solubility product of gypsum ($K_{sp,gypsum}$). Evidence suggests that a_w is well characterised because any inaccuracies would manifest in the modelled solubility of other minerals in frozen aqueous solutions, which is not observed for mirabilite (Butler et al., 2016) or hydrohalite (section 6.4.4). Results from mirabilite solubility in identical conditions indicate that the computation of $\gamma_{SO_4^{2-}}$ is accurate (Butler et al., 2016). Furthermore, in the case of synthetic brines used here, the $\gamma_{CaCO_3^0}$ and $\gamma_{HSO_4^-}$ are negligible compared to the experimental uncertainty. It therefore seems likely that the differences between measured and modelled gypsum solubility result from inaccuracies in the computation of either $\gamma_{Ca^{2+}}$ or $K_{sp,gypsum}$. The $\gamma_{Ca^{2+}}$ is computed using the specific ion interaction model described by the Pitzer formalism within FREZCHEM, whilst $K_{sp,gypsum}$ is described as a function of temperature at infinite dilution (Marion and Farren, 1999; Marion and Kargel, 2008). For gypsum solubility, there are 7 critical Pitzer equation parameters that are used to derive $\gamma_{Ca^{2+}}$ (Marion and Farren, 1997), which are estimated for sub-zero temperatures from limited gypsum solubility data (Spencer et al., 1990; Marion and Farren, 1997). Further to the scarcity of gypsum solubility data at sub-zero temperatures, the difficulty in obtaining $K_{sp,gypsum}$ in these conditions is complicated due to its sparing solubility (Marion and Farren, 1997, 1999), resulting in a dependence upon extrapolation from

measurements carried out at warmer temperatures (Marion and Farren, 1997; Marion and Kargel, 2008). At this stage, attributing the discrepancies in modelled and measured gypsum solubility specifically to $\gamma_{Ca^{2+}}$ or $K_{sp,gypsum}$, would require further experimental investigation. Related work would aid in improving model predictions of gypsum solubility in sea ice brines and other cryospheric environments.

6.4.2 Gypsum dynamics in metastable mirabilite supersaturation

When seeded with gypsum, brines exhibiting metastable mirabilite supersaturation at −7.1 °C ($\Omega_{mirabilite} = 1.252$) and −8.2 °C ($\Omega_{mirabilite} = 1.717$) precipitated gypsum by 3.7 ± 0.14 mmol kg_{sol}^{-1} ($\Omega_{gypsum} = 1.171$) and 7.54 ± 0.47 mmol kg_{sol}^{-1} ($\Omega_{gypsum} = 1.358$), respectively. Such degrees of supersaturation would be expected upon extrapolating the trend observed in Ω_{gypsum} between −1.8 and −6.0 °C (figure 6.2, cross markers). These results imply that if mirabilite precipitation is inhibited by a limitation of suitable nucleation sites within sea ice brine inclusions, then gypsum may precipitate if appropriate seed is available. Although gypsum precipitation can occur upon appropriate seeding in these conditions, once mirabilite precipitation is initiated, the composition returns to the equilibrium solubilities displayed in figure 6.1 and table 6.2. This suggests that, if gypsum precipitation occurs via this mechanism in natural sea ice, then its presence may be transient. Ultimately this mechanism of gypsum precipitation is contingent with the availability of suitable seed to promote either mirabilite or gypsum precipitation within sea brine inclusions. These properties cannot be inferred based on the lack of understanding of mineral nucleation at the microscale of sea ice brine inclusions.

6.4.3 Hydrohalite-mirabilite-gypsum interaction

As outlined in section 6.4.1, a substantial shift in solution composition would have to arise in order for gypsum to reach saturation in sea ice brines, based on solubility measurements between 0.2 and −22.2 °C. Measurements indicate that this shift is provided upon the onset of hydrohalite precipitation. The precipitation of hydrohalite is associated with substantial freezing of the solution (Butler and Kennedy, 2015). The combination of physical concentration of the brine and hydrohalite precipitation results in a very different overall solution composition (table 6.4), par-

ticularly with respect to Na^+, K^+, Mg^{2+} and Ca^{2+}. Our experiments at −23.7 and −25.0 °C indicate that the change is sufficient to supersaturate the brine with respect to gypsum to a small extent ($\Omega_{gypsum} = 1.070$ at −23.7 °C, and 1.083 at −25.0 °C). Furthermore, the associated reduction in $[Na^+]_T$ undersaturates the brine with respect to mirabilite, which, if available to the brine, dissolves. Our experiments that seeded this undersaturated brine with mirabilite resulted in similar observations to that of Marion et al. (1999), whereby the SO_4^{2-} liberated through mirabilite dissolution accelerated the precipitation of gypsum markedly. Measurements of gypsum precipitation resulting from this process yielded estimates of Ω_{gypsum} equivalent to 1.266 at −23.7 °C and 2.264 at 25.0 °C, precipitating gypsum in concentrations of 24.09 and 80.44 mmol kg_{sol}^{-1}, respectively.

The main limitation in relation to this dynamic is that the precipitation of gypsum is highly dependent on the availability of mirabilite to the brine, the rate at which it can dissolve, and the rate at which gypsum can then precipitate. Given the cold temperatures and slow kinetics of SO_4^{2-} minerals (Kargel, 1991; Hogenboom et al., 1995; Marion and Kargel, 2008), these reactions were observed to occur over weeks, even with regular mixing and excess seed. Furthermore, considerable experimental manipulation was required in order to study this dynamic, which mainly relates to ways in which ice and hydrohalite fill the brines inclusions with a heterogenous mixture at these temperature. To fully examine the behaviour of hydrohalite and ice, and the consequent likelihood of hydrohalite-mirabilite-gypsum interaction being facilitated in sea ice, the measurements of hydrohalite solubility must first be discussed.

Table 6.4: FREZCHEM predictions of brine composition before (−22.8 °C) and after (−26.0 °C) hydrohalite precipitation, with mineral interaction disabled.

	−22.8 °C	−26.0 °C
Ion	$S_A = 229.71$ g kg_{sol}^{-1}	$S_A = 232.53$ g kg_{sol}^{-1}
% Na^+	30.56	19.56
% K^+	1.27	2.88
% Mg^{2+}	4.10	9.25
% Ca^{2+}	1.33	2.99
% Cl^-	62.13	64.26
% SO_4^{2-}	0.61	1.06

6.4.4 Hydrohalite solubility

The excellent agreement between our measurements of $pK^*_{\text{sp,hydrohalite}}$ and the predictions from the FREZCHEM model is testament to the models accuracy in computing γ_{Na^+}, γ_{Cl^-}, a_w and $K_{\text{sp,hydrohalite}}$ in the experimental conditions of this investigation. All experimental (Gitterman, 1937; Nelson and Thompson, 1954) and model (Marion et al., 1999; Marion and Kargel, 2008) evidence is in agreement that hydrohalite precipitates $\leqslant -22.9$ °C in sea ice, however its dynamics in undersaturated sea ice brines have never been considered. Between −14 and −26 °C hydrohalite displays two distinct phases with respect to $pK^*_{\text{sp,hydrohalite}}$ (figure 6.3) and $\Omega_{\text{hydrohalite}}$ (figure 6.4). The first phase occurs in the undersaturated region, and the second in the supersaturated region. The observed changes can be allocated to individual changes in $[Na^+]_T$ and $[Cl^-]_T$ (figure 6.6). Based on the $[Cl^-]_T$ between −14 and −22.8 °C (figure 6.6, bottom), hydrohalite decreases in solubility by approximately 145 mmol kg^{-1}_{sol}. The reduction in $[Na^+]_T$ within this temperature range (figure 6.6, top) equates to 568 mmol kg^{-1}_{sol} because the data are implicit of mirabilite precipitation and the consequent removal of Na^+. The reduction in hydrohalite solubility in the undersaturated brines, combined with the physical concentration of the solution between -14 and −22.8 °C, results in less hydrohalite needing to dissolve in order to attain saturation, hence $\Omega_{\text{hydrohalite}}$ increases from 0.454 to 0.999.

Upon cooling below −22.9 °C the brines precipitate hydrohalite, resulting in rapid inflections in the $pK^*_{\text{sp,hydrohalite}}$ (figure 6.3) and $\Omega_{\text{hydrohalite}}$ (figure 6.4). The abrupt change is reflected in the rate at which hydrohalite precipitates in a closed frozen seawater system (from a starting S_A of 35.165 g kg^{-1}_{sol}). By −23.0 °C hydrohalite is present in concentrations of 5.5 g kg^{-1} (figure 6.7). Upon cooling to −26.0 °C this increases to 30.5 g kg^{-1}. Such rapid precipitation would not be expected based on the changes in $\Omega_{\text{hydrohalite}}$ in the undersaturated region (figure 6.4). Evidence instead indicates that hydrohalite precipitates as an ice-hydrohalite eutectic aggregate (Light et al., 2009; McCarthy et al., 2007; Butler and Kennedy, 2015).

Prior to the onset of hydrohalite precipitation, Na^+ and Cl^- comprise 92.7 % of the total weight of dissolved ions in the brine (table 6.4), therefore the changes that occur upon its precipitation are analogous to a binary $NaCl-H_2O$ close to its eutectic composition (McCarthy et al., 2007). Upon the initial onset of hydrohalite

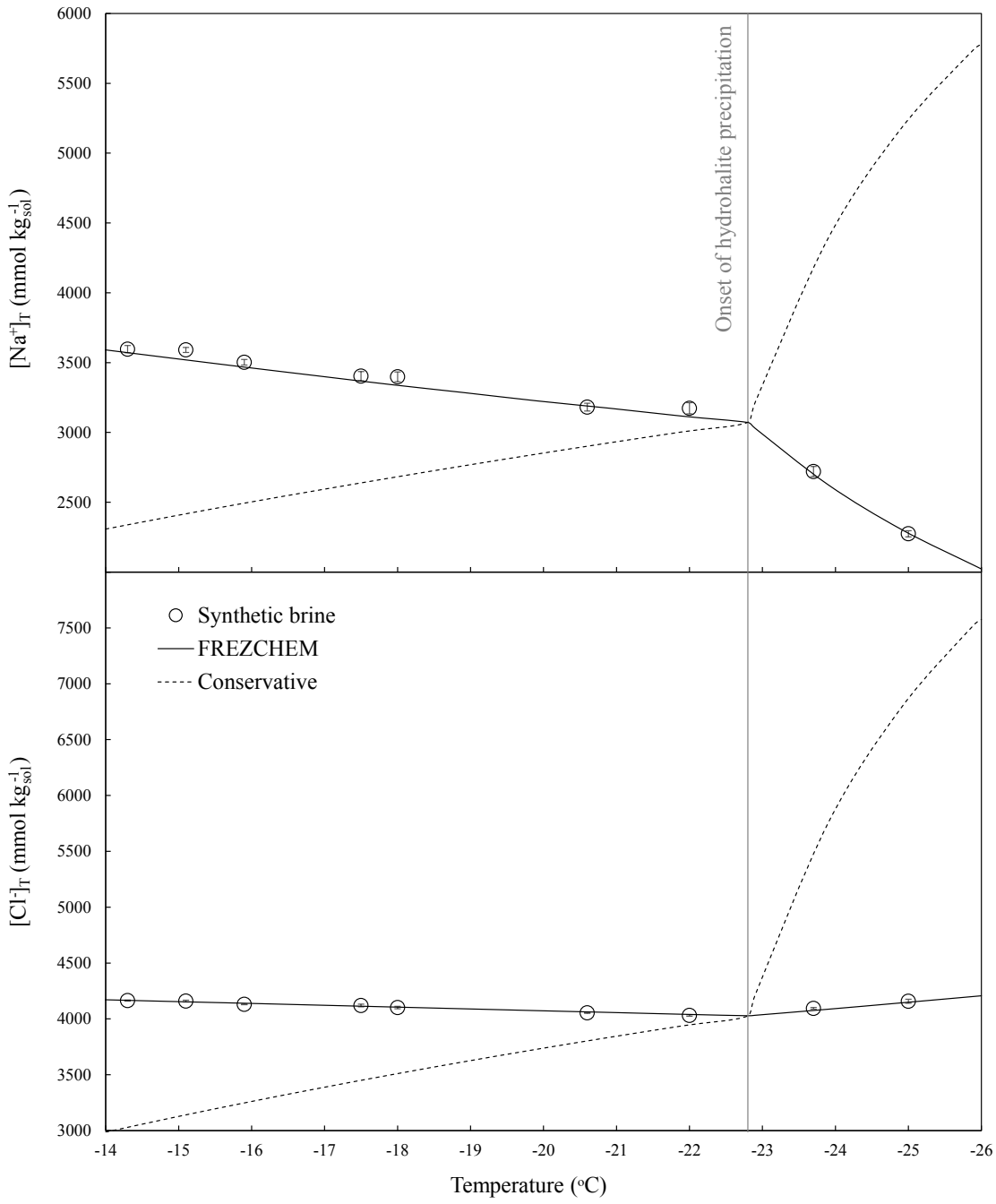

Figure 6.6: $[Na^+]_T$ and $[Cl^-]_T$ in equilibrium sea ice brines. The vertical line at -22.8 °C marks the point of which the concentrations begin to become affected by precipitation of hydrohalite. The dashed line represents the estimated concentration based on a conservatively concentrated solution in absence of hydrohalite dissolution or precipitation.

precipitation, the reduced ionic strength of the brine from removal of Na^+ and Cl^- promotes ice formation, which concentrates the brine in response to its increased freezing point. Concentration of the brine then results in further hydrohalite precipitation. This process propagates the formation of both solid phases, whilst the volume of remaining brine diminishes. Between −22.9 and −26 °C in a closed seawater system (1 kg of Standard Seawater, $S_A = 35.165$ g kg_{sol}^{-1}), there is an increase in ice formation by approximately 50 g (Butler and Kennedy, 2015), which crucially decreases the amount of liquid water remaining in the ice from 105 to 41 g (figure 6.8). In sea ice, this would equate to a reduction in brine volume by more than 60 % within 3 °C.

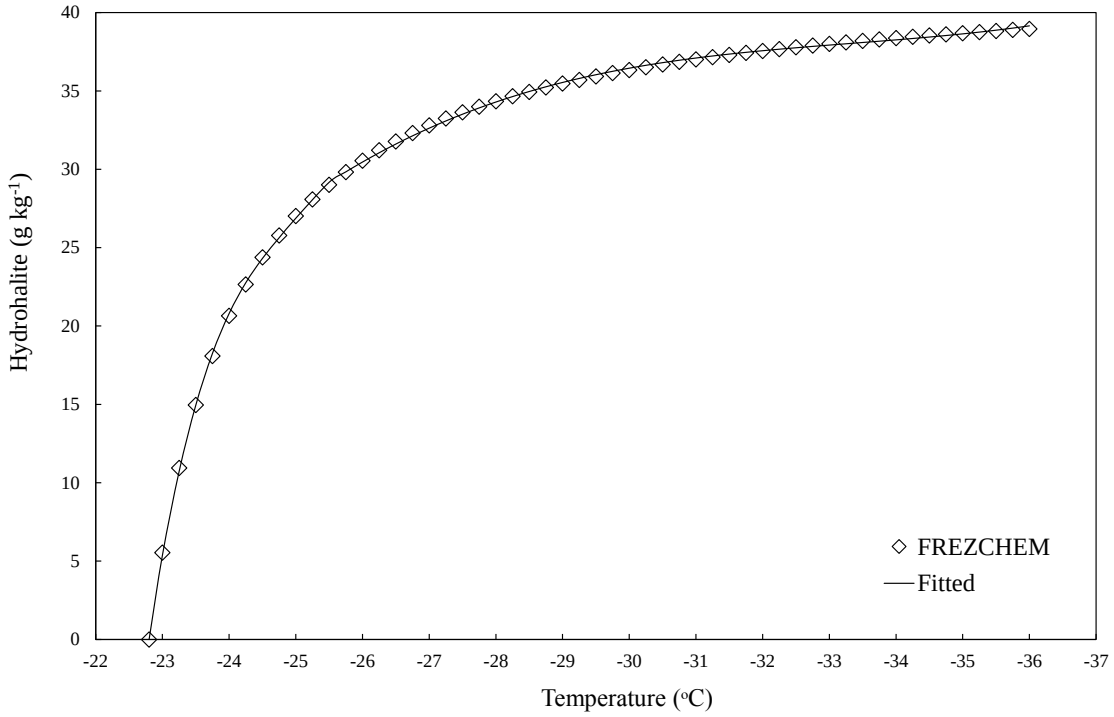

Figure 6.7: The weight of hydrohalite predicted to precipitate from 1 kg of seawater ($S_A = 35.165$ g kg_{sol}^{-1}) between −22.9 and −36 °C. Also plotted is the fitted relationship of hydrohalite concentration (g kg^{-1}) as a function of temperature (using equation 6.2) described by coefficients given in table 6.1.

If hydrohalite precipitation in sea ice occurs via a mechanism comparable to the formation of a eutectic aggregate, then the properties of brines pockets in sea ice below −22.9 °C may be analogous to those studied in binary $Na-Cl-H_2O$ solutions of eutectic composition (McCarthy et al., 2007). Within our experiments at −23.7 and −25.0 °C, white irregular flocs of crystals were observed to form upon cooling

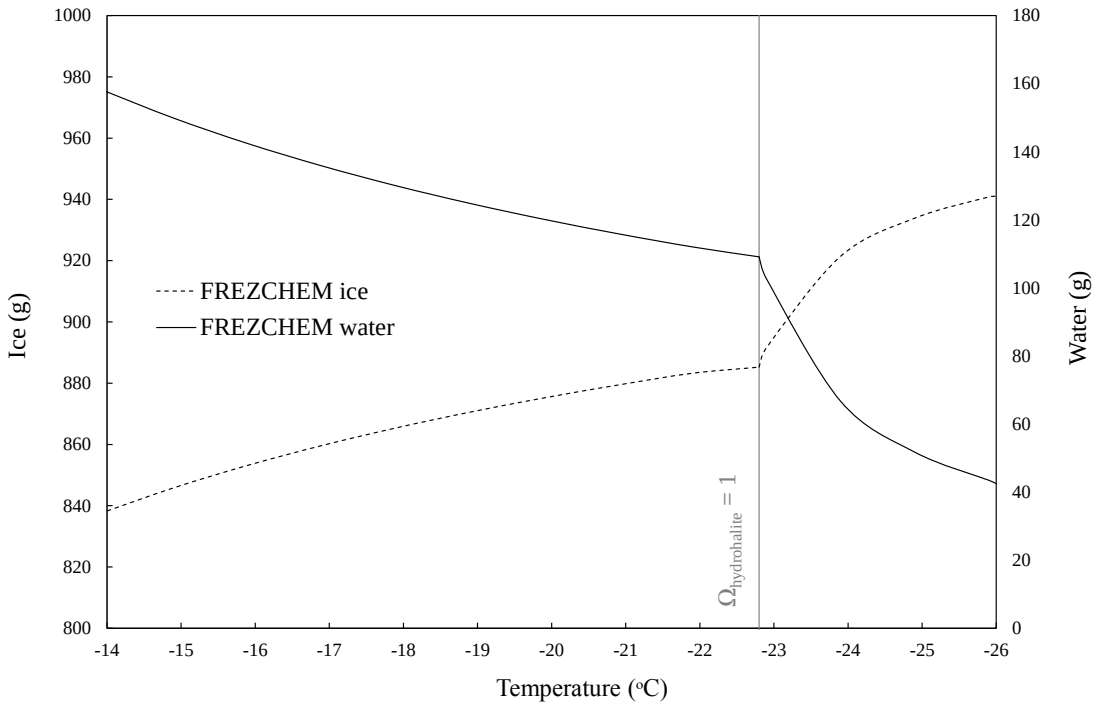

Figure 6.8: FREZCHEM predictions of the change in ice and water content in 1 kg of frozen seawater between −14 and −26 °C The vertical line at −22.8 °C marks the point of which the system begins to become affected by precipitation of an ice-hydrohalite aggregate.

the brine to its target temperature, which floated towards the surface. Once cooled to the surrounding conditions, the flocs had grown to effectively fill the bottle, displaying a mottled bright white colouration concurrent with available observations of hydrohalite (Nelson and Thompson, 1954; Assur, 1960; Light et al., 2009). The phase that formed trapped brine within its own microstructure, making sampling of remaining solution increasingly difficult. These observations correspond to the description of eutectic aggregates from binary systems (McCarthy et al., 2007), which, firstly, can be less dense than the surrounding solution. It is feasible that when ice forms in close association with hydrohalite (Light et al., 2003, 2009), the density of ice (0.92 g cm^{-3} (Cox and Weeks, 1988)) could be sufficient to offset the density of hydrohalite (1.63 g cm^{-3} (Light et al., 2009)) compared to that of the brine (1.20 g cm^{-3} at −30 °C, FREZCHEM), resulting in positive buoyancy. Further to this buoyancy, the microstructure of eutectic aggregates is understood to be quite different to that of a single solid. The phases are understood to form cooperatively as a fine intergrowth of the mineral and ice phases in regular, repeating lamellae

(McCarthy et al., 2007; Croker et al., 1975a,b). The microstructure of the lamellae are then understood to effect the mechanical response of the solid. If the lamellae are prevented from forming by disturbing their formation (e.g. by mixing), then the strength of the aggregate does not differ to that of pure ice (Durham et al., 2005). In contrast, undisturbed samples of eutectic aggregates are understood to be significantly more absorbing of mechanical energy and display a greater stiffness (McCarthy et al., 2007). In relation to sea ice, the combination of the structural properties of a eutectic aggregate, combined with a 60 % reduction in brine volume of the ice within 3 °C, could result in changes to the mechanical properties of sea ice in the region of hydrohalite precipitation (Assur, 1960; Weeks, 2010).

With respect to the hydrohalite-mirabilite-gypsum interaction during equilibrium crystallisation (Marion et al., 1999; Butler and Kennedy, 2015), the mechanism of hydrohalite precipitation and its association with ice may act as a hindrance. Mirabilite crystals are understood to sink to the bottom of brine inclusions (Light et al., 2003), however when hydrohalite forms as a eutectic aggregate, it fills the pore space and consequently restricts the volume of brine available for mirabilite to interact with. Furthermore, positive buoyancy of an ice-hydrohalite aggregate within the brine inclusion, may separate it from the mirabilite crystals below as it forms. The result is a microstructure with very limited mixing and surface area for brine and mineral interaction, acting to limit the dissolution of mirabilite and consequent precipitation of gypsum. Although hydrohalite-mirabilite-gypsum interaction was observed by Butler and Kennedy (2015), the experimental protocol required continual spinning of the sample, which may have promoted mineral interaction by mixing the brine and minerals as the sample warmed and cooled. Testing the effect of sample mixing on mineral interaction *in-situ* would help develop the understanding of these processes within sea ice, which can result in substantial changes to the geochemistry of the system (Nelson and Thompson, 1954; Gitterman, 1937; Marion et al., 1999; Butler and Kennedy, 2015).

To relate the described dynamics of hydrohalite from laboratory experiments and thermodynamic models to that of natural sea ice, the hydrohalite solubility data has been incorporated into a 1D model describing the growth and desalination of first-year sea ice.

6.4.5 Hydrohalite modelling in first-year sea ice

The FREZCHEM model output of the weight of hydrohalite to precipitate in a 1 kg parcel of frozen seawater (figure 6.7) was fitted to a stepwise polynomial function of temperature (table 6.1, rows 11 and 12). This data was integrated into a 1D model (via equation 6.4) describing the temperature and salinity profiles of first-year sea ice in the Arctic Basin as it grows over winter months, and the distribution of hydrohalite within it (figure 6.9).

The temperature at the surface of the modelled ice pack drops below −22.9 °C after 1 month from the onset of freezing. At this point (early November), the ice pack is 73.5 cm thick, and the incoming shortwave radiation for the region is 0 W m^{-2}. Between the start of November and end of February, the modelled ice pack thickens to 210 cm, while the surface temperature decreases to −32.1 °C. Given the absence of sunlight and low temperatures, these conditions likely represent the most challenging and least studied aspects of Arctic sea ice dynamics.

As the ice pack thickens and the surface temperature decreases, the modelled hydrohalite concentration increases (figure 6.9). When the ice pack is 75 cm thick, hydrohalite is only present in the upper 1 cm, however as the winter progresses, the occurrence of hydrohalite deepens, and by mid-February when the ice is over 2 m thick, hydrohalite is present within the upper 65 cm. The depth distribution of hydrohalite in the ice is governed by the temperature (assumed linear between the surface and ocean) and salinity profiles (figure 4.6). As a result of these two forcings, hydrohalite develops towards an 'S' shaped depth profile as the ice pack grows, reaching a maximum concentration of 10.3 g kg^{-1}, comprising up to 1.03 % of the total weight of sea ice.

Given the rapid precipitation of hydrohalite between −22.9 and −26 °C (figure 6.7), its presence within sea ice could display considerable daily or localised fluctuations (precipitation and dissolution) due to local weather patterns. Such high resolution dynamics, however, cannot be accounted for with this idealised model. Given that hydrohalite precipitation did not initiate within the modelled ice pack until incoming shortwave radiation had reduced to 0 W m^{-2}, its contribution to the albedo feedback mechanism (Light et al., 2004; Carns et al., 2015) in polar environments seems limited, and is likely to be more relevant to the energy balance of

'Snowball Earth' during the Neoproterozoic (Light et al., 2009; Carns et al., 2015). Furthermore, the winter conditions in which hydrohalite precipitates likely hinder its identification in the field by researchers, and add to the difficulty in examining its dynamics in the sea ice system.

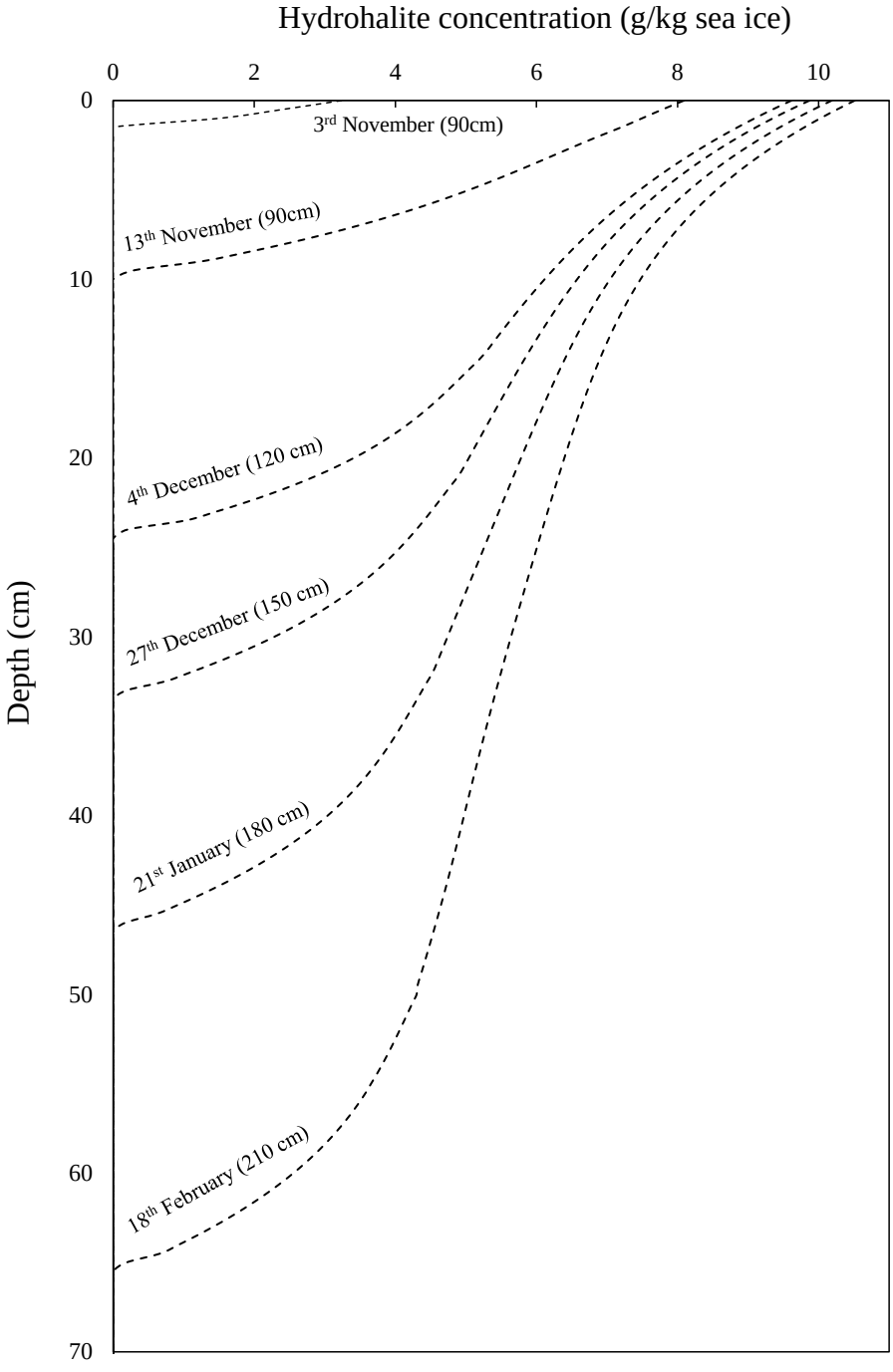

Figure 6.9: Modelled hydrohalite concentrations during the formation of first-year snow-free sea ice in the Arctic Basin. The full depth of the ice pack is not displayed, but is instead annotated at each increment.

6.4.6 The existence of gypsum in sea ice

The available mirabilite (Butler et al., 2016), gypsum and hydrohalite solubility data can be related to the existence of gypsum in sea ice. When Ca^{2+} and SO_4^{2-} occur together in aqueous solutions, it is generally expected that precipitation of a calcium sulphate mineral will result (Azimi et al., 2007). However, in sea ice, this expectation is complicated by the dynamics of minerals that precede and succeed the possible scenarios in which gypsum may precipitate. The tendency of gypsum formation is severely constrained by mirabilite precipitation at temperatures $\leqslant -6.4$ °C, and highly dependent on mirabilite dissolution $\leqslant -22.9$ °C.

Our measurements of gypsum undersaturation between 0.2 and −22.2 °C (section 6.4.1 and figure 6.2) are contrary its identification in experimental (at the Sea-ice Environmental Research Facility (SERF)), and natural (North East Greenland) sea ice described by Geilfus et al. (2013). Within their investigation, ice was sampled at temperatures between −1.9 and −10 °C, and upon careful extraction by melting of the samples, gypsum was observed as elongated crystals up to 100 μm long. The gypsum crystals were distributed throughout the ice pack, and were observed within hours of initial sea ice formation. The observation of gypsum at temperatures as high as −1.9 °C conflicts with our measured and modelled gypsum solubility at this temperature, which show that gypsum is undersaturated by approximately 18 mmol kg_{sol}^{-1} ($\Omega_{gypsum} = 0.25$). Furthermore, the gypsum crystals identified in experimental sea ice at SERF, formed during the freezing of synthetic seawater that was deficient in Ca^{2+} and SO_4^{2-} by 17 % and 40 %, respectively, relative to Standard Seawater (Geilfus et al., 2013; Millero et al., 2008). The deficiency of this solution with respect to the ions that constitute gypsum would only act in impeding its approach to saturation.

In light gypsum solubility measurements presented here, we propose three mechanisms to explain the identification of gypsum in experimental and natural sea ice. The first relates to its precipitation in metastable conditions of mirabilite supersaturation, which could result in a transient presence of gypsum in sea ice (section 6.4.2) given suitable seed to nucleate gypsum in favour of mirabilite. The second relates to the brief storage ($<$ 4 hours) of sea ice samples at −25 °C prior to analysis carried out by Geilfus et al. (2013). At this temperature gypsum can precipitate

in sea ice brines in low concentrations, whilst elevated concentrations could form if mirabilite-hydrohalite-gypsum interaction is facilitated. Finally, the gypsum crystals that were observed in experimental and natural sea ice may not be authigenic, and could instead derive from external sources. Gypsum is a common mineral observed in aerosol particles (Prospero et al., 1981; Schütz and Sebert, 1987; Zimmermann et al., 2008), the deposition of which is understood to be the source of its identification in ice cores taken from the Greenland Ice Sheet (Biscaye et al., 1997; Steffensen, 1997). Gypsum can persist in an ice sheet due to its sparing solubility in aqueous solutions (Steffensen, 1997) combined with the general property of solid-solid (i.e., gypsum-ice) solubility being extremely limited (McCarthy et al., 2007). Therefore, if gypsum aerosols settle on sea ice and become encapsulated by pure ice, rather than a brine inclusion, then they may be sufficiently stable to allow for extraction and identification even when the conditions in the brine pockets are undersaturated with respect to gypsum.

In summary- gypsum displays complex dynamics in the sea ice system compared to that of mirabilite and hydrohalite. Despite detailed solubility data and its identification in the field, the processes relating to its existence and persistence in sea ice require additional investigation, particularly if the proposition of gypsum as a marine deposit in polar seas is to be pursued further.

6.5 Conclusions

Determination and discussion of gypsum and hydrohalite solubilities in equilibrium sea ice brines has revealed the dynamics of each mineral within the sea ice system. Gypsum displays particularly complex changes in solubility throughout the polar temperature spectrum from 0.2 to -25.0 °C, and the tendency for its precipitation is severely hindered by the dynamics of mirabilite $\leqslant -6.4$ °C, which acts as the dominant SO_4^{2-} sink in sea ice. Gypsum precipitation is therefore largely dependent upon either metastable conditions of mirabilite supersaturation between at ~ -7 to -8 °C, or mirabilite dissolution upon the onset of hydrohalite precipitation. The solubility of hydrohalite contrasts greatly to that of gypsum, displaying distinct changes between the undersaturated and supersaturated regions, with its precipitation initiating at -22.9 °C. The rapid precipitation of hydrohalite would

not be predicted based on the rate at which it approaches saturation between −14 and −22.8 °C, and is instead explained as a process analogous to the formation of a eutectic aggregate. During this process, ice and hydrohalite form cooperatively as an intergrowth, likely displaying similar properties to eutectic aggregates from binary systems (McCarthy et al., 2007). The heterogeneous mixtures fills the brine inclusions, resulting in sudden compositional changes to the little brine that remains, and affecting the microstructure of the ice substantially.

Modelling of gypsum and hydrohalite solubilities with the FREZCHEM code shows contrasting accuracy. Gypsum solubility is consistently underestimated by the FREZCHEM model, with discrepancies in $[Ca^{2+}]_T$ reaching at 25.33 mmol kg_{sol}^{-1} at −22.2 °C. Measured and modelled hydrohalite solubilities display excellent agreement (within experimental error), and the model output was therefore used to predict to weight of hydrohalite that would precipitate from 1 kg of Standard Seawater. Incorporating these weights into a 1D model for the growth of Arctic sea ice, shows that hydrohalite concentrations in the ice pack are concentrated towards the surface, reaching up to 10 g kg^{-1}, and extending down to a depth of 65 cm. The onset of hydrohalite precipitation in the modelled ice pack occurs once the incoming shortwave radiation to the region drops to 0 W m^{-2} limiting any effects that hydrohalite may have upon the albedo of sea ice. The interest in hydrohalite as an authigenic mineral ice is therefore more related to its effects on the physical properties of the ice, which remain far for clear. Despite the comprehensive assessment of gypsum solubility in a large range of brine compositions and temperatures, its complex dynamics still require further investigation to elucidate its potential as a marine deposition in polar seas.

Chapter 7

Discussion and outlook

The work presented in this thesis has aimed to refine the understanding of mineral dynamics in sea ice based on the laboratory investigations described in the previous 4 chapters. In this chapter, the results from all 4 investigations are synthesised and discussed in relation to the objectives outlined in section 1.4. The discussion is combined with an assessment of the limitations of this work, and outlines potential directions for future research in sea ice geochemistry.

7.1 Equilibrium and fractional crystallisation in sea ice

The two paradigms that are often used to describe the mineral sequence precipitated during seawater freezing to its eutectic, the Gitterman and Ringer-Nelson-Thompson Pathways (section 1.3), are assigned to represent processes of equilibrium and fractional crystallisation, respectively (section 3.1). The significance between equilibrium and fractional crystallisation relates not only to the sequence of minerals that precipitate during freezing, but also to the temperature at which seawater reaches its eutectic (table 1.1). Though both forms of crystallisation are feasible, there was an absence of *in-situ* evidence for either process.

The investigation carried out in chapter 3, which used synchrotron X-ray powder diffraction to identify mirabilite and hydrohalite in seawater brines exposed to warming and cooling experiments, provided direct measurement of equilibrium crystallisation. The results from this investigation are the first crystallographic evidence of mirabilite and hydrohalite in frozen seawater brines, and, crucially, the first evidence of their interaction. Mineral interaction occurs upon hydrohalite precipitation,

where the removal of Na^+ from the brine results in undersaturation with respect to mirabilite. The observations support the Gitterman Pathway for seawater freezing, therefore indicating that sea ice can undergo equilibrium crystallisation. This process has implications for the existence of gypsum in sea ice, though the experiments were unable to identify its presence within the frozen brines.

Several reasons were initially proposed (section 3.4.2) for the absence of gypsum in the frozen samples, that included: detection limits of the instrument, time constraints on the experiment, and the possibility that gypsum remained undersaturated within the brines. The measurement of gypsum solubility in chapter 6 aided in this interpretation with respect to the time constraints and gypsum undersaturation theories. The solubility studies at -23.7 and -25.0 °C showed that gypsum could precipitate in response to a hydrohalite-mirabilite interaction in sea ice, this required experimental manipulation of the brines with appropriate seeding, in addition to the reactions occurring over the order to weeks. Therefore, though the results in chapter 3 provide clear evidence for hydrohalite-mirabilite interaction, the additional interaction with gypsum still remains unclear in the context of a sea ice microstructure.

The experimental protocol employed in chapter 3 has limitations that can be advanced upon through future research. The first limitation relates to the use of concentrated seawater brines, which had salinities approximately 2.9 and 3.8 times higher than Standard Seawater. The identification of mirabilite and hydrohalite in the experiment may not have been possible without the use of these concentrated solutions, however the microstructure of the frozen phase in the experiments may have displayed a greater brine volume fraction than samples with salinities in the oceanic range ($\sim$35). A greater brine volume could act to promote mineral interaction within the frozen microstructure due to a greater porosity, though this remains untested. Further to the use of concentrated solutions, the instrument used for the experiments required the sample to be spinning at all times to enhance the diffraction patterns. Whether or not spinning of the sample acted to promote mineral interaction remains unknown, but could be tested using similar experimental protocols.

A potential direction for future research into the crystallisation properties of sea

ice concerns the mineral assemblage at the systems eutectic. The minimum temperature investigated in the experiments in chapter 3 was −40 °C, which according to all known predictions, should result in the precipitation of relatively high concentrations of $MgCl_2 \cdot 12H_2O$ (figure 3.5). The absence of $MgCl_2 \cdot 12H_2O$ in these experiments (section 3.4) is therefore a possible area for further investigation, in particular relation to its precipitation and the eutectic temperature of seawater. A potential hypothesis relating to this is the possibility that the low temperature and restricted pore space causes minerals to precipitate as amorphous glasses. Amorphous phases have been described for aqueous solutions relevant to Mars (Toner et al., 2014), and because they do not have a crystalline structure, would not be directly detected by X-ray powder diffraction. If amorphous phases did precipitate in sea ice, then their detection using this technique could instead be inferred through changes in ice formation rate, as was observed for hydrohalite in figure 3.6 and section 3.4.2.

7.2 Mineral solubilities and dynamics in sea ice brines

This thesis has comprehensively investigated the solubilities of mirabilite, gypsum and hydrohalite in sea ice brines at thermal equilibrium, and related the measurements to the dynamics of each mineral in the environment. The measurement of mirabilite solubility (chapter 4) determined that mirabilite becomes supersaturated in sea ice brines at -6.38 ± 0.07 °C, and is likely to have a near ubiquitous presence in first year sea ice. Mirabilite displays particularly large changes in solubility with temperature compared to of gypsum and hydrohalite. As a result, 92 % of SO_4^{2-} is removed as mirabilite by −20.6 °C, which has profound consequences on the dynamics of gypsum. The removal of SO_4^{2-} from the brine during mirabilite precipitation is also proposed to affect the measurement of pH on the total and seawater proton scales (section 4.4.1), which is a potential direction for future research in sea ice brine geochemistry. The solubility measurements were used to propose that the absence of mirabilite identification in the field is due to its rapid increase in solubility upon warming above −6.38 °C, combined with low concentrations that would be difficult to identify even with the most powerful X-ray facilities in the

world (section 4.4.1). At present, methods used for extracting minerals from sea ice involve careful melting of the ice (Dieckmann et al., 2008; Geilfus et al., 2013; Fischer et al., 2013), which has resulted in successful extraction of sparingly soluble minerals such as ikaite and gypsum, but would not be suited for highly soluble minerals like mirabilite and hydrohalite.

Similarly to mirabilite, the measurement of hydrohalite solubility (chapter 6) showed excellent agreement with the FREZCHEM model computation. All model predictions and laboratory measurements of hydrohalite precipitation are in agreement that it initiates at −22.9 °C. Modelling hydrohalite precipitation during the formation of first year sea ice indicated that it may not precipitate until the incoming shortwave radiation to the region approaches 0 W m^{-2} (section 6.4.5), which limits any effects that it may have upon the albedo of sea ice despite concentrations at ice surface reaching 10 g kg^{-1} (Light et al., 2004, 2009; Carns et al., 2015). The significance of hydrohalite in sea ice therefore relates to its *in-situ* physical and chemical properties. Evidence indicates that an ice-hydrohalite eutectic aggregate fills the brine inclusions (section 6.4.4) at temperatures below −22.9 °C. The little brine that remains develops a substantially different composition from the standard stoichiometry of seawater (table 5.1), and ends up encapsulated within the pore space of the eutectic aggregate. Sympagic biota that are subjected to this process would therefore experience large changes in osmotic conditions of the brine, as well as further restrictions on available space within the microstructure. These aspects of hydrohalite precipitation, combined with the changes that may result to the physical properties of sea ice, remain unexplored and therefore represent a potential direction for future investigations.

Through measurements of its solubility in a range of sea ice brine conditions, gypsum dynamics have been shown to display a high dependence on that of mirabilite and hydrohalite. Between 0.2 and −22.2 °C gypsum is undersaturated in sea ice brines (section 6.4.1). If mirabilite is inhibited from forming at temperatures below −6.4 °C, then gypsum would be expected to precipitate, however the rapid change in mirabilite solubility relative to gypsum greatly hinders the chances of gypsum precipitation in sea ice. Upon hydrohalite precipitation the shift in brine composition (table 6.4) is sufficient to undersaturate the brine with respect to mirabilite,

and slightly supersaturate it with respect to gypsum. If mirabilite dissolution is facilitated, then gypsum precipitation can be greatly accelerated via the liberated SO_4^{2-}. The pressing question with respect to this interaction, is whether the structure of the brine inclusion in the presence of an ice-hydrohalite eutectic aggregate is a suitable setting to promote this process, which remains unresolved.

Interpreting the gypsum solubility data holistically in the range of brine conditions studied, indicates that it has a low likelihood of precipitating and persisting in sea ice. This observation is contrary to the successful extraction and identification of gypsum crystals in experimental and natural sea ice by Geilfus et al. (2013). Within the temperature range that gypsum was identified (-1.9 to -10.0 °C), the only mechanism to explain its formation would relate to its precipitation in solutions that remained in a metastable supersaturated state with respect to mirabilite (section 6.4.2). However, given the transient nature and confined temperature of this scenario, it does not explain the existence of gypsum throughout the ice pack. Again, this knowledge gap could provide scope for further investigation with laboratory and field investigations.

The FREZCHEM model has been to shown to accurately compute mirabilite and hydrohalite equilibria in sea ice brines, and is therefore a powerful tool in enriching the study of their dynamics in this environment. In contrast, the model is consistently inaccurate in its prediction of gypsum equilibria. This inaccuracy is assigned to either the computation of $\gamma_{Ca^{2+}}$ via the Pitzer formalism, or the thermodynamic solubility product of gypsum ($K_{sp,gypsum}$) that is described as a function of temperature (section 6.4.1). Further refinement of the parameters used to compute $\gamma_{Ca^{2+}}$ and $K_{sp,gypsum}$ in the FREZCHEM code could improve its accuracy in determining gypsum dynamics in sea ice, in-line with its computation of mirabilite and hydrohalite.

The main limitation with respect to solubility measurements and modelling with FREZCHEM, is that they are not designed to account for the length of time required for attainment of mineral-solution equilibrium. To determine the rates at which minerals dissolve and precipitate within sea ice requires experiments specifically designed to measure reaction kinetics (Papadimitriou et al., 2014). There is tentative information about the rate at which hydrohalite and mirabilite precipitate/dissolve

in section 3.2.2, indicating that mirabilite may display slower kinetics than hydrohalite. The methods used for the investigation in chapter 3 could therefore be well suited for a more detailed assessment of *in-situ* mirabilite and hydrohalite kinetics, which would provide valuable information that can be used to better understand their existence and persistence in the environment.

7.3 Sea ice brine salinity

The evaluation of practical and absolute salinity measurements in sea ice brines (chapter 5) has proven that the practical salinity scale is, understandably, unsuitable for the direct measurement of sea ice brines affected by mirabilite precipitation. The observation of practical salinity deviating from absolute salinity when mirabilite precipitates in sea ice brines indicates that the validity of practical salinity measurements in these conditions requires consideration. Given the ease with which conductivity can be measured compared to the analysis required to quantify absolute salinity, measurement of sea ice brines on the practical salinity scale will unquestionably continue to dominate salinity measurements in laboratory and field investigations. To therefore facilitate an accurate measurement of absolute salinity whilst maintaining the practical advantages of conductivity measurement, a conversion factor has been formulated that can estimate absolute salinity from practical salinity in sea ice brines (equations 5.13 and 5.14). The potential effects of other mineral precipitates, such as ikaite (Papadimitriou et al., 2013) or hydrohalite, on sea ice brine salinity concepts, would require further investigation to define.

Since the salinity of sea ice brines is such a crucial variable for determining physical sea ice parameters, and is a primary environmental constraint imposed upon sympagic biota, defining it accurately is of particular importance. Measurements of brine salinity are typically carried in volumes ranging from millilitres to litres, and therefore $S - T_{fr}$ equations (section 5.4) reflect this. When compared to the microlitre volume of individual brine inclusions, the effectiveness of these equations for calculating the *in-situ* sea ice salinity as a function of temperature is, however, unknown. Furthermore, extracellular organic substances produced by micro-organisms within sea ice may affect the accuracy of empirical $S - T_{fr}$ relationships in sea ice, which again would require investigation on the micrometer scale of individual brine

inclusions.

7.4 Confounding factors and future directions

This thesis has applied laboratory investigations to further the understanding of mineral dynamics in natural sea ice. Despite the greater accuracy and precision of laboratory measurements, a natural sea ice brine system has greater complexity than the experiments used throughout this work. For this reason, the confounding factors that may hinder easy application of the experiments to natural sea ice environments must be identified.

7.4.1 Equilibrium and nucleation assumptions

The first caveat relates to the temperature regime of sea ice and the current assumption that sea ice brines exist at thermal and chemical equilibrium. The prerequisite of solubility measurements is that they are carried out at solution-mineral equilibrium, and throughout sea ice brine research it has always been assumed that this condition is met (Assur, 1960; Cox and Weeks, 1986; Papadimitriou et al., 2013). Tentative data on the temperature variability within sea ice provided in figure 1.7, indicates that daily temperature fluctuations 10 cm below the ice surface may be in the region of 0.60 ± 0.44 °C (Ewert and Deming, 2013). This temperature variability within the ice column would decrease towards the ice-ocean interface, where it remains near constant at the freezing point of the underlying seawater. These relatively small temperature fluctuations, combined with the microscopic volumes of brine contained within individual inclusions (Light et al., 2003), likely means that the assumption of thermal equilibrium is justified. However, the time and conditions required to attain brine-mineral equilibrium in sea ice are currently undefined for mirabilite, hydrohalite and gypsum, and cannot be accounted for with this investigation. Measurement of mineral dissolution and precipitation kinetics in sea ice brines (Papadimitriou et al., 2014) would provide valuable information on the time required for sea ice minerals to equilibrate within the sea ice brine system, and hence elucidate the validity of assuming brine-mineral equilibrium. This kinetic information could then be combined with solubility measurements to further refine the description of each minerals dynamics.

Further to the kinetic properties of sea ice minerals, the final process relating to their precipitation is mineral nucleation (Kashchiev and Van Rosmalen, 2003). Both mirabilite and hydrohalite can exist in metastable supersaturated conditions in the absence of a suitable nucleation site for the mineral (Butler et al., 2016; Light et al., 2009; Carns et al., 2015). Though sea ice brines likely contain a range of biogenic particles suitable for ice nucleation (Wilson et al., 2015), the suitability of these particles to nucleate mineral precipitation is unknown. During mineral dissolution, metastable conditions of undersaturation cannot exist, which can result in hysteresis, whereby mineral nucleation and total dissolution occur at different temperatures. Hysteresis of hydrohalite precipitation and dissolution in laboratory sea ice was observed by Light et al. (2009) and Carns et al. (2015), indicating that metastable supersaturation could persist in sea ice brines. The tendency for sea ice to remain in these metastable conditions is currently undefined, and could affect the application of equilibrium solubility data to the natural environment.

Combined measurements of mineral kinetics and nucleation in sea ice would require accurate replication of the *in-situ* conditions of brine inclusions, largely relating to their microscale properties and the limitation of mixing. Non-invasive spectroscopic techniques (Bonales et al., 2013; Muñoz-Iglesias et al., 2013; Butler and Kennedy, 2015) could shed light on these aspects of sea ice brine geochemistry, progressing towards a closer representation of the natural environment and helping to elucidate whether sea ice brines exist at, or close to, chemical equilibrium.

7.4.2 Effects of biological exudates

An additional confounding factor that may hinder application of this investigation to natural sea ice concerns the potential effects of biological exudates. Given the confined nature of sea ice brine inclusions, the community of sympagic microorganisms possess the means to alter and ameliorate their surrounding environment by extracellular responses (Ewert and Deming, 2013). One such response is the production of extracellular polymeric substances (EPS), which are observed in high concentrations in sea ice brines (Krembs et al., 2002, 2011; Underwood et al., 2010) due to the abundance of microorganisms combined with physical concentration processes during freezing. EPS are complex organic macromolecules that include lipids, nucleic

acids, proteins and carbohydrates (Underwood et al., 2010), which together exhibit complex behaviour in aqueous solutions (Krembs et al., 2011). Their production by sympagic microalgae and bacteria facilitates adhesion of cells to the surface of brine inclusions (Krembs et al., 2000). Furthermore, the increase in brine viscosity associated with EPS production acts as a protective agent against harmful physico-chemical conditions (Wettlaufer, 2010), and may be an evolutionary adaptation for increasing the volume of habitable liquid in sea ice (Underwood et al., 2010; Krembs et al., 2011).

In addition to EPS, sea ice microorganisms can also modify the freezing properties of brine inclusions by the production of antifreeze proteins (AFP) (Janech et al., 2006; Raymond et al., 2007). The presence of AFP inhibits the crystallisation of ice, and can therefore lower the freezing point of sea ice brines to a temperature below its melting point, an effect known as thermal hysteresis (Bayer-Giraldi et al., 2011). This process has been shown to cause freezing point depression in buffers by approximately 0.9 °C in low salinity conditions and 2.5 °C at high salinity (Bayer-Giraldi et al., 2011), which could contribute to the observed hysteresis of hydrohalite in sea ice outlined previously (Light et al., 2009; Carns et al., 2015).

The combined effect of EPS and AFP on ice formation under *in-situ* conditions relevant to microbial life in sea ice remains largely unknown (Ewert and Deming, 2013). With respect to the work carried out for this thesis, the specific effects on brine freezing properties could compromise the application of mineral solubility data to the natural environment. This mainly relates to the potential for sea ice brine to persist in a supercooled state through the inhibition of freezing. This process could result in altered salinity-temperature relationships for sea ice, with a potential tendency for lower salinity brines to persist upon cooling. Such effects could potentially compromise the accuracy of phase relations (brine-mineral-ice) in sea ice (chapter 5), and also affect brine drainage during ice formation through changes in solution viscosity (Ewert and Deming, 2013). Given the way in which AFP can promote thermal hysteresis (Krembs et al., 2011), it is also possible that the phase relations upon cooling and warming of natural sea ice may be distinct from one-another.

Highlighting confounding factors for applying solubility data to the natural en-

vironment aids in identifying research directions that could resolve the validity of applying these laboratory experiments to natural sea ice. In light of recent advances in the understanding of EPS and AFP in sea ice, there is scope for an assessment of the freezing properties of sea ice brine that is inclusive of biological exudates. Of particular relevance is the measurement of these properties at the microscale of individual brine inclusions, which has never been considered for the sea ice environment. Measurement of microscale freezing properties poses analytical challenges, however it may be feasible to apply methods that have been developed for the study of ice nucleation in supercooled water droplets by aerosol scientists (Whale et al., 2015). Aside from the brine's freezing properties, of additional interest is the potential for EPS to interact with dissolved metals in sea ice brine. The binding of bivalent cations to polysaccharides has already been observed in simple aqueous solutions (Bergmann et al., 2008), and similar processes in sea ice could have implications for the salinity and *p*H of *in-situ* brines (Ewert and Deming, 2013). Such effects may extend to alterations in the mineral dynamics of sea ice defined in this thesis.

Ultimately, investigating the relationships between sympagic microorganisms and the *in-situ* physico-chemical properties of sea ice brine would provide an enhanced understanding of this important physical, chemical and biological system. When used in tandem with the laboratory measurements outlined in this thesis, an evermore robust description of sea ice biogeochemistry can be derived.

7.5 Summary

To summarise, this investigation has provided new and detailed information about the behaviour of mirabilite, gypsum and hydrohalite in the context of sea ice, with their existence ultimately being determined by mineral solubility. The practical difficulties of investigating sea ice minerals in the field has likely resulted in their dynamics being overlooked for many years. Applying laboratory experiments to the natural sea ice system has provided an understanding of these minerals that can be now be advanced upon in solutions with increasing chemical and biological complexity. The results from this work can help to affirm the environmental significance of mirabilite, gypsum, and hydrohalite in sea ice, and hopefully aid in directing researchers to new knowledge gaps for further exploration.

Bibliography

Aagaard, K., Coachman, L., and Carmack, E. (1981). On the halocline of the arctic ocean. *Deep Sea Research Part A. Oceanographic Research Papers*, 28(6):529–545.

Assur, A. (1960). Composition of sea ice and its tensile strength. Technical report, 44, Arctic Sea Ice, U.S. National Academy of Sciences, National Research Council, U.S.A.

Azimi, G., Papangelakis, V., and Dutrizac, J. (2007). Modelling of calcium sulphate solubility in concentrated multi-component sulphate solutions. *Fluid Phase Equilibria*, 260(2):300–315.

Bayer-Giraldi, M., Weikusat, I., Besir, H., and Dieckmann, G. (2011). Characterization of an antifreeze protein from the polar diatom *Fragilariopsis cylindrus* and its relevance in sea ice. *Cryobiology*, 63(3):210–219.

Bergmann, D., Furth, G., and Mayer, C. (2008). Binding of bivalent cations by xanthan in aqueous solution. *International journal of biological macromolecules*, 43(3):245–251.

Berner, R. (1980). *Early Diagenesis: A Theoretical Approach*. Princeton series in geochemistry. Princeton University Press.

Bintanja, R., Van Oldenborgh, G., Drijfhout, S., Wouters, B., and Katsman, C. (2013). Important role for ocean warming and increased ice-shelf melt in Antarctic sea-ice expansion. *Nature Geoscience*, 6(5):376–379.

Biscaye, P. E., Grousset, F. E., Revel, M., Van der Gaast, S., Zielinski, G. A., Vaars, A., and Kukla, G. (1997). Asian provenance of glacial dust (stage 2) in the Greenland Ice sheet Project 2 Ice Core, Summit, Greenland. *Journal of Geophysical Research: Oceans*, 102(C12):26765–26781.

Boeyens, J. C. A. and Ichharam, V. V. H. (2002). Redetermination of the crystal structure of calcium sulphate dihydrate, $CaSO_4 \cdot 2H_2O$. *Zeitschrift fur Kristallographie*, 217:9–19.

Bonales, L., Muñoz-Iglesias, V., Santamaría-Pérez, D., Caceres, M., Fernandez-Remolar, D., and Prieto-Ballesteros, O. (2013). Quantitative Raman spectroscopy as a tool to study the kinetics and formation mechanism of carbonates. *Spectrochimica Acta Part A: Molecular and Biomolecular Spectroscopy*, 116:26–30.

Brand, H. E. A., Fortes, A. D., Wood, I. G., Knight, K. S., and Vočadlo, L. (2009). The thermal expansion and crystal structure of mirabilite ($Na_2SO_410D_2O$) from

4.2 to 300 K, determined by time-of-flight neutron powder diffraction. *Physics and Chemistry of Minerals*, 36(1):29–46.

Butler, B. M. and Kennedy, H. (2015). An investigation of mineral dynamics in frozen seawater brines by direct measurement with synchrotron X-ray powder diffraction. *Journal of Geophysical Research: Oceans*, 120(8):5686–5697.

Butler, B. M., Papadimitriou, S., Santoro, A., and Kennedy, H. (2016). Mirabilite solubility in equilibrium sea ice brines. *Geochimica et Cosmochimica Acta*.

Carns, R. C., Brandt, R. E., and Warren, S. G. (2015). Salt precipitation in sea ice and its effect on albedo, with application to Snowball Earth. *Journal of Geophysical Research: Oceans*, 120(11):7400–7412.

Collins, R. E., Carpenter, S. D., and Deming, J. W. (2008). Spatial heterogeneity and temporal dynamics of particles, bacteria, and pEPS in Arctic winter sea ice. *Journal of Marine Systems*, 74(3):902–917.

Cox, G. and Weeks, W. (1986). Changes in the salinity and porosity of sea-ice samples during shipping and storage. *Journal of Glaciology*, 32(112):371–375.

Cox, G. F. and Weeks, W. F. (1975). Brine drainage and initial salt entrapment in sodium chloride ice. Technical report, DTIC Document.

Cox, G. F. N. and Weeks, W. F. (1983). Equations for determining the gas and brine volumes in sea ice samples. *Journal of Glaciology*, 29(102):306–316.

Cox, G. F. N. and Weeks, W. F. (1988). Numerical simulations of the profile properties of undeformed first-year sea ice during the growth season. *Journal of Geophysical Research: Oceans*, 93(C10):12449–12460.

Croker, M., Baragar, D., and Smith, R. (1975a). Anomalous eutectic growth: II. the relationship between faceted/non-faceted eutectic structures. *Journal of Crystal Growth*, 30(2):198–212.

Croker, M., McParlan, M., Baragar, D., and Smith, R. (1975b). Anomalous eutectic growth: I. the determination of the eutectic structures of Bi-T1Bi_2, Bi-Sn, Sb-Pb and Sb-InSb using an accelerated growth technique. *Journal of Crystal Growth*, 29(1):85–97.

Dieckmann, G. S. and Hellmer, H. H. (2010). The importance of sea ice: An overview. *Sea Ice*, 2:1–22.

Dieckmann, G. S., Nehrke, G., Papadimitriou, S., Göttlicher, J., Steininger, R., Kennedy, H., Wolf-Gladrow, D., and Thomas, D. N. (2008). Calcium carbonate as ikaite crystals in Antarctic sea ice. *Geophysical Research Letters*, 35(8):L08501.

Dittmar, W., Thomson, C., and Buchanan, J. (1873). *Report on Researches Into the Composition of Ocean-Water*. Report on the scientific results of the voyage of H.M.S. Challenger during the years 1873-1876. Physics and chemistry.

DOE (1994). Handbook of methods for the analysis of the various parameters of the carbon dioxide system in sea water; version 2. *A. G. Dickson & C. Goyet*, ORNL/CDIAC.

Dugan, H. A. and Lamoureux, S. F. (2011). The chemical development of a hypersaline coastal basin in the high arctic. *Limnology and Oceanography*, 56(2):495–507.

Durham, W. B., Stern, L. A., Kubo, T., and Kirby, S. H. (2005). Flow strength of highly hydrated Mg and Na-sulfate hydrate salts, pure and in mixtures with water ice, with application to Europa. *Journal of Geophysical Research: Planets*, 110(E12). E12010.

Ebert, E. and Curry, J. (1993). An intermediate one-dimensional thermodynamic sea ice model for investigating ice-atmosphere interactions. *Journal of Geophysical Research*, 98(C6):10085–10109.

Eicken, H. (1992a). The role of sea ice in structuring Antarctic ecosystems. *Polar Biology*, 12(1):3–13.

Eicken, H. (1992b). Salinity profiles of antarctic sea ice: Field data and model results. *Journal of Geophysical Research: Oceans*, 97(C10):15545–15557.

Ewert, M. and Deming, J. W. (2013). Sea ice microorganisms: Environmental constraints and extracellular responses. *Biology*, 2(2):603–628.

Fischer, M., Thomas, D. N., Krell, A., Nehrke, G., Göttlicher, J., Norman, L., Meiners, K. M., Riaux-Gobin, C., and Dieckmann, G. S. (2013). Quantification of ikaite in Antarctic sea ice. *Antarctic Science*, 25(3):421–432.

Fofonoff, N. (1985). Physical properties of seawater: A new salinity scale and equation of state for seawater. *Journal of Geophysical Research: Oceans (1978–2012)*, 90(C2):3332–3342.

Forchhammer, G. (1865). On the composition of sea-water in the different parts of the ocean. *Philosophical Transactions of the Royal Society of London*, 155:203–262.

Fortes, A. D., Wood, I. G., Grigoriev, D., Alfredsson, M., Kipfstuhl, S., Knight, K. S., and Smith, R. I. (2004). No evidence for large-scale proton ordering in Antarctic ice from powder neutron diffraction. *The Journal of chemical physics*, 120(24):11376.

Garrison, D. L., Jeffries, M. O., Gibson, A., Coale, S. L., Neenan, D., Fritsen, C., Okolodkov, Y. B., and Gowing, M. M. (2003). Development of sea ice microbial communities during autumn ice formation in the Ross Sea. *Marine Ecology Progress Series*, 259:1–15.

Gavish, E. and Friedman, G. M. (1973). Quantitative analysis of calcite and Mg-calcite by X-ray diffraction: effect of grinding on peak height and peak area. *Sedimentology*, 20:437–444.

Geilfus, N.-X., Carnat, G., Papakyriakou, T., Tison, J.-L., Else, B., Thomas, H., Shadwick, E., and Delille, B. (2012). Dynamics of pCO_2 and related air-ice CO_2 fluxes in the Arctic coastal zone (Amundsen Gulf, Beaufort Sea). *Journal of Geophysical Research: Oceans*, 117(C9).

Geilfus, N.-X., Galley, R. J., Cooper, M., Halden, N., Hare, A., Wang, F., Søgaard, D. H., and Rysgaard, S. (2013). Gypsum crystals observed in experimental and natural sea ice. *Geophysical Research Letters*, 40(24):6362–6367.

Geilfus, N.-X., Tison, J.-L., Ackley, S. F., Galley, R. J., Rysgaard, S., Miller, L. A., and Delille, B. (2014). Sea ice pCO_2 dynamics and air-ice CO_2 fluxes during the Sea Ice Mass Balance in the Antarctic (SIMBA) experiment - Bellingshausen Sea, Antarctica. *The Cryosphere*, 8(6):2395–2407.

Genkinger, S. and Putnis, A. (2007). Crystallisation of sodium sulfate: supersaturation and metastable phases. *Environmental Geology*, 52:329–337.

Gent, P. R., Danabasoglu, G., Donner, L. J., Holland, M. M., Hunke, E. C., Jayne, S. R., Lawrence, D. M., Neale, R. B., Rasch, P. J., Vertenstein, M., Worley, P. H., Yang, Z.-L., and Zhang, M. (2011). The Community Climate System Model Version 4. *Journal of Climate*, 24(19):4973–4991.

Gitterman, K. E. (1937). Thermal analysis of seawater. Technical report, CRREL TL287, USA Cold Region Research and Engineering Laboratory, Hanover, N.H.

Glassley, W. E. (2001). Elemental composition of concentrated brines in subduction zones and the deep continental crust. *Precambrian Research*, 105:371–383.

Gleitz, M., vd Loeff, M. R., Thomas, D. N., Dieckmann, G. S., and Millero, F. J. (1995). Comparison of summer and winter inorganic carbon, oxygen and nutrient concentrations in Antarctic sea ice brine. *Marine Chemistry*, 51(2):81–91.

Golden, K., Ackley, S., and Lytle, V. (1998). The percolation phase transition in sea ice. *Science*, 282(5397):2238–2241.

Golden, K. M., Eicken, H., Heaton, A. L., Miner, J., Pringle, D. J., and Zhu, J. (2007). Thermal evolution of permeability and microstructure in sea ice. *Geophysical Research Letters*, 34:L16501.

Goosse, H., Campin, J.-M., Fichefet, T., and Deleersnijder, E. (1997). Impact of sea-ice formation on the properties of antarctic bottom water. *Annals of Glaciology*.

Goosse, H. and Fichefet, T. (1999). Importance of ice-ocean interactions for the global ocean circulation: A model study. *Journal of Geophysical Research: Oceans*, 104(C10):23337–23355.

Grasby, S. E., Rod Smith, I., Bell, T., and Forbes, D. L. (2013). Cryogenic formation of brine and sedimentary mirabilite in submergent coastal lake basins, Canadian Arctic. *Geochimica et Cosmochimica Acta*, 110:13–28.

Grenfell, T. C. (1977). The optical properties of ice and snow in the Arctic Basin. *Journal of Glaciology*, 18(80).

Griewank, P. J. and Notz, D. (2013). Insights into brine dynamics and sea ice desalination from a 1-D model study of gravity drainage. *Journal of Geophysical Research: Oceans*, 118(7):3370–3386.

Hassol, S. (2004). *Impacts of a Warming Arctic - Arctic Climate Impact Assessment*. Cambridge University Press.

He, S. and Morse, J. W. (1993). The carbonic acid system and calcite solubility in aqueous Na-K-Ca-Mg-Cl-SO_4 solutions from 0 to 90 °C. *Geochimica et Cosmochimica Acta*, 57(15):3533–3554.

Hogenboom, D., Kargel, J., Ganasan, J., and Lee, L. (1995). Magnesium sulfate-water to 400 MPa using a novel piezometer: Densities, phase equilibria, and planetological implications. *Icarus*, 115(2):258–277.

Holland, P. R. and Kwok, R. (2012). Wind-driven trends in Antarctic sea-ice drift. *Nature Geoscience*, 5(12):872–875.

Horner, R., Ackley, S. F., Dieckmann, G. S., Gulliksen, B., Hoshiai, T., Legendre, L., Melnikov, I. A., Reeburgh, W. S., Spindler, M., and Sullivan, C. W. (1992). Ecology of sea ice biota. *Polar Biology*, 12(3-4):417–427.

Howarth, R. W. (1978). A rapid and precise method for determining sulfate in seawater, estuarine waters, and sediment pore waters. *Limnology and Oceanography*, 23(5):1066–1069.

Hunke, E. C., Lipscomb, W. H., Turner, A. K., Jerrery, N., and Elliot, S. (2015). CICE: the Los Alamos Sea Ice Model documentation and software users manual version 5.1 LA-CC-06-012. *T-3 Fluid Dynamics Group, Los Alamos National Laboratory*, 675.

Jackett, D. R., McDougall, T. J., Feistel, R., Wright, D. G., and Griffies, S. M. (2006). Algorithms for density, potential temperature, conservative temperature, and the freezing temperature of seawater. *Journal of Atmospheric and Oceanic Technology*, 23(12):1709–1728.

Janech, M. G., Krell, A., Mock, T., Kang, J.-S., and Raymond, J. A. (2006). Ice-binding proteins from sea ice diatoms(Bacillariophyceae). *Journal of Phycology*, 42(2):410–416.

Kargel, J. S. (1991). Brine volcanism and the interior structures of asteroids and icy satellites. *Icarus*, 94:368–390.

Kashchiev, D. and Van Rosmalen, G. (2003). Review: nucleation in solutions revisited. *Crystal Research and Technology*, 38(7-8):555–574.

Kester, D. R., Duedall, I. W., Connors, D. N., and Pytkowicz, R. M. (1967). Preparation of artifical seawater. *Limnology and Oceanography*, 12(1):176–179.

King, B. A., Firing, E., and Joyce, T. M. (2001). *Ocean Circulation and Climate: Observing and Modelling the Global Ocean*, chapter Shipboard observations during WOCE. International geophysics series. Academic Press, San Fransisco CA, USA.

Klewe, B. and Pederson, B. (1974). The crystal structure of sodium chloride dihydrate. *Acta Crystallographica*, B30:2363–2371.

Koutsoukos, P. G., Kofina, A. N., and Kanellopoulou, D. G. (2007). Solubility of salts in water: Key issues for crystal growth and dissolution processes. *Pure and Applied Chemistry*, 79(5):825–850.

Krembs, C., Eicken, H., and Deming, J. W. (2011). Exopolymer alteration of physical properties of sea ice and implications for ice habitability and biogeochemistry in a warmer arctic. *Proceedings of the National Academy of Sciences*, 108(9):3653–3658.

Krembs, C., Eicken, H., Junge, K., and Deming, J. (2002). High concentrations of exopolymeric substances in Arctic winter sea ice: implications for the polar ocean carbon cycle and cryoprotection of diatoms. *Deep Sea Research Part I: Oceanographic Research Papers*, 49(12):2163–2181.

Krembs, C., Gradinger, R., and Spindler, M. (2000). Implications of brine channel geometry and surface area for the interaction of sympagic organisms in Arctic sea ice. *Journal of Experimental Marine Biology and Ecology*, 243(1):55–80.

Kubicki, J. D. (2008). *Kinetics of water-rock interaction*. Springer, New York, NY.

Leppäranta, M. (1993). A review of analytical models of sea ice growth. *Atmosphere-Ocean*, 31(1):123–138.

Levy, H. A. and Lisensky, G. (1978). Crystal structures of sodium sulfate decahydrate (Glaubers salt) and sodium tetraborate decahydrate (borax). Redetermination by neutron diffraction. *Acta Crystallographica Section B*, B34:3502–3510.

Lewis, E. (1980). The practical salinity scale 1978 and its antecedents. *IEEE Journal of Oceanic Engineering*, 5(1):3–8.

Light, B., Brandt, R. E., and Warren, S. G. (2009). Hydrohalite in cold sea ice: Laboratory observations of single crystals, surface accumulations, and migration rates under a temperature gradient, with application to Snowball Earth. *Journal of Geophysical Research*, 114(C7):C07018.

Light, B., Maykut, G. A., and Grenfell, T. C. (2003). Effects of temperature on the microstructure of first-year Arctic sea ice. *Journal of Geophysical Research*, 108(C2):3051.

Light, B., Maykut, G. A., and Grenfell, T. C. (2004). A temperature-dependent, structural-optical model of first-year sea ice. *Journal of Geophysical Research*, 109:C06013.

Loeb, V., Siegel, V., Holm-Hansen, O., Hewitt, R., Fraser, W., Trivelplece, W., and Trivelplece, S. (1997). Effects of sea-ice extent and krill or salp dominance on the Antarctic food web. *Nature*, 387(6636):897–900.

Marion, G. M. (1997). A theoretical evaluation of mineral stability in Don Juan Pond, Wright Valley, Victoria Land. *Antarctic Science*, 9(1):92–99.

Marion, G. M. and Farren, R. E. (1997). Gypsum solubility at subzero temperatures. *Soil Science Society of America Journal*, 61:1666–1671.

Marion, G. M. and Farren, R. E. (1999). Mineral solubilities in the Na-K-Mg-Ca-Cl-SO_4-H_2O system: A re-evaluation of the sulfate chemistry in the Spencer-Moller-Weare model. *Geochimica et Cosmochimica Acta*, 63(9):1305–1318.

Marion, G. M., Farren, R. E., and Komrowski, A. J. (1999). Alternative pathways for seawater freezing. *Cold Regions Science and Technology*, 29:259–266.

Marion, G. M. and Grant, S. G. (1994). FREZCHEM: A chemical thermodynamic model for aqueous solutions at subzero temperatures. Technical report, DTIC Document.

Marion, G. M. and Kargel, J. S. (2008). *Cold Aqueous Planetary Geochemistry with FREZCHEM*. Springer, Heidelberg.

Marion, G. M., Mironenko, M. V., and Roberts, M. W. (2010). FREZCHEM: A geochemical model for cold aqueous solutions. *Computers & Geosciences*, 36:10–15.

Martin, S. and Kauffman, P. (1981). A field and laboratory study of wave damping by grease ice. *Journal of Glaciology*, 27:283–313.

Maykut, G. and Light, B. (1995). Refractive-index measurements in freezing sea-ice and sodium chloride brines. *Applied Optics*, 34(6):950–961.

Maykut, G. A. (1978). Energy exchange over young sea ice in the central Arctic. *Journal of Geophysical Research: Oceans*, 83(C7):3646–3658.

McCaffrey, M., Lazar, B., and Holland, H. (1987). The evaporation path of seawater and the coprecipitation of Br^- and K^+ with halite. *Journal of Sedimentary Research*, 57(5):928–937.

McCarthy, C., Cooper, R. F., Kirby, S. H., Rieck, K. D., and Stern, L. A. (2007). Solidification and microstructures of binary ice-I/hydrate eutectic aggregates. *American Mineralogist*, 92(10):1550–1560.

McCleskey, R. B., Nordstrom, D. K., Ryan, J. N., and Ball, J. W. (2012). A new method of calculating electrical conductivity with applications to natural waters. *Geochimica et Cosmochimica Acta*, 77:369–382.

Miller, L. A., Papakyriakou, T. N., Collins, R. E., Deming, J. W., Ehn, J. K., Macdonald, R. W., Mucci, A., Owens, O., Raudsepp, M., and Sutherland, N. (2011). Carbon dynamics in sea ice: A winter flux time series. *Journal of Geophysical Research: Oceans*, 116(C2). C02028.

Millero, F. (2005). *Chemical Oceanography, Third Edition*. Marine science series. Taylor & Francis.

Millero, F. J., Feistel, R., Wright, D. G., and McDougall, T. J. (2008). The composition of Standard Seawater and the definition of the Reference-Composition Salinity Scale. *Deep Sea Research Part I*, 55:50–72.

Millero, F. J. and Huang, F. (2009). The density of seawater as a function of salinity (5 to 70 g kg^{-1}) and temperature (273.15 to 363.15 K). *Ocean Science*, 5(2):91–100.

Millero, F. J. and Leung, W. H. (1976). The thermodynamics of seawater at one atmosphere. *American Journal of Science*, 276(9):1035–1077.

Millero, F. J. and Poisson, A. (1981). International one-atmosphere equation of state of seawater. *Deep Sea Research*, 28A(6):625–629.

Milliman, J. D. and Bornhold, B. D. (1973). Peak height versus peak intensity analysis of X-ray diffraction data. *Sedimentology*, 20:445–448.

Muñoz-Iglesias, V., Bonales, L. J., and Prieto-Ballesteros, O. (2013). *p*H and salinity evolution of Europa's brines: Raman spectroscopy study of fractional precipitation at 1 and 300 bar. *Astrobiology*, 13:693–702.

Mucci, A. (1983). The solubility of calcite and aragonite in seawater at various salinities, temperatures, and one atmosphere total pressure. *American Journal of Science*, 283:780–799.

Mulvaney, R., Abram, N. J., Hindmarsh, R. C., Arrowsmith, C., Fleet, L., Triest, J., Sime, L. C., Alemany, O., and Foord, S. (2012). Recent Antarctic Peninsula warming relative to Holocene climate and ice-shelf history. *Nature*, 489(7414):141–144.

Munro, D. R., Dunbar, R. B., Mucciarone, D. A., Arrigo, K. R., and Long, M. C. (2010). Stable isotope composition of dissolved inorganic carbon and particulate organic carbon in sea ice from the Ross Sea, Antarctica. *Journal of Geophysical Research: Oceans*, 115(C9). C09005.

Nelson, K. H. and Thompson, T. G. (1954). Deposition of salts from sea water by frigid concentration. Technical report, 29, Office of Naval Research, Arlington, VA.

Norman, L., Thomas, D. N., Stedmon, C. A., Granskog, M. A., Papadimitriou, S., Krapp, R. H., Meiners, K. M., Lannuzel, D., van der Merwe, P., and Dieckmann, G. S. (2011). The characteristics of dissolved organic matter (DOM) and chromophoric dissolved organic matter (CDOM) in antarctic sea ice. *Deep Sea Research Part II: Topical Studies in Oceanography*, 58(910):1075–1091.

Norrish, K. and Taylor, R. (1962). Quantitative analysis by X-ray diffraction. *Clay Minerals Bulletin*, 5(28):98–109.

Notz, D. (2005). *Thermodynamic and fluid-dynamical processes in sea ice*. PhD thesis, University of Cambridge.

Notz, D. and Worster, M. G. (2009). Desalination processes of sea ice revisited. *Journal of Geophysical Research*, 114:C05006.

Oswald, I. D. H., Hamilton, A., Hall, C., Marshall, W. G., Prior, T. J., and Pulham, C. R. (2008). *In-situ* characterization of elusive salt hydrates. The crystal structures of the heptahydrate and octahydrate of sodium sulfate. *Journal of the American Chemical Society*, 130:17795–17800.

Papadimitriou, S., Kennedy, H., Kattner, G., Dieckmann, G., and Thomas, D. (2004). Experimental evidence for carbonate precipitation and CO_2 degassing during sea ice formation. *Geochimica et Cosmochimica Acta*, 68(8):1749–1761.

Papadimitriou, S., Kennedy, H., Kennedy, P., and Thomas, D. N. (2013). Ikaite solubility in seawater-derived brines at 1 atm and sub-zero temperatures to 265 K. *Geochimica et Cosmochimica Acta*, 109:241–253.

Papadimitriou, S., Kennedy, H., Kennedy, P., and Thomas, D. N. (2014). Kinetics of ikaite precipitation and dissolution in seawater-derived brines at sub-zero temperatures to 265 K. *Geochimica et Cosmochimica Acta*, 140:199–211.

Papadimitriou, S., Thomas, D. N., Kennedy, H., Haas, C., Kuosa, H., Krell, A., and Dieckmann, G. S. (2007). Biogeochemical composition of natural sea ice brines from the Weddell Sea during early austral summer. *Limnology and Oceanography*, 52(5):1809–1823.

Pawlowicz, R. (2012). The electrical conductivity of seawater at high temperatures and salinities. *Desalination*, 300:32–39.

Pawlowicz, R. (2015). The absolute salinity of seawater diluted by riverwater. *Deep Sea Research Part I: Oceanographic Research Papers*, 101:71–79.

Perkin, R. G. and Lewis, E. L. (1980). The Practical Salinity Scale 1978: fitting the data. *Oceanic Engineering*, 5(1):9–16.

Petrich, C. and Eicken, H. (2010). Growth, structure and properties of sea ice. *Sea Ice*, 2:23–77.

Pitzer, K. (1991). Ion interaction approach: theory and data correlation. *Activity coefficients in electrolyte solutions*, 2:75–153.

Pitzer, K. S. (1973). Thermodynamics of electrolytes. I. theoretical basis and general equations. *The Journal of Physical Chemistry*, 77(2):268–277.

Pitzer, K. S. and Mayorga, G. (1973). Thermodynamics of electrolytes. II. activity and osmotic coefficients for strong electrolytes with one or both ions univalent. *The Journal of Physical Chemistry*, 77(19):2300–2308.

Plummer, L. N., Parkhurst, D., Fleming, G., and Dunkle, S. (1988). A computer program incorporating Pitzer's equations for calculation of geochemical reactions in brines. Technical report, Department of the Interior, US Geological Survey.

Pringle, D., Eicken, H., Trodahl, H., and Backstrom, L. (2007). Thermal conductivity of landfast Antarctic and Arctic sea ice. *Journal of Geophysical Research: Oceans*, 112(C4).

Prospero, J., Glaccum, R., and Nees, R. (1981). Atmospheric transport of soil dust from Africa to South America. *Nature*, 289:570–572.

Pytkowicz, R. and Hawley, J. (1974). Bicarbonate and carbonate ion-pairs and a model of seawater at 25 °C. *Limnology and Oceanography*, 19(2):223–234.

Pytkowicz, R. M. and Kester, D. R. (1969). Harned's rule behavior of NaCl-Na_2SO_4 solutions explained by an ion association model. *American Journal of Science*, 267(2):217–229.

Raymond, J. A., Fritsen, C., and Shen, K. (2007). An ice-binding protein from an Antarctic sea ice bacterium. *FEMS microbiology ecology*, 61(2):214–221.

Rees Jones, D. W. and Worster, M. G. (2014). A physically based parameterization of gravity drainage for sea-ice modeling. *Journal of Geophysical Research: Oceans*, 119(9):5599–5621.

Reznik, I. J., Gavrieli, I., and Ganor, J. (2009). Kinetics of gypsum nucleation and crystal growth from Dead Sea brine. *Geochimica et Cosmochimica Acta*, 73(20):6218–6230.

Richardson, C. (1976). Phase relationships in sea ice as a function of temperature. *Journal of Glaciology*, 17(77):507–519.

Ringer, W. E. (1906). De varanderingon in samenstelling van zeewater bij het bevriezen. *Chemisch Weekblack*, 3:223–249.

Roedder, E. (1984). Fluid inclusions. *Reviews in Mineralogy*, 12:1–646.

Rysgaard, S., Bendtsen, J., Delille, B., Dieckmann, G. S., Glud, R. N., Kennedy, H., Mortensen, J., Papadimitriou, S., Thomas, D. N., and Tison, J.-L. (2011). Sea ice contribution to the air–sea CO_2 exchange in the Arctic and Southern Oceans. *Tellus B*, 63(5):823–830.

Rysgaard, S., Glud, R., Lennert, K., Cooper, M., Halden, N., Leaky, R., Hawthorne, F., and Barber, D. (2012). Ikaite crystals in melting sea ice–implications for pCO_2 and pH levels in Arctic surface waters. *The Cryosphere Discussions*, 6:1–8.

Rysgaard, S. and Glud, R. N. (2004). Anaerobic N_2 production in Arctic sea ice. *Limnology and Oceanography*, 49(1):86–94.

Schallenberg, M., Hall, C. J., and Burns, C. W. (2003). Consequences of climate-induced salinity increases on zooplankton abundance and diversity in coastal lakes. *Marine Ecology Progress Series*, 251:181–189.

Schütz, L. and Sebert, M. (1987). Mineral aerosols and source identification. *Journal of Aerosol Science*, 18(1):1–10.

Sha, L. (2012). Concurrent fractional and equilibrium crystallisation. *Geochimica et Cosmochimica Acta*, 86:52–75.

Shaffer, L. H. (1967). Solubility of gypsum in sea water and sea water concentrates at temperatures from ambient to 65. degree. *Journal of Chemical and Engineering Data*, 12(2):183–189.

Spencer, R. J., Moller, N., and Weare, J. H. (1990). The prediction of mineral solubilities in natural waters : A chemical equilibrium model for the Na-K-Ca-Mg-Cl-SO_4-H_2O system at temperatures below 25 °C. *Geochimica et Cosmochimica Acta*, 54:575–590.

Steffensen, J. P. (1997). The size distribution of microparticles from selected segments of the Greenland Ice Core Project ice core representing different climatic periods. *Journal of Geophysical Research: Oceans*, 102(C12):26755–26763.

Stumm, W. and Morgan, J. (1996). *Aquatic chemistry: chemical equilibria and rates in natural waters*. Environmental science and technology. Wiley.

Sturm, M. and Massom, R. A. (2010). Snow and sea ice. *Sea Ice*, 2:153–204.

Thomas, D. N. and Dieckmann, G. S. (2002). Antarctic Sea ice – a habitat for extremophiles. *Science*, 295:641–644.

Thomas, D. N., Papadimitriou, S., and Michel, C. (2010). Biogeochemistry of sea ice. *Sea Ice*, 2:425–467.

Toner, J., Catling, D., and Light, B. (2014). The formation of supercooled brines, viscous liquids, and low-temperature perchlorate glasses in aqueous solutions relevant to Mars. *Icarus*, 233:36–47.

Turner, A. K., Hunke, E. C., and Bitz, C. M. (2013). Two modes of sea-ice gravity drainage: A parameterization for large-scale modeling. *Journal of Geophysical Research: Oceans*, 118(5):2279–2294.

Underwood, G. J., Fietz, S., Papadimitriou, S., Thomas, D. N., and Dieckmann, G. (2010). Distribution and composition of dissolved extracellular polymeric substances (EPS) in Antarctic sea ice. *Marine Ecology Progress Series*, 404:1–19.

Vancoppenolle, M., Bitz, C. M., and Fichefet, T. (2007). Summer landfast sea ice desalination at point barrow, alaska: Modeling and observations. *Journal of Geophysical Research: Oceans*, 112(C4). C04022.

Vaughan, D., Comiso, J., Allison, I., Carrasco, J., Kaser, G., Kwok, R., Mote, P., Murray, T., Paul, F., Ren, J., Rignot, E., Solomina, O., Steffen, K., and Zhang, T. (2013). *Observations: Cryosphere*, book section 4, page 317382. Cambridge University Press, Cambridge, United Kingdom and New York, NY, USA.

Vavouraki, A. I. and Koutsoukos, P. G. (2012). Kinetics of crystal growth of mirabilite in aqueous supersaturated solutions. *Journal of Crystal Growth*, 338(1):189–194.

Wang, Y. W., Kim, Y. Y., Christenson, H. K., and Meldrum, F. C. (2012). A new precipitation pathway for calcium sulfate dihydrate (gypsum) via amorphous and hemihydrate intermediates. *Chemical Communications*, 48(4):504–506.

Weeks, W. (2010). *On Sea Ice*. University of Alaska Press.

Weeks, W. F. and Ackley, S. F. (1986). *The growth, structure, and properties of sea ice*. Springer.

Wettlaufer, J. S. (2010). Sea ice and astobiology. *Sea Ice*, 2:579–591.

Whale, T. F., Murray, B. J., O'Sullivan, D., Wilson, T. W., Umo, N. S., Baustian, K. J., Atkinson, J. D., Workneh, D. A., and Morris, G. J. (2015). A technique for quantifying heterogeneous ice nucleation in microlitre supercooled water droplets. *Atmospheric Measurement Techniques*, 8(6):2437–2447.

Wilson, T. W., Ladino, L. A., Alpert, P. A., Breckels, M. N., Brooks, I. M., Browse, J., Burrows, S. M., Carslaw, K. S., Huffman, J. A., Judd, C., Kilthau, W. P., Mason, R. H., McFiggans, G., Miller, L. A., Najera, J. J., Polishchuk, E., Rae, S., Schiller, C. L., Si, M., Temprado, J. V., Whale, T. F., Wong, J. P. S., Wurl, O., Yakobi-Hancock, J. D., Abbatt, J. P. D., Aller, J. Y., Bertram, A. K., Knopf, D. A., and Murray, B. J. (2015). A marine biogenic source of atmospheric ice-nucleating particles. *Nature*, 525(7568):234–238.

Wu, X., He, W., Guan, B., and Wu, Z. (2010). Solubility of calcium sulfate dihydrate in Ca-Mg-K chloride salt solution in the range of 348.15 to 371.15 K. *Journal of Chemical Engineering Data*, 55:2100–2107.

Zimmermann, F., Weinbruch, S., Schtz, L., Hofmann, H., Ebert, M., Kandler, K., and Worringen, A. (2008). Ice nucleation properties of the most abundant mineral dust phases. *Journal of Geophysical Research: Atmospheres*, 113(D23). D23204.

Zolotov, M. Y. and Shock, E. L. (2001). Composition and stability of salts on the surface of europa and their oceanic origin. *Journal of Geophysical Research: Planets*, 106(E12):32815–32827.